The study of magnetic and polaronic microstructure in $Pr_{1-x}Ca_xMnO_3$ manganite series

Dissertation

zur Erlangung des mathematisch-naturwissenschaftlichen Doktorgrades

"Doctor rerum naturalium"

der Georg-August-Universität Göttingen

im Promotionsprogramm ProPhys

der Georg-August University School of Science (GAUSS)

vorgelegt von

Sangeeta Rajpurohit

aus Mount Abu, Indien

Göttingen, 2018

Betreuungsausschuss

Prof. Dr. Peter E. Blöchl,
Institut für Theoretische Physik,
Technische Universität Clausthal

Prof. Dr. Christian Jooss,
Institut für Materialphysik Physik,
Georg-August-Universität Göttingen

Prof. Dr. Marcus Müller,
Institut für Theoretische Physik,
Georg-August-Universität Göttingen

Mitglieder der Prüfungskommission

Prof. Dr. Peter E. Blöchl,
Institut für Theoretische Physik,
Technische Universität Clausthal

Prof. Dr. Christian Jooss,
Institut für Materialphysik Physik,
Georg-August-Universität Göttingen

Weitere Mitglieder der Prüfungskommission

Prof. Dr. Marcus Müller,
Institut für Theoretische Physik,
Georg-August-Universität Göttingen

PD. Dr. Salvatore R. Manmana,
Institut für Theoretische Physik,
Georg-August-Universität Göttingen

PD. Dr. Martin Wenderoth,
4$^{\text{th}}$ Institute of Physics,
Georg-August-Universität Göttingen

Prof. Dr. Michael Seibt,
4$^{\text{th}}$ Institute of Physics,
Georg-August-Universität Göttingen

Tag der muïndlichen Prűfung: 16 July, 2018

Abstract

Manganites have been studied intensively due to their extraordinary properties: colossal magnetoresistance and ferroelectricity. The inhomogeneities present in certain regions of the phase diagram are believed to be responsible for these novel properties. The nature of these inhomogeneities that critically depends on the interaction between charge, atomic and spin degrees of freedom are yet poorly understood. Furthermore, there still remains a significant scope to theoretically investigate the characteristics of the long-living metastable states experimentally found in manganites. We propose a microscopic model of manganites to study the overall electronic, atomic and magnetic microstructure of the three-dimensional $Pr_{1-x}Ca_xMnO_3$ manganite series.

Firstly, we investigate the phase diagram of a hypothetical one-dimensional system to find out the relevant length scales. The study of relaxation dynamics in the one-dimensional system under external light pulse give us the relevant timescales of the response from the charge, lattice and spin subsystem. The length and time scales extracted from our one-dimensional study assist us to investigate the three-dimensional real systems.

Secondly, we carried out a comprehensive study of the low-temperature phase diagram of the three-dimensional $Pr_{1-x}Ca_xMnO_3$ manganite series with the proposed model. The model predicts several distinct phases with characteristic charge and orbital ordering together with an associated magnetic structure. The structures at $x=0.125$, 0.25, 0.66 and 0.25 are different from the one obtained by earlier theoretical studies. With the large system size, our study reveals the presence of inhomogeneous phases in certain doping regions. The nature of the inhomogeneous states are capable of demonstrating several experimental findings in manganites. The model also allowed us to study the non-collinear spin structures. The charge and orbital order at $x=0.125$ and $x=0.66$ are associated with canted and a spiral spin-structure. The defect-induced local disorders in the CE-type phase leads to formation of the metastable structures close to $x=0.5$.

Finally, we studied the dynamics of the three-dimensional manganites under external light pulse to investigate the role of spin and lattice degrees of freedom in their relaxation mechanisms. The system subjected to the high-and low-intensity light pulse undergo different relaxation pathways. In the low-intensity case at $x=0.5$, a long-lived carrier state characterised by no charge and orbital ordering is observed due to emergence of ferromagnetism in the system. On the other hand, the electronic subsystem relaxes through conical interactions and form single site JT polarons in the high-intensity case. The conical intersection is lattice and spin assisted. The longer timescale relaxation process is dominated by thermally activated polaron hopping. [1]

Acknowledgements

First of all, I would like to express my deepest gratitude to my supervisor Prof. P. E. Blöchl for his invaluable guidance and advice that he provided me all the way from the beginning to the end of my PhD. I would like to thank him for his continuous encouragement and providing me every bit of guidance and for allowing me to grow as a researcher.

I also want to thank Dr. Salvatore Manmana and Prof. Christian Jooss for the project related several helpful discussions with them. I would like to thank Debanjan Basu, Robert Schade, Mohsen Sotoudeh and Michael Brink for all the help and support during my PhD. My special thank to Sigrid Frömmel for her help related to the bureaucratic and University paper work. I appreciate the help of Axel Ehrich related to all the technical issues.

Contents

List of Figures

x

List of Tables

Chapter 1

Manganites: A short review

1.1 Introduction

The study of strongly correlated electron systems that involve 3d or 4f elements is among the most challenging branches of solid state physics. The interaction between electrons, or between electrons and phonons, or electrons and spins, in these materials leads to a correlated state, which results in several novel physical phenomena ranging from high-T_c superconductivity in layered cuprates, metal-insulator transition (Mott insulator) in nickel oxides, to colossal magnetoresistance and multiferroicity in manganites [2–5]

The theoretical progress in the field of manganites is greatly curiosity driven due to the involvement of the fundamental physical aspects. The CMR effect was theoretically tried to understand in the framework of double-exchange (DE) mechanism by Zener [6], which explains the coupling between magnetic and charge degree of freedom. Thereafter, Anderson and Hasegawa [7] and de Gennes followed the work by detailed study. Later, Millis recognised that the double-exchange mechanism and theories related are not enough to explain the quantitative changes in the resistivity and the low transition temperature [8–10]. Millis et al. emphasised on the participation of phonons by polaron formation to explain the quantitative agreement with the experiments. Subsequently several other mechanism like charge and orbital ordering together with polaron formation were proposed to understand the physics behind the subtle properties found in these system. Nowadays, the sophisticated models that involve the important effects, such as Jahn-Teller (JT), super-exchange interaction, and Coulomb (Hubbard U) interactions are capable of predicting most of the part of the phase diagram of manganites. But the inadequacy of the presents models to elucidate the nature of inhomogeneities in the phase-separation region of the phase diagram gives a wide scope to new theoretical models to fill.

More recently, the attention towards manganites has been extended due to their interaction with light, i.e., the photovoltaic properties [11, 12]. This further adds an extra external coupling possibility to these materials due to the photo-induced effect, making them one of the promising candidates for future energy devices. In the work of

Ichikawa et al. [13, 14], it is shown that when the $Nd_{0.5}Sr_{0.5}MnO_3$ shone by visible light, a new macroscopic excited state is achieved that exhibits completely different structural, electronic and magnetic orders, when compared to its ground state. This is knows as "photo-induced phase transition". It may lead to a long-lived metastable state that could have a slow relaxation process. On theoretical side, one of the major challenges is to understand the nature of the metastable state in which the system may remain trapped leading to long-lived excited states. Exploring the nature of charge-carrier, and their creation and separation mechanisms are the other additional aspects of the relaxation dynamics which still need to be answered. On the one hand, there is a need to have a information about the band structure and the electronic-lattice structural state with the local magnetic moments to govern the probing of the material externally. On the other hand, a great interest has arisen to understand the relaxation dynamics particularly through non-adiabatic process which a strong effect on the dynamics of a system and the recombination rates on femtosecond timescale.

1.2   Outline of the thesis

In the present thesis, we will primarily focus on the electronic, lattice and magnetic order in the $Pr_{1-x}Ca_xMnO_3$ series where the modulation of these orders with doping is analysed carefully. Later we study the role of spin as well as lattice degrees of freedom in relaxation mechanism in the perovskite manganites. Broadly, we divide our studies into two categories: one-dimensional chain and three-dimensional systems. Chapter 1 is devoted to a brief literature study to summarise the experimental and theoretical work conducted in the context of perovskite manganites, especially $Pr_{1-x}Ca_xMnO_3$ series. Chapter 2 introduces the microscopic model extracted from the ab-initio calculations, which we use in later Chapters. In Chapter 3, we study the phase diagram in the one-dimensional system and propose a coarse grained polaron model. In Chapter 4, we investigate the low temperature electronic, atomic and magnetic microstructure as a function of doping. A complete low-temperature phase diagram of $Pr_{1-x}Ca_xMnO_3$ is put forward. The following two Chapters 5 and 6 are devoted to the relaxation dynamics under external light pulse for the one-dimensional and three-dimensional systems, respectively, and the role of lattice and spin degrees of freedom in relaxation mechanism is investigated. The possibilities to manipulate the physical properties of the system goes beyond these few examples given above. Lastly, the work presented in the thesis is summarised and an outlook into future research possibility is given in Chapter 7.

In the present chapter, we briefly review the literature on the mixed-valence perovskite manganite systems, especially $Pr_{1-x}Ca_xMnO_3$ series. Furthermore, issues like the exchange interactions, the metal-insulator transition, the electronic transport mechanisms, the polaron formation and the Jahn-Teller effect are discussed in the context of the well established theoretical and experimental understanding of these materials.

1.3 Perovskite-type oxides

Originally, the 'perovskite' name was given to the mineral calcium titanate $CaTiO_3$. Nowadays, this name is used for the class of materials that has the crystal structure of $CaTiO_3$. By and large, two types of manganite perovskites have played a crucial role in the field of CMR oxides: the conventional perovskite structured and the Ruddlesden-Popper structured oxides. The perovskite structure has a ABX_3-type chemical formula where B is a 3d transition metal element (e.g., Cr, Mn, Fe, Co) and X is a non metallic anion. In the case of oxides, X is an oxygen (O) atom. The common examples of these oxide classes are titanates and manganites where Ti (titanium) is the B-type central cation ion in the former and the later has Mn ion. We focus on perovskite manganites in this thesis.

1.3.1 Mn based oxides: Manganites

The perovskite manganite is one of the most fascinating class of transition metal oxides where the states near the Fermi level are mainly composed of the d-orbitals of B-type cations ($B = Mn^{3+}/Mn^{4+}$) and dictate the transport properties of the system. A prototypical example is the undoped antiferromagnetic insulator $PrMnO_3$ (PMO). The perovskite manganites show very rich phase diagram as their properties can be changed by altering the composition of the elements. For example, the bandwidth of $Nd_{0.5}Sr_{0.5}MnO_3$ can be reduced by replacing Nd atom by La atom. Similarly, the undoped low-temperature insulating system can be changed to a metallic system by an optimal hole doping via the divalent ions, such as Ca and Sr.

1.4 Crystal structure

Figure 1.1 shows a typical ABO_3 perovskite structure with the corresponding isolated unit cell. The B-type ions (Mn^{3+}/Mn^{4+}) fill the voids at the centres of the octahedral cages created by O atoms while the A-type ions (Ca^{2+}, Sr^{2+}, La^{3+}, Pr^{3+}, etc.) occupy
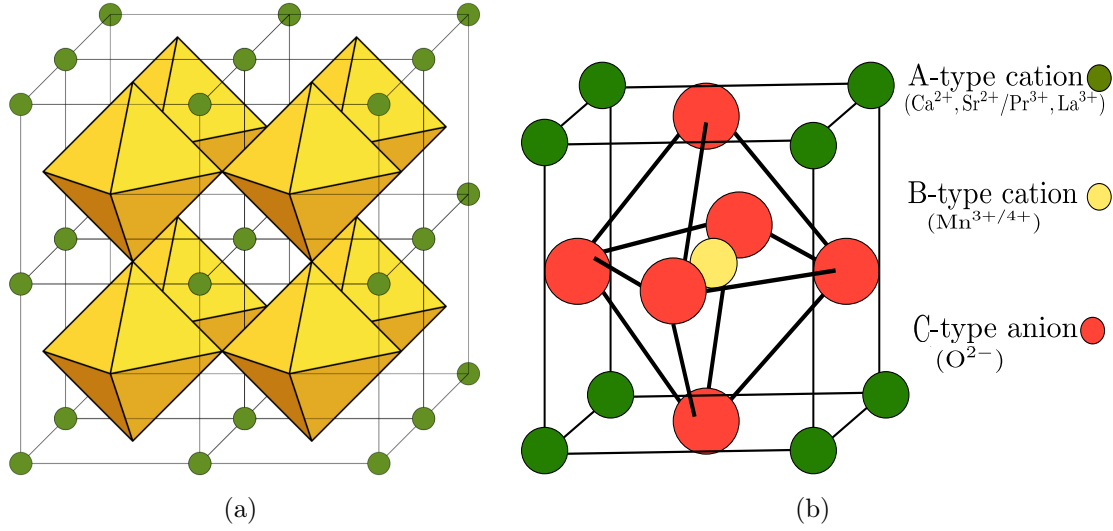
Figure 1.1: Structure of ABO_3 type perovskite manganite system. (a) Three dimensional cubic crystal structure of ABO_3 type perovskite oxides. (b) single unit cell of perovskite-manganite with O ligands and Mn cation, in the presence of A-type cation (Figure credit: *Quantum Mechanics of the Chemical Bond* by P.E. Blöchl)

the interstitial spaces surrounded by the O-octahedra. In the centro-symmetrical cubic perovskite systems, the B-type ions sit at the centre, the O-type ions at the face-centre and the A-type ions at the corners of the cube.

Various interesting functionalities of manganites originate directly from the characteristic perovskite crystal structure due to the crystal field splitting in the presence of the O ligands. In an octahedral ligand field of O atoms, the fivefold 3d orbitals of the central Mn cation split into the subset of the e_g ($d_{3z^2-r^2}$ and $d_{x^2-y^2}$) and t_{2g} (d_{xy}, d_{yz} and d_{zx}) orbitals (Figure 2.1). As the lobes of the e_g orbitals directly point towards the ligands, they lie higher in energy than the corresponding t_{2g} orbitals where the lobes are pointing in between the O ligands. This separation between the e_g and t_{2g} states is given by the crystal field energy ΔCF, which is around 2 eV [15]. If one of the e_g state of a Mn ion is occupied, the degeneracy of the e_g subset further lifts up due to simultaneous distortion of the O-octahedra surrounding the Mn ion. This lattice distortion due to the occupied e_g state is know as the Jahn-Teller (JT) effect (discussed in Section 2.2.1).

The observed steric distortions in the system of an ideal cubic structure are driven by the Jahn-Teller effect and the bending of the Mn-O-Mn bridge, due to tilting, of the connected octahedra due to the misfit of a A-type cation. The JT effect and the tilting have direct influence on the structural, magnetic and electrical properties of the system.
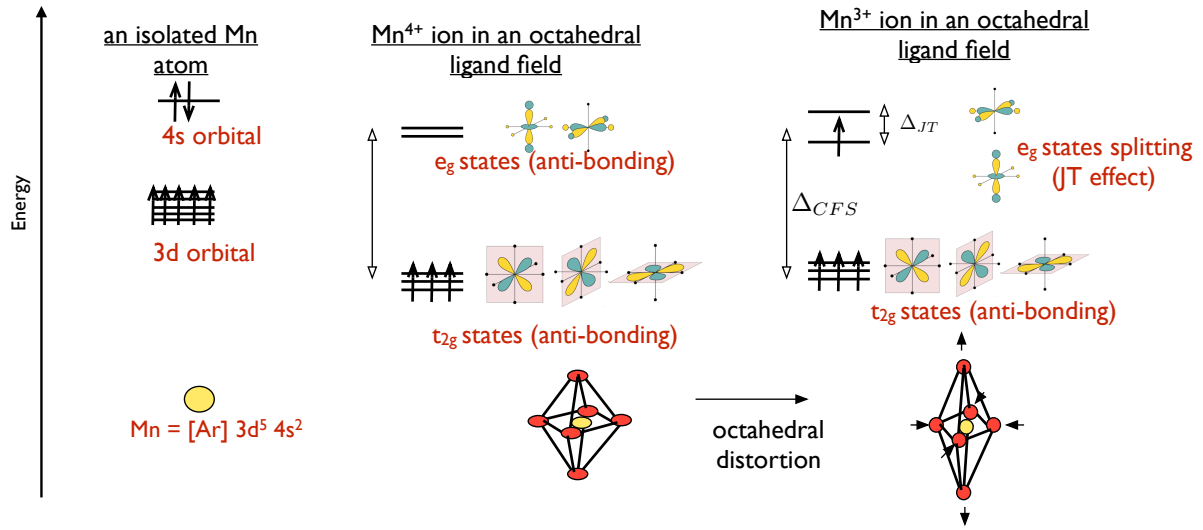
Figure 1.2: Crystal field splitting in the presence of O ligands: the d-states of Mn ion split into two groups: the low-lying localised t_{2g} states, which has three electrons and the high-lying localised e_g states which has either one (Mn^{3+}) or no electron (Mn^{4+})

1.4.1 Jahn-Teller effect

In manganite systems with Mn^{3+} or Mn^{4+} ions, the Mn-d states are not purely d-type but anti-bonding in nature. The Mn-d states are formed due to hybridisation of nearby O-p states (see Figure 2.1). Out of these five anti-bonding d-states, the majority t_{2g} states are occupied. If any of the two remaining anti-bonding e_g states is occupied, the octahedron surrounding the Mn^{3+} ion distorts. When an octahedron distorts, an additional crystal field is produced at the central Mn^{3+} site, and the symmetry of this additional crystal field reflects the symmetry of the distortion. Now, the two e_g orbitals of the Mn^{3+} ion interact and hybridise differently with the O-p states of the nearby oxygen anions in the presence of this additional potential. Therefore, a local octahedral distortion induces a splitting of the local Mn e_g anti-bonding states with the low lying occupied state having the symmetry of the corresponding O-octahedral distortion. For an octahedral distortion of an isolated Mn^{3+} site, the total energy of the system does not depend on the type of the occupied anti-bonding e_g state as long as it is accompanied by an octahedron distortion of appropriate symmetry. This distortion of the O-octahedra that breaks the degeneracy of the e_g states ultimately lowering the energy of the e_g electron is known as Jahn-Teller effect and is an example of a strong electron-phonon coupling.

1.4.2   Orbital and lattice ordering

As discussed above, we often meet a situation in manganites where the e_g orbital degeneracy is lifted at the Mn^{3+} ion site due to the Jahn-Teller distortion. The occupied e_g state can be described in the basis set of $|z^2\rangle$ and $|x^2 - y^2\rangle$ state as follows,

$$|\gamma\rangle = \cos\frac{\gamma}{2}|z^2\rangle + \sin\frac{\gamma}{2}|x^2 - y^2\rangle \tag{1.1}$$

Figure 1.3 represent the occupied state $|\gamma\rangle$ in the γ plane as shown in .
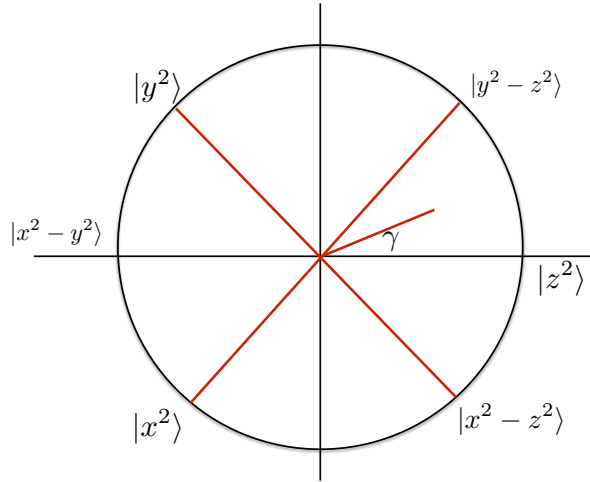
Figure 1.3: γ plane to describe the possible orbital states of Equation 1.1.

This kind of representation for the occupied state $|\gamma\rangle$ is convenient to understand several kind of orbital orderings experimentally observed in manganites (discussed in Section 1.5.3 and 1.6).

Due to the coupling between the e_g electron and the Jahn-Teller octahedral modes (Figure 2.3), the octahedron surrounding a Mn^{3+} ion with a given orbital ordering distorts simultaneously defining a specific octahedral/lattice ordering for the Mn^{3+} site. The electrons are trapped in the local lattice distortion in the form of polarons. Since the O-octahedra are connected to each other, the Jahn-Teller effect can be cooperative that may influence the long-range orbital as well as octahedral/lattice ordering of the system. The cooperative effect is important in the undoped or low-doped system with high concentration of Mn^{3+} ions. For example, an undoped $LaMnO_3$ system has a long-range staggered orbital ordering (see Section 2.3.2 and 2.4).

In the optimally doped systems, the local distortion patterns form small polarons. The large magnetoresistance effect in the optimally doped system may be seen as the collapsing of the polaronic state into a ferromagnetic state [16–19]. The experimental studies by

Alexandrov et al. [16], Zhao et al. [17], Doloc et al. [18] and Dai et al. [19] etc. demonstrate the strong interlinking of various degrees of freedom, such as charge, spin and lattice in the manganite. In Section 1.4.3, 1.5.2 and 1.6, these coupling between various degrees of freedom and their effects on the phase diagram of the system is discussed in more details.

1.4.3 Effect of cation size and disorder on properties

The prototypical cubic structure (i.e., space group-Pm3m) of the ABO_3 perovskite manganite can undergo distortion if the average size of the A-type cation varies converting the structure into a orthorhombic(i.e., Pbnm). This lowering of the symmetry from cubic to orthorhombic is due to tilting of the MnO_6 octahedra because of the size misfit between Mn and A-type ions. The octahedra tilting in a perovskite leads to Mn-O-Mn bond bending.

The physical quantities which are relevant and reflect these symmetry lowering effects are the tolerance factor T_f [20] and the bandwidth B_{width}. The tolerance factor and bandwidth are defined as:

$$T_f \propto \frac{r_A + r_O}{r_{Mn} + r_O} \propto \frac{d_{A-O}}{d_{Mn-O}}, \tag{1.2}$$

$$B_{wdth} \propto \frac{\cos(\pi - \theta_{Mn-O-Mn})}{d_{Mn-O}}. \tag{1.3}$$

r_A, r_O and r_{Mn} in the above Equation (1.2) are the radius of the A-type, O and Mn ions, respectively. d_{A-O} and d_{Mn-O} are the A-O and Mn-O bond length. $\theta_{Mn-O-Mn}$ in Equation (1.3) is the Mn-O-Mn bond angle. The angle $\theta_{Mn-O-Mn}$ itself depends on the radii r_A and r_O.

The perovskite manganite has the tendency to be cubic for $T_f \sim 1$ where Mn-O-Mn bonds are almost straight ($\theta_{Mn-O-Mn}=180^o$). The lower value of T_f suggests a higher degree of strain due to smaller A-type ion that does not fill the space between MnO_6 octahedra giving rise to other low symmetric structures.

The role of the tolerance factor T_f is studied experimentally with samples having different kinds of A-type ions keeping the electronic doping fixed [21]. Such kinds of experimental studies were motivated by the idea that the one-electron bandwidth B_{wdth} of the system was a strongly varying function of $\theta_{Mn-O-Mn}$ which in turn could be controlled by varying T_f on introducing an appropriate A-type ion. Thus, the smaller the value of r_A, the smaller would be the bandwidth B_{wdth}. Later, the structural studies of various manganite

systems suggested that the variation in B_{wdth} due to T_f alone is smaller than expected indicating towards additional effects which are supposed to be due to the local Jahn-Teller effects in the optimally doped systems [22].

The tilting and Jahn-Teller effects significantly modify the overlap integrals between inter-atomic d-orbitals and hence, affect the stability of various phases in the phase diagram of manganites. For example, there are ferromagnetic metallic regions in the phase diagram (see Figure 1.8) of systems with large-sized A-type ions. These ferromagnetic metallic regions are missing for the system with A-type ions of comparably smaller size. The angle $\theta_{Mn-O-Mn}$ decreases for smaller T_f leading to a decrease in the overlap between the d-orbitals of nearby Mn ions. With the same B-type (.i.e., Mn ion) transition metal ion, the perovskite manganites with smaller A-type ions with $T_f<1$ have smaller bandwidth B_{wdth}. The decrease in the overlap integral decreases the delocalisation of the e_g electrons near the Fermi level giving insulating characters to the system.

The steric distortions discussed above, tilting and Jahn-Teller effects, become important factors at several intermediate doping regions in the phase diagram where various phases compete with each other. For example, in most of the region of the phase diagram below $x=0.5$, the $La_{1-x}Ca_xMnO_3$ system which has larger A-type ion is observed to be in metallic phase while the $Pr_{1-x}Ca_xMnO_3$ system with smaller A-type ion shows insulting phases (see Figure 1.8 and 1.9).

1.4.4   Structural phase diagram

The structural properties of perovskite manganite are mainly determined by the three types of normal octahedral modes: 1) Jahn-Teller, 2) symmetric breathing and 3) tilting accompanied rotation. The frequency of the Jahn-Teller modes is higher than the breathing modes while the tilting modes are low-frequency modes [23, 24].

The structural phase diagram of $Pr_{1-x}Ca_xMnO_3$ is shown in Figure 1.4 depicting various structural phases. On doping the parent $PrMnO_3$ system with holes, the system undergoes several phase transitions [25]. At high temperature, the system appears to be in O-pseudocubic structure for the entire doping range except $0<x<3$.

This is not true for the low temperature region. The undoped $PrMnO_3$ structure is O'- orthorhombic with Pbnm space group at low temperature. In $PrMnO_3$, the orbital ordering is staggered $d_{3x^2-r^2}/d_{3y^2-r^2}$-type in the ab plane (see Figure 1.6). This kind of orbital ordering result in expansion of the lattice constant in the ab plane and compression in the c direction.
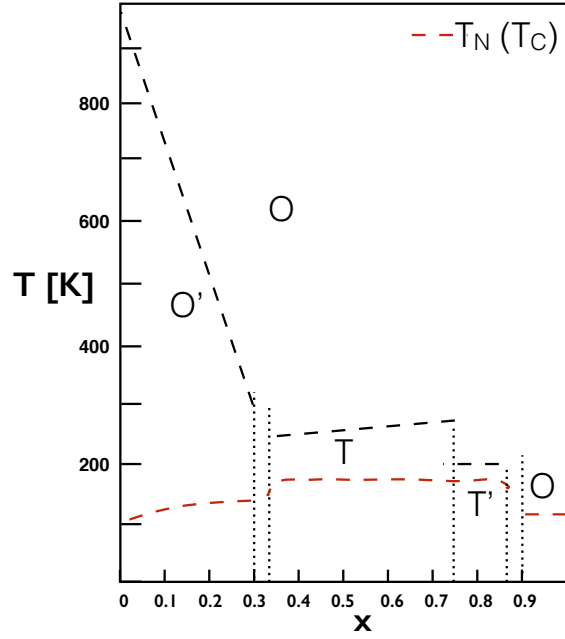
Figure 1.4: Structural phase diagram of system $Pr_{1-x}Ca_xMnO_3$ of the manganite group as a function of doping (X axis) and temperature (Y-axis). **Abbreviations**: O' - orthorhombic phase ($a<c/\sqrt{2}<b$), T'-tetragonal phases ($\frac{c/\sqrt{2}}{a}>1$), T'-tetragonal phases ($\frac{c/\sqrt{2}}{a}<1$) and O-pseudocubic phase ($a=b=c/\sqrt{2}$) Figure adapeted from Jirak et al. [25].

The lattice structure away from $x=0$ shows tendency towards rhombohedral ($a=b=c$) as the number of Mn^{4+} ions increases in the high temperature region. Around $x=0.3$, a phase transition from the O'- orthorhombic to the T'-tetragonal is observed at low temperature. As the number of the Jahn-Teller active Mn^{3+} ion decreases with hole doping, the cooperative distortion pattern due to staggered-orbital ordering disappears in the ab plane which result in the O'-T' transition.

The T'-tetragonal phase within the $0.3<x<0.7$ region can be attributed to the CE-type structure where the $d_{x^2-3r^2}/d_{y^2-3r^2}$-type orbitals in the ab planes are occupied. Thus, the lattice constants expand in the ab plane and shrink in the c direction.

The C-type magnetic order appear at $x=0.75$. The $d_{z^2-3r^2}$-type states pointing in the direction of the ferromagnetism are occupied. Thus, the lattice constant expands in the c direction. This results in the T-tetragonal structure in the $0.75<x<0.85$ region of the phase diagram.

The $0.9<x<1$ region of the phase diagram is characterised by the O-pseudocubic structure which is mainly composed of Mn^{4+} ions that do not undergo Jahn-Teller distortion.

In the next section, we explain the origin of magnetic interactions which will be followed by the discussion of various kind of magnetic orders experimentally observed in the manganites.

1.5   Magnetic interactions

The magnetic interactions between electrons are a result of the Fermi statistics and the Coulomb repulsion (U). The Fermi statistics does not allow the electrons with same spin to occupy same state. On the other hand, the Coulomb repulsion (U) depends on the spatial part of the electronic wave function. Generally, these interactions are restricted to electrons within different orbitals on same site (intra-atomic) or nearest site (inter-atomic). The inter-atomic magnetic interactions are subtle in nature and depend on various aspects, such as the electron occupancy, bond length, the nature of participating anion/cation and symmetry of the orbital involved. The inter-atomic interactions may also be either direct exchange or indirect exchange (super-exchange) interactions.

In the manganite oxides, the low-lying t_{2g} states of Mn cation form a core with a magnetic moment of $3\,\mu_B$. These t_{2g} electrons are mostly localised. In Mn oxides with Mn^{2+}, Mn^{3+} or Mn^{4+} ions, the intra-atomic interactions favour all of the d-electrons to have a parallel alignment of the spins and minimise the energy penalty due to J_H (Hund's coupling). The hybridisation of the occupied e_g orbitals of the nearby Mn sites forming a covalent or semi-covalent bond occurs through the 2p-states of the intermediate O anion.

Anderson [26] presented a formulation to the ideas about the possibility of an exchange spin-coupling through an intermediate non-magnetic atoms, which was first suggested by Kramer [27] for magnetic systems. Slater, Goodenough and Loeb [28], and Anderson and Hasegawa [7] introduced the concept of the covalence and semicovalent exchange between the non-magnetic anion (O^{2-}) and cations (Mn^{4+}/Mn^{3+}), which consistently explains the variation of the experimentally crystal structure with the experimentally observed magnetic ordering for most of the doping cases. Later, Kanamori [29] provided empirical rules to understand the sign of the exchange interactions between the involved orbitals of the cations and anions. Together with Goodenough and Anderson work, these set of empirical rules are knows as Goodenough-Kanamori-Anderson rules of super-exchange interaction. Next, ee discuss these inter-atomic exchange interaction (direct and super-exhange), individually.

1.5.1   Direct exchange

We take an example of a hydrogen molecule to discuss the direct exchange interaction. The H_2 molecule has two electrons. The overall Hamiltonian of the system of the hydrogen molecule

$$\hat{\mathcal{H}} = \hat{\mathcal{H}}^o + \hat{\mathcal{H}}^{ex} \tag{1.4}$$

is comprised of the H^o part

$$\hat{\mathcal{H}}^o = -\frac{\hbar^2}{2m_e}\left(\nabla_1^2 + \nabla_2^2\right) - \frac{e^2}{|\vec{R}_A - \vec{r}_1|} - \frac{e^2}{|\vec{R}_B - \vec{r}_2|} \tag{1.5}$$

and the $\hat{H}^{ex}$ part, which we treat as perturbation

$$\hat{\mathcal{H}}^{ex} = -\frac{\hbar^2}{2m_e}\left(\frac{e^2}{R_{ab}} + \frac{e^2}{|\vec{r}_1 - \vec{r}_2|} - \frac{e^2}{|\vec{r}_1 - \vec{R}_b|} - \frac{e^2}{|\vec{r}_2 - \vec{R}_a|}\right) \tag{1.6}$$

Here, $\vec{R}_a$ and $\vec{R}_b$ are the coordinates for the two nuclei a and b, and $R_{ab} = |\vec{R}_a - \vec{R}_b|$ is the distance between them. $\vec{r}_1$ is the coordinate of the electron of atom a and $\vec{r}_2$ is that of the electron of atom b. ∇_i^2 acts on the ith electron.

We fix the distance between atoms and then, find out the electron energy eigenstate within the Born-Oppenheimer approximation. Furthermore, we suppose the $\phi_a(\vec{r}_1)$ and $\phi_b(\vec{r}_2)$ to be spatial wave functions and corresponding energy eigenstate of the first and second electron in an isolated hydrogen atom. Assuming these wave functions to be orthogonal, the total wave function of the system with indistinguishable particles can be written as the anti-symmetric and symmetric combination of the product of these two wave functions, i.e.,

$$\Psi_{(\vec{r}_1, \vec{r}_2)\pm} = \frac{1}{\sqrt{2}}[\phi_a(\vec{r}_1)\phi_b(\vec{r}_2) \pm \phi_b(\vec{r}_1)\phi_a(\vec{r}_2)] \tag{1.7}$$

On top of the above combinations of the spatial wave functions, we also need to specify the spin part of the wave functions. Similar to the spatial part, these spin parts can also be symmetric, i.e., $\uparrow_1\downarrow_2 + \uparrow_2\downarrow_1$ or antisymmetric, i.e., $\uparrow_1\downarrow_2 - \uparrow_2\downarrow_1$. According to the Fermi statistic, the total wave function must be anti-symmetric under the exchange of two electrons. Hence, the spatial part must be symmetric if the spin part is antisymmetric and vice versa.

The energy eigenvalues of the system are found as:

$$E_\pm = E^o + \frac{C \pm J_{ex}}{1 \pm B^2} \tag{1.8}$$

where E^o is the energy eigenvalue of the non-interacting Hamiltonian $\hat{H}^o$ (Equation 1.5), E_+ is energy for the spatially symmetric/spin-singlet wave function and E_- is energy of the spatially antisymmetric/spin-triplet wave function.

In Equation 1.8, the constants C, B and J_{ex} correspond to the Coulomb integral, overlap integral and exchange integral, respectively. These integral are as follows:

$$C = \int \phi_a(\vec{r}_1)^2 \Big(\frac{1}{R_{ab}} + \frac{1}{\vec{r}_{12}} - \frac{1}{\vec{r}_{1a}} - \frac{1}{\vec{r}_{2b}} \Big) \phi_b(\vec{r})^2 d^3\vec{r}_1 d^3\vec{r}_2 \tag{1.9}$$

$$B = \int \phi_b(\vec{r}_2) \phi_a(\vec{r}_2) d^3\vec{r}_2 \tag{1.10}$$

$$J_{ex} = \int \phi_a(\vec{r}_1) \phi_b^*(\vec{r}_2) \Big(\frac{1}{R_{ab}} + \frac{1}{r_{12}} - \frac{1}{\vec{r}_{1a}} - \frac{1}{\vec{r}_{2b}} \Big) \phi_b(\vec{r})^2 \phi_a(\vec{r}_1) \phi_a(\vec{r}_2) d^3\vec{r}_1 d^3\vec{r}_2 \tag{1.11}$$

$$\tag{1.12}$$

where we use $|\vec{r}_1 - \vec{r}_2| = \vec{r}_{12}$, $|\vec{r}_1 - \vec{R}_b| = \vec{r}_{1b}$ and $|\vec{r}_2 - \vec{R}_a| = \vec{r}_{2a}$.

In the Heisenberg-exchange kind model, the Hamiltonian of the system is written as

$$H_h = -2J_{ab}\langle \vec{s}_a.\vec{s}_b \rangle \tag{1.13}$$

where J_{ab} is the exchange coupling which is a function of the above C, B and J_{ex}:

$$J_{ab} = -\frac{1}{2}(E_+ - E_-) = \frac{J_{ex} - CB^2}{1 - B^4} \tag{1.14}$$

Clearly, Equation 1.14 and relations for C, B, and J_{ex} (Equation 1.10, 1.11 and 1.12) tell us that the J_{ab} coupling is a short-range that depends on the distance between the atoms as the overlap between the wave functions dies at larger distances. Depending on the sign of the J_{ab} coupling, there are two kind of direct exchange interactions:

- **Direct ferromagnetism:** If the J_{ab} is positive, the spins of the electrons tend to be parallel and result in ferromagnetism. In other words, this arises due to the mutual electron repulsion when the nearby atoms are far apart, resulting in a parallel spin alignment in the anti-bonding state.

- **Direct anti-ferromagnetism:** If the J_{ab} is negative, the exchange interaction favours antiferromagnetic alignment of the spins which leads to antiferromagnetism. This arises due to the mutual electron repulsion when the nearby atoms are far apart, resulting in a parallel spin alignment in the anti-bonding state.

1.5.2 Super-exchange or indirect Interaction

Since the d-orbitals are localised, the direct exchange coupling discussed above cannot explain the anti-ferromagnetism observed in the transition-metal compounds. But interestingly, the strong overlapping between the wave functions of a metal and an intermediate ligand in transition metal compounds give rise to an another kind of exchange coupling between cation spins, i.e., indirect or super-exchange (SE) coupling. The super-exchange is a coupling between cation spins through the medium of the nearest-neighbour anion ligand. There are three different kinds of indirect-exchange interactions that depend on the spin and valency of the two corner sites involved:

- **Indirect anti-ferromagnetism:** It is an antiferromagnetic ordering between two corner cations, M_a and M_b, with fairly localised wave functions mediated by orbital overlapping with the central anion. The situation is shown in Figure 1.5(a). The indirect anti-ferromagnetism is a two-electron super-exchange process that occurs between sites M_a and M_b sites. An electron from the intermediate anion (it is O^{2-} in manganites) is transferred to the adjacent cation M_a leading to virtual $M_a^{(n+1)}$ state at a cost of the excitation energy W as follows.

$$M_a^{n+} + M_b^{n+} \rightarrow M_a^{(n+1)+} + M_a^{(n-1)+} + W. \qquad (1.15)$$

At the same time, the hole on the intermediate anion site is filled by an electron from the other adjacent cation M_b. The W is the excitation energy that depends on the transfer integral t between M_a/M_b atom and ligand (see Figure 1.5(a)). This kind of coupling requires two cation with same valance charge and a bridging ligand.

In manganite, the coupling between the t_{2g} electrons at two nearby sites via the central O^{2-} ligand has the same origin. If two Mn cation sites have an antiferromagnetic spin configuration, then a spin $\uparrow$ electron from the intermediate O-p state is transferred to the nearby spin $\downarrow$ t_{2g} state (spin $\uparrow$ t_{2g} states are empty and lie above the Fermi level) leaving behind a hole in the spin $\uparrow$ O-p state of the O^{2-} anion. This hole in the O-p state of anion can only be filled if the t_{2g} $\uparrow$ electron from the second neighbouring Mn anion is transferred to this O-p state of the anion. Thus, the electron transfer appears to be complete from the first Mn site to the second Mn site, but its not a complete transfer between Mn sites. As the transfer is not real, It is know as virtual spin transfer through t_{2g} states.
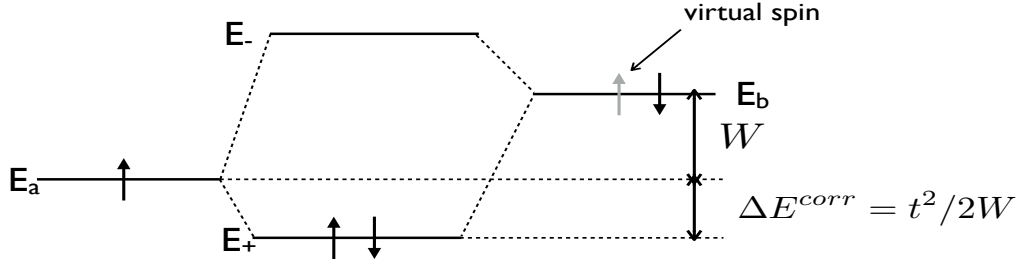
(a) correlated spins between site a and b to create an antiferromagnetic order due to virtual (grey) two-electron transfer. t is the overlap integral and W is an excitation energy required for virtual electron transfer process. The spin $\uparrow$ electron from the central ligand is transferred to M_a site followed by filling of the hole on ligand by the $\uparrow$ electron from M_b site. In reality, the electron transfer only occur between ligand and one of the adjacent atom, but can be seen as virtual transfer of electron between corner sites M_a and M_b
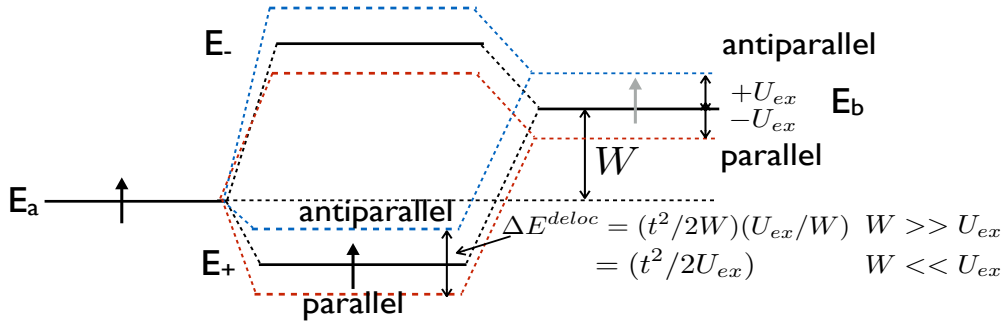
(b) ferromagnetic exchange with delocalised spin due to real one-electron semi-covalent exchange between site a and b. U_{ex} is an exchange energy, the cost of spin parallel (negative) and antiparallel configuration (positive).
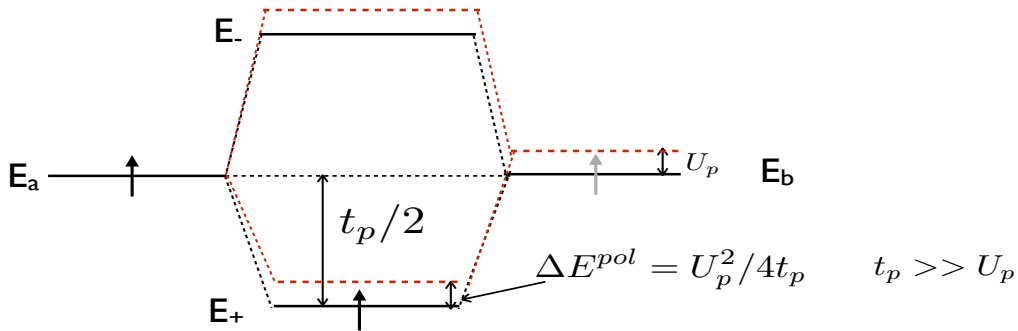
(c) ferromagnetic exchange due to real electron transfer between site a and b. It is a special case of above b) situation where the combined energy of the initial and final states of mixed-valence M_a and M_b are unchanged in an adiabatic transfer event. The ferromagnetism in the system in this case may be promoted through spin transfer by mean of polaron carriers whose mobility is activated by the thermal hopping of electrons across energy barriers generally defined as $U_p = U_o + U_{ex}$ where U_o is a trap energy of a small polaron.

Figure 1.5: Molecular-orbital diagrams indicating the origin of the exchange coupling between sites a and b with onsite energy E_a and E_b: a) two electron anti-ferromagnetism **b)** one-electron ferromagnetism (general case), and **c)** one-electron ferromagnetism double-exchange, special case of mixed-valence charge transfer. The figures adapted from Magnetic Oxides by Gerald F. Dionne citation

- **Indirect ferromagnetism:** In addition to the above indirect anti-ferromagnetic mechanism (Figure 1.5(b)), an another kind of indirect mechanism (Figure 1.5(b)), which is ferromagnetic in nature is possible. The ferromagnetic indirect exchange dominates when two corner cations are dissimilar, i.e., with different average valence charges. In such situation, an electron exchange between the dissimilar ions, M_a and M_b, through intermediate anion can be described as:

$$M_a^{n+} + M_b^{(n+1)} \rightarrow M_a^{(n+1)+} + M_a^{n+} + W \pm U_{ex}. \tag{1.16}$$
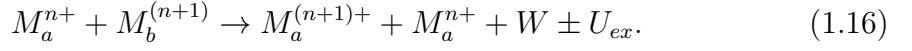
U_{ex} is the adjustment of the exchange energy of the spin stabilisation (i.e., U_{ex} is positive) within a parallel spin configuration or the destabilisation (i.e. U_{ex} is negative) within an antiparallel spin configuration. As depicted in Figure 1.5(b), a transfer of electron within a parallel spin configuration of M_a and M_b is favoured.

- **Double exchange ferromagnetism:** The observation of simultaneous ferromagnetism with an itinerant electron behaviour (i.e., the metallic system) in the perovskite manganites is explained by the Zener double exchange model [6, 30]. This model explains that the hopping of an electron from Mn^{3+} ($3d^4$:$t_{2g}^3 e_g^1$: S = 2) to Mn^{4+} ($3d^3$:$t_{2g}^3 e_g^0$: S=3/2) takes place via O-p states. Within double exchange mechanism, a transfer of the e_g electron from Mn^{3+} by the intervention of the O-p state occurs with the simultaneous transfer of an electron from the same O^{2-} to the other nearby Mn^{4+}.

For a general case, illustrated in Figure 1.5(c), the double exchange ferromagnetism occurs due to a transfer of an electron between two similar cations M_a and M_b via an intermediate anion according to

$$M_a^{n+} + M_b^{(n+1)} \leftrightarrow M_a^{(n+1)+} + M_a^{n+}. \tag{1.17}$$
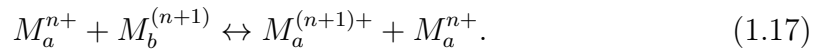
In manganite systems, the exchange energy associated with such kind of transfer is non-vanishing only if the corresponding t_{2g} spins of the two Mn site involved are aligned parallel.

In the double exchange, an electron is equally delocalised over two sites whereas in the super-exchange, the electrons are rather localised. Thus, the double-exchange mechanism enhances the conductivity of the system. Beside the super-exchange and double-exchange, there is another possibility for the spin moments on two Mn sites to be coupled over a relatively larger distance with an intermediary non-magnetic ion through the itinerant electrons. This interaction is termed as 'Ruderman-Kittel-Kasuya-Yoshida interaction' (RKKY) [31–33]. The origin of an exchange interaction in insulators is through the

super-exchange while the RKKY and double-exchange are important in the case of metals. Next, we discuss the coupling between the orbital and spin degrees of freedom in manganites giving rise to several kinds of magnetic orders.

1.5.3   Interplay between orbital and magnetic ordering

There are several experimental techniques to examine the orbital ordering indirectly by probing the structure of the system, e.g., by neutron diffraction. Wollan and Koehler [34, 35] studied the magnetic and crystallographic lattices in the manganite series with the compositions $La_{1-x}A_xMnO_3$ as a function of Mn^{4+} ion. The most commonly observed magnetic orders are shown in Figure 1.6.

The end members of the series, $CaMnO_3$ and $LaMnO_3$, show the A-type ($x=0$) and G-type ($x=1$) magnetic order, respectively. Away from the extreme doping cases, several other types of ordering are also observed. Goodenough [28, 36] predicted the magnetic structure of the $La_{1-x}A_xMnO_3$ series on the basis of the super-exchange interaction (discussed in Section 1.5.2) between the cation and anion, and the predicted spin order agreed very well with the experimental results by Wollan and Koehler [34, 35].
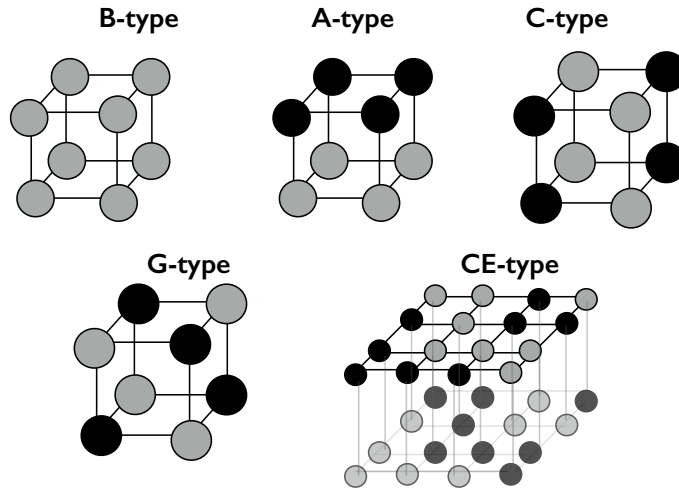
Figure 1.6: Different type of magnetic ordering commonly found in perovskite manganites, first introduced by Wollan and Kohler [34]. The two colours (black and grey) shows opposite magnetic moment directions.
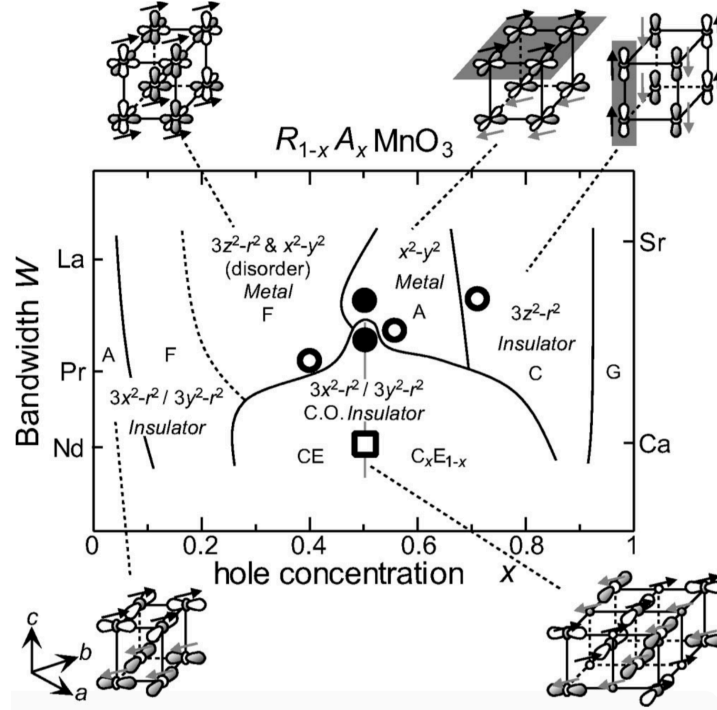
Figure 1.7: Phase digram showing magnetic ordering as a function of hole doping x and bandwidth w (i.e., different type of A-type cation) and corresponding orbital ordering. For large bandwidth systems, the B-type metallic phase dominate. On the other hand, the intermediate and small-bandwidth systems show several magnetic phases [37].

In the case of high-bandwidth $La_{1-x}Ca_xMnO_3$, the phase diagram is dominated by ferromagnetic (B-type) magnetic order. However, several other kinds of spin orders are observed in the lower bandwidth $Pr_{1-x}Ca_xMnO_3$ and $Na_{1-x}Sr_xMnO_3$ series. Below are the possible magnetic ordering generally found in manganites, discussed in the context of $Pr_{1-x}Ca_xMnO_3$.

- **A-type:** In the A-type magnetic order, the ferromagnetic xy planes of system are antiferromagnetically aligned in the z direction. The Jahn-Teller electron-phonon coupling of Mn^{3+} ions to the lattice results in cooperative effects in the undoped ($x=0$) system [28]. At $x=0$, the e_g electrons in the orthorhombic structure occupy the alternating $d_{3x^2-r^2}$ and $d_{3y^2-r^2}$ orbitals. All other upper empty orbitals lie perpendicular to the lower filled orbitals. The super-exchange coupling between the empty and filled orbital favours a ferromagnetic ordering in the xy plane. The magnetic ordering in the z direction is antiferromagnetic due to the super-exchange coupling between the filled t_{2g} states.

- **B-type:** In the B-type magnetic structure, spin ordering is ferromagnetic in all the three directions. In $0.2 < x < 0.3$ doping region of $Pr_{1-x}Ca_xMnO_3$ series, this B-type magnetic order is an insulating. For high-bandwidth manganites, there is no preferred orbital ordering in the B-type magnetic structure if the system is metallic

due to active ferromagnetic double exchange mechanism in all the three directions. Theoretically, correct orbital ordering in the insulating B-type phase is still to be resolved completely.

- **C-type:** In the C-type magnetic order, the spins are antiferromagnetically arranged in the xy plane and ferromagnetically in the z direction. The system shows tendency to be in the C-type magnetic order in the doping region $0.75 < x < 0.85$. The e_g electrons occupy the $d_{3z^2-r^2}$ orbitals that point in the z direction. Hence, such an orbital ordering can be approximated as an one-dimensional chain of ferromagnetically coupled Mn ions in the z direction. The double exchange mechanism prevails in the z direction. The super-exchange coupling between t_{2g} states dominates in the xy plane which in contrast to what is observed in the A-type phase.

- **G-type:** In the G-type magnetic order, the spin arrangement is antiferromagnetic in all three direction. This kind of magnetic ordering is typically seen in $CaMnO_3$ ($x=1$) due antiferromagnetic super-exchange coupling between the t_{2g} states of nearby sites in all the three direction.

- **CE-type:** It can be inferred as the superposition of the C- and E-type of magnetic ordering. The CE-type magnetic ordering is observed around half filling ($x=0.5$) to accommodate the cooperative ordering of $d_{3x^2-r^2}/d_{3y^2-r^2}$-type orbital order in the xy plane. We emphasise on this kind of ordering in Chapters 5 and 6 while studying the half-filled system.

1.6   Different phases and phase competition

In the present section, firstly, we briefly discuss the experimental phase diagrams of the most well-studied systems, i.e., large-bandwidth $La_{1-x}Sr_xMnO_3$ (LSMO), medium-large Nd_{1-x},Sr_xMnO_3 (NSMO) and small-bandwidth $Pr_{1-x}Ca_xMnO_3$ (PCMO). Secondly, we focus specifically on PCMO in Section 1.6.1.

Figure 1.8 shows the phase diagrams illustrating the temperature vs doping plane of three different bandwidth compounds, namely LSMO, NSMO and PCMO [38]. The average size of the A-type cations and hence, the tolerance factor (see Section 1.4) decreases from La, Sr to Pr, Ca through Nd, Sr. The bandwidth of these systems also decrease in the same order due to the tilting effect (discussed in Section 1.4.3). The high bandwidth LSMO has a large part of the phase diagram as ferromagnetic-metallic ($0.5 > x > 0.2$) due to the dominating double exchange mechanism. The phase diagram of the low bandwidth PCMO does not shown any ferromagnetic-metallic phase. The medium-bandwidth

NSMO shows various phases coexisting within specific regions of doping as a result of competition between the super-exchange mechanisms and the orbital-charge ordering. The observed asymmetry in the physical properties w.r.t. $x = 0.5$ doping for all band-width compounds reveals the dominance of different physical mechanisms in different part of phase diagram.

The high-doped manganites lack the cooperative effect of distortion due to large average distance of Mn^{3+} ions because of a small ratio of Mn^{3+}/Mn^{4+} ion as compared to the low-doped systems. Thus, while the cooperative distortion pattern leads to several types of atomic structure, such as orthorhombic ($x{\sim}0$), tetrahedral ($0.75{>}x{>}0.5$) in the low-doped systems, the high-doped systems tend to be cubic.

The strong cooperative octahedral distortion in the undoped ($x{=}0$) manganites results in the $d_{3x^2-r^2}/d_{3y^2-r^2}$-type orbital ordering in the *ab* plane. The spin magnetic order is the A-type for all bandwidth systems. The strong lattice distortions close to the $x{=}0$ doping for systems with a low tolerance factor results in significant next-nearest neighbour antiferromagnetic interactions. This in turn lead to a canted-spin structure with a long-period of modulation. The spin order in the insulating phase become more and more canted in the *c* direction on increasing the hole doping.
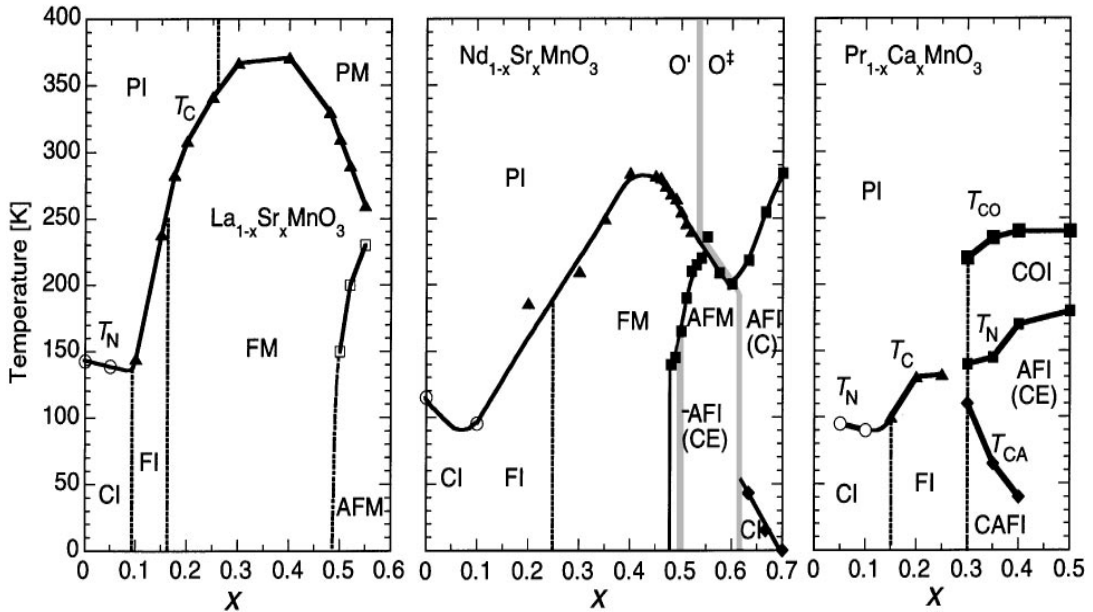
Figure 1.8: Phase diagram of three members, $La_{1-x}Sr_xMnO_3$ (left), $Nd_{1-x}Sr_xMnO_3$ (centre) and $Pr_{1-x}Ca_xMnO_3$ (right), of manganites as a function of doping and temperature. CI: canted-spin in-sulating; FI: ferromagnetic insulating; FM: ferromagnetic metallic; PI: paramagnetic insulator; AFI: antiferromagnetic insulating; AFM: antiferromagnetic metallic; CAFI: Canted antiferromagnetic insu-lating; and COI: charge ordered insulating [38].

Theoretically, de Gennes [39] explained this canted-spin structure as a result of a delo-calisation of the hole states along the direction of the spin canting.

As we go little higher in the doping, the spin structure of the system completely converts ferromagnetic. For example, the region around $x{\sim}0.08$, $x{\sim}0.10$ and $x{\sim}0.17$ doping for LSMO, NSMO and PCMO, respectively is ferromagnetic-insulating. Interestingly, this ferromagnetic-insulating phase is believed to be due to the ferromagnetic super-exchange interaction instead of the double exchange mechanism, as suggested by various models [40, 41].

Within $0.5{>}x{>}0.3$ doping, the high and intermediate bandwidth systems show a ferromagnetic-metallic phase with no sign of orbital ordering. On the other hand, the low bandwidth PCMO system is an antiferromagnetic-insulator around $x{\sim}0.5$. A charge-orbital ordering pattern is observed at $x{=}0.5$ in the low band-width PCMO. This ordered phase with zig-zag spin chain is known as CE-type phase.

While going higher in the doping, i.e., above half filling ($x{>}0.5$), the high bandwidth systems start showing an antiferromagnetic insulating phase. The spin structure is supposed to be A-type with a very different orbital ordering than the one observed at $x{=}0$. This A-type antiferromagnetic-insulating phase above half filled is assigned to the dominating double exchange mechanism within the ab plane due to the $d_{x^2-y^2}$-type orbital ordering. The intermediate bandwidth systems shows the C-type phase with pseudo one-dimensional features above half doping. For example, NSMO at $x{=}0.62$ and PCMO at $x{=}0.75$ show the C-type magnetic order where the ferromagnetic chains run in the c direction with the $d_{3z^2-r^2}$-type orbital ordering.

The fully doped system ($x{=}1$) across entire bandwidth is the G-type, i.e., antiferromagnetic in all three directions. The G-type magnetic order is due to dominating nearest neighbour super-exchange antiferromagnetic coupling between filled t_{2g} states.

1.6.1 $Pr_{1-x}Ca_xMnO_3$ **phase digram**

Figure 1.9 summarises the experimental phase diagram of the $Pr_{1-x}Ca_xMnO_3$ system [25, 38, 42–51]. The system is insulating for the entire doping range at low temperature. The undoped $PrCaMnO_3$ system (region **I**) exhibits the A-type magnetic ordering in the orthorhombic structure [25]. In the lightly-doped regime $0{<}x{<}0.15$ (region **II**), the system appears to exhibit electron-poor and electron-rich planes with a canted spin-structure [25, 42]. On adding additional holes, a phase-transition from the A-type to the B-type magnetic phase is observed. At $x{\sim}0.2$ (region **IV**), the system is found to be in the B-type insulating phase [40, 44].

The low temperature zone within $0.30{<}x{<}0.50$ doping region (region **V**) is not yet fully understood. While several experiments suggest CE-type phase close to half doping [47, 52,

53], others hint towards a charge-ordered state with absence of a long-range orbital order [43]. Two kinds of charge-order are observed experimentally at $x=0.4$: checkerboard-type [52] and Zener polaron-type [54–56] (discussed in Section 4.7). The phase-separation with these two phases in this region is also seen as one of the possibility [44, 46, 55–57]. The region around $x{\sim}0.30$ is the first of the two region in the phase diagram where CMR effect is observed.
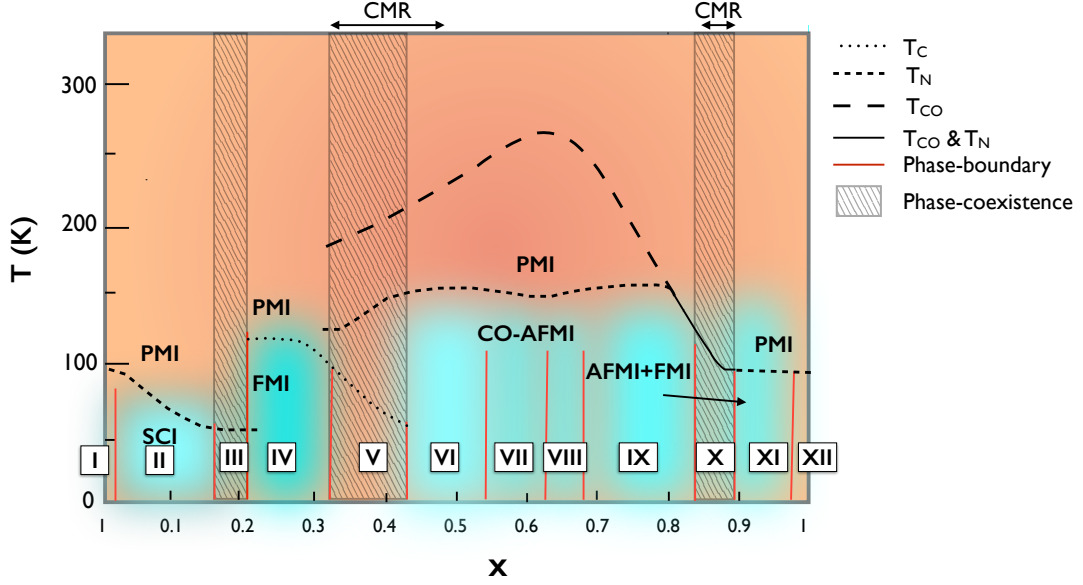
Figure 1.9: Experimental phase diagram of $Pr_{1-x}Ca_xMnO_3$ as a function of doping (x-axis) and temperature (y-axis). T_{CO}, T_C and T_N are charge-ordered, Curie and Neel temperature, respectively. While the regions in cyan color shows homogeneous phase at low temperature, the red color paramagnetic insulator at high temperatures. The CMR domain is noted by arrows in the upper part of the graph. The FMI, AFMI ,PMI and SCI abbreviation stands for Ferromagnetic insulator, Antiferromagnetic insulator, paramagnetic insulator and canted-spin insulator, respectively. The low temperature phase diagram is divided into twelve segments (I to XII) as follows: **I** - A-type , **II** - canted A-type , **III** - phase coexistence, **IV** - B-type, **V** - phase coexistence, **VI** - CE-type, **VII** - canted CE-type , **VIII** - stripe phase(i.e., Wigner crystal, bistripe phase), **IX** - C-type, **X** - mixed phase of FMI cluster/C-type/G-type, **XI** - FMI cluster embedded into G-type, **XII** - G-type [25, 44–46]. The A-, B-, C-, G- and CE-type are the standard abbreviation for magnetic order defined by Wollan and Koehler and are discussed in more detail in Section 1.5.3 and Figure 1.7.

At $x=0.5$ (region **VI**), the CE-type magnetic order with charge-ordered phase is confirmed by numerous experiments [47].

While most of the experimental studies in $Pr_{1-x}Ca_xMnO_3$ series are focused on the low-doped members, the $0.75{<}x{<}0.5$ region is yet to be explored completely. We study the region above half filling in the light of other well studied members of manganite series such as LCMO. The periodicity of the superstructure changes drastically w.r.t. doping for $x{>}0.5$ system [25, 45, 48, 49]. A narrow region (region **VII**) above half-doping is observed to exhibit CE-type behaviour. At $x{\sim}0.66$ (region **VIII**), various charge-ordered pattern

are observed such as bistripe, single-stripe, Wigner-crystal [45, 50]. With a rod-like uni-directional orbital ordering, the C-type magnetic phase is confirmed within $0.75<x<0.85$ (region **X**) [25]. A mixed phase of the C-type and ferromagnetic polarons embedded into the G-type structure is observed in the doping region $0.85<x<0.90$ (region **X**) [58]. The doping region $0.90<x<1$ has ferromagnetic clusters embedded into the G-type magnetic matrix (region **XI**) [51]. The $CaMnO_3$ ($x=1$) have the G-type magnetic order (region **XII**) [25]].

1.6.2   Phase-separated region and percolation channels

The experimental confirmation of coexistence of domains of different phases [51, 58], identified by specific orbital and charge ordering, on the nanoscale put forward another mechanism to understand the conductivity and the CMR effect: the percolation mechanism. The percolation picture is capable of explaining many features of the manganites in a wide doping range, in particular the CMR effect [59]. For example, the study of $Pr_{1-x}Ca_xMnO_3$ and $La_{1-x}Ca_xMnO_3$ systems in high doping region ($1>x>0.85$) shows the presence of ferromagnetic clusters within the antiferromagnetic parent compound and the long-range spin canting behaviour [51, 58]. The random nature of the substitution of the A-type ions leads to a statistical distribution of these ferromagnetic clusters, and their growth can be treated by the percolation theory. Recently, it is argued that the percolation transport mechanism through the ferromagnetic domains also plays an important role besides the polaron formation and double exchange mechanism in the large CMR effect observed in the low-T_c systems [60]. The percolation theory can describe very well the strongly nonlinear I-V characteristics of these systems [61]. Dagotto et al. [62] theoretically studied the large systems and showed inhomogeneities due to the coexistence of different phases leading to the M-I transitions.

1.7   Theoretical model

This section briefly surveys the existing theoretical model and their limitation to study manganite system. Initially, the double exchange model [6] with its extension, forming a basis of theoretical understanding, successfully explained the existence of the metallic phase. The model failed to predict the magnetic insulating phases below half filling $x<0.5$. Later, the two-band tight binding (TB) models were introduced for these materials to incorporate the physics of complex orbital ordering due to the e_g orbital degeneracy and emergence of insulating phases in the low-doped systems [63]. The widely used models, such as Hotta and Dagotta model [64] take into account the orbital degeneracy and

Jahn-Teller effect coupling and are capable of explaining the charge and orbital ordering pattern in different doping region of the phase diagram. Below we discuss these models individually.

1.7.1 DE model

Early theoretical models of manganites were mostly concentrated on explaining the existence of the ferromagnetism and M-I transition by the double exchange mechanism introduced by Zener[6]. This work was followed by focussing on the double exchange mechanism in a magnetic crystal, which was first studied by Gennes [39] and Anderson et al. [7]. The double exchange model used to describe the electron hopping between nearby sites as follows:

$$\hat{\mathcal{H}} = -\sum_{ij} t_{ij}(\theta_{ij}) \hat{c}_j^\dagger \hat{c}_j. \tag{1.18}$$

$\tilde{c}_j^\dagger$ and $\tilde{c}_j$ are the creation and annihilation operators of spin-less fermions, and $t_{ij}(\theta_{ij})$ is the hopping matrix element for the electron between adjacent lattice sites i and j. The $t_{ij}(\theta_{ij})$ value is dependent on the angle between the spins of the ions at these sites. Anderson et al. [7] used the following relation for the hopping between sites i and j with the spin angle θ_{ij}:

$$t_{ij}(\theta_{ij}) = b \cos \frac{\theta_{ij}}{2}. \tag{1.19}$$

When the ionic spins S_i and S_j at site i and j are parallel, $t_{ij}(\theta_{ij})$ is maximum and equal to constant b. For the antiparallel spin arrangement, $t_{ij}(\theta_{ij})$=0.

1.7.2 Kondo Hamiltonian

The next natural choice to study manganite system is an one-orbital model for the e_g electronic sector with the localised classical t_{2g} spin (ferromagnetic Kondo model) defined as:

$$\hat{\mathcal{H}} = -\sum_{ij\sigma} t_{ij} \hat{a}_{j\sigma}^\dagger \hat{a}_{j\sigma} - J_H \sum_i \boldsymbol{S}_i.\boldsymbol{s}_i \tag{1.20}$$

The first term describes the hopping of the e_g electron between i and j sites with spin σ and the second term is for the Hund's coupling. $\boldsymbol{S_i}$ is the classical spin vector of the localised t_{2g} states and $\boldsymbol{s_i}$ is the spin of the e_g electron, which can be written in terms of operators as follows:

$$\boldsymbol{s_i} = \frac{1}{2} \sum_{\sigma\sigma'} \hat{a}^{\dagger}_{i\sigma} \boldsymbol{\sigma}_{\sigma\sigma} \hat{a}_{i\sigma'}. \tag{1.21}$$

Here, the vector $\boldsymbol{\sigma}$ is composed of the Pauli spin matrices. In the limit of $J_H \to \infty$, low-energy properties are well described by the Hamiltonian as described in Equation 1.20 [7, 39].

The one-orbital ferromagnetic Kondo model in the dynamical mean field theory approach (DMFT) showed three dominating regions in the phase diagram of manganites [65]: 1) a ferromagnetic phase, 2) the coexistence of hole-undoped antiferromagnetic and hole-rich ferromagnetic domain and 3) a phase with strong spin correlations with a small Hund coupling. They also studied the effect of the onsite Coulomb repulsion term in one-dimensional system and found that the ferromagnetism appears at smaller values of $\frac{J_H}{t_{ij}}$ with inclusion of the onsite Coulomb interaction.

1.7.3 Orbital degeneracy in the double exchange model

Anderson [66] showed that the super-exchange interactions between the magnetic ion in an insulator depends on the symmetry of the degenerate orbitals and crystal geometry. Kugel and Khomskii [67] put forward a complete picture of the these interactions with the Jahn-Teller ions background. The spin and orbital degrees of freedom are strongly coupled and may give rise to a several kinds of orbital ordering. Later, the effect of orbital degeneracy was studied with the existing double exchange model [63, 68].

The two-orbital double exchange model can be written as:

$$\hat{\mathcal{H}} = -\sum_{ij\sigma\alpha\beta} t^{\alpha\beta}_{ij} \hat{a}^{\dagger}_{j\sigma\alpha} \hat{a}_{j\sigma\beta} - J_H \sum_{i\sigma\sigma'\alpha} \boldsymbol{S_i}.\hat{a}^{\dagger}_{i\sigma\alpha} \boldsymbol{\sigma}_{\sigma\sigma} \hat{a}_{i\sigma'\alpha} + J' \sum_{ij} \boldsymbol{S_i S_j}. \tag{1.22}$$

In the above equation, α and β are the indexes for orbitally-degenerate e_g states, $d_{3z^2-r^2}$ (α=1) and $d_{x^2-y^2}$ (α=2), which belong to the two fold degenerate level of e_g symmetry. The term with J' is added to include the direct antiferromagnetic coupling between the nearby sites by using classical spin vectors $\boldsymbol{S_i}$ for the occupied spin-polarised t_{2g} state.

The double exchange model with orbital degeneracy leads to several anisotropic magnetic orders. The A-, B- and C-type of magnetic phases were observed by studying the

degenerate e_g electron model [63]. The A-, B- and C-type phases were predicted to be stable in the doping region x≤0.5 (A-type), 0.5≥x≤0.6 (B-type) and x≥0.5 (C-type), as shown in Figure 1.8.

1.7.4 Effects of electron-lattice interaction

The physical properties studied by all of the model discussed previously emphasise, strictly, on the magnetic and the electronic phases leaving behind the atomic structure. It is now well known that the manganite materials have a high el-ph coupling, which is proven by the earlier experimental evidences [69–71] of the polaron as a charge carrier, and its theoretical concept was given by Millis et al. [8]. Millis et al. [8] argued that the double exchange model alone cannot explain the M-I transition but needs an additional electron-phonon coupling[8, 72]. The presence of a strong electron-phonon coupling may lead to the polaron formation at high temperatures with paramagnetic phase where the electrons are trapped in the local distortions of lattice. The lowering the temperature may again lead to a ferromagnetic state that is delocalised over several sites. The later situation explains the observed resistivity of the CMR materials above T_c. A first-order M-I transition with a single orbital model with lattice and spin degrees was reported by Verges et al. [73]. This theoretical observation further emphasised the importance of the electron-lattice interaction in CMR effect.

The model with electron-phonon coupling is as follows:

$$
\begin{aligned}
\hat{\mathcal{H}} &= -\sum_{ij\sigma\alpha\beta} t_{ij}^{\alpha\beta}\hat{a}_{j\sigma\alpha}^{\dagger}\hat{a}_{j\sigma\beta} - J_H \sum_{i\sigma\sigma'\alpha} \boldsymbol{S}_i.\hat{a}_{i\sigma\alpha}^{\dagger}\boldsymbol{\sigma}_{\sigma\sigma}\hat{a}_{i\sigma'\alpha} + J'\sum_{ij} \boldsymbol{S_i S_j} \\
&+ \hat{\mathcal{H}}_{el-ph} + \hat{\mathcal{H}}_{ph}.
\end{aligned}
\tag{1.23}
$$

The $\mathcal{H}_{el-ph}$ is the part of Hamiltonian, which describes the el-ph interaction and $\mathcal{H}_{ph}$ is a pure vibronic term given by

$$
\hat{\mathcal{H}}_{el-ph} = g\sum_{i\alpha\beta\sigma} \boldsymbol{Q_i}\hat{a}_{i\sigma\alpha}^{\dagger}\hat{a}_{j\sigma\beta}.\boldsymbol{\tau_{\alpha,\beta}}
\tag{1.24}
$$

$$
\hat{\mathcal{H}}_{ph} = \sum_i \frac{1}{2}kr_i^2.
\tag{1.25}
$$

The degeneracy of the e_g state is lifted by $\hat{\mathcal{H}}_{el-ph}$. $\boldsymbol{\tau} = (\tau^z, \tau^x)$ is a vector of Pauli matrices in orbital space. $\boldsymbol{Q_i}=(Q_z, Q_x)$ (with $Q_z=r\cos\phi$ and $Q_x=r\sin\phi$) is a two-component vector for site i giving information about the symmetry and magnitude of the distortion.

Yunoki et al. [74] investigated the phase space of the manganite with the above multi-orbital model (Equation 1.23) with the Jahn-Teller effect by describing the phonons classically. The phase separation regime induced by the orbital degrees of freedom was observed in the phase diagram. It was speculated that the Coulomb interactions will break the large regions involved in phase-separation for the above model into small domains of one phase embedded into the other.

1.7.5   Realistic manganite model with Coulomb U

An important qualitative difference regarding the order of the CMR transitions was still to be resolved theoretically with the above mentioned models. Until then, the Monte-Carlo simulations carried out at realistic hole densities, such as $x=0.33-0.25$, had indicated the presence of a rapid crossover, yet continuous, transition from the low-temperature ferromagnetic metal to the high-temperature paramagnetic (PM) insulator [75].

The above two-orbital model, Equation 1.23, with the Jahn-Teller effect was extended to take into account the onsite Coulomb interaction (U) [64, 76] between the electrons with mean field approximation (MFA). The onsite Coulomb interaction between electrons is not negligible in the case of undoped or low-doped systems. Hence, in addition to the above two-orbital Hamiltonian, the e-e interaction term $\hat{H}_{e-e}$ is included as follows:

$$
\begin{aligned}
\hat{\mathcal{H}}_{e-e} &= \frac{U}{2} \sum_{i\alpha} \hat{\rho}^{\dagger}_{i\uparrow\alpha} \hat{\rho}_{i\downarrow'\alpha} + U' \sum_{i\sigma\sigma'} \hat{\rho}^{\dagger}_{ia\sigma} \hat{\rho}_{ib\sigma'} \\
&+ \frac{U}{2} \sum_{i\alpha} \hat{d}^{\dagger}_{ia\sigma} \hat{d}^{\dagger}_{ib\sigma'} \hat{d}_{ia\sigma'} \hat{d}_{ib\sigma} + V \sum_{\langle i,j \rangle} \hat{\rho}^{\dagger}_{i} \hat{\rho}_{j}.
\end{aligned}
\tag{1.26}
$$

Here, $\hat{d}^{\dagger}_{i\sigma\alpha}$ and $\hat{d}^{\dagger}_{i\sigma\alpha}$ are the creation and annihilation operators of electron, respectively, at site i in orbital α with spin σ, and $\hat{\rho}^{\dagger}_{i\sigma\alpha} = \hat{d}^{\dagger}_{i\sigma\alpha} \hat{d}_{i\sigma\alpha}$ is the number operator. The first term of $\hat{\mathcal{H}}_{e-e}$ stands for inter-spin Coulomb repulsion. The second term stand for the inter-orbital repulsion with same spin. The V term is for the nearest-site Coulomb repulsion.

Hotta et al. [64] studied the above model (defined in (Equation 1.26)) in the limit of the large Hund's coupling. The model successfully explains the main properties of the manganite, just by including the Jahn-Teller phononic model by ignoring the onsite Coulomb interactions. They argued that the Coulomb effect can be renormalised into the effective electron-phonon coupling term of the Hamiltonian and showed that at the mean field level, the Jahn-Teller phononic model can reproduce the CE-type structure at $x=0.5$,

which is in agreement with the previous study by Yunoki et al. [76]. In a similar way, the qualitative physics was reproduced by including the renormalised Coulomb term and neglecting the Jahn-Teller phononic terms. It was emphasised that the percolating phase and the CMR effect arise due to the competition between the metallic and insulating phase, and can be achieved by including the Coulomb or the Jahn-Teller interactions individually. A first-order CMR transition is first reported theoretically with this above two orbital model at doping $x=0.25$, which explained the theory-experiment discrepancy of the order of CMR effect [75].

1.7.6 Phase inhomogeneities and long-range Coulomb repulsion

The experimental confirmation of phase-inhomogeneity [60, 77–81] in manganites hints towards the importance of long-range Coulomb repulsion in charge segregation. The manganite, indeed, shows a tendency to phase separate into electron-rich and electron-poor regions due to short-range interactions. However, if the long-range Coulomb repulsion is included, the instability with macroscopic separation is frustrated due to the cost of electrostatic energy. As a result, these macroscopic regions would breaks into smaller clusters. The electronic structure still remain highly inhomogeneous where domains, with size of the order of nanometer, of various forms of one phase are embedded into the other phase [80].

Once a long-range Coulomb repulsion effect is added to a phase separated state, the charge segregation in cuprates has been considered at a scale comparable to the inter-particle distance to explain the origin of striped states [82–85] once a long-range Coulomb repulsion effect is added to a phase separated state. Similar kind of explanation has been provided in the context of formation of Wigner crystal, bistripe and checkerboard kind of charge ordering in manganites. Yunoki et al. [74, 86] suggested that the Coulomb interactions beyond the on-site term are important to avoid the charge aggregation by the phase separation process. The study performed by the models that include this offsite Coulomb repulsion term shows that the long-range Coulomb repulsion is not the dominating mechanism for CO ordered phase at $x=0.5$ [64, 76].

1.7.7 d-p type Hatree-Fock (HF) model

T. Mizokawa el al [87] performed the Hartree-Fock calculations on the multi-band d-p type lattice model and explained the importance of the concept of the 'orbital polaron', which was introduced by R. Kilian et al. [88]. The study shows that the e_g orbitals surrounding the holes in the low-doped systems points towards the hole due to steric reasons and

promotes the ferromagnetic super-exchange interactions between Mn^{3+} and Mn^{4+} ions. The results obtained by this model at $x = 1/4$ showed the stability of the ferromagnetic-insulating phase over the antiferromagnetic phase. The ferromagnetic-insulating phase is stabilised by the breathing and Jahn-Teller-type lattice distortions.

1.7.8   Mn-O bond length and Mn-O-Mn angle-dependent bandwidth

In last few years, the tight-binding ab-initio models [89–91] are extracted and used to study fully doped manganites. The hopping amplitude t_{ij} between the e_g state, in the above mentioned model, are sensitive to the energy difference between the e_g and intermediate O states involved [89, 90]. As the energy difference between the e_g levels increases, the hybridisation between the O-p states and e_g states decreases, resulting in smaller t_{ij} values. Ederer et al. [89] showed a quantitative analysis of the effect of variation in Mn-O bond length and octahedral rotations on hopping.

Recently, Mukherjee et al. [92] presented a phase diagram study of two dimensional manganite thin films by incorporating the effect of Mn-O bond lengths and tilting angles on the hopping integral between Mn sites. The effect of the external magnetic field on the CMR was also studied by comparing the resistivity of the system at x=0.5. This study showed the possibility of a strain driven transition where the insulating phase can be metallic under strain.

1.7.9   Limitations of existing theoretical model

- There is still a lack of knowledge of a clear range for a few of the physical parameters of the model described in Section 2.5. The wide range of values used by theoretical models may be comparable to the energy difference between different phases of these systems. For example, most of the models use an overestimated value of the antiferromagnetic coupling J_{AF} between nearest sites, i.e., between $25 - 45 \, \mathrm{meV}$, which is beyond the energy scale of ferromagnetic and antiferromagnetic phases around $x = 0.5$, resulting in improper understanding of physics in these regions.

- The lattice cooperative effects are crucial to understand the behaviour of systems in the low-doping regime where electrons in the paramagnetic phase are localised as polarons. The high density of polarons at low doping further elucidate the importance of the lattice degrees and cooperative effect in the transport properties

of the system at high temperatures. In spite of the importance of cooperative Jahn-Teller effective, there are not enough theoretical studies carried out in this direction. Most of the models [64, 74, 89, 90, 92] ignore the cooperative effect of octahedral distortion, which is an important effect to understand the long-range structural and orbital ordering, confirmed by the ab-initio calculations [93]. On the other hand, these studies are limited to the prototypical, i.e., $x=0$, 0.5 and 1, members of the manganite series [76, 94–99]

- While the models discussed above have been extensively studied to investigate the low temperature electronic, magnetic and structural properties, the time-dependent properties of the system under external fields have either not been studied. These kind of time-dependent studies of the manganite system on external perturbation are ideal tools to investigate the role of various degrees of freedom in relaxation processes which still remain still remain elusive [100, 101].

- The numerical solution of the most of the models are limited to one or two dimensional systems of a finite size. Therefore, it is not easy to capture the physics of three dimensional systems, involving complex phases and the phase competition at boundaries, which is found experimentally in large region of the phase diagram.

Chapter 2

Tight binding model of perovskites

This chapter aims at presenting a tight binding model for the perovskite manganites to provide a conceptual framework for understanding their overall physical properties arising from the interplay between the atomic, magnetic and electronic degrees of freedom. The proposed model takes into account the important cooperative nature of the JT phonons, which has an important effect on the low-temperature physical and structural properties as well as the high-temperature transport process.

2.1 Crystal structure and crystal field splitting

The perovskite structural units with ABO_3 formula form a three dimensional network of the corner-connected octahedra, described in Chapter 2. While O^{2-} anions are located at the vertices of these octahedra, B-cations (Mn^{3+}/Mn^{4+}) occupy the centres. The A-type cations fill the interstitial voids formed by the O-octahedra. A typical crystal structure of the perovskite system and the corresponding unit cell are shown in Figure 2.1. Under the O ligand field, the fivefold degeneracy of Mn-d states splits into the two subset: the e_g orbitals ($d_{3z^2-r^2}$ and $d_{x^2-y^2}$) and t_{2g} orbitals (d_{xy}, d_{yz} and d_{zx}).

In the $Pr_xCa_{1-x}MnO_3$ series of manganite, the e_g orbitals are partially occupied with $(1-x)$ electrons per Mn^{3+} ion. Figures 2.1 shows the density of states (DoS) of the end members, i.e., $CaMnO_3$ (CMO) and $PrMnO_3$ (PMO), of $Pr_xCa_{1-x}MnO_3$ series. The low lying bonding states in both the cases are mainly O-p type (red). Little higher to it are the t_{2g} states (green). The Mn t_{2g} states are involved in a weak π and δ overlapping with the nearby O states. Hence, they do not shift higher in energy as much as the Mn e_g states (yellow), which participate in a strong σ overlapping with the O-p states. The t_{2g} states are occupied by three t_{2g} electrons in the d^4 (Mn^{3+}) or d^3 (Mn^{4+}) configuration. These three electrons remain in the high spin configuration, i.e., the spin parallel t_{2g} states, to minimise the e-e repulsion. The t_{2g} states of other spin shift higher in energy, shown in green, above the Fermi level. In the case of PMO where the e_g states has one electron, the degeneracy of the e_g states is lifted, shifting the occupied state lower in energy, simultaneously accompanied by a lattice distortion of the same symmetry. The
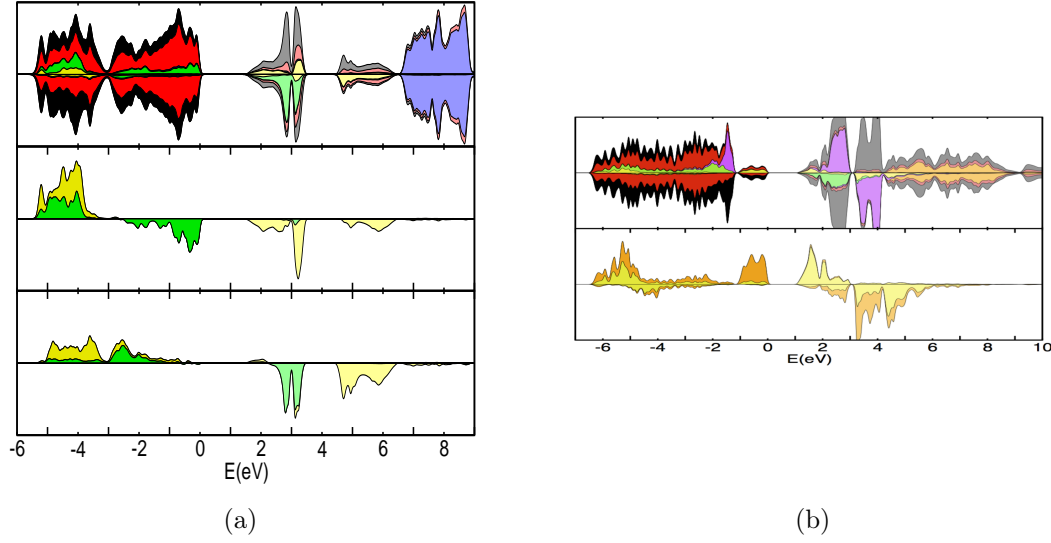
Figure 2.1: Density of states and COOP for CaMnO$_3$ G-type and PrMnO$_3$ A-type. (a) density of states, and COOP between O-p and Mn-d states for the CaMnO$_3$ G-type (left) obtained from first-principle calculations, the top portion of the graph shows total DOS shown in black, with the projected DoS for O-p (red), Mn-t$_{2g}$ (green), Mn-e$_g$ (yellow), Ca-d (blue) stacked on top of each other. The two spin densities are shown with opposite sign. The graph in the middle shows the COOP between a Mn-t$_{2g}$ orbital and anti-bonded O-p state in green and the COOP between a Mn-e$_g$ orbital and anti-bonded p-state in yellow for the majority- spin direction. Unlike the DoS, the COOPs have positive and negative values, so that two spin direction can not be combined into one graph. The two COOPs for t$_{2g}$ (green) and e$_g$ (yellow) states are stacked on top of each other. The bottom graph shows the same information for the minority- spin direction. The energy zero is aligned with the valence band top. Empty states are drawn with a lighter colour than filled states. (b) top portion of the graph shows density of states for the PrMnO$_3$ A-type, the bottom portion shows the splitting of two e$_g$ states shown in yellow and orange due to JT effect [15](credit: Mohsen Sotoudeh)

.

amplitude of the distortion shows the strength of the electron-phonon coupling in the system.

2.2   Dynamical variables

Various theoretical models proposed earlier for the perovskite manganites explicitly take into account the e$_g$ wave functions and describe the t$_{2g}$ state by classical spins. The studies of the physical properties by these model emphasise on the magnetic and the electronic phases, leaving behind the atomic structure [7, 39, 65]. The subsequent experimental evidences as well as theoretical work hinted towards the polaron playing a crucial role as a charge carrier at high temperature in the paramagnetic phase [8, 10]. To take into account the electron-phonon coupling, some of the theoretical models include the JT and breathing modes of O-octahedron as additional degree of freedom besides the e$_g$ wave functions and classical t$_{2g}$ spin. However, most of these models completely ignore the

cooperative effect of the octahedral distortion [64, 74, 89, 90, 92] although the assumption of neglecting the cooperative effect does not agree with the earlier experimental studies. In manganites with corner-connected octahedra, the nearby O-octahedra share a common O atom. If one of the O-octahedra distorts, the other also feels the strain, which in turn alters the e_g orbital ordering on both the sites, ultimately leading to a long-range structural as well as orbital ordering.

In this chapter, we introduce a microscopic tight-binding model that incorporates all the important degrees of freedom, i.e., the e_g electron, the t_{2g} spins and O atoms together with the cooperative effect of octahedral distortion. We define these degrees of freedom individually, and discuss our proposed tight-binding model in the subsequent sections.

2.2.1 Atomic variable

The atomic degrees of freedom in our manganite model consist of Mn and O atoms. The position of Mn and O atoms are defined by three kind of dynamical variables: $\vec{\delta}_{\vec{j}}^{Mn}$, $\gamma_{\vec{j},3}$, and lattice variables (defined by a, b and c).

In a rectangular grid of Mn atoms, the position of the jth Mn site is $\vec{R}_{\vec{j}}^{Mn}$ where $\vec{j}$ is the vector that defines the indexing of Mn sites on the grid. The Mn position vector $\vec{R}_{\vec{j}}^{Mn}$ can be written as

$$\vec{R}_{\vec{j}}^{Mn} = \frac{j_1 - 1}{N1}a + \frac{j_2 - 1}{N2}b + \frac{j_3 - 1}{N3}c + \vec{\delta}_{\vec{j}}^{Mn}, \tag{2.1}$$

where N_1, N_2 and N_3 are the number of Mn atoms that defines the size of the unit cell in the x, y and z direction of the lattice vector, respectively. a, b and c are lattice vectors along the x, y and z direction, respectively. $\vec{\delta}_{\vec{j}}^{Mn}$ is the displacement of the jth Mn from the equilibrium, as shown in Figure 2.2.

Once $\vec{R}_{\vec{j}}^{Mn}$'s are known, the corresponding O atom positions can be denoted by $\vec{R}_{\vec{j},m}^{O}$. Each of the Mn are attributed three O atoms identified by the index m along the x, y and z direction w.r.t. the Mn position. The O atom positions are as follows:

$$R_{\vec{j},1}^{O} = \frac{1}{2}\left(R_{\vec{j}}^{Mn} + R_{\vec{j}+(-1,0,0)}^{Mn}\right) + \vec{\delta}_{\vec{j},1}^{O}$$
$$R_{\vec{j},2}^{O} = \frac{1}{2}\left(R_{\vec{j}}^{Mn} + R_{\vec{j}+(0,-1,0)}^{Mn}\right) + \vec{\delta}_{\vec{j},2}^{O}$$
$$R_{\vec{j},3}^{O} = \frac{1}{2}\left(R_{\vec{j}}^{Mn} + R_{\vec{j}+(0,0,-1)}^{Mn}\right) + \vec{\delta}_{\vec{j},3}^{O} \tag{2.2}$$

a) **O-Mn-O bond bending**   b) **Straight bond approximation**
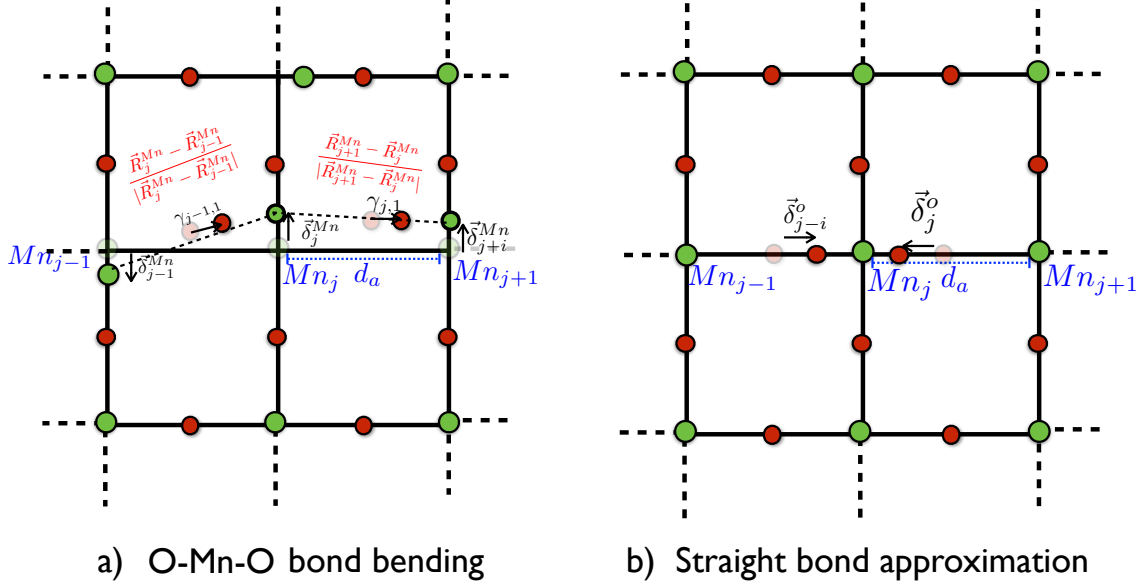
Figure 2.2: Positions of Mn and O atoms in the *ab* lattice plane if $\vec{\delta}_{\vec{j}}^{Mn} \neq 0$' (a) and straight bond approximation (b). The Mn atoms are shown in green and O atoms are shown in red. O atoms are restricted to move along the Mn-Mn directions in both the cases. The faded colors shows the corresponding equilibrium positions. **a)** O-Mn-O bond need not to be straight and γ_j^o shows the shifting of O atom connecting j^{th} and $(j+1)^{nth}$ Mn atom. (b) O-Mn-O bond bending is not allowed.

where $\vec{\delta}_{\vec{j},1}^{O}$, $\vec{\delta}_{\vec{j},2}^{O}$ and $\vec{\delta}_{\vec{j},3}^{O}$ are the displacement vectors of O atoms and given by

$$
\vec{\delta}_{\vec{j},1}^{O} = \frac{\vec{R}_j^{Mn} - \vec{R}_{j,(-1,0,0)}^{Mn}}{|\vec{R}_j^{Mn} - \vec{R}_{j,(-1,0,0)}^{Mn}|} \gamma_{\vec{j},1}
$$

$$
\vec{\delta}_{\vec{j},2}^{O} = \frac{\vec{R}_j^{Mn} - \vec{R}_{j,(0,-1,0)}^{Mn}}{|\vec{R}_j^{Mn} - \vec{R}_{j,(0,-1,0)}^{Mn}|} \gamma_{\vec{j},2}
$$

$$
\vec{\delta}_{\vec{j},3}^{O} = \frac{\vec{R}_j^{Mn} - \vec{R}_{j,(0,0,-1)}^{Mn}}{|\vec{R}_j^{Mn} - \vec{R}_{j,(0,0,-1)}^{Mn}|} \gamma_{\vec{j},3} \tag{2.3}
$$

$\gamma_{\vec{j},m}$'s introduced in the above equations are the second set of dynamical variables besides $\vec{\delta}_{\vec{j}}^{Mn}$'s. Here, we have introduced the straight Mn-O-Mn bond approximation where the O atoms are constrained to move along the direction joining the two Mn atoms connected to it. Due to octahedra rotational modes in the real perovskite manganites, the Mn-O-Mn bonds are not straight as the Mn-O-Mn bond angles $\theta_{Mn-O-Mn} \neq 180^o$. The experimental structural analysis studies of the $Pr_{1-x}Ca_xMnO_3$ series [25] reveals that the $\theta_{Mn-O-Mn}$ are in the range 149°-160° (see Section 4.3.1). The consequences of the octahedra rotational modes are discussed separately in Section 2.2.2.

The distance between two O atoms of the octahedron surrounding the jth Mn along the x, y and z direction is given by

$$d_{1,j}^{o-o} = |R_{\vec{j},1}^O - R_{\vec{j}+(-1,0,0),1}^O|$$
$$d_{2,j}^{o-o} = |R_{\vec{j},2}^O - R_{\vec{j}+(0,-1,0),2}^O|$$
$$d_{3,j}^{o-o} = |R_{\vec{j},3}^O - R_{\vec{j}+(0,0,-1),3}^O| \tag{2.4}$$
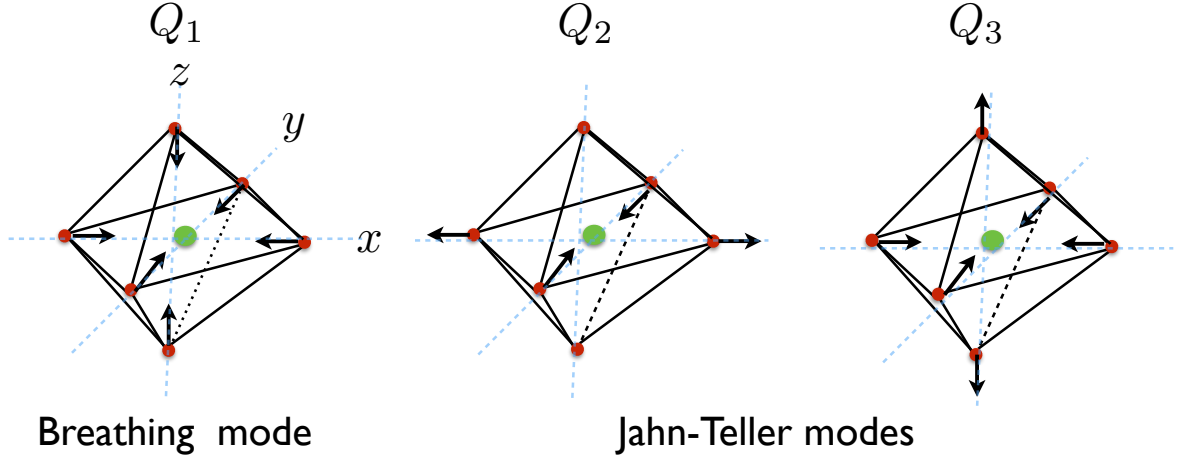
Figure 2.3: Breathing mode (Q_1) and Jahn-teller type mode (Q_2 and Q_3) of oxygen octahedron in ABO_3 perovskite manganite. O atoms are shown in red and Mn atoms are shown in green. Arrows indicate the direction of displacement of O atoms from their equilibrium positions.

The amplitudes $Q_{i,j}$ of the normal octahedra mode at j^{th} Mn site are the functions of $d_{k,j}^{o-o}$ (k ϵ $\{1,2,3\}$) and given by:

$$Q_{1,j} = \frac{1}{\sqrt{3}}\left(d_{1,j}^{o-o} + d_{2,j}^{o-o} + d_{3,j}^{o-o} - (d_a^{o-o} + d_b^{o-o} + d_c^{o-o})\right) \tag{2.5}$$

$$Q_{2,j} = \frac{1}{\sqrt{2}}(d_{1,j}^{o-o} - d_{2,j}^{o-o}) \tag{2.6}$$

$$Q_{3,j} = \frac{1}{\sqrt{6}}(-d_{1,j}^{o-o} - d_{2,j}^{o-o} + 2d_{3,j}^{o-o}) \tag{2.7}$$

where d_a^{o-o}, d_b^{o-o} and d_c^{o-o} are the equilibrium O-O bond length obtained from the ab-initio calculations of the CMO system. The index i implies the kind of octahedra mode ($i \epsilon \{1,2,3\}$). We take into account the breathing mode ($Q_{1,j}$) and two JT modes ($Q_{2,j}$ and $Q_{3,j}$) of the octahedral distortion. Figure 2.3 illustrate these octahedra modes. The Q_1 mode is an isotropic expansion of an octahedron. While the Q_2 mode describes a compression and an expansion in the xy plane of the octahedron, the Q_3 mode denotes an expansion in the z direction and a compression in the xy plane.

There are two approximation, which we can follow at this stage:

- **Straight O-Mn-O bond approximation:** This is a simplest possible way to study the distortion in the system. Under this approximation, the $\vec{\delta}_{\vec{j}}^{Mn}=0$ and $\vec{\delta}_{\vec{j},m}^{O}$'s are the only free variables among the atomic degrees of freedom as shown in Figure 2.2 (b). Allowing $\vec{\delta}_{\vec{j}}^{Mn}$ (Figure 2.2 (a)) to vary leads to a bending of the O-Mn-O bond. We use this approximation in the present thesis work.

- **Effect of compression and expansion of unit cell** - Figure 2.2 (a) depicts this possibility. In the high doping regime of a real system, the unit cell expands anisotropically. For example, the unit cell expands in the *ab* plane and shrinks in the *z* direction in PMO. We can include this sort of effect by letting the $\vec{\delta}_{\vec{j}}^{Mn}$ (Figure 2.2 (a)) to vary instead of keeping $\vec{\delta}_{\vec{j}}^{Mn}=0$. In such conditions, the restoring force tends to straighten the bond again. We do not include the O-Mn-O bond bending due to the lack of the information about this restoring force constant and keep $\vec{\delta}_{\vec{j}}^{Mn} = 0$.

  There is also an alternative way to study the same effect of the unit cell expansion and compression by treating the a, b and c in Equation 2.1 as variable. These lattice constants are expressed in terms of the equilibrium bond lengths, d_a, d_b and d_c (where $a = d_a N_1$, $b = d_b N_2$ and $c = d_c N_3$). Allowing d_a, d_b and d_c (see Figure 2.2 (b)) to vary implies simultaneous lengthening and shortening of all the Mn-O-Mn bonds in the x, y and z directions, respectively. It is a particular case of the above discussed Straight O-Mn-O bond approximation where $\vec{\delta}_{\vec{j}}^{Mn}$ are treated as variable. We use a, b and c as variables in the present thesis work unless stated otherwise.

2.2.2   Octahedra tilting and Mn-O-Mn bond bending

The origin of the octahedral tilting is described in Section 1.4.3 and 4.3.1. Due to A-type ion size effect on octahedra tilting, the average experimental Mn-O-Mn bond angle $\theta_{Mn-O-Mn}$ in the high band-width systems (e.g., $La_{1-x}Ca_xMnO_3$) found to be larger than the corresponding angle in the low band-width systems (e.g., $Pr_{1-x}Ca_xMnO_3$) [37, 102]. As discussed in Section 1.4.3, the bandwidth B_{wdth}, and thus the hopping amplitude (i.e., t_{hopp}), for the manganite systems depend on the average Mn-O-Mn bond angle, i.e., $\theta_{Mn-O-Mn}$ (Equation 1.3). Smaller the $\theta_{Mn-O-Mn}$ angle, the smaller is the hopping t_{hopp} and vice-versa. In the present study, we treat the Mn-O-Mn bond as straight (see Equation 2.3) which is not the case in the real systems. However, the unique hopping amplitude t_{hopp} used in our model is the value which we obtained through the ab-initio calculations of the $Pr_{1-x}Ca_xMnO_3$ series where $\theta_{Mn-O-Mn}\neq180^o$. The t_{hopp} is determined by taking its average over all the Mn-O-Mn bonds present in the unit cell used for

the calculations of the systems at $x=0$, 0.5 and 1, discussed in Section 2.4.1. But, the effect of the non-uniform $\theta_{Mn-O-Mn}$ bond angles in a atomic structure on the hopping is ignored. The presence of non-uniform $\theta_{Mn-O-Mn}$ bond angles has the following consequences:

1. Variable hopping amplitude: Within the particular atomic structure, the $\theta_{Mn-O-Mn}$ values are also found to be changing from one oxygen bridge to other oxygen bridge [25, 55]. In such systems with non-uniform $\theta_{Mn-O-Mn}$ angles, the hopping parameter t_{hopp} (Equation 2.12, 2.13 and 2.14), which depends on the band-width B_{wdth}, is site dependent. Most of the previous models, discussed in Section 1.7, use a constant hopping t_{hopp} assume a constant value for $\theta_{Mn-O-Mn}$ (such that $\theta_{Mn-O-Mn} \neq 180^o$). There are only few site-dependent hopping models for the manganite systems that include the effect of the non-uniform Mn-O-Mn bond bending on the t_{hopp} between the nearby Mn sites [89, 91, 92, 103]. In these models, the t_{hopp} between nearby Mn sites depends on individual $\theta_{Mn-O-Mn}$'s.

2. Effect on exchange interactions: Brink and Khomskii [104] explained the effect of the $\theta_{Mn-O-Mn}$ angle on the super-exchange mechanism involving t_{2g} states and double-exchange mechanism involving e_g states. In order to optimise the exchange between two Mn sites, the intermediate O^{2-} anion not only shifts in longitudinal direction but also in transverse direction. This shift of O^{2-} anions modify the exchange constants. The super-exchange mechanism tends to force $\theta_{Mn-O-Mn}$ towards 180° for the antiparallel spin configuration and away from 180° if the spins are parallel [104]. However, in the case of double-exchange mechanism between Mn sites, $\theta_{Mn-O-Mn}$ tends to increase towards 180° for ferromagnetic bond and away from 180° for the antiferromagnetic bond [104]. These two opposite effect for the double-exchange and super-exchange mechanism leads to transverse shift of the oxygen in the same direction along the ... ↑↑↓↓ ....-type continuous spin chains of FM and AFM bonds in the E-type magnetic order. The net shift of O^{2-} anions in the same direction results in net polarisation which is orthogonal to the ... ↑↑↓↓ ....-type chain [104].

2.2.3 e_g electron wave function and t_{2g} classical spin

The electrons in the e_g states are described by the one-particle wave functions $|\Psi_n\rangle$ where n is the band index

$$|\Psi_n\rangle = \sum_{\sigma,\alpha,R} |\chi_{\sigma,\alpha,R}\rangle \psi_{\sigma,\alpha,R,n}. \tag{2.8}$$

In the above equation, $|\chi_{\sigma,\alpha,R}\rangle$ are the local e_g orbitals at site R of spin σ ($\sigma \epsilon \{\uparrow, \downarrow\}$). The two different e_g orbitals are denoted by the index $\alpha \epsilon \{a, b\}$ (where a and b corresponds to $d_{x^2-y^2}$ and $d_{3z^2-r^2}$).

The t_{2g} states are taken into account by considering a classical spin vector $\vec{S}_R$ at site R of length $|\vec{S}_R| = 1.5\hbar$. The index l indicates the kind of the octahedra mode ($l \epsilon \{1, 2, 3\}$). The three modes corresponds to the breathing and JT kinds of distortion, as explained in 2.7 and illustrated in Figure 2.2.

A Mn^{3+} ion has d^4 configuration where three of its d-electrons occupy the t_{2g} states of parallel spins. The filled majority t_{2g} states lie far away from the Fermi level and are almost non-dispersive and localised, see a review by Salamon et al. [105] and references therein. Hence, it is reasonable to treat the spin-polarised t_{2g} states by classical spin vectors. As the crystal field splitting is larger than the Hund's coupling, the t_{2g} states corresponding to the other spin direction lie higher in energy than the majority e_g states.

2.3   The microscopic model

In the previous section, four important degrees of freedom, i.e., O atoms positions (Section 2.2.1), electron wave functions (Section 2.2.3), occupation number (Section 2.2.3),and t_{2g} spin (Section 2.2.3) were defined. Now, starting with a DFT (density functional theory) kind of framework, the total energy functional of the system is given by

$$E_{pot} = E_e + E_s + E_{ph} + E_{e-ph} + E_{e-S} \tag{2.9}$$

where E_{pot} is the potential energy of the system. E_e and E_s are the energy of the e_g electron and t_{2g} subsystem, respectively. E_{ph} is the energy of the lattice subsystem. The energy associated with the coupling between electron and phonon is E_{e-ph} and that between the e_g electrons and spin is E_{e-S}. The ground state properties of the manganites are studied by optimising the E_{pot} functional w.r.t. the variable degrees of freedom. The above energy functional E_{pot} incorporates all the important terms. Next, we discuss these energy terms individually.

2.3.1 Electron subsystem energy E_e

The energy of the electronic sub-system comprises of the kinetic energy E_{kin} associated with hopping and e-e interaction energy E_U between the e_g electrons, i.e.,

$$E_e = E_{kin} + E_U \tag{2.10}$$

- **Hopping:** E_e of an electron system consists of the kinetic energy of the e_g electrons resulting from the hopping from one Mn site to another, which is given by:

$$E_{kin} = \sum_{R,R'} \sum_{f_n} f_n \sum_{\sigma} \sum_{\alpha,\beta} \psi^*_{\sigma,\alpha,R,n} T_{\alpha,\beta,R,R'} \psi_{\sigma,\alpha,R,n} \tag{2.11}$$

where $\mathbf{T}$ is the hopping matrix in the basis set of the e_g orbital obtained by downfolding the intermediate O-p orbitals. The hopping between the nearest-neighbour sites, R and R', is spin-dependent and restricted to the same spin σ orbitals on both the sites. The matrix elements of $\mathbf{T}$ depend on the angular momentum character of the orbital involved, i.e., the d-orbital of both the Mn and p-orbital of the intermediate O atom. The overall direction-dependent hopping matrices $T_{R,R'}$ are as follows:

$$T^z_{R,R'} = -t_{hopp} \begin{pmatrix} 0 & 0 \\ 0 & 1 \end{pmatrix} \tag{2.12}$$

$$T^x_{R,R'} = -t_{hopp} \begin{pmatrix} 3/4 & -\sqrt{3}/4 \\ -\sqrt{3}/4 & 1/4 \end{pmatrix} \tag{2.13}$$

and

$$T^y_{R,R'} = -t_{hopp} \begin{pmatrix} 3/4 & \sqrt{3}/4 \\ \sqrt{3}/4 & 1/4 \end{pmatrix} \tag{2.14}$$

- **e-e Interaction**- The local e-e interaction among the e_g electrons can be expressed by the onsite density matrix elements,

$$\rho_{\sigma,\alpha,\sigma',\beta,R} = \sum_n f_n \psi_{\sigma,\alpha,R,n} \psi^*_{\sigma',\beta,R,n}. \tag{2.15}$$

The corresponding diagonal elements are represented by

$$n_{\sigma,\alpha,R} = \rho_{\sigma,\alpha,\sigma,\alpha,R} \tag{2.16}$$

$$
\begin{aligned}
E_U &= \frac{U}{2}\underbrace{\left(\sum_{\sigma_1 \neq \sigma_2, \alpha_1} n_{\alpha_1,\sigma_1} n_{\alpha_1,\sigma_2}\right)}_{\text{intra-orbital}} - \frac{U}{2}\left(\sum_{\sigma_1 \neq \sigma_2, \alpha_1} \rho_{\alpha_1\sigma_1,\alpha_1\sigma_2}\rho_{\alpha_1\sigma_2,\alpha_1\sigma_1}\right) \\
&+ \frac{U-3J}{2}\underbrace{\left(\sum_{\sigma_1, \alpha_1 \neq \alpha_2} n_{\alpha_1,\sigma_1} n_{\alpha_2,\sigma_1}\right)}_{\text{inter-orbital same spin}} - \frac{U-3J}{2}\left(\sum_{\sigma_1, \alpha_1 \neq \alpha_2} \rho_{\alpha_1\sigma_1,\alpha_2\sigma_1}\rho_{\alpha_2\sigma_1,\alpha_1\sigma_1}\right) \\
&+ \frac{U-2J}{2}\underbrace{\sum_{\sigma_1 \neq \sigma_2, \alpha_1 \neq \alpha_2} n_{\alpha_1,\sigma_1} n_{\alpha_2,\sigma_2}}_{\text{inter-orbital diff. spin}} - \frac{U-2J}{2}\sum_{\sigma_1 \neq \sigma_2, \alpha_1 \neq \alpha_2} \rho_{\alpha_1\sigma_1,\alpha_2\sigma_2}\rho_{\alpha_2\sigma_2,\alpha_1\sigma_1} \\
&- \frac{J}{2}\sum_{\sigma_1 \neq \sigma_2, \alpha_1 \neq \alpha_2} \rho_{\alpha_1\sigma_1,\alpha_1\sigma_2}\rho_{\alpha_2\sigma_2,\alpha_2\sigma_1} + \frac{J}{2}\sum_{\sigma_1 \neq \sigma_2, \alpha_1 \neq \alpha_2} \rho_{\alpha_1\sigma_1,\alpha_2\sigma_1}\rho_{\alpha_2\sigma_2,\alpha_1\sigma_2} \\
&- \frac{J}{2}\sum_{\sigma_1 \neq \sigma_2, \alpha_1 \neq \alpha_2} \rho_{\alpha_1\sigma_1,\alpha_2\sigma_2}\rho_{\alpha_1\sigma_2,\alpha_2\sigma_1} + \frac{J}{2}\sum_{\sigma_1 \neq \sigma_2, \alpha_1 \neq \alpha_2} \rho_{\alpha_1\sigma_1,\alpha_2\sigma_1}\rho_{\alpha_1\sigma_2,\alpha_2\sigma_2} \quad (2.17)
\end{aligned}
$$

There are three important terms in the above E_U expression: i) intra-orbital, ii) inter-orbital same spin and iii) inter-orbital different spin. The filled e_g band of the manganites is already spin polarised due to the large Hund's coupling. Firstly, the intra-orbital term shifts the lower unoccupied e_g band of the minority-spin higher in energy by $\sim U$ w.r.t. the majority occupied e_g band. Secondly, the onsite inter-orbital same spin term shifts the unoccupied e_g band of the majority-spin higher by an energy $\sim (U-3J)$ w.r.t. the occupied e_g band. Lastly, the inter-orbital different spin term shifts the unoccupied upper e_g band of the minority-spin higher by an energy $\sim (U-2J)$ with w.r.t. the occupied e_g band. The first term (i.e., intra-orbital) enhances the spin polarisation which is already there in manganite system due to Hund's coupling while the inter-orbital terms of Equation 2.17 reinforce the JT effect, i.e., onsite orbital polarisation. The detailed description of the form of the E_U is given in Appendix A.

2.3.2   Lattice subsystem energy E_{ph}

The shifting of O atoms from their equilibrium positions due to electron-phonon coupling give rise to the restoring force acting on the deformed octahedra which is given by

$$
E_{ph} = \frac{1}{2}k_{jt}\sum_R (Q_{2,R}^2 + Q_{3,R}^2) + \frac{1}{2}k_{br}\sum_R Q_{1,R}^2 \qquad (2.18)
$$

The O-octahedra modes (Q_i where $i \in \{1,2,3\}$) are defined in Equation (2.7) (see Figure 2.2). The O-octahedron distortion is cooperative. We include this cooperative effect by

treating the oxygen positions $\vec{R}_{\vec{j},m}$ defined in Equation 2.2 as dynamical variables instead of independent $Q_{i,R}$ modes for each site. The inclusion of cooperative effect makes sure that if a particular octahedron distort, it also affect the neighbours as they share common O atoms.

2.3.3 t_{2g} spin subsystem energy E_s

The inter-site antiferromagnetic spin interaction is described by a classical Heisenberg kind of interaction term between the nearby sites as follows

$$E_s \;=\; \frac{1}{2} J_{AF} \sum_{R,R'} \left(\frac{3\hbar}{2} \right)^{-2} \vec{S}_R \vec{S}_{R'} \tag{2.19}$$

In the above equation, $\vec{S}_R$ and $\vec{S}_{R'}$ are the classical t_{2g} spins at site R and R'.

2.3.4 Electron-phonon coupling energy E_{e-ph}

An electron in the e_g state is strongly coupled to the O-octahedra modes $Q_{1,R}$, $Q_{2,R}$ and $Q_{3,R}$. This electron-phonon coupling contribution to the total energy function E_{tot} (Equation 2.9) is described by the E_{e-ph} term as

$$E_{e-ph} \;=\; g_{JT} \sum_{R,\sigma} \sum_{\alpha,\alpha'} \rho_{\sigma,\alpha,\sigma,\alpha'} M^Q_{\alpha,\alpha'} \{Q_{2,R}, Q_{3,R}\} \tag{2.20}$$

where the matrix $\mathbf{M^Q}$ is expressed as:

$$\mathbf{M^S} = \begin{pmatrix} Q_{3,R} & Q_{2,R} \\ Q_{2,R} & -Q_{2,R} \end{pmatrix} \tag{2.21}$$

The $Q_{1,R}, Q_{2,R}$ and $Q_{3,R}$ modes of O-octahedron are defined in Equation 2.7.

2.3.5 Electron-spin coupling energy E_{e-S}

The e_g electron is coupled to the t_{2g} spin $\vec{S}_R$ on each Mn site due to the Hund's coupling, and this interaction between the t_{2g} spin and e_g electron is taken into account by the following energy term in the total energy functional:

$$E_{e-S} \;=\; J_H \sum_{R,\alpha} \sum_{\sigma,\sigma'} \rho_{\sigma,\alpha,\sigma',\alpha} M^S_{\sigma',\sigma} \tag{2.22}$$

The Matrix $\mathbf{M^S}$ is expressed as

$$\mathbf{M^S} = \left(\frac{\mathbf{3\hbar}}{\mathbf{2}}\right)^{-1} \begin{pmatrix} S_z & S_x - iS_y \\ S_x + iS_y & -S_z \end{pmatrix} \tag{2.23}$$

where the S_x, S_y and S_z are the x, y and z component of the classical spin vector $\vec{S}_R$.

2.4   Parameter determination: ab-initio calculations

The parameters of the model presented in Section 2.3 are obtained by the first-principle calculation of the $CaMnO_3$ and $PrMnO_3$ system. All parameters, except t_{hopp} and J_{AF}, can be obtained by considering an onsite model of an isolated Mn ion surrounded by the O octahedra.

For an onsite model of an isolated Mn ion, we only take into account the terms of energy functional that are defined in Equation 2.9, which contribute to a single Mn site. Here, the entire contribution of the octahedral distortion is ascribed to the $Q_{3,R}$ and $Q_{1,R}$ mode. Furthermore, the t_{2g} spin $\vec{S}_R$ is assumed to point in the z direction. These two assumptions are valid if the energy functional is invariant in spin, orbital and real space as in the present case. The optimised values of the O modes w.r.t. the occupation are expressed as:

$$
\begin{aligned}
Q_1 &= g_{br}\frac{g_{br}}{k_{br}}\Big(\sum_\sigma n_{\sigma,b} + n_{\sigma,a}\Big) \\
Q_3 &= g_{JT}\frac{g_{JT}}{k_{JT}}\Big(\sum_\sigma n_{\sigma,b} - n_{\sigma,a}\Big)
\end{aligned}
\tag{2.24}
$$

which is a function of the diagonal element of density matrix, $n_{\sigma,a}$ and $n_{\sigma,b}$.
The energy functional of the onsite model with optimised Q_1 and Q_3 values is given by:

$$
\begin{aligned}
E[n_{\sigma,\alpha}] &= J_H \sum_\alpha \big(n_{\uparrow,\alpha} - n_{\downarrow,\alpha}\big) + \frac{g_{JT}^2}{k_{JT}} \sum_\alpha \Big(\sum_\sigma n_{\sigma,\alpha}\Big)^2 \\
&+ J_{xc}2\big[\big(\sum_\alpha n_{\uparrow,\alpha}n_{\downarrow,\alpha}\big) + \big(\sum_\alpha n_{\uparrow,\alpha}\big)\big(\sum_\alpha n_{\downarrow,\alpha}\big)\big] \\
&+ \frac{1}{2}(U - 3J_{xc})\big[\big(\sum_{\alpha,\sigma} n_{\sigma,\alpha}\big)^2 - \sum_{\alpha,\sigma} n_{\sigma,\alpha}^2\big]
\end{aligned}
\tag{2.25}
$$

The four energy levels from the above energy functional can be obtained by Janak's theorem [106] that defines the energy level as derivative of energy w.r.t. the occupation $\epsilon_{\sigma,\alpha} = \frac{\partial E}{\partial n_{\sigma,\alpha}}$. Hence, the energy levels can be calculated from the onsite model, described

by Equation 2.25 for a single e_g electron system, assuming the sites as spin polarised and choosing the occupation number for the filled majority states as

$$\rho_{\uparrow,a,\uparrow,a} = n_a \text{ and } \rho_{\uparrow,b,\uparrow,b} = n_b \tag{2.26}$$

$$\rho_{\downarrow,\alpha,\downarrow,\alpha} = 0 \tag{2.27}$$

The energy level obtained are as follows:

$$\epsilon_{\uparrow,a} = -J_H - 2\frac{g_{jt}^2}{k_{jt}}n_a + (U - 3J_{xc})n_b$$

$$\epsilon_{\uparrow,b} = -J_H - 2\frac{g_{jt}^2}{k_{jt}}n_b + (U - 3J_{xc})n_a$$

$$\epsilon_{\downarrow,a} = +J_H - 2\frac{g_{jt}^2}{k_{jt}}n_a + (U - 3J_{xc})(n_a + n_b) + J_{xc}(3n_a + n_b)$$

$$\epsilon_{\downarrow,b} = +J_H - 2\frac{g_{jt}^2}{k_{jt}}n_b + (U - 3J_{xc})(n_a + n_b) + J_{xc}(n_a + 3n_b) \tag{2.28}$$

For a system with single e_g electron per Mn site, i.e., $PrMnO_3$, we use $n_a = 1$ and $n_b = 0$. Similarly, we use $n_a = 0$ and $n_b = 0$ for $CaMnO_3$. The following observations are made by the calculated energy levels of $PrMnO_3$ and $CaMnO_3$:

- The Hund's coupling J_H is extracted by the spin splitting Δ_H between the e_g states of different spin channels, i.e., $\Delta_H(x = 1) = 2J_H$.

- The splitting of the majority e_g states $\Delta^{\uparrow}$, is ascribed to the JT effect and el-el interaction, i.e., $\Delta^{\uparrow}(x = 0) = 2\frac{g_{JT}}{K_{JT}} + U - 3J_{xc}$.

- The splitting of the minority e_g states is also due to the JT effect and el-el interaction, i.e., $\Delta^{\downarrow}(x = 0) = 2\frac{g_{JT}}{K_{JT}} - 2J_{xc}$.

$\Delta_H(0) = 1.306$ eV	$J_H = 0.654$ eV	$g_{br} = 2.988$ eV/A
$\Delta_H(1) = 2.909$ eV	$U = 2.514$ eV	$k_{br} = 9.04$ eV/A^2
$\Delta^{\uparrow} = 2.165$ eV	$J_{xc} = 0.692$ eV	$J_{AF} = 0.014$ eV
$\Delta^{\downarrow} = 0.343$ eV	$g_{JT} = 2.113$ eV/A	$t_{hop} = 0.585$ eV
$\sqrt{Q_2^2 + Q_3^2} = 0.409$ A	$K_{JT} = 5.173$ eV/A^2	$d = 1.923$ A

Table 2.1: Ab-initio energy level splitting and model parameters

The above splitting energies (i.e., $\Delta_H(0)$, $\Delta_H(1)$, $\Delta^{\uparrow}$) and $\Delta^{\downarrow}$ are compared with the one deduced from the density of states of the first-principle calculations performed on the $CaMnO_3$ system with G-type magnetic order and $PrMnO_3$ system with A-type magnetic order (as described in Appendix G). These splitting energies are reported in Table 2.1.

2.4.1   Parameters

We use the first principle electronic structure calculations [15] (credit: Mohsen Sotoudeh) with the local hybrid density functionals to obtain the parameters of the present model of manganites. The Density of states of the PMO and CMO system are shown in Figure 2.1. The splitting $\Delta_H(x = 1)$ is calculated by finding the energy difference between the majority and minority states of CMO whereas the splitting between the two e_g states for the majority and minority channels, .i.e, $\Delta^\downarrow(x = 0)$ and $\Delta^\uparrow(x = 0)$, are calculated from the PMO data. The resulting parameters are reported in Table 2.1.

To obtain the hopping parameter t_{hopp}, we calculated the average value of all the hopping amplitude for PMO, CMO and PCMO across all the Mn-Mn bonds. These t_{hopp} values are shown in Figure 3.2 where t_{hopp} versus $\frac{(\epsilon_1+\epsilon_2)}{2}$ is plotted. ϵ_1 and ϵ_2 are the energy levels of the orbitals at the two nearby Mn sites that point towards the bridging O atom between them. A correlation between t_{hopp} and the average energy of the involved states is observed. As the average energy $\frac{(\epsilon_1+\epsilon_2)}{2}$ of these levels on two Mn sites shifts higher, the corresponding t_{hopp} decreases.
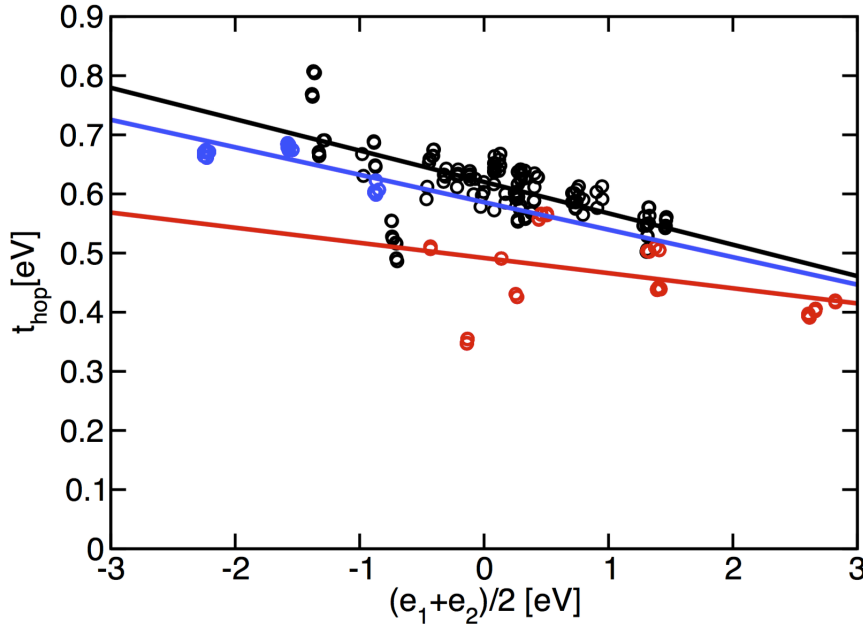
Figure 2.4: Hopping parameters t_{hop} extracted from the generalised DoS for $PrMnO_3$ **(red),** $Pr_{1/2}Ca_{1/2}MnO_3$ **(black) and** $CaMnO_3$ **(blue), as the function of the mean orbital energies** ϵ_1 **and** ϵ_2 **in a bond**: The straight lines are linear interpolations [15].

The determination of J_{AF} value requires the total energy per Mn ion for the G-type and B-type of the CMO system. The entire energy difference between these two magnetic ordering is due to the antiferromagnetic coupling between the nearby sites. Once the

number of FM and AFM bonds are known in the G-type and B-type spin configuration, the J_{AF} value can be obtained.

The breathing parameter can be obtained by two ways. The first approach completely relies on the theoretical rationale, which tells that the JT distortion of an octahedron changes the position of the axial d-orbital only, and the orbital with δ-symmetry remain unaltered. An elongation along an axis with unchanged Mn-O distances in the other directions implies a fixed ratio between the JT distortion amplitude and breathing amplitude, i.e.,

$$\sqrt{Q_2^2 + Q_3^2} = Q_1\sqrt{2} \qquad (2.29)$$

As a result of this distortion, only one of the e_g level shifts and the other remains fixed if $g_{br} = \sqrt{2}g_{JT}$. The restoring force constant k_{br} for the breathing mode is determined in a way that fulfils the condition where if the $d_{3z^2-r^2}$ orbital is occupied, the distortion results in the elongation of the axial bonds along the z direction and rest of the bonds remain fixed. This requires

$$g_{br}/k_{br} = (g_{JT}/k_{JT})/\sqrt{(2)}. \qquad (2.30)$$

Thus, we have the following two conditions to determine the breathing parameters:

$$g_{br} = g_{JT}\sqrt{2} \qquad (2.31)$$
$$k_{br} = 2k_{JT} \qquad (2.32)$$

This gives g_{br}=2.988 eV/A^o and k_{br}=10.346 eV/A^2.

In the second approach, we use g_{br}=2.988 eV/A^o and fix the k_{br} value such that it reproduces the correct $\frac{\sqrt{Q_2^2+Q_3^2}}{Q_3}$ ratio, obtained from the ab-initio calculations, for the A-type PMO system with the present model. We obtain $k_{br}\sim$9.04 (i.e., $k_{br}\sim$1.5k_{JT}). The experimental Raman spectra studies show $k_{br}\sim$1.25$-$1.75 k_{JT} [23, 24].

2.5 Car-Parrinello molecular dynamics

The molecular dynamics (MD) allows us to investigate a detailed dynamical behaviour of the system comprised of many degrees of freedom. The same molecular dynamic is known as ab-initio molecular dynamic when the constituting degrees of freedom are atoms and electrons. Otherwise, the molecular dynamics is a classical molecular dynamics. While the forces on the atoms extracted in the classical molecular dynamic at each time step

are parameterised, the same in the ab-initio molecular dynamics are directly calculated from an electronic structure calculation. There are two kinds of the ab-initio molecular dynamics: Born-Oppenheimer molecular dynamic and Car-Parrinello molecular dynamic [107].

The Car-Parrinello molecular dynamics exploits the fact of the separation of the fast moving electron and the slow motion of nuclei, and it maps the two-component quantum-classical problem to an entirely two-component classical problem, which has two well-separated energy scales. This kind of mapping is possible at the expense of loosing the time-dependent information of the quantum-mechanical subsystem. In the Lagrangian formulation, the system is described by its Lagrangian $\mathcal{L}$:

$$\mathcal{L} = \sum_i \frac{1}{2} M_i \dot{\vec{R}}_i^2 + \sum_i f_i \mu \langle \dot{\psi}_i | \dot{\psi}_i \rangle - \sum_o f_o \langle \psi_o | \hat{\mathcal{H}}_e | \psi_o \rangle + \text{orthonormality constraints} \quad (2.33)$$

where the first term is the kinetic energy of atoms and the second term is the fictitious kinetic energy of electrons. μ is the fictitious mass of the electronic degrees of freedom and $\langle \psi_o | \mathcal{H}_e | \psi_o \rangle$ is the potential energy of the system. The physical kinetic energy of the electrons $\sum_i f_i \langle \psi_i | \frac{\vec{p}^2}{2m_e} | \psi_i \rangle$ system is the part of the potential energy functional, which is taken care by the hopping term. The corresponding classical equation of motion of atoms and electrons can be obtained from the Euler-Lagrange equations,

$$M \ddot{\vec{R}}_i = -\nabla_{\vec{R}_i} \langle \psi_o | \hat{\mathcal{H}}_e | \psi_o \rangle \quad (2.34)$$

and

$$\mu | \ddot{\psi}_i \rangle = -\frac{\partial \langle \psi_o | \hat{\mathcal{H}}_e | \psi_o \rangle}{\partial \psi_i^\dagger} + \sum_j \frac{1}{f_i} \Lambda_{ji} | \psi_j \rangle, \quad (2.35)$$

respectively. The constraints of the expression 2.35 add extra forcefields. In the absence of an external field, the total energy E_{tot} of the system is the constant of motion and is given by:

$$E_{tot} = \sum_i \frac{1}{2} M_i \dot{\vec{R}}_i^2 + \sum_i f_i \mu \langle \dot{\psi}_i | \dot{\psi}_i \rangle + \sum_o f_o \langle \psi_o | \hat{\mathcal{H}}_e | \psi_o \rangle \quad (2.36)$$

While atoms evolve at the instantaneous physical temperature $T_{atom} \propto \sum_i M_i \vec{\dot{R}}_i^2$, the electrons can be attributed a fictitious temperature $T_{el} = \sum_j \mu_i \langle \dot{\psi}_i | \dot{\psi}_i \rangle$. The electrons remain close to the Born-Oppenheimer (BO) surface if they are cold enough (i.e., low fictitious temperature). Hence, if the electrons are initially at the Born-Oppenheimer surface, they will remain close to the Born-Oppenheimer surface during the dynamics as long as they are kept, somehow, at low-temperature.

The Car-Parrinello molecular dynamics can also be used as an optimising tool to find out the minimum energy configuration. To locate a minima of the total energy functional defined in Equation 2.9 as a function of dynamical variable, a term that acts as a friction is added in the equations of motion (Equation 2.34 and 2.35).

2.5.1 Finite temperature dynamics: Nose-Hover thermostat

To study the temperature-dependency in ab-initio molecular dynamics, a atom thermostat is used. We use the Nose-Hoover type thermostat [108–110]. It keeps the atoms and hence, the physical system at the desired temperature $T_{atom} \sim \frac{1}{2} g k_B T$ throughout the dynamics. This is done by introducing an additional friction term in equation of motion of atom (Equation 2.34), which is governed itself by a dynamical variable $\vec{x}_r$.

$$M \vec{\ddot{R}}_i = -\nabla_{\vec{R}_i} \langle \psi_o | \mathcal{H}_e | \psi_o \rangle - M \vec{\dot{R}}_i \dot{x}_r \tag{2.37}$$

$$Q_e \ddot{x}_r = 2 \left[\frac{1}{2} \sum_i M \dot{\vec{R}}_i^2 - \frac{1}{2} g k_B T \right] \tag{2.38}$$

The extended system (i.e., system + atom thermostat) has an energy conserving dynamics.

Equations 2.37 and 2.38 sample a micro-canonical distribution for the extended system (.i.e, actual physical system + atom thermostat) and a canonical distribution for the physical system. The physical temperature of the system remains $T_{atom} = \frac{1}{2} g \, k_B T$ according to the above equation.

2.5.2 Optimisation strategy

We use the Car-Parrinello method not only to study the dynamics of the system but also as a tool to perform minimisation of a function in the parameter space with the given constraints. Here, we use the Car-Parrinello method to study the ground state properties of the system by performing an optimisation on the total energy functional E_{pot} defined in 2.9 w.r.t. randomly chosen dynamical variable, initially. The constrains

on the electronic states ensure that the wave functions always remain orthonormal. Once the forces on the wave functions and other dynamical variables are known, the above mentioned equations of motion (Equations 2.34 and 2.35) can be integrated with the help of any of the available integrating schemes. We use the Verlet algorithm [111] as a time integrating scheme, which is described in Appendix E. There is no prescribed way to do the optimisation under friction. In order to reach to the ground state or any of the metastable state, we use the following scheme:

- First, we investigate the natural frequency with which various variables (i.e., wave function, occupation, spin, atom and lattice constant) evolve when allowed to move independently without any friction. This step doesn't need to be repeated for every optimisation unless the system and model parameter are changed, considerably.

- As a next step, we tune the oscillating frequencies for the dynamical variables by varying the fictitious mass of the same. This should be done in such a way that all the degrees of freedom approximately have similar frequency. Table 2.2 summarises the values of the fictitious masses (i.e., M_R for oxygen atoms, μ for e_g wave functions, M_s for t_{2g} spin vector, M_o for occupation variable and M_{lc} for lattice constants) together with the time-step (Δ_t) that we use in the optimisation.

Δ_t=0.15 a.u.	M_R =0.2 a.u.	μ=0.03 a.u.
M_s=0.03 a.u.	M_o =0.2 a.u.	M_{lc}=0.03 a.u.
	$a_R = 2 \times 10^{-4}$ a.u.	a_ψ=2 × 10^{-4} a.u.
a_s=5 × 10^{-5} a.u.	$a_o = 5 \times 10^{-5}$ a.u.	$a_{lc} = 2 \times 10^{-4}$ a.u.

Table 2.2: Time step, fictitious mass and the friction value for the dynamical variables during optimisation calculation. All the values are in atomic units (a.u.)

- Finally, the kinetic energies of the dynamical variables are annealed out, gradually, to reach the global minimum. Generally, this can be done in two different ways: by decreasing or increasing the friction parameter. We adopt a scheme with constant friction values (i.e., a_R for oxygen atoms, a_ψ for e_g wave functions, a_s for t_{2g} spin vector, a_o for occupation variable and a_{lc} for lattice constants) that are reported in Table 2.2. There are two situations during optimisation that need to be carefully examined:

  1. Metastable states- Often in a calculation of a larger unit cell, the system get trapped into one of the many metastable states with different spin and atomic configurations (mostly characterised by few sites in the crystal with flipped spin or orbital order). To allow the system to get out of these local minima of the energy functional, the atoms and spins need to have a significant kinetic energy. Hence,

instead of quenching the system quickly with high friction values, we use a constant but small friction, as reported in Table 2.2.

2. Over-damped trajectories- Use of higher friction value may lead to the over-damped trajectories which require unexpectedly longer time for the simulations to converge.

Chapter 3

One dimensional model

The present chapter focuses on the one-dimensional system study. Further, a coarse-grained model of polarons is introduced that can be employed to study larger time and length scale thermodynamical properties of the real materials [112]. The tight binding model that is used in this chapter is extracted from the three dimensional model, described in Chapter 2 and also described in Sotoudeh et al. [15]. The results of the present chapter are published in the article Kohler et al. [113].

3.1 Ground state properties at different doping

There are few modification that are to be done to the three-dimensional model, discussed in Chapter 2, before studying the one-dimensional system. The one-dimensional system of manganite consists of the chain of corner connected octahedra. The d-orbitals that point along the chain can form band as a result of hopping. The other δ orbitals can not interact with the intermediate O-p orbital and hence, remain localised. We do not include the breathing mode. The model parameters are same as that obtained for the three dimensional system study, except the antiferromagnetic coupling J_{AF}. We use $J_{AF} = 32.6$ meV instead of 3.32 meV, which is extracted from ab-initio calculations [15]. With a small J_{AF} value, the phase diagram of the one-dimensional system as a function of doping is completely dominated by the FM phase. The larger value of AFM coupling J_{AF} was used to describe the analogous physics of three-dimensional system, which shows the presence of several kind of antiferromagnetic magnetic structure at different doping region in their phase diagram besides the FM phase.

3.1.1 Electron and hole polarons

In this section, the behaviour of one-dimensional perovskite manganite system is studied in greater details. We start looking at the patterns that comes forth as a stable configuration at different doping cases. By selecting 12-site unit cell size, the results are shown in the table 3.1. We observe a repeated existence of few particular small structural units that

N_e	spin order	composition	$(E - \sum_i E[n_k])$[meV]	E [eV]
0	↑↓↑↓↑↓↑↓↑↓↑↓	V_{12}	0	-0.3912
1	↑↓↓↓↑↓↑↓↑↓↑↓	$P^e V_9$	0	-1.98129
2	↑↓↓↓↑↓↓↓↑↓↑↓	$P^e_2 V_6$	0.5	-3.57088
3	↑↓↓↓↑↓↓↓↑↓↓↓	$P^e_3 V_3$	10.7	-5.15075
4	↑↑↑↓↓↓↑↑↑↓↓↓	P^e_4	59.3	-6.69231
5	non-collinear	$P^Z_3 P^e_2$	-16.2	-8.08389
6	↑↑↓↓↑↑↓↓↑↑↓↓	P^Z_6	-46.7	-9.38383
7	↑↑↓↓↑↓↓↑↑↑↓↓↓	$P^Z_4 P^h P^J T$	-46.7	-10.46353
8	↑↑↑↓↓↑↓↑↑↓↑↑	$P^Z_3 P^h P^{JT}_5$	-12.0	-11.51915
9	↑↑↓↑↑↓↑↓↑↑↑↓	$P^Z_2 P^h P^{JT}_5$	-68.9	-12.51556
10	↑↓↑↓↓↑↓↑↑↓↑↓	$P^Z_2 P^{JT}_8$	-74.4	-13.51869
11	↑↓↓↓↑↓↑↓↑↓↑↓	$P^h P^{JT}_9$	0	-14.47726
12	↑↓↑↓↑↓↑↓↑↓↑↓	P^{JT}_{12}	0	-15.47453

Table 3.1: Magnetic order, polaron composition and energy difference between total energy calculated from tight binding model (E) and energy calculated from polaron model (E_{PM}) as a function of number of electrons for system of 12 site unit cell [112].

are examined carefully. These structural units are the trapped charges in the deformed sites in the form of polarons that may extend from a single site to three sites. Table 3.1 shows the magnetic structure and the total energy of the system at various doping. We used these energies of the individual structural units to build up a coarse-grained model. Depending on the nature of the patterns, following polarons are recognised:

- **a vacant site V**: These are the single empty sites without any e_g electrons. The interaction between these empty sites V can only take place via antiferromagnetic kind of coupling J_{AF}. The fully doped manganite system, i.e., $CaMnO_3$ would consists of these tightly packed V sites.

- **three site electron polaron** P^e: It is a trimer that consist of FM aligned Mn sites and is occupied by a single e_g electron. P^e is analogous to an electron polaron in $CaMnO_3$. P^e has three spin polarised electron states delocalised over three sites. The lowest state is occupied and is fully bonding. The second state is unoccupied and nonbonding. The occupied bonding state is mainly concentrated on the central site, whereas the nonbonding state is mainly distributed over the outer sites of the trimer. The third state is fully anti-bonding and is unoccupied.

- **two site Zener polaron** P^Z: It is a dimer of FM aligned Mn-sites and has a single electron that is equally shared between them. The half-doped material analogous to $Pr_{0.5}Ca_{0.5}MnO_3$ can be described as a crystal of these Zener polarons which are AFM coupled to each others. The Zener polaron has two states in the majority spin direction, namely an occupied bonding and an empty anti-bonding state.

- **three site hole polaron** P^h**:** It is a trimer of FM aligned Mn-sites occupied by two electrons. P^h is analogous to a hole polaron in $PrMnO_3$. The electronic structure of P^h is same as that of the P^Z, however in this case, the middle non-bonding state is occupied as well.

- **single site JT polaron** P^{JT}**:** It consist of an electron that occupies a single Mn site. A crystal of JT polarons is analogous to $PrMnO_3$.

3.1.2   Formation energies of polarons

Figure 3.1 shows the density of states of the above mentioned polarons, which reflect their electronic structure properties. The delta peaks in the density of state for each spin is due to the isolated e_g orbitals that are perpendicular to the chain direction, whereas the other orbital forms a band due to the inter site hopping t_{hopp}. Within a single polaron, the charge disproportion between sites depends on t_{hopp} if only one one band is filled. Otherwise, the onsite Coulomb repulsion U plays a crucial role due to inter-band e-e interaction that alters the charge disproportion between sites.

polaron	V	P^e	P^Z	P^h	P^{JT}
E_f^k [meV]	0	-398.3	-274.4	-324.9	0
N_s^k [meV]	1	3	2	3	1
N_e^k [meV]	0	1	1	2	1

Table 3.2: Formation energies of polarons, number $N_s^{(k)}$ of sites occupied by the polaron $P^{(k)}$, and number $N_e^{(k)}$ of electrons on it [112].

It is worth to calculate the binding energies of the structural units to study the stability of these units with respect to the doping x of the system. In order to do so, the energies of the structural units are determined. We start by setting the reference μ_0 for the electron chemical potential to the coexistence value of the electron-poor ($N_e = 0$) and the electron-rich ($N_e = N_s$) systems that are analogous to $CaMnO_3$ and $PrMnO_3$, respectively. While the number of sites in the unit cell is indicated by N_s, the number of electrons per unit cell is defined by N_e . We obtain $\mu_0 = 1.25694417\,eV$. The composition of the system can be identified by its magnetic order and the total number of electrons. The magnetic order and the resulting polaron composition are presented in Table 3.1. The formation energies of the polarons are determined in such a way that the energy

$$E_{PM}[n_V, n_e, n_z, n_h, n_{JT}] = \sum_{k \epsilon \{e, Z, h, JT\}} n_k(E_f^{(k)} + \mu_o N_e^{(k)} - J_{AF}) \qquad (3.1)$$
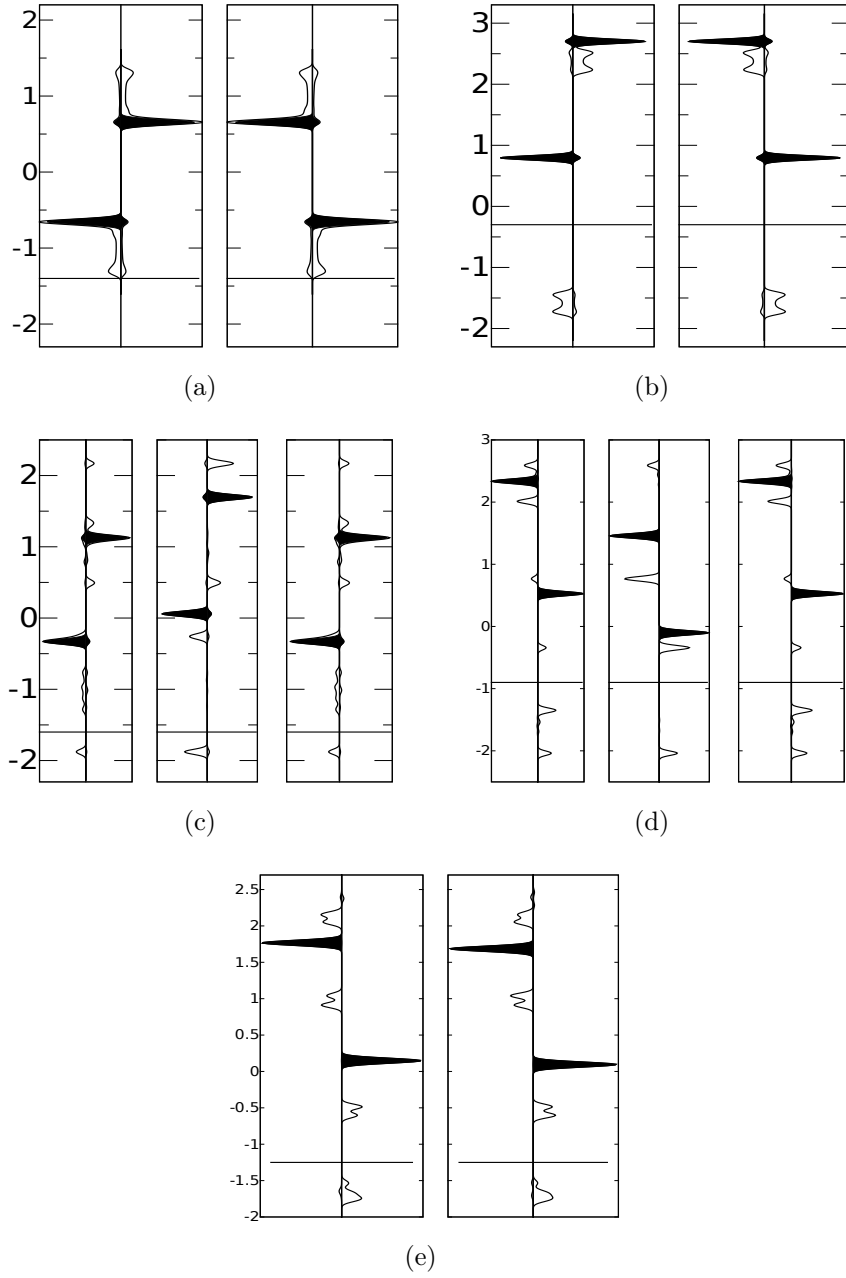
Figure 3.1: Projected density of states of the tight-binding model for the polarons in the one-dimensional manganite chain as function of energy in eV. (a) Two adjacent unoccupied sites V, (b) two adjacent JT polarons P^{JT}, (c) electron polaron P^e, (d) hole polaron P^h, (e) Zener polaronP^Z. The horizontal line indicates the Fermi level. Empty and filled lines indicate $d_{3z^2-r^2}$ orbitals pointing along the chain and the $d_{x^2-y^2}$ orbitals orthogonal to the chain, respectively. The density of states is broadened.

of the polaron model matches the total energies obtained from the tight-binding calculation given in Table 3.2. We denote the number of polarons $P^{(k)}$ with n_k where k ϵ $\{e, Z, h, JT\}$ denotes the polaron type. In the above equation, $E_f^{(k)}$ and $Ne^{(k)}$ represent the polaron formation energy and the number of electrons of the respective polaron, respectively. The values are presented in Table 3.2 . The polaron-formation energies have been extracted so that the energies of the model calculations are reproduced for $N_e = 0$,
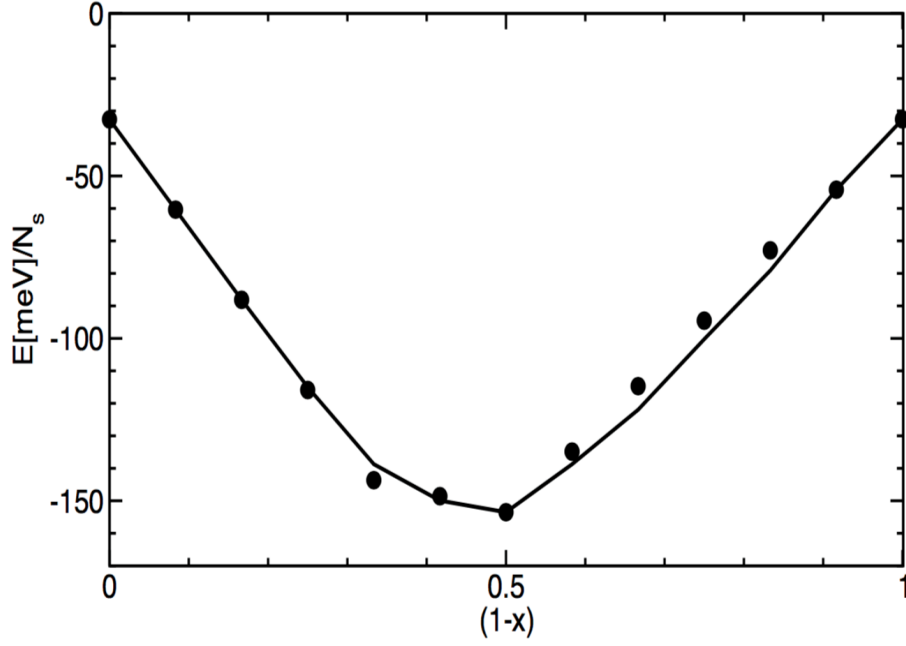
Figure 3.2: Energy per Mn-site of the model calculation (line) as function of the electron occupation $x = \frac{N_e}{N_s}$ compared to the sum of polaron energies given in 3.1: The energy $(x)\mu_o$ of the particle reservoir has been included [112].

1, 6, 11 and 12 by polaron model. The energies of these structural units are presented in Table 3.2.

The mechanism limiting the size of the electron polaron P^e is the competition of the kinetic energy with the antiferromagnetic coupling. On the one side, increase in the size of the electron polaron lowers the kinetic energy of the electron as it can further spread over a larger region. On the other side, there is a penalty for aligning more sites FM. The maximum size of the electron polaron is reached when the delocalisation energy gained by extending the electron polaron by one site is exceeded by the antiferromagnetic coupling. Hence, in the limit of large Hund's coupling J_H, the size of the polaron is determined by the ratio t_{hop}/J_{AF} of the hopping parameter and the antiferromagnetic coupling. With our set of parameters, this maximum size is three sites.

The electron polarons avoid the direct interaction due to the Coulomb interaction, which explains the observation that electron polarons in the dilute limit are separated by at least one vacant site.

3.1.3   Phase competition and domain wall

Because of the kinetic energy cost, the smaller polarons are energetically less favourable than the larger polarons. Thus, they become relevant only when the electron density is

such that the larger polarons, namely the electron polaron P^e, are densely packed. For the chosen 1D system, this occurs at $N^e/N^s = 1/3$. The electron polarons P^e and the Zener polarons P^Z coexist beyond this N^e/N^s value until the Zener polarons are densely packed. This is the case for half-doping, i.e., $N^e/N^s = 0.5$. The favourable defect for doping the electron-rich phase with holes is the Zener polaron P^Z. In analogy with the electron-poor manganite, one would have expected that the extended defect P^h was favourable compared to the smaller Zener polaron P^Z. The reason for the preference of the Zener polaron is that the formation of hole polarons P^h from Zener and JT polarons requires substantial energy

$$P_{JT} + P_Z = P_h - 50.5 \text{ meV} \tag{3.2}$$

Nevertheless, we encounter hole polarons in our calculations. They are formed in response to spin frustration.

The single electron Zener polaron P^Z is more stable than the hole polaron which involves two electrons. Contrarily, the hole polaron P^h is more stable than the two electron Zener polaron as the additional electron enters into an anti-bonding state, which is energetically highly unfavourable. Interestingly, the importance of Coulomb U must be also be acknowledged within P^h polaron that makes P^Z phase around at half filling stable. The system around half doping disclose interesting physics of spin frustration and phase competition among P^Z, P^h and P^e phases.

In the electron-rich phase with $N^e/N^s = 1$, the system forms a crystal of AFM coupled JT polarons P^{JT} where the electron is confined to a single site. Similarly, the nature of an isolated domain walls can also be rationalised from the point of view of a Zener polaron P^Z. The insertion of a hole into the electron-rich material by forming a Zener polaron would, at the same time, introduce a domain wall into the antiferromagnetic order. An isolated domain wall can either annihilate with another domain wall or combine with a Zener polaron to form a hole polaron. With the hole polaron, we identified a structural unit that does not contribute to the ground state at $0\,K$, but that plays an important role for the interconversion of polarons.

The nature of an isolated domain wall can be rationalised from the point of view of a Zener polaron. An abrupt domain wall in the electron-rich material is equivalent to a Zener polaron with an additional electron. This additional electron enters into an anti-bonding state, which is energetically highly unfavourable. Furthermore, the onsite Coulomb U between these two filled states within the Zener polaron leads to formation of a hole polaron where the electron is transferred into the non-bonding state of the hole polaron, which is energetically favourable. In other words, the hole polaron with two

electron is more stable than the Zener polaron for the same number of electrons.

The occurrence of non-collinear spin arrangements indicates that the phase boundary can also delocalise and form a spin spiral. Combining sites into structural units such as polarons is analogous to the formation of molecules out of atoms. The energy scale of forming these polarons is of the order of $0.3\,eV$. The conversion of polarons into each other is analogous to chemical reaction and this energy is already smaller than the energy per polaron itself. An example for such a reaction between polarons is the formation of a hole polaron from a JT and a Zener polaron in Equation 3.2. The interaction between polarons is limited to a substantially smaller scale defined by the Heisenberg exchange J_{AF} and the antiferromagnetic coupling of JT polarons. The energy scale for the interaction between polarons is of the order $10\,$meV.

In this section, a coarse grained description is obtained from the tight-binding model. These models are valuable for mapping out the dynamics of the polaronic and magnetic order in large length and time scales

3.2 Polaron model for larger system and longer timescale

The present chapter put forward a coarse-grained model that has several kinds of polaron as their constituting units. The coarse-grained model can be extended to deal, efficiently, the larger system and longer timescale dynamics calculations as long as the nature of carriers remain one of the kinds of the polarons discussed in the present chapter. In high-temperature zone where the system is no more ordered, the thermodynamics properties and the equilibrium dynamics is studied by calculating the entropy associated with the disordered configurations and by minimising the free energy functional of the system.

Chapter 4

Three-dimensional system study

This chapter aims at studying the ground state structural properties of perovskite manganite as a function of doping at low temperature. We explore the phase diagram of the manganite series with chemical formula $Pr_{1-x}Ca_xMnO_3$ as a function of doping x. A detailed analysis of the electronic, atomic and magnetic properties within individual doping regime is carried out, and the discussion on the possible physical mechanisms dominating within individual regime is put forward. The obtained results are compared with the experimental evidences and the other theoretical models, which are extensively used to describe these systems in past.

As highlighted in Section 2.4, the experimental evidences confirms that the $Pr_{1-x}Ca_xMnO_3$ systems manifests several regions of phase-separation and phase-inhomogeneity in the phase diagram. The size scale of these inhomogeneities in the system can vary from nanometers to as large as micrometers. The existence of phase inhomogeneities raises several interesting questions about their microscopic origin. It is also equally relevant to find out the reason behind the length-scales of these inhomogeneities, i.e., from nanometers to micrometers. In the present chapter, we try to understand the nature of the inhomogeneities found in the phase separation region of the experimental phase diagram.

4.1 Calculation setup

The manganite model described in Chapter 2 is employed to study the phase diagram of $Pr_{1-x}Ca_xMnO_3$ series as a function of doping x at 0 K. Three kinds of the tetragonal unit cell are used, with the condition $L_a=L_b \neq L_c$ where L_a, L_b and L_c are the lattice constant in the x, y and z direction, respectively. The lattice and k-grid size of these unit cell are reported in Table H.10 together with their regions of formation in phase diagram. Firstly, the calculations with different kinds of unit cell is needed to confirm the stability of superlattice structures that do not fit in one or other. Secondly, it also allows us to properly analyse the physics of phase coexistence and phase competition that may require a fairly large unit cell.

While the **I-** and **II-type** unit cell are used for the entire doping region, the largest unit cell, namely **III-type** is used to investigate the charge defects and the large nano-sized ferromagnetic cluster observed in experimental studies [51, 58] in the high-doped system. Thus, the **III-type** unit cell is used for the calculations for the doping region of $0.85 < x < 1$.

unit-cell type	Mn site grid $(N_1 \times N_2 \times N_3)$	k-point grid $(N_1 \times N_2 \times N_3)$	doping region
I-Type	$4 \times 4 \times 4$	$4 \times 4 \times 4$	$0 < x < 1$
II-Type	$6 \times 6 \times 2$	$3 \times 3 \times 3$	$0 < x < 1$
III-Type	$6 \times 6 \times 6$	$4 \times 4 \times 4$	$0.85 < x < 1$

Table 4.1: Types of unit cell, specified by size of Mn-site grid, k-point grid and the doping regime, which is studied.

The procedure adopted to do the calculation with the present model is described in Section 2.5.2 and Appendix H.

4.2 Three dimensional polaron model

Our model shows a tendency of the three dimensional $Pr_{1-x}Ca_xMnO_3$ manganites towards particular local patterns of the orbital, atomic, and spin degrees of freedom across the entire doping regime. Given the possible patterns as basic building block, examining the physics of the system over the entire doping range become easier as it is dictated by the ordering of these building blocks in the lattice. Such stable local patterns emerge out due to a specific charge and orbital orderings together with an associated atomic distortion. We call these distinguishable pattern or entity as 'electron polaron'. The single electron polaron may be highly localised such as the JT polarons or involve more than one site.

Depending on the number of sites involved and the nature of orbital ordering, the electron polarons are categorised into seven types: P^H, P^{JT_1}, P^{JT_2}, P^U, P^{Pl}, P^{Br} and P^{Lr}. Figure 4.1 presents the orbital ordering on individual site of the electron polarons. Table 4.2 summaries the number and nature of sites, charges and orbital ordering on individual sites and doping region of their formation for each of the seven polarons.

The six types of electron polarons are as follows:

Single-site hole (P^H). It is a hole at Mn^{4+} sites in the lattice. The P^H is one of the main building block of electron-poor system ($x > 0.5$). In the electron-rich system ($x < 0.5$), the orbitals on the Mn^{3+} sites points towards the nearby P^H site.

(a) P^H: a hole

(b) P^{JT_1}: Single-site JT polaron (with $d_{3x^2-r^2}$ type orbital ordering)

(c) P^{JT_2}: Single-site JT polaron (with $d_{x^2-y^2}$ type orbital ordering)

(d) P^U: Three-site unidirectional polaron

(e) P^{Pl}: Five-site planar polaron

(f) $P^{P_{Br}}$: Seven-site breathing polaron

(g) $P^{P_{Lr}}$: thirteen-site breathing polaron
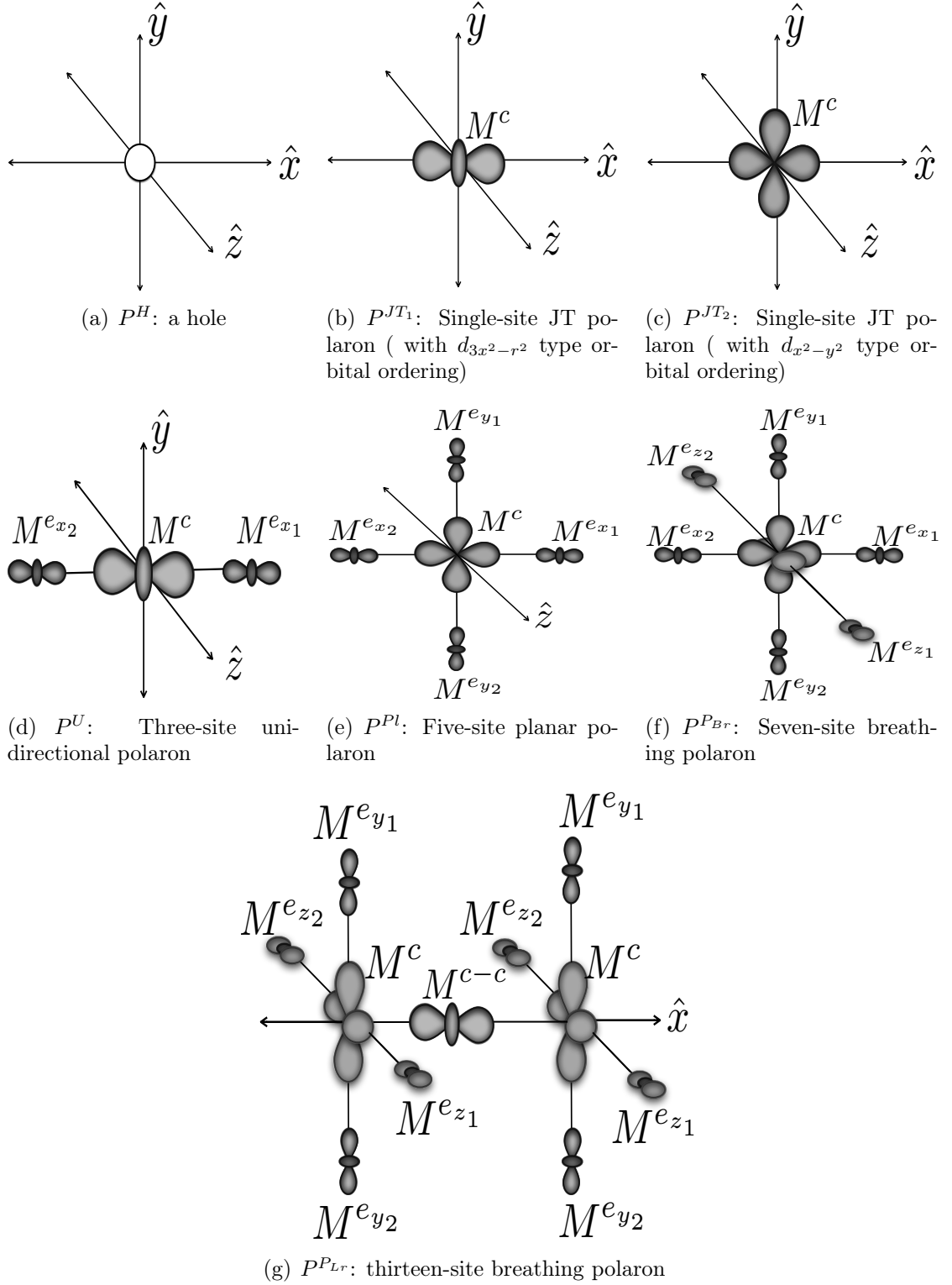
Figure 4.1: Orbital ordering of different kind of polarons found in $Pr_{1-x}Ca_xMnO_3$ across entire doping regime $x \in \{0,1\}$. M^c or M^{c-c} (Mn^{3+}) and M^e (Mn^{4+}) are the central and corner site within polaron. The orbital ordering, charge ordering and doping region in which they are found are compared in Table 4.2. The spins of M^c and M^e sites are parallel. All polarons are single-electron polaron except P^{Br} and P^{Lr}. The P^{Br} is two-electron and P^{Lr} is three-electron polaron.

Single-site JT polaron (P^{JT_1}): It is an one-electron, single-site polaron known as JT polaron. The involved Mn^{3+} site (i.e., M^c site in Figure 4.1(b)) has a $d_{3z^2-r^2}$-type orbital order. The staggered kind of ordering of these JT polarons in the xy plane favours the A-type magnetic arrangement of the PMO (see Fig 4.6). The single-site P^{JT_1} polaron remains an important building block in the low-doped systems ($1<x<0.15$). The electron in the P^{JT_1} polaron gains extra kinetic energy by delocalising over nearest P^H sites in the low-doped systems. This delocalisation is facilitated by spin-canting between the P^{JT_1} polaron and nearby P^H sites.

Single-site JT polaron (P^{JT_2}): It is also an one-electron, single-site JT polaron. The P^{JT_2} polaron has $d_{x^2-y^2}$-type planar orbital pattern. The orbital ordering is illustrated in Figure 4.1(c). This kind of orbital order is also been referred as 'cross-orbital ordering'. The P^{JT_2} polarons are crucial to understand the ferromagnetic insulating phase at $x\sim0.25$.

Three-site uni-directional polaron (P^U): It is a polaron that mainly appears at and below half doping. The P^U polaron is an one-electron polaron and involves three sites (i.e., trimer) in a row that are ferromagnetically coupled. The e_g electron occupies the bonding state of the trimer (Figure 4.1(d)). The resulting uni-directional rod-like features of the P^U polaron plays a key role in the CE-type (see Section 4.5) and C-type (see Section 4.9.3) magnetic ordering as well as in the stripe structures such as Wigner-crystal phase (see Section 4.9.2).

Five-site planar polaron (P^{Pl}): It is a single-electron polaron, which prevails as a important entity in the high-doped system, i.e, $x>0.85$. It involves five sites. The e_g electron occupies the bonding state formed by the hybridisation between the $d_{x^2-y^2}$-type state on the Mn^c central site and the $d_{3x^2-r^2}/d_{3y^2-r^2}$-type states on the nearby Mn^e sites in the positive and negative x/y directions (Figure 4.1(e)). All of the five site have spin parallel configuration. The existence of the P^{Pl} polaron leads to a strong negative Q_3 mode (expansion of octahedron in the xy plane and contraction in z direction) on the Mn^c site.

Seven-site breathing polaron (P^{Br}): It is a two-electron polaron involving seven-site, i.e., a Mn^c central site and six nearest Mn^e sites in all the three direction (Figure 4.1(f)). All the seven sites are in the spin parallel configuration. Both the e_g orbitals on the Mn^c site maintain degeneracy as both the orbitals participate in bond formation with the nearby Mn^e sites. The first e_g electron occupies the bonding state similar to the above P^{Pl} polaron. The second e_g electron occupies the bonding state formed by the $d_{3z^2-r^2}$-type orbital of the same Mn^c site with the $d_{3z^2-r^2}$-type orbitals of the nearest Mn^e sites in the positive and negative z directions. The octahedron on the Mn^c site with equally

Polaron type	No. of M^c and M^e sites	formation region in phase space	charge (in e⁻ units) and orbital ordering on polaron sites
P^H	one M^c	x∼1 - 0.65	a =0, no electron
P^{JT_1}	one M^c	x∼0-0.75	M^c=1.0, $d_{3x^2-r^2}/d_{3y^2-r^2}/d_{3z^2-r^2}$
P^{JT_2}	one M^c	x∼0-0.75	M^c=1.0, $d_{x^2-y^2}/d_{y^2-z^2}/d_{z^2-x^2}$
P^U	one M^c and two M^e	x∼ 0.5-0.8	M^c=0.68, $d_{3x^2-r^2}/d_{3y^2-r^2}/d_{3z^2-r^2}$ M^e=0.16, $d_{3x^2-r^2}/d_{3y^2-r^2}/d_{3z^2-r^2}$
P^{Pl}	one M^c and four M^e	x∼0.86-1	M^c=0.36, $d_{x^2-y^2}/d_{y^2-z^2}/d_{z^2-x^2}$ M^e=0.16, $d_{3x^2-r^2}/d_{3y^2-r^2}/d_{3z^2-r^2}$
P^{Br}	one M^c and six M^e	x∼0.86-1	M^c=1.04, orbitally unpolarised M^e=0.16, $d_{3x^2-r^2}/d_{3y^2-r^2}/d_{3z^2-r^2}$
P^{Lr}	one M^c, two M^{c-c} and ten M^e	x∼1 - 0.85	M^c=0.36, $d_{x^2-y^2}$ M^{c-c}=0.68, $d_{3z^2-r^2}$ M^e=0.16, $d_{3x^2-r^2}/d_{3y^2-r^2}/d_{3z^2-r^2}$

Table 4.2: Six type of electron polarons, region of their presence in phase space, the charge and orbital ordering of the involved sites. The sites within the polarons are distinguishable as central site Mn^c or M^{c-c}(in P^{Lr}) on which most of the charge resides and nearby charge-poor Mn^e sites. All polarons are single-electron polaron except P^{Br} and P^{Lr}. The P^{Br} is two-electron and P^{Lr} is three-electron polaron.

occupied e_g orbitals displays a positive breathing mode (Q_1), i.e., octahedron expands isotropically in all the three direction.

Thirteen-site large polaron (P^{Lr}): It is a three-electron large polaron and comprises of thirteen Mn sites, as shwon in Figure 4.1(g). The first two electrons reside in the bonding states, which are mainly concentrated at the Mn_1^c and Mn_2^c sites. The Mn_1^c and Mn_2^c sites with their neighbouring Mn^e sites can be looked as two isolated five-site P^{Pl} polarons. The third electron goes into the bonding state that is formed due to the merging of these two five-site polaron at a common Mn^{c-c} site as illustrated in Figure 4.1(g). The occupied orbital at the Mn^{c-c} site points at the nearby Mn_1^c and Mn_2^c sites. Such kind of orbital ordering at the Mn^{c-c} site absorbs the strain field induced due to the JT distortion at the Mn_1^c and Mn_2^c sites.

The entropy contribution towards the free energy of the manganite system is negligible at 0 K. On the other hand, the thermodynamical properties of the system can be studied by finding out the configurational-entropy due to several possible arrangements of the above discussed electron polarons, which are accessible by the system at high temperatures. In the present work, we investigate these arrangement of the electron polarons under short and long-range interactions between them at low temperature.

While the kinetic energy and e-e interaction compete over each other around half doping, the long-range Coulomb and elastic interactions due to the cooperative JT effect is mainly

responsible for the patterns formation such as the bi-stripe and Wigner-crystal phase away from half doping.

In the high-doped system, the competition between the anti-ferromagnetic coupling and kinetic energy determines the maximum number of sites involved in the large-sized polarons, i.e., seven sites in P^{Br} polaron and thirteen sites in the P^{Pl} polaron. The gain in the kinetic energy of the e_g electron by delocalisation to an additional site is smaller than the anti-ferromagnetic coupling (J_{AF}) between nearby sites. Our model study establishes a general trend of the number of participating sites in the electron polarons: it increases from a single site in P^{JT_1} polaron at $x=0$ to seven sites in the P^{Br} polaron around $x\sim0.95$.

For $x<0.25$ region of the phase diagram obtained from the model, the sizes of regions identified by certain polaron types are determined by the competition between the kinetic energy and the onsite e-e repulsion.

While the $x<0.25$ system is largely composed of the P^{JT_1} polaron due to the large onsite e-e repulsion, the single-site P^{JT_2} polarons occupy only the sites which has two or more than two P^H neighbouring sites. The P^{JT_2} polaron posses an orbital ordering that is oriented towards the P^H holes.

There are six P^{JT_2} polarons surrounding a common P^H site in the ferromagnetic phase at $x=0.25$, see Figure 4.12. The onsite e-e repulsion on the P^H site is smaller than the kinetic energy gain of the electrons of the P^{JT_2} polarons surrounding the P^H site.

In contrast to P^{JT_1} and P^{JT_2}, the P^U polarons occupy a large part of the phase diagram around half filling ($x=0.5$). At half doping, the CE-structure can be obtained by close packing of the P^U polarons. These P^U polarons share Mn^e sites with the other P^U polarons in the CE-type structure, as shown in Figure 4.7. In the CE-type structure, the two e_g orbitals on the Mn^e site pointing in the x and y participate in the bond formation with the nearest Mn^c sites of the P^U polarons of same spin in the x and y direction, respectively. This situation will be discussed in detail in Section 4.1. It is worth mentioning here the importance of cooperative effect of the lattice which drives the system to ferromagnetic zig-zag chains instead of the uni-directional arrangement found at $x=0.75$ in the C-type magnetic order. Khomskii et al. [95] studied the effect of long-range elastic interactions at $x=0.5$ and suggested the same mechanism for the origin of ferromagnetic zig-zag chain over the other possible orderings of the P^U polarons.

Besides the doping regimes just discussed above, there are regions (for example $x\sim0.66$ region) in the overall phase diagram (Figure 4.2) where the system shows stable structure with charge-stripe phases, such as the bi-stripe (Figure 4.17 (b)) and Wigner-crystal phase

(Figure 4.17 (a)). The Wigner-crystal phase is obtained as the ground state at $x \sim 0.66$. In the Wigner-crystal phase, the P^U polarons do not share any Mn^e which is in contrast to the bi-stripe phase.

In the region $0.85 > x > 0.75$, the C-type phase is found to be the most stable phase. The P^U polarons in this phase are oriented in a single direction which is the only ferromagnetism direction in the C-type magnetic order (Figure 4.18 and 4.19).

In the high-doped ($x > 0.89$) system, the ferromagnetic P^{Lr} polarons are embedded into the G-type anti-ferromagnetic parent compound (Figure 4.22). The P^{Lr} polarons remain isolated from each other as much as possible.

4.3   Phase separation phenomenon

First of all, we look at phase transition process, i.e., a shift from one phase to another that may or may not have a stage with mixed phases, by analysing the graph of energy density $\mathcal{E}$ versus x (doping), provided in Figure 4.2. The thermodynamics of phase separation process can be explained by the free energy $F(T, N_e, V)$ ($F(T, N_e, V) = E - TS$) of the system, which is a function of the temperature T, the electron numbers N_e and the system volume V. We attribute the size parameter of the system to the number of Mn sites N instead of the volume V. At zero temperature, F is equal to the total energy E of the system. Let us consider two different doping case, x_1 and x_2, where the system exists in two different homogeneous phases. The system in the 1st phase has energy density $\mathcal{E}(x_1)$ ($\mathcal{E}(x_1) = \frac{E(x_1)}{N_{x_1}}$) at x_1 and has energy density $\mathcal{E}(x_2)$ ($\mathcal{E}(x_2) = \frac{E(x_2)}{N_{x_2}}$) in the 2nd phase at x_2. N_{x_1} and N_{x_2} are the number of Mn sites in the 1st and 2nd homogeneous phase, respectively. The condition of phase separation in the region $x_1 < x < x_2$ of electron density x is

$$N_x \mathcal{E}(x) \geq N_{x_1} \mathcal{E}(x_1) + N_{x_2} \mathcal{E}(x_2) \tag{4.1}$$

together with

$$N_x = N_{x_1} + N_{x_2} \tag{4.2}$$

where N_x is the total number of Mn sites of the phase-separated region. Using Equation (4.2) in Equation (4.1), we express a function $\mathcal{E}'(x)$ as

$$\mathcal{E}'(x) = N_{x_2} \mathcal{E}(x_2) + \frac{N_x - N_{x_2}}{N_{x_1} - N_{x_2}} (\mathcal{E}(x_1) - \mathcal{E}(x_2)) \tag{4.3}$$

Now, looking at the function $\mathcal{E}'(x)$ defined in Equation (4.3) as a function of x, we receive a straight line between the two points x_1 and x_2 on the $\mathcal{E}$ versus x graph. The value of $\mathcal{E}'(x)$ at x on this line where $x_1 < x < x_2$ should be compared to the corresponding energy density $\mathcal{E}(x)$ of the homogeneous system, which is a point on the original curve $\mathcal{E}(x)$. If

$$\frac{\partial^2 \mathcal{E}}{\partial x^2} < 0, \tag{4.4}$$

then $\mathcal{E}' > \mathcal{E}$, i.e., the total energy density of the system increases if the system undergo phase separation. The system in the doping region $x_1 < x < x_2$ separate into two subsystem with the x_1 and x_2 electron densities.
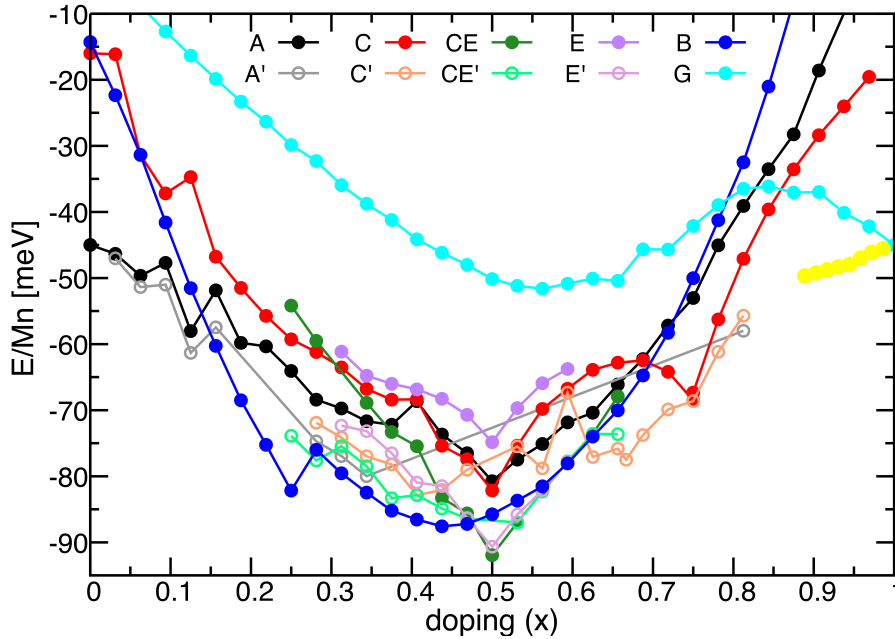
Figure 4.2: Energy per Mn, $\mathcal{E}$ ($\mathcal{E} = E_{tot}/N_s - (1-x)\mu_o$) where N_s is total number of Mn sites and x is doping) as a function of doping $\mathrm{Pr_{1-x}Ca_xMnO_3}$. The chemical potential μ_o is set same for the PMO($x=0$) and CMO($x=1$) system. μ_o is size independent and has a value $\mu_o = 513.81$ meV for all the three kind of unit cells. The energies for different magnetic orders .i.e., A-, B-, C-, G- and CE-type are compared. The canted spin structure corresponding to the A-type, C-type and CE-type are also included. The yellow solid circle indicates the energies of the phase with 7-13 sites ferromagnetic clusters in the $0.89 < x < 1$ region (Section 4.9. The calculations for canted spin structure are performed by allowing the t_{2g} spin degrees to vary during when the system is close to the corresponding respective collinear magnetic orders during optimisation procedure. The points on the dashed line are the zero temperature distinct phases, i.e., $x = 0, 0.25, 0.5, 0.66, 0.75, 0.95$ and 1.

As discussed above, the phase separation condition is a thermodynamic instability that is associated with a violation of the condition of the stability, i.e., $\chi = \frac{\partial^2 \mathcal{E}}{\partial x^2} > 0$. If $\chi < 0$, there is no phase separation and the system exhibits single homogenous phase. Hence, its obvious that the $\mathcal{E}$ versus x graph of an infinite system with only pure phases is a convex-type in nature. Let us analyse the complete $\mathcal{E}$ versus x graph in detail, obtained from our model for $\mathrm{Pr_{1-x}Ca_xMnO_3}$ system.

Figure 4.2 represents the $\mathcal{E}$ versus x graph for the complete doping regime for $Pr_{1-x}Ca_xMnO_3$ system obtained from our model. The chemical potential μ_o is set such that it has same value for PMO and CMO system. Our results confirm homogenous phase at x=0, 0.125, 0.25, 0.5, 0.66, 0.75 and 1.0. It is clear that the regions in the immediate vicinity of x=0.5 display phase coexistence. The electron-poor side of the $x = 0.5$ doping shows the coexistence of the CE-type and charge-stripe phases. The electron-rich side also exhibits a tendency of coexistence of the CE-type and B-type phase. The second phase coexistence region in the electron-rich side in Figure 4.2 is between the B-type phase at x=0.25 and the canted A-type phase at x=0.125. Reis et al. [46] also ascribed these two regions (x∼0.20 and x∼0.375) of the phase diagram as phase-separated regions in the electron-rich side.

4.3.1   Lattice constants versus doping

Figure 4.3(a) displays the variation of the lattice vectors, L_a and L_c (where L_b=L_c), along the x and z direction as a function of doping x. The corresponding experimental graph is shown in Figure 4.3(b).

The present model does not allow tilting and assumes constant Mn-O-Mn bond angle (see Section 2.2.1). This assumption is valid for most of the doping regime where the Mn-O-Mn angle θ_{ab} in the ab plane and θ_c in the c direction remain same. But, the lattice constants obtained from the model calculations is expected to differ from the experimentally obtained lattice constants when the θ_{ab} and θ_c strongly differ from each other. Besides the JT-type modes, the perovskite manganites also exhibit octahedral rotational modes. Before discussing the lattice constant versus doping graph, we look at the octahedral rotation and tilting pattern in the $Pr_{1-x}Ca_xMnO_3$ series.

Figure 4.4 (a) shows a rotational and tilting induced $GdFeO_3$-type distortion pattern, commonly found in $Pr_{1-x}Ca_xMnO_3$ systems, of the corner-connected octahedra. Figure 4.4 (b) shows the variation of the in-plane (θ_{ab}) and out-of-plane (θ_c) Mn-O-Mn bond angles, observed experimentally, as a function of doping x [25]. The in-plane Mn-O-Mn bond angles θ_{ab} are smaller than the corresponding θ_c angle, in the c direction, for a large region in the phase diagram.

(a)

(b)
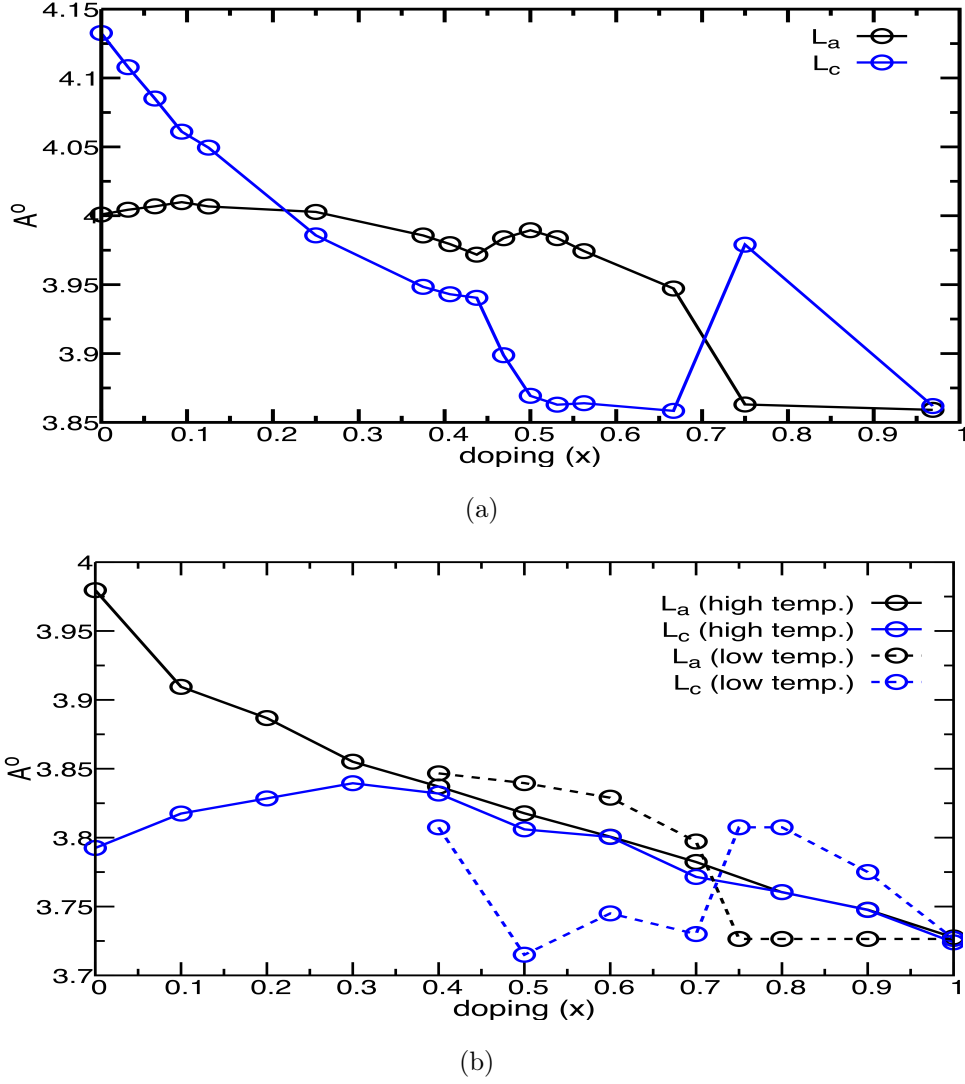
Figure 4.3: Atomic structure of $Pr_{1-x}Ca_xMnO_3$ system as a function of doping. (a) lattice constants obtained from the model. (b) experimental lattice constants [25]. The lattice constants obtained from the model are in good agreement with the experimental lattice constant at low temperature, except for the region near $x = 0$. Experimentally, the system is observed to exhibit orthorhombic structure (O) ($\geq x \geq 0.3$) in the region $0 \geq x \geq 0.2$ of the discrepancy. We also perform calculations with experimentally found lattice constant in this region of discrepancy.

The A-type ions in $Pr_{1-x}Ca_xMnO_3$ series (i.e., Pr and Ca) are too small to fit into the interstitial space formed between the MnO_6 octahedra. This leads to cooperative rotation and tilting of the octahedra forming an orthorhombic structure with a *Pbnm* symmetry at low temperature [25]. In the orthorhombic structure obtained from the cubic perovskite structure, as shown in Figure 4.4 (a) and (b), the adjacent octahedra are rotated in anti-phase about the x and y direction and in-phase about the z direction. In the Glazer's nomenclature [114], this rotation pattern of Figure 4.4 (a) is characterised by $a^-a^-c^+$ kind tilting of the MnO_6 octahedra.

(a)

(b)
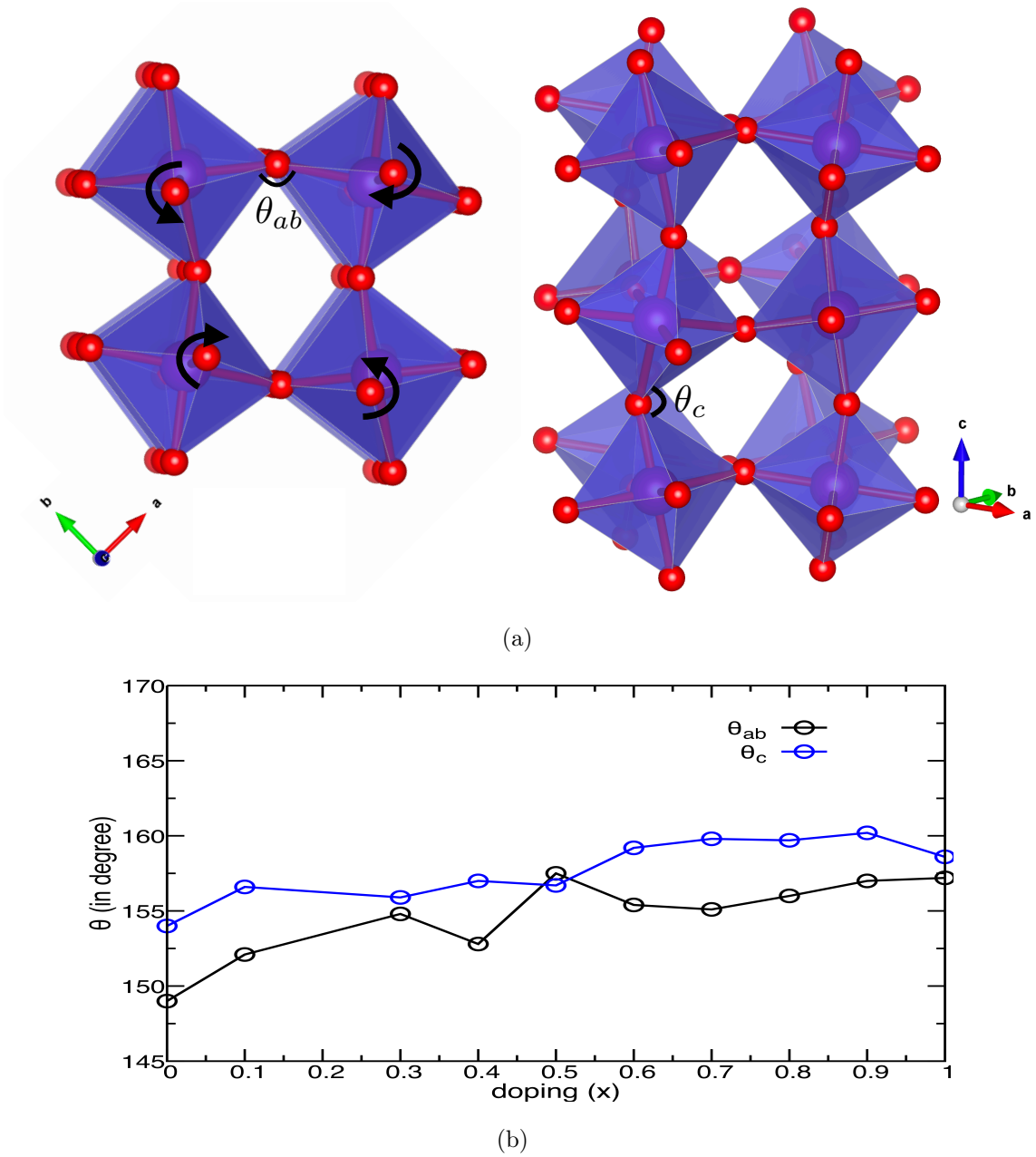
Figure 4.4: Tilting pattern in the ab plane and along the c direction (a) and variation of experimental $Mn - O - Mn$ bond angle as a function of doping x at room temperature (b) [25]. The direction of rotation about the c direction is denoted by black arrows for the octahedra of the ab plane. The rotation of each octahedra remain anti-phase with respect to the nearby octahedra in the ab plane and in-phase with the nearby octahedra in the c direction.

The lattice constants versus x graph obtained from the model underlines a general trend of average lattice constant: increases from right ($x=1$) to left ($x=0$), which is in the agreement to the experimental trend. The average Mn-O bond length commensurates with the number of Mn^{3+} ions while going from $x=1$ to $x=0$ and hence, the unit cell expands.

The larger the Mn-O-Mn angle, the larger is the hopping amplitude. The smaller value of θ_{ab} around $x=0$ suggests a weaker hybridisation between occupied e_g orbitals on a site and empty e_g orbitals with the same spin on the nearest sites in the xy plane. This in turn stabilises the $d_{3x^2-r^2}/d_{3y^2-r^2}$-type staggered orbital order in the xy plane which is identical to the experiments finding near $x=0$. As we do not include the effects of tilting in our present model, we find a discrepancy in lattice constants with the experimental results in the region near $x=0$. Due to strong hybridisation between the lower occupied states and empty states on nearby sites, $d_{x^2-z^2}/d_{y^2-z^2}$-type orbital ordering is favoured as found in our calculations as we do not include the tilting. To resolve this inconsistency of our model related to incorrect orbital ordering discussed above in this low-doped region, we use the experimental lattice constants for the region below $x=0.25$.

The calculated L_c decreases sharply w.r.t. x in the region $0.2>x>0$. The removal of electrons from PMO introduces charge-deficient sites leading to the conversion of P^{JT_1} polaron of $d_{3x^2-r^2}/d_{3y^2-r^2}$-type orbital order into P^{JT_2} polaron of $d_{x^2-y^2}$-type orbital order (see Figure 4.13). This new P^{JT_2} polaron with $d_{x^2-y^2}$-type orbital order expands the Mn-O bonds in the xy plane and contracts the same in the z direction. Hence, the calculated L_c decreases w.r.t. x in this region.

The lattice constants in the region around $x{\sim}0.25$ are almost equal which can be rationalised by the close packing of the three-fourth P^{JT_2} polarons of $d_{x^2-y^2}/d_{y^2-z^2}/d_{z^2-x^2}$-type orbital order together with the one-fourth P^H sites in the B-type magnetic structure. We discuss this B-type insulating phase in greater detail in Section 4.8.3.

The experimental ratio $\frac{L_c}{L_a}$ is smaller than 1 in most of the region below half doping, 1 around $x \sim 0.25$ and again smaller than 1 in the $0.5{<}x{<}0.75$ region. The $\frac{L_c}{L_a}$ is larger than 1 in the narrow region $0.85{<}x{<}0.75$ and remain equal to 1 in the region above $x{>}0.85$. This is explained as follows:

The P^U polaron replaces P^{JT_1} and P^{JT_2} polarons while going from $x=0$ to $x=0.5$. At half filling, the ferromagnetic zig-zag chains of the P^U polarons is preferred over a ferromagnetic uni-directional chains. It is due to the hybridisation of the e_g states on the M^e sites pointing in the x and y directions with the M^c sites of the P^U polarons of same spin in the x and y direction, respectively. Hence, the P^U polaron oriented in the y (x) direction shares corner sites with the P^U polarons in the x (y) direction. The ratios $\frac{L_c}{L_a}$ is smaller than 1 for the region $0.75{>}x{>}0.5$ as the P^U polarons are still oriented in the x or y direction promoting the expansion of the lattice parameters in the xy plane. The system goes through a transition from the Wigner-crystal phase at $x{\sim}0.66$ to the C-type at $x{\sim}0.75$. The P^U polarons have a single orientation direction (i.e., the z direction) in the C-type structure within the region $0.75{<}x{<}0.85$ (Section 4.9.3). This single orientation

direction is the direction of ferromagnetism. This kind of one-dimensional arrangement of the P^U polarons causes the expansion of unit cell in the direction of ferromagnetism (i.e., the z direction) and is supported by the $\frac{L_c}{L_a}>1$ in this doping region. The trend $\frac{L_c}{L_a}>1$ is valid until $x=0.85$. The lattice parameters are equal above $x=0.85$. In this region of high-doping, the lattice strain induced by a single Mn^{3+} site is absorbed by another Mn^{3+} site by forming a large ferromagnetic cluster P^{Lr} in the background of the G-type magnetic order.

4.3.2 Magnetic and charge ordering trends

Figure 4.5 and Figure 4.2 present the energetic of the different magnetic structures and band gap as a function of the doping x. Several metastable states with canted-spin structures are encountered in our model calculations. The canted A-type and canted CE-type magnetic order dominate the low temperature phase diagram in the vicinity of $x=0.5$ and $x=0$, respectively, besides the collinear A- and CE-type magnetic orders.

The region $x\sim 0$ shows the stability of the A-type order over all other magnetic order. The band gap of 0.92 eV is obtained in our calculation for the PMO A-type structure. It must be noted here that besides the A-type magnetic order, we obtained several possible disordered metastable structures for the other kind of magnetic orders for the PMO system. These metastable structures are very different from the ordered structures obtained through the ab-initio calculations [15], with experimental atomic structure, for the respective magnetic order at $x=0$. But nevertheless, the energies for different magnetic structures follow a trend which is similar to the ab-initio calculations and increase in the order: A-, B-, C-, and G-type. As the lattice constants and the atomic structures obtained, by our present model, do not agree with the experimental studies in the low-doped region $0.25>x>0$, we also tried to analyse the system by performing calculations with the experimental lattice constant in this doping region (see Section 4.4).

The band gap for canted A-type system at $x=0.125$ is reduced significantly to 0.43 eV. The unfilled states close to the Fermi level are the states mainly localised on the P^H sites. The P^H hole site has a very small charge density with without any orbital polarisation. The band gap arises from the separation of the occupied e_g states on the Mn^{3+} sites and the weakly split e_g states on the P^H sites.

A low-temperature magnetic phase transition from the A-type to the B-type is indicated from our results as the PMO system is doped with holes, i.e., Ca ions. Figure 4.2 shows this phase transition while going from $x=0$ to $x\sim 0.25$. The system around $x\sim 0.25$ displays the B-type magnetic structure with a weak charge ordering at low temperature.

It is worth mentioning here from Figure 4.2 that this region ($x{\sim}0.25$) is the only region in the entire doping range which can be associated with a non-zero band gap for the B-type magnetic order. This phase transition from the A-type to the B-type is verified by numerous experiments [25, 44, 46, 115].
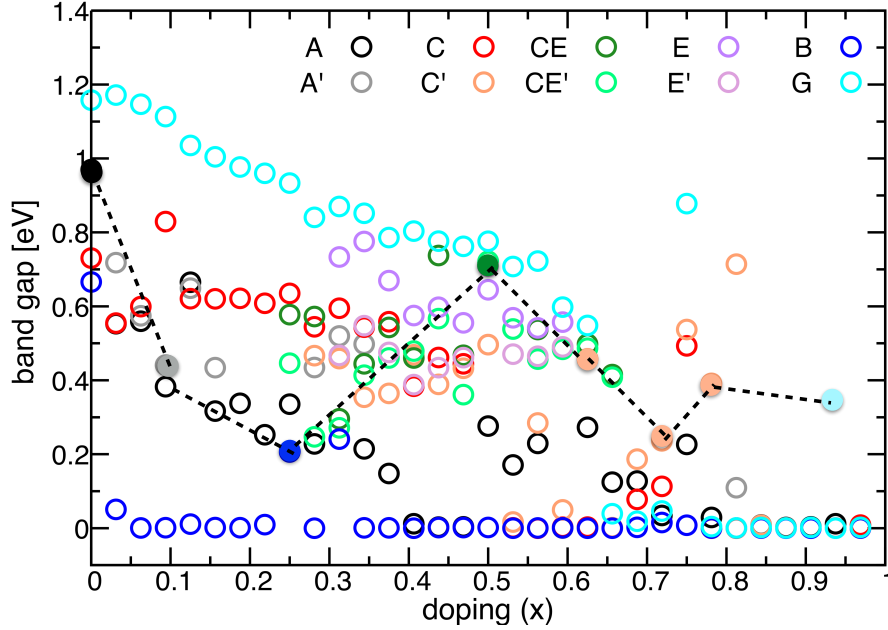
Figure 4.5: Comparison between the band gap of different magnetic orders as a function of doping x for $Pr_{1-x}Ca_xMnO_3$. The black dashed line connect the solid circles that are values of the band-gap of the homogenous phases in the phase diagram. The band gap of the A-type structure of PMO is 0.92 eV, while that of the PCMO CE-type structure is 0.70 eV. The band gap in PMO is entirely due to the JT splitting of the upper and lower e_g state on each Mn site and inter-orbital Coulomb U interaction between these states. In the region $0.3{<}x{<}0.5$, the band gap of canted spin structures lie in the range 0.6-0.35 eV. The B-type ferromagnetic phase is metallic in the entire doping scale, except in the small region $0.25{<}x{<}0.30$.

The low-temperature charge and orbitally structure of the CE-type at $x{\sim}0.5$ obtained from the present model is in good agreement with the other theoretical findings [15]. A band gap of 0.712 eV is obtained from our calculations at $x{=}0.5$.

Interestingly, our study shows that the electron-poor region close proximity to $x{=}0.5$ doping exhibit collinear CE-type structure with a strong charge ordering. The calculated band gap at $x{\sim}0.53$ abruptly reduces to 0.512 eV.

The experimental charge ordering temperature T_{CO} rises while going from $x{\sim}0.5$ to $x{\sim}0.7$. We attribute this rise of charge ordering temperature T_{CO} to the transition from the CE-type phase to mixed-stripe (Section 4.9.1) or Wigner crystal phase (Section 4.9.2). Similar to the CE-type structure, the Mn^{3+} sites are isolated from each other in the xy plane of the Wigner-crystal structure. In the Wigner crystal phase, the charge ordering in the xy plane become even more stronger as the P^U polarons become do not share M^e sites. At $x = 0.625$, the mixed-stripe phase exhibits charge ordering not only

in the xy plane but also in the z direction. Hence, the Wigner-crystal and mixed-stripe structure are example of a strong charge-ordered state, stabilised due to the long-range elastic and the e-e interactions [95]. The T_{CO} has its peak around $x\sim0.7$, which can be understood in the context of the Wigner-crystal and the C-type phase observed at $x\sim0.66$.

Around $x=0.75$, our calculations reveals a largest charge disproportion and a band gap of 0.5 eV in the C-type phase. In this C-type phase, a strong tendency towards a unidirectional orbital arrangement, i.e., a rod-like ordering of the P^U polarons, in the z direction drives the spin order to almost ferromagnetic in the z direction at low temperature. The charge-ordered phase is detected in our study till $x\sim0.85$ that abruptly ended with a phase of glassy domains in the $0.85<x<0.89$ region.

The region $0.89<x<0.92$ in the experiments is attributed to the CMR effect with a sudden increase in the net magnetisation, which falls to lower value in the higher doping region. The experimental measurement of the magnetic and transport properties of the high-doped compounds forecast the presence of glass domain of metallic cluster in the region $0.89<x<0.92$. This feature of metallic glass domains is characterised by a maximum magnetisation around $x\sim0.90$. Our present study shows ferromagnetic clusters distributed randomly in the G-type parent in $1<x<0.89$ region corroborating with the mentioned experimental findings [44]. Doping the system further to $x=1$ drives it to the G-type anti-ferromagnetic where the anti-ferromagnetic coupling dominates between the P^H sites.

In the next sections, we investigate the electronic, atomic and spin structure in greater detail at each doping region individually.

4.4 Undoped system ($x=0$): PMO

The electron-rich PMO system displays an unique orbital ordering and distortion pattern. In the PMO system, each of the Mn sites has one e_g electron. This e_g electron is confined to a single site forming P^{JT_1} polaron; see Figure 4.1. The occupancy of the e_g electron on Mn site breaks the rotational symmetry of the occupied orbital due to the JT electron-phonon coupling. The preference of the e_g electron for one of the e_g orbitals lifts the degeneracy of the e_g subset with a simultaneous asymmetric octahedral distortion that is concomitant with the occupied state. The A-type magnetic order is the most stable and the G-type is the least stable in these undoped systems ($x=0$). The most favourable orbital ordering pattern with A-type magnetic order is demonstrated in Figure 4.6 for two adjacent xy planes that is obtained with the high-temperature experimental lattice

constant [25]. The figure indicates a $d_{3x^2-r^2}/d_{3y^2-r^2}$-type staggered orbital ordering in the xy plane.

To carefully analyse the orbital ordering pattern, the one-particle wave functions are projected onto the orthogonal states, $|w_{l_x}\rangle$ and $|w_{h_x}\rangle$, that are linear combination of the e_g states, $d_{3z^2-r^2}$ and $d_{3x^2-y^2}$, i.e.,

$$|w_{l_x}\rangle \;=\; -|d_{3z^2-r^2}\rangle\cos(\gamma) + |d_{3x^2-y^2}\rangle\sin(\gamma) \tag{4.5}$$

$$|w_{h_x}\rangle \;=\; -|d_{3z^2-r^2}\rangle\cos(\gamma) - |d_{3x^2-y^2}\rangle\sin(\gamma) \tag{4.6}$$

$|w_l\rangle$ in (4.9) is the orbital pointing in the x direction. The orthogonal orbital $|w_{h_x}\rangle$, in Equation (4.6), points in the yz plane. Similarly, the orbital pointing in the y direction and corresponding orthogonal orbital in the xz plane are given by

$$|w_{l_y}\rangle \;=\; -|d_{3z^2-r^2}\rangle\cos(\gamma) - |d_{3x^2-y^2}\rangle\sin(\gamma) \tag{4.7}$$

$$\tag{4.8}$$

and

$$|w_{h_y}\rangle \;=\; -|d_{3z^2-r^2}\rangle\cos(\gamma) + |d_{3x^2-y^2}\rangle\sin(\gamma), \tag{4.9}$$

respectively. The angle γ is the mixing angle. The electronic structure of the PMO system can be understood from the above occupied Wannier states $|w_{l_x}\rangle$ and $|w_{l_y}\rangle$, which points in the x and y direction, respectively. The e_g orbital subset on each Mn site split into the lower $d_{3x^2-r^2}/d_{3y^2-r^2}$ occupied orbital and the upper $d_{x^2-z^2}/d_{y^2-z^2}$ unoccupied planer orbitals.

Our calculations with variable lattice constants show $L_c>L_a$ (with $L_a=L_b$) which is not in agreement with the experimental findings. While the occupied states are strongly localised on the Mn sites, there still remains a weak hybridisation of the lower e_g orbital on a particular site with the higher e_g orbital on the adjacent site in the same direction as the orientation of the lower e_g state on the former. We obtain a mixing angle $\gamma \sim 37^o$ from our model with variable lattice constants hinting towards a $d_{x^2-z^2}/d_{y^2-z^2}$-type orbital ordering which is in contrast to the experimentally found $d_{3x^2-r^2}/d_{3y^2-r^2}$-type orbital ordering [25]. When the calculations are performed with the experimental lattice constant [25], we obtain a mixing angle $\gamma \sim 55^o$. The mixing angle is almost same as one obtained by the ab-initio calculations. This suggests a $d_{3x^2-r^2}/d_{3y^2-r^2}$-type orbital ordering, which is in agreement with the experimentally verified orbital ordering. The study of PMO system by Hotta et al. with variable lattice parameter also pointed out this discrepancy
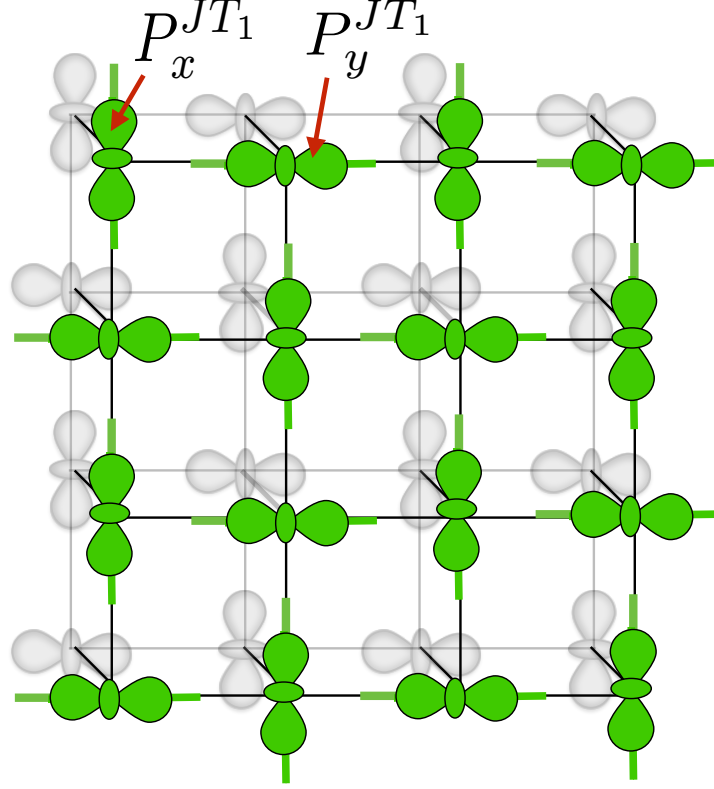
Figure 4.6: Orbital and spin structure of the two xy plane of the A-type order at $x=0$. The charge disproportion between sites is highlighted by the size of the orbital. The green and grey color indicate the spin up and spin down directions of the t_{2g} spin. The 1st xy plane is anti-ferromagnetically coupled to the 2nd xy plane. The P^{JT_1} polaron ($P_x^{JT_1}$ or $P_y^{JT_1}$) is present on every Mn (i.e., Mn^{3+}) site as all sites are. The orbital order is rotated by 90° from a site to the nearest site in the ferromagnetic xy plane. The P^{JT_1} polaron order is in phase in the z direction which is direction of anti-ferromagnetism in the A-type magnetic order.

between the orbital ordering obtained by the model and experimental results [116]. They ascribe this deviation to the tilting of the Mn-O-Mn bond. The different tilting angles in the xy plane and z direction changes the $T_{1,1}^z$ (see Equation 2.14) hopping matrix element to a non-zero value stabilising the $d_{3x^2-r^2}/d_{3y^2-r^2}$-type ordering in the xy plane.

If the e$_g$ electron occupies the $d_{3x^2-r^2}$-type orbital on the first site, the electron on the nearby sites in the xy plane must reside in the $d_{3y^2-r^2}$-type states to reduce the lattice strain associated with the JT distortion at the first site. This staggered orbital ordering and distortion pattern is in-phase in the z direction (Figure 4.6). This particular orbital ordering and corresponding distortion pattern promote unequal lattice constants L_a, L_b and L_c (such that $L_a=L_b{\neq}L_c$), as shown in Figure 4.3 at $x=0$ doping.

In PMO system, the B-type magnetic order lies energetically closer to the A-type than other magnetic order, i.e., C- and G-type. As the electrons are trapped on individual sites with deformed octahedra forming highly localised P^{JT_1} polarons, the conduction properties may be significantly affected by the contribution of the dynamics of these polarons as charge carriers at high temperature.

While the onsite transition from the filled state to the empty states is dipole forbidden in PMO, the optical dipole-allowed transition from the filled state to the empty d-states on the adjacent site is a charge-transfer excitation.

4.5   Half doped system ($x=1/2$): PCMO

The half-doped PCMO system has an orbital and a charge ordered state within the CE-type magnetic arrangement of the t_{2g} spins. The calculated electronic structure of the CE-type phase reveals a band gap $\Delta_{gap} \sim 0.712$ eV. The total energy of the system corresponding to different magnetic order together with the other measurable quantities, such as band gap and atomic distortion (Q_1, Q_2, and Q_3 values), are compared in Table 4.7.

Magnetic order	Energy/Mn (eV)	mode amplitude $|Q_2|/|Q_3|, |Q_1|$ (A^o)	band gap (eV)
A	2.4883	{0.166/0.227, 0.242} {0.00/0.033, 0.087}	0.2762
B	2.4833	{0.024/0.001, 0.16}	0.0
C	2.4869	{0.00/ 0.321, 0.264} {0.0/0.066, 0.065}	0.4963
G	2.5189	*	0.7761
E	2.4942	*	0.6449
CE	2.4771	{0.259/0.163, 0.257} {0.00/0.033, 0.074}	0.7216

Table 4.3: Magnetic order, ground state energy and octahedral modes, band gap and charge densities for PCMO system. The two set of $\{|Q_2|/|Q_3|, |Q_1|\}$ correspond to octahedral mode at electron-rich and electron-poor sites

The orbital ordering pattern with the corresponding spin of the CE-type structure is shown in Figure 4.7. The CE-type magnetic structure obtained from the our model consists of quasi one-dimensional ferromagnetic zig-zag chains, shown by green and blue, anti-ferromagnetically coupled to each other in the xy plane. These CE planes are anti-ferromagnetically stacked onto top of each other in the z direction. The ordered structure can be seen as an arrangement of the P^U polarons (Figure 4.1) sharing corner sites. All the sites display strong spin-polarisation due to the large Hund's coupling. On the other hand, only one-half of the total Mn sites that are the M^c sites of the P^U polarons are orbitally ordered and JT distorted. The other-half of the total Mn sites are weakly orbitally-polarised as they are the M^e sites shared between two P^U polarons that are orthogonal to each other in the xy plane. Thus, the M^e sites exhibit a very weak JT

distortion (see Table 4.7). The orbitally ordered (i.e., M^c sites of the P^U polarons) sites hybridise with the weakly orbitally-polarised M^e sites in the x or the y direction along the CE chain forming bonding states that are occupied.

Experimentally, it has been verified [25] that the charge ordering in the xy CE plane stacks along the z-axis rather than being shifted by one lattice point from one plane to the next. This charge stacking can also be verified with the CE-type structure obtained by our model, as illustrated in Figure 4.7. This kind of stacking of the charge-ordering in the z direction suggests that the Coulomb repulsion is not the dominating interaction at x=0.5. In Chapter 6, we describe the CE-type structure with the help of the relevant Wannier-like states.
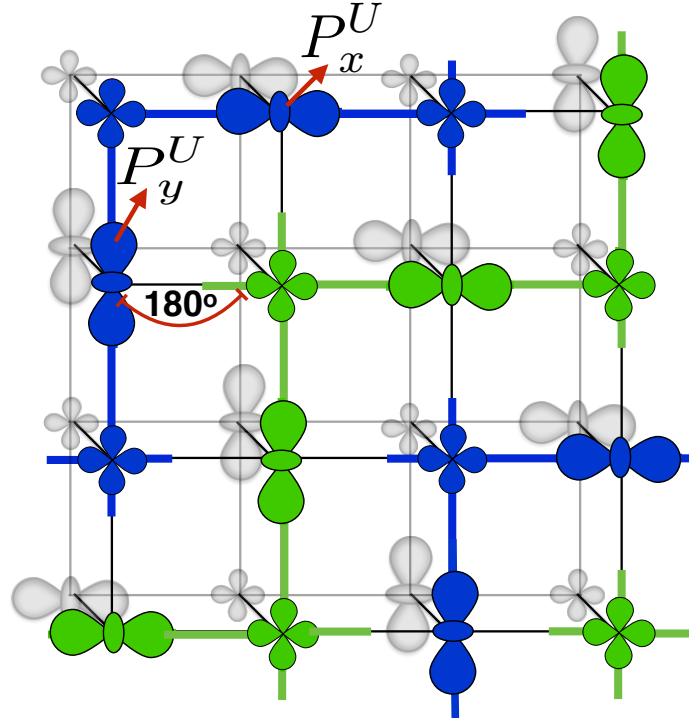
Figure 4.7: Orbital and spin structure of the two xy plane of the CE-structure at half filling x=0.5. The charge disproportion between the sites is highlighted by the size of the orbital. The blue and green indicate two different orientation of the t_{2g} spins that are anti-ferromagnetically coupled. Within a single zig-zag ferromagnetic chain, the P^U polarons alternate their orientation. The corner sites of the P_x^U polaron overlap with the nearby P_y^U polarons within the zig-zag chain and vice versa. As these corner sites are shared equally by the P_x^U and P_y^U polarons, the orbital ordering at these sites is $d_{x^2-y^2}$. The grey colored sites in the 2nd xy plane are anti-ferromagnetically coupled to 1st xy plane. While the ordering of the P^U polarons remain in phase in the z direction, the magnetic order is anti-ferromagnetic in this direction.

The charge on the corner M^e and central M^c site is $0.5 \pm \Delta$, where Δ=0.25 is the charge disproportion. This strong charge-disproportion between Mn ions is in agreement with the checkerboard-type charge ordering observed experimentally at x=0.5 [52]. However, the experimental structural analysis by Aladine et al. [54] shows a dimerised phase at x=0.4 which suggests a charge ordering that is different from the another experimentally

and theoretically proposed checkerboard-type ordering of the Mn^{3+}/Mn^{4+} ions [28, 52]. While the octahedra around each Mn site is asymmetrically distorted in the ab plane (i.e., plane within which the ferromagnetic zig-zag chains runs), half of the Mn sites in the checkerboard-type structure remain undistorted. The checkerboard-type charge ordering is suggested by the ionic bonding where the holes and the e_g electrons reside on the Mn cations and the oxygen 2p-shells remain fully occupied. Therefore, according to the rigid ionic-bond picture, oxygen anion role is not dominating in the overall electronic and magnetic structure of the system. In contrast to the checkerboard-type ordering, the presence of equivalent Mn sites observed in dimerised phase by several experimental studies [54–56] cannot be resolved by this rigid ionic-bond picture. The Zener polaron model proposed by Aladine et al. for the experimentally found dimerised phase at $x{=}0.4$ suggests a hole on the intermediate O^- anion, which is shared by the nearby Mn^{3+} ions. The observation of the predominant oxygen 2p-character of the electrons (or holes) near the Fermi level in several x-ray absorption experiments [117–121] at Mn K edge, in case of $La_{1-x}Sr_xMnO_3$ and $La_{1-x}Ca_xMnO_3$ series, further validates the significance of the hybridisation between the oxygen 2p-states and Mn 3d-states, and possibility of the presence of hole on O^- ion site also in the case of $rmPr_{1-x}Ca_xMnO3$ system.

While most of the theoretical studies shows the checkerboard kind charge and orbital ordering, few recent theoretical ab-initio calculations, most of them performed for $La_{1-x}Ca_xMnO_3$, point towards a charge-ordering, similar to the experimental Zener-polaron phase around $x{=}0.5$ [122–126]. The ab-initio study by Patterson et al. for $La_{0.5}Ca_{0.5}MnO_3$ shows the formation of Zener polarons (i.e., $Mn(d^4)$-O^--$Mn(d^4)$) in which each Mn ions have 3.5 valence [124, 125]. The hole resides on the oxygen anion, which is connected to these Mn ions with 3.5 valence. The study by Ferrari et al. [126] suggested another possibility: a charge-density wave of the oxygen holes. There are still theoretical studies required to validate the experimental observation of the Zener polaron phase in the $Pr_{1-x}Ca_xMnO_3$ series around in the region $x{=}0.5{-}0.3$.

In our present model study, the Zener polaron structure can be understood in the context of four Wannier-like states (see Figure 6.1) that are used to describe the checkerboard charge-ordered CE-type structure at $x{=}0.5$. For this purpose, the hybridisation between the oxygen 2p-states and Mn 3d-states need to be considered. The low-lying occupied oxygen-2p states that are not included in our model are bonding in nature. As the oxygen 2p-states are down-folded in the current model, the non-bonding states of Mn and oxygen, just below the Fermi level, appears as the bonding $|w_1\rangle$ states (see Figure 6.1), in the basis set of the Wannier-like states. These $|w_1\rangle$ states (see Figure 6.1) are filled at $x{=}0.5$. Now, there are two possibilities: **case I)** the Mn e_g-states (O p-states) contribution in the low-lying bonding states increases (decreases) if the Mn and oxygen

p-states hybridise strongly or **case II)** the contribution of the Mn e_g-states (O p-states) decreases (increases) for a weaker hybridisation. For the **case II**, the weightage of the O p-states in the unoccupied anti-bonding states ($|w_2\rangle$ and $|w_3\rangle$ in Figure 6.1) above the Fermi level increases. Now, the hole on the O$^-$ anion in the Zener polaron can be explained in this **case II**.

The recent experimental structure analysis shows that the Mn-O-Mn bond angle θ_{ab} bond angles vary along the zig-zag chain, in the *ab* plane of the CE-type magnetic structure at x=0.4 and x=0.5 [54, 55]. The θ_{ab} angles are largest within the Zener polarons [54, 55]. This larger θ_{ab} angle within the Zener polaron suggests a higher delocalisation of the electron in the bonding states which leads to the above discussed oxygen hole (i.e., presence of O$^-$ ions) scenario. The variation of θ_{ab} angles along the zig-zag chains is also observed in the checkerboard-type ordering, but with the two inequivalent Mn ions: a JT distorted and an undistorted. The recent theoretical study by Barone et al. [103] with an extended degenerate double-exchange Hamiltonian, where the tilting dependence of hopping is included, hints towards formation of a dimerised phase, characterised as the Zener polaron phase. The study shows that the presence of the JT coupling further stabilises this dimerised phase [103]. Additional theoretical studies with more sophisticated models are required to reconcile the importance of the bending of the Mn-O-Mn bond in the Zener polaron phase.

The CE structure of PCMO is expected to show a strong optical absorption due to excitation of electrons from the bonding state to the non-bonding state, which is symmetry allowed transition. In Chapter 6, we study the excitation and relaxation process of the CE-type phase under external light pulse.

4.6 Fully doped system ($x = 1$): CMO

The electron-deficient system CMO, indicated as XII in Figure 1.9, has no electron in the e_g states. Therefore, the unoccupied e_g orbitals are degenerate on each site. In these fully-doped systems, the only energy contribution in E_{pot} (Equation 2.9) comes from the super-exchange anti-ferromagnetic coupling between the t_{2g} states of nearby sites. The super-exchange favours an anti-ferromagnetic alignment of the t_{2g} spins in the absence of e_g electron in the system. The bandwidth of the e_g bands increases while moving from the G-type to the B-type through the intermediate A-type and C-type magnetic order. The G-type system consists of fully anti-ferromagnetically coupled sites where the Hund's coupling separates the spin states on each site. Therefore, these states undergo a very weak hybridisation with the same spin states on the neighbour sites. The same spin

states lie energetically lower on each site in the B-type system leading to the formation of a e_g band with a large bandwidth due to the possibility of stronger hybridisation between the orbitals belonging to different sites. The individual sites retain cubic symmetry as there is no JT distortion at these Mn^{+4} sites.

The number of ferromagnetic bonds starts increasing while going from the G-type to the B-type in the CMO system. The ground state energies of the magnetic orders also follow a similar trend: lowest for G-type order and highest for B-type order, as presented in Table 4.4.

The CMO system displays an optical absorption due to a charge transfer excitation where the electrons from the O-p states excite to the e_g state.

Magnetic order	Energy/Mn (eV)
B	0.050
A	0.0169
C	-0.0169
G	-0.050

Table 4.4: Magnetic order and ground state energy for the CMO system

4.7   Defect-induced disorders at x=0.5

Our study shows that the introduction of the electron or hole defects in the CE-type phase at $x = 0.5$ induces a local disorder in the system. These defect-induced disorders may be associated with the local spin, orbital, or structural disorder in the system. The individual local disorders in the system may remain separated from each other or may aggregate to form a new kind of larger disorder. The nature of these hole- and electron-induced disorders in the CE-type structure at $x = 0.5$ are shown in Figure 4.8. If the formation energy of a defect or disorder is small, they may play an important role at high temperature. The corresponding formation energy of these defects in summarised in Table 4.5.

If an electron is added to the CE-type system of x=0.5, this additional electron localises on one of the corner site M^e of the P^U polarons (see Figure 4.7) forming a local D_s^e-type disorder as shown in Figure 4.8 (a). Instead of forming another D_s^e-type disorder, a new local D_l^e disorder is induced on adding a second electron to the CE-type structure. The shaded region in Figure 4.8 (b) indicates the D_l^e disorder.

It is to be noted here that the octahedra around D_s^e site and the nearby $P^{U'}$ polaron site has expands in the same direction in the xy plane (Figure 4.8 (b)).

Table 4.5: Types of defect-induced disorders in the CE-type phase at $x = 0.5$, the type of defect involved and formation energies. The type of polaron involved in the formation of the disorder is also mentioned.

disorder type	number of defects	formation energy (meV)	involved polarons type
D_s^e	$N^e=1$	179.6	$P_{xz}^{JT_2}/P_{yz}^{JT_2}$
D_l^e	$N^e=2$	276.0	$P_{xz}^{JT_2}/P_{yz}^{JT_2}$
D_s^h	$N^h=1$	72.2	$P_{xy}^{JT_2}$
D_l^h	$N^h=2$	144.4	$P_{xy}^{JT_2}$

(a) D_s^e (b) D_l^e (c) D_s^h (d) D_l^h
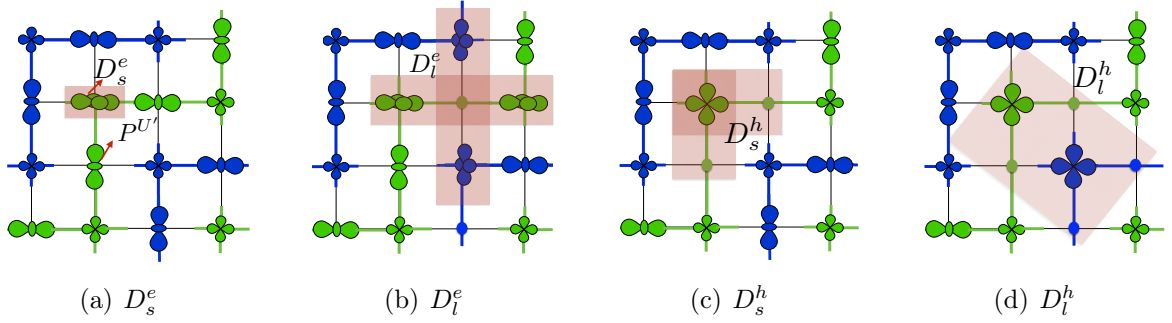
Figure 4.8: Types of defect-induced disorders in the CE-type phase at $x = 0.5$. The charge dispro-portion between the sites is highlighted by the size of the orbital. Blue and green colored sites have different t_{2g} spin orientation that are anti-ferromagnetically coupled. The magnetic order is not always collinear as depicted. The non-collinear magnetic structure of D_l^e and D_s^h is shown in Figure 4.9 and 4.16, respectively. The non-collinear structure of D_s^e and D_l^e is discussed in Appendix H

The D_s^e defect and the $P^{U'}$ polaron sites have equal charge and also form a similar structure as a single dimer unit proposed by Aladin et al. at $x=0.4$. The possibility of presence of these dimer units in high temperature region due to segregation of the D_l^e disorders into the D_s^e cannot be ruled out. We will discuss the D_s^e disorders again in Section 4.8.1.

In the hole doped region around $x=0.5$, two kinds of hole-induced disorders are found: D_s^h and D_l^h. The shaded regions in Figure 4.8 (a) and (b) indicate D_s^h and D_l^h disorder, respectively. These hole-induced disorders are induced due to formation of $P_{xy}^{JT_2}$ polaron as shown in Figure 4.8 (c). We will discuss these hole-induced disorders in detail in Section 4.9.1.

4.8 System below half doped

The present model shows that the region below $x=0.5$ in the phase diagram can be identified by two distinct phases: at $x=0.125$ and $x=0.25$. We obtain a low-energy metastable structure with a D_l^e-type disorders in the CE-type phase at $x=0.44$. At

x=0.375, we discuss two metastable states where two kind of charge ordering coexist in the CE-type magnetic order in the xy plane. These metastable states are accessible by the system at low temperature. The system undergoes a clear phase-separation around x=0.1875 where we do not find any low-lying metastable structure. Interestingly, we encounter a A-type canted-spin metastable structure at x=0.31 that has distinct domains of weak ferromagnetically coupled electron-poor sites and anti-ferromagnetically coupled electron-rich sites. The suppression of the chemical potential in the region $0.5 > x > 0.25$ as observed by K. Ebata et al. [127] through photoemission spectroscopy also endorses the spin-canting and phase separation scenario.

Table 4.6: Magnetic structure, average Mn-Mn distance in x/y and z direction (L_a and L_c), band gap and amplitude of octahedral distortion on individual sites below $x = 0.5$ doping. The $P^{U_{M^c}}$ and $P^{U_{M^e}}$ sites indicate the central and corner sites of the P^U polaron, respectively. N_e indicates the total number of electrons and N_{tot} indicates the total number of Mn sites in the unit cell.

doping	magnetic structure	site type	$\|Q_1\|$	$\|Q_2\|$	$\|Q_3\|$	Lattice constant (A^o)	band gap (eV)
0.125	collinear A-type	P^{JT_1}	0.289	0.153	0.110	L_a=3.9341 L_c=3.8370	0.92
0	canted A-type	P^{JT_1} P^{JT_2} P^H	0.285 0.000 0.000	0.098 0.374 0.082	0.090 0.100 0.137	L_a=4.0067 L_a=4.0853	0.55
0.25	collinear B-type	P^{JT_2} P^H	0.153 0.005	0.159 0.010	0.294 0.110	L_a=3.9970 L_c=3.9974	0.28
0.31	canted A-type	P^{JT_2} P^H	0.140 0.015	0.206 0.017	0.284 0.092	L_a=3.9977 L_c=3.9601	0.52
0.375	**I-type** modified CE	$P^{U_{M^c}}$ P^{JT_2} $P^{U_{M^e}}$	0.242 0.156 0.021	0.137 0.224 0.018	0.274 0.287 0.088	L_a=3.9781 L_c=3.9635	0.6460
0.375	**I-type** modified CE (1st xy plane)	$P^{U_{M^c}}$ P^{JT_2} $P^{U_{M^e}}$	0.242 0.156 0.021	0.137 0.224 0.018	0.274 0.287 0.088	L_a=3.9781 L_c=3.9635	0.6460
0.375	**I-type** modified CE (2nd & 4th xy plane)	$P^{U_{M^c}}$ $P^{U_{M^e}}$	0.242 0.030	0.137 0.009	0.274 0.097	L_a=3.9781 L_c=3.9635	0.6460
0.375	**I-type** modified CE (3rd xy plane)	$P^{U_{M^c}}$ P^{JT_2}	0.242 0.001	0.137 0.035	0.274 0.070	L_a=3.9781 L_c=3.9635	0.6460
0.44	canted CE-type	$P^{U_{M^c}}$ P^{JT_2} $P^{U_{M^e}}$	0.290 0.182 0.010	0.085 0.166 0.028	0.273 0.273 0.074	L_a=3.9718 L_c=3.9405	0.567
0.5	collinear CE-type	$P^{U_{M^c}}$ $P^{U_{M^c}}$	0.259 0.000	0.163 0.033	0.257 0.074	L_a=3.9895 L_c=3.8693	0.723

Next, we discuss the individual phases briefly mentioned above for $x < 5$ below where

the arrangement of the P^{JT_1} and P^{JT_2} polarons together with the holes (P^H) remains a critical issue to be analysed. Furthermore, the role of the long-range strain field, induced due to the JT distortion on the charge-rich Mn^c sites, and the e-e interaction on the M^e sites in the arrangement of these polarons is also needed to be investigated.

4.8.1 Low-temperature spin-canted structure ($0.5 > x > 0.44$)

Our model shows a tendency of phase-separation in the electron-rich region close to $x\sim0.5$, as indicated in Figure 4.2, where the CE phase with an average electron concentration $x=0.5$ and a electron-rich region with $x\sim0.25$ coexist. This phase-coexistence occurs at 0 K. The energy density graph (see Figure 4.1) suggests that the metastable state which closely resembles the CE-type structure (Section 4.5) remain highly probable structure away from $x=0.5$ at finite but low temperature. The additional e_g electrons below $x=0.5$ in the parent CE-type structure are strongly localised on single sites and form local D_l^e disorders (Figure 4.8(b)).
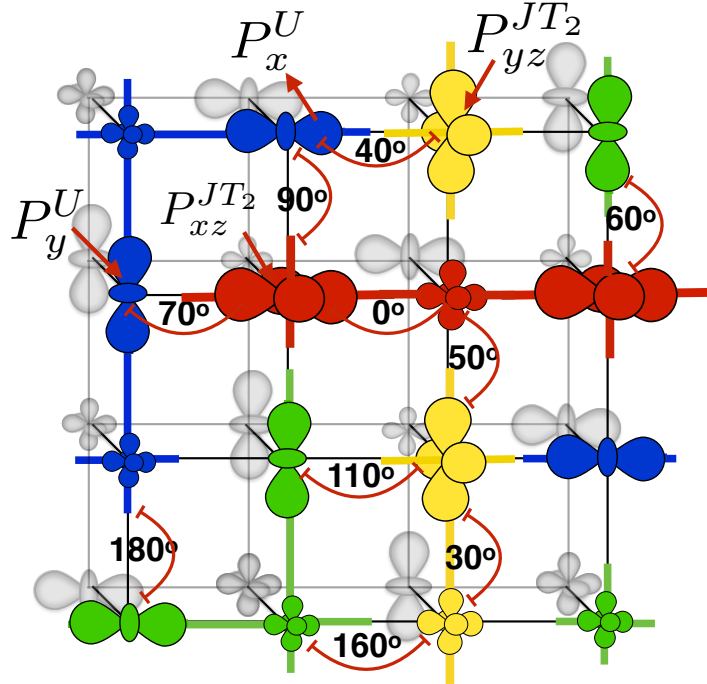
Figure 4.9: Orbital ordering and spin structure of the two consecutive xy plane of the canted CE-type order at $x=0.43$. The charge disproportion between sites is highlighted by the size of the orbital. Blue, green, and yellow colored sites have different t_{2g} spin orientation. The spin angle between different colored sites is specified. The grey colored sites in the 2nd xy plane are anti-ferromagnetically coupled to the sites in the 1st xy plane. The two extra electrons below $x=0.5$ form two new $P_{xz}^{JT_2}/P_{yz}^{JT_2}$ polarons simultaneously converting two other nearby P^{JT_1} polarons into P^{JT_2} polarons. The spin structure deviate considerably in the locality of these P^{JT_2} sites.

The charge-ordered CE phase at $x=0.5$ reveals quasi-one dimensional features along the ferrromagnetic zig-zag chain (see Section 4.5). At $x=0.5$ doping, the band structure of

the system below the Fermi level consists of mainly filled bonding states. The bonding states are delocalised on three sites of the trimer, which constitute x or y segment of the zig-zag ferromagnetic chain forming P^U polarons. The empty bands above the Fermi level are either non-bonding or anti-bonding in nature. The former bands lie lower in energy than the later. If an additional electron below $x=0.5$ goes into one of these non-bonding states and if the spin order of the CE-type phase remains intact, the newly occupied non-bonding state would remain non-dispersive. This would in turn result in a concave total energy density ($\mathcal{E}$) surface for a certain span of doping below $x=0.5$. But, our findings at $x{\sim}0.44$ suggest that these newly added e_g electrons form P^{JT_2} polarons. The e_g electron in the P^{JT_2} polaron tends to gain kinetic energy by delocalising over nearby electron-poor sites. The delocalisation is facilitated by a weak spin-canting forming a local disorder of characteristic orbital and spin order. This local disorder consists of the P^{JT_2} polarons and nearby electron-poor sites. Let us discuss the modification of the atomic and spin ordering at the D_l^e disorder sites in more details.

Figure 4.9 illustrate the nature of the orbital ordering and magnetic structure at $x=0.43$. The green and blue colored orbital ordering resembles the ordering within two adjacent zig-zag chains of the CE-type structure of $x=0.5$ (Figure 4.7) but interrupted by the appearance of the P^{JT_2} polarons (indicated by $P_{yz}^{JT_2}$ and $P_{xz}^{JT_2}$ in Figure 4.9). If we compare the orbital order at $x=0.5$ and $x=0.43$ case, not only two new P^{JT_2} polarons are formed, but two P^U polarons from the parent CE structure also convert into the P^{JT_2} polarons. The t_{2g} spins at these P^{JT_2} polarons sites and its vicinity (shown in yellow and red) also deviate from the original spin pattern of the CE-type phase.

The arrangement of the P^{JT_2} polarons is explained as follows: To accommodate the extra P^{JT_2} polaron below $x=0.5$ within a CE-type structure, one of the P^U polaron of the ferromagnetic zig-zag chain converts into the P^{JT_2} polaron. This P^{JT_2} shifts one lattice point within the chain such that the two P^{JT_2} polarons now occupy the corner sites of the trimer segment. Thus, only the structure of the x or y segment of the CE chain with P^{JT_2} polarons on the corner sites is modified, and rest remains the same. These modified x and y segments of the CE chains are shown in red and yellow (see Figure 4.9), respectively. The spin angle between the connecting sites of the original ferromagnetic segment (green/blue) and the modified segment (red/yellow) of the chain changes from 0° to $40^o{-}60^o$.

The spatial distribution of the modified x or y segment discussed above is not random but strictly governed by the cooperative JT distortion. In Figure 4.9, four P^{JT_2} polarons surround an electron-poor site (red charge-deficient site) that has a spin angle of around 45° and 30° with the nearby P^{JT_2} polaron sites. Due to weak delocalisation of the electrons of each P^{JT_2} polaron to this electron-poor site, the site remain orbitally unpolarised. The

local D_l^e disorder (region involving yellow and red sites) in the 1st xy plane is stabilised in two ways: 1) the strain field created by the modified x segment of the CE chain in the y direction (red segment) is absorbed by a similarly modified segment that is oriented in the y direction (yellow segment). 2) The double exchange mechanism between the P^{JT_2} polaron site of these modified y segment and the electron-poor site of the orthogonal x segment favours ferromagnetic coupling of the spins of the two segment.

The distribution of the D_l^e local disorders discussed above induced by additional electrons in the CE-type phase below $x = 0.5$ is not unique and may have several possibilities. Moreover, the emergence of the long-range interaction between these D_l^e disorders due to the strain field induced by the cooperative nature of the JT distortion may restrict the number of possible configurations. Given the local modification of the spin order and lattice distortion, a glass like behaviour is expected in the low temperatures region. Recently, the spin glass or structural glass behaviour in this doping region ($x{\sim}0.4$) was recovered, experimentally, [128] below 90 K.

4.8.2   Modified CE-structure ($x{\sim}0.375$)

Although, the region around $x{\sim}0.375$ exhibits phase coexistence (see Figure 4.10), the CE-type structure still remains the most probable structure in the low-temperature zone. Our results clearly confirm several metastable structure with distinct magnetic and orbital orderings around $x{\sim}0.375$. We obtain two kinds of metastable structures at $x{=}0.375$: a canted-CE phase, similar to $x{=}0.43$ (Section 4.8.2) and a modified CE-type structure.

In the canted-CE structure, the orbital ordering at the sites of the extra electrons below $x = 0.5$ is $d_{z^2-y^2}/d_{z^2-x^2}$-type forming P^{JT_2} polarons, similar to the structure shown in Figure 4.9. As discussed in Section 4.8.2, the spin structure deviates considerably in the vicinity of these P^{JT_2} polaron sites ($P_{xz}^{JT_2}$- and $P_{yz}^{JT_1}$-type sites in Figure 4.9).

(a) 1st xy plane   (b) 2nd xy plane   (c) 3rd xy plane   (d) 4th xy plane
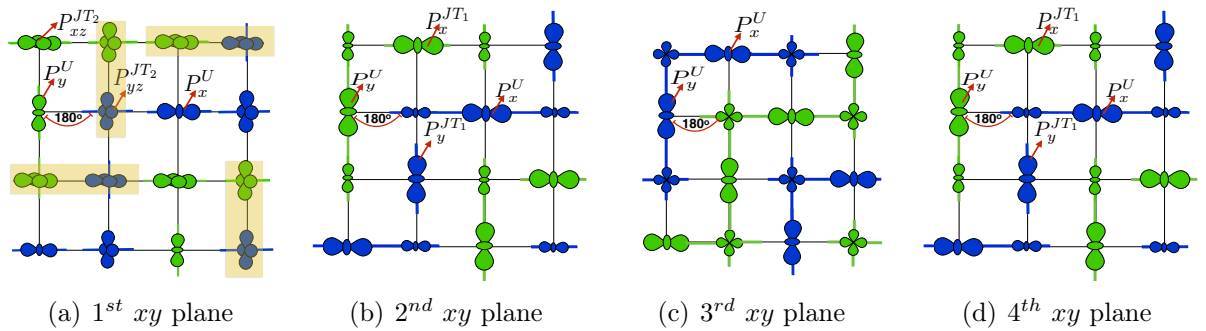
Figure 4.10: Orbital and spin structure of the four consecutive xy plane of the **I-type** modified CE-structure at $x{\sim}0.375$. The charge disproportion between the sites is highlighted by the size of the orbital. Blue and green colored sites have different t_{2g} spin orientation that are anti-ferromagnetically coupled.

(a) 1st xy plane   (b) 2nd xy plane   (c) 3rd xy plane   (d) 4th xy plane
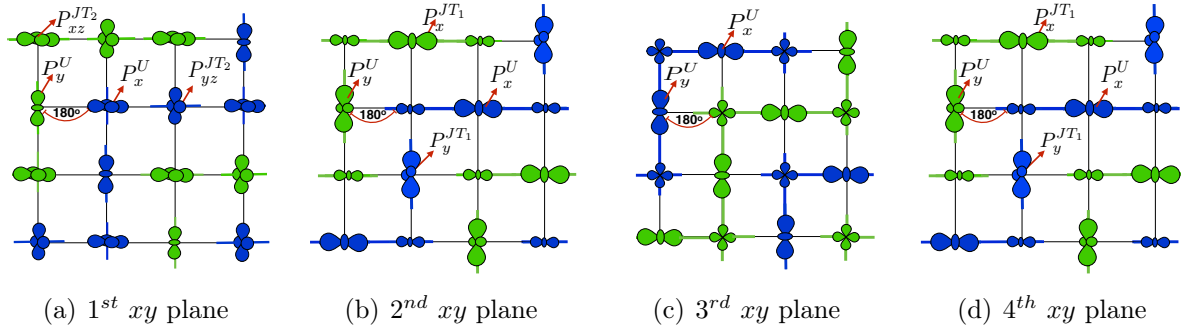
Figure 4.11: Orbital and spin structure of the four consecutive xy plane of the **II-type** modified CE-structure at $x{\sim}0.375$. The charge disproportion between the sites is highlighted by the size of the orbital. Blue and green colored sites have different t_{2g} spin orientation that are anti-ferromagnetically coupled.

The second structure, i.e., the modified collinear CE-type consists of the xy planes with spin structure similar to that of the CE-type of $x{=}0.5$ within xy plane. However, the magnetic ordering in the z direction is no more consistently anti-ferromagnetic. Our model predicts two kinds of metastable modified CE-type structure with different orbital ordering. We call these two degenerate structures as **I-type** and **II-type**.

The orbital and spin ordering of the **I-type** and **II-type** type structures are provided in Figure 4.10 and 4.11, respectively. In both the structures, the extra electrons below $x{=}0.5$ populate a particular xy planes (1st xy plane in Figure 4.10 and 4.11) forming P^{JT_2} polarons instead of going to random lattice sites. While the CE spin-order remains fully intact in the xy plane, the spin order between the electron-rich plane (1st xy plane) and neighbouring planes (2nd and 4th xy plane) in the z direction changes from anti-ferromagnetic to ferromagnetic. The super-exchange interaction between the occupied states of the P^{JT_2} polaron of the 1st xy plane and high-lying e_g orbital, pointing in the z direction, on the M^e sites of the P^U polarons of the nearby xy planes (2nd and 4th xy plane) promotes ferromagnetism between the planes. This out of plane hybridisation alters the weak planar orbital polarisation on the M^e sites originally present in the $x{=}0.5$ case, of the 2nd and 4th xy plane. The orbital order of the M^e sites of these two planes (2nd and 4th xy plane) is now weakly $d_{x^2-z^2}/d_{y^2-z^2}$-type in contrast to the weak $d_{x^2-y^2}$-type orbital ordering of the CE-type phase of $x{=}0.5$ case.

The changed orbital polarisation on the M^e sites in the xy plane leads to a stronger hybridisation with one of the two nearby M^c sites of the P^U polaron within same ferromagnetic chain forming almost separated P^U and P^{JT_1} polarons. This can be seen in the orbital ordering of the 2nd and 4th xy plane of Figure 4.10 and 4.11. The P^{JT_1} polarons are confined to single sites, and it is in sharp contrast to the CE planes of the $x{=}0.5$ case where the P^U polarons share the M^e sites. In the 2nd and 4th xy plane of Figure 4.10 and 4.11, these separated P^U and P^{JT_1} polarons oriented in the x (y) direction are indicated

by P_x^U (P_y^U) and $P_x^{JT_1}$ ($P_y^{JT_1}$), respectively.

In the **I-type** type structure, the 1st xy plane can be seen as the close packed structure of the D_l^e-type disorders (Section 4.7). The electron-poor central site of the D_l^e-type polaron is occupied by the $P_{xz}^{JT_2}/P_{yz}^{JT_2}$ polarons. The octahedral distortion in the xy plane along the shaded zig-zag chain in Figure 4.10 resembles the distortion pattern proposed by Aladine et al. [54]. This shaded zig-zag chain does not the corresponds to the ferromagnetic zig-zag chain of the CE-type magnetic order.

In the **II-type** type structure, the orbital ordering in the 1st xy plane resembles the staggered orbital ordering of the $x = 0$ case.

The high configurational-entropy associated with the these low-lying insulating metastable structures makes them more favourable over the ferromagnetic (B-type) metallic phase; see Figure 4.2.

4.8.3 Cross orbital polarons at x∼0.25

At x=0.25, $Pr_{1-x}Ca_xMnO_3$ manganites exhibit an insulating phase in the phase diagram obtained with the B-type magnetic order. Due to high degree of misfit strain associated with the holes introduced in the environment of the P^{JT_1} polarons, the holes in PMO system prefer certain sites that are surrounded by the electron-rich Mn^{3+} sites. Moreover, the planar P^{JT_2} polarons start appearing on the Mn^{3+} sites which are attributed to the axial P^{JT_1} polarons at x=0. The electrons in the planar polarons have a possibility to delocalise comparatively over larger number of nearby P^H sites than the axial polarons.

The schematic Figure 4.12 illustrates the magnetic and orbital order of the four consecutive xy planes at x=0.25. In the B-type phase at x=0.25, the lobes of the occupied orbitals of the P^{JT_2} polarons are directed towards the P^H site. The electrons in the P^{JT_2} polarons gain kinetic energy by delocalising over the adjacent P^H sites. Each P^H site is surrounded by six P^{JT_2} polarons such that the P^{JT_2} orbital lobes are directing towards the P^H site. The P^H site remains orbitally unpolarised as every occupied orbitals on the nearby P_2^{JT} sites hybridise equally to it resulting in the rotational invariant orbital order on the P^H site. The kinetic energy gain of the e_g electron, resulted from the mentioned hybridisation, is larger than the penalty of the inter-orbital e-e repulsion at the P^H sites. The ferromagnetic super-exchange mechanism between the occupied orbitals and the un-occupied orbital of the adjacent P^{JT_2} polarons further stabilises the B-type phase over any other anti-ferromagnetic phase.

Given the arrangement of the P^{JT_2} around every P^H site, the configuration with the lowest possible energy is the one with the minimum lattice strain. A $2\times2\times2$ supercell

(a) 1st xy plane   (b) 2nd xy plane   (c) 3rd xy plane   (d) 4th xy plane
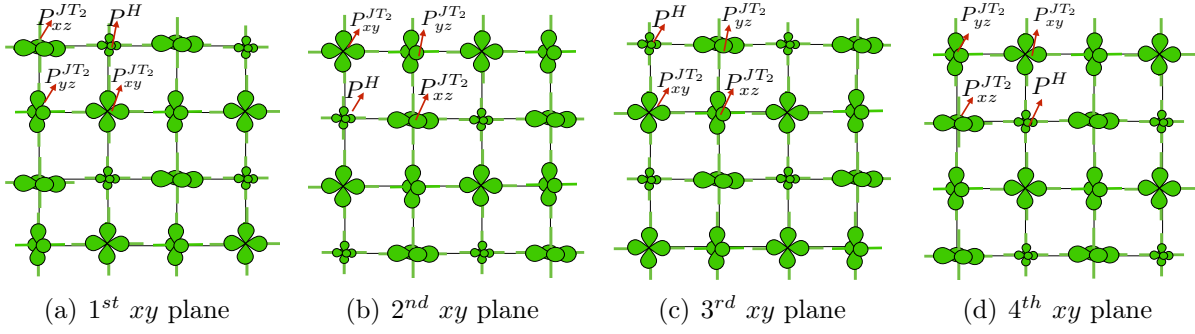
Figure 4.12: Orbital and spin structure of the four xy plane of the B-type order at x=0.25. The charge disproportion between the sites is highlighted by the size of the orbital. The charge-deficient and charge-rich sites corresponds to the P^H polaron and P^{JT_2} polaron respectively. The arrangement of the P^{JT_2} and P^H polarons is such that the P^H are surrounded by six P^{JT_2} polarons. The smallest supercell of minimum lattice strain is composed of $2 \times 2 \times 2$ Mn sites. This $2 \times 2 \times 2$ unit cell corresponds to upper left 2×2 cell of the 1st and 2nd xy plane. The two P^H sites lie diagonally to each other and maintain maximum possible distance within this supercell. There are several possible ways to arrange the P^{JT_2} and P^H polarons in the third and fourth plane once the orbital ordering within the 1st and 2nd xy plane is fixed. All of these possible configuration are energetically very close to each other (0-3 meV).

of minimum lattice strain consists of the upper left 2×2 supercells of the 1st and 2nd xy plane in Figure 4.12 that involve the sites indicated as P^H, $P^{JT_2}_{xy}$, $P^{JT_2}_{yz}$, and $P^{JT_2}_{zx}$.

The theoretical study by Mizokawa et al. [87] claims that the system at this doping consists of an ordered structure of orbital polarons, i.e., a P^H site surrounded by six P^{JT_1} polarons pointing towards it. The orbital polaron idea, suggesting a strong polarisation of the orbitals in the locality of holes, was first introduced by Kilian [88] to understand the metal-insulator transition in these systems. These theoretical studies established that the ferromagnetic coupling between P^H and P^{JT_1} polarons is more stable than the anti-ferromagnetic coupling. The ferromagnetic state obtained through these calculations exhibits band gap, which mostly accounts from the splitting of the e_g states on the P^{JT_1} sites. The experimental study by Zimmermann et al. [43] reveals that the magnetic structure suggested by Mizokawa et al. [87] is inconsistent with the above orbital ordering at x=0.25, which allows the possibility of a different structure.

The theoretical model study performed by Mizokawa et al. [87] completely ignored the long-range elastic interactions induced by the cooperative effect of the octahedral distortions. As these elastic interactions are included in our model, the system exhibits the cross orbital ordering on the sites of the P^{JT_2} polarons instead of the P^{JT_1} polarons.

4.8.4   Insulating spin-canted structure at x∼0.125

Our model study at the $x \sim 0.125$ doping discloses the presence of the electron-poor xy planes (1st xy plane) with the intercalated electron-rich ab planes (2nd xy plane) as shown

in Figure 4.13. As described in Section 4.3.1 and 4.3.2, these calculations are carried out with the high temperature experimental lattice constants from Jirak et al. [25]. But, the separation of the charge-rich plane and charge-poor plane remains there also in the structure optimised with variable lattice constant.
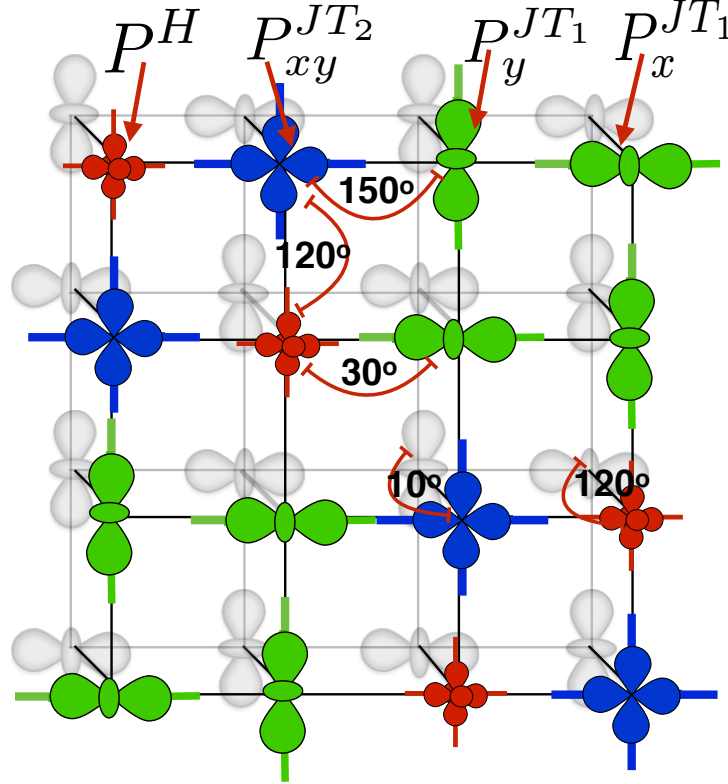
Figure 4.13: Orbital and spin structure of the two xy plane of the canted A-type order at x=0.125. The charge disproportion between the sites is highlighted by the size of the orbital. Blue, green and red colored sites have different orientation of the t_{2g} spins. The t_{2g} spins of the grey colored sites in the 2nd xy plane are anti-ferromagnetically coupled to the 1st xy plane, except the blue sites that have 10° spin angle. Half of the P^{JT_1} polarons at the nearby sites to the P^H sites are transformed into the P^{JT_2} polarons in the xy plane. Clearly the 1st xy plane is the hole-rich plane, and the planes below and above it are hole-poor planes.

The orbital ordering on one-half of the nearby sites around the P^H (shown in red in Figure 4.13) in the 1st xy plane changes from the $d_{3x^2-r^2}/d_{3y^2-r^2}$-type of the P^{JT_1} polaron (shown in green) to the $d_{x^2-y^2}$-type of the P^{JT_2} polarons (shown in blue). The ferromagnetic coupling due to hybridisation between empty state on P^H site and occupied states on the nearby electron-rich Mn^{3+} sites leads to small t$_{2g}$ spin angle forming a domain of canted spins. The nearby electron-rich plane (shown in grey) has similar staggered orbital ordering as that of the x=0 case.

Besides the electrons of the nearby Mn^{3+} sites of the xy plane, the electron of the P^{JT_1} sites nearest to the P^H hole in the z direction delocalises to this hole site. This can be confirmed by the lack of any orbital polarisation on the P^H sites as shown in Figure 4.13. Hence, every P^H hole is surrounded by P^{JT_1} site in the z direction. It must be noted

that the canted spin domains are separated from each other in the z direction (see Figure I.3 of Appendix H). These canted spin domains in the xy planes are separated from each other due to onsite e-e Coulomb repulsion term. The presence of a single large canted spin domain in the xy plane would result in larger inter-orbital e-e repulsion on the P^H sites. Hence, the Coulomb repulsion term promotes charge segregation process.

The experimental observation of a long-range structural modulation in the z direction further backs this scenario of the charge-rich and charge-poor planes [129–132]. Furthermore, the spin-canting behaviour observed in our calculation is also in agreement with the experimental studies [25, 46]. Under external magnetic field, the size of the above discussed domains are expected to grow through percolation mechanism.

Further increase in hole doping above $x = 0.125$ drives the system into a phase-coexisting situation around $x \sim 0.20$ (see Figure 4.2) in our studies where the B-type insulating phase and the canted-A type phase discussed above appear simultaneously.

4.8.5   Metastable structure at $x \sim 0.31$

Experimentally, the manganite series $Pr_{1-x}Ca_xMnO_3$ found to exhibit the CMR effect in the two region of the phase space: hole doped and the electron doped region (Figure 1.9). We obtain several canted-spin metastable structures with energies vary close to each others at $x \sim 0.31$ (see Figure 4.2). These metastable states are insulating (see Figure 4.5) with finite energy band gaps. The orbital order and spin structure of the lowest energy metastable state with canted A-type structure is shown in Figure 4.14. We obtain this canted A-type metastable structure through a non-collinear calculation by allowing the spin degree of freedoms to optimise once the structure with frozen A-type structure is close to convergence. The exact t_{2g} spin direction is difficult to analyse with a global reference direction. However, the spin angles between Mn sites is shown in Figure 4.14.

Instead of the three dimensional orbital polaron as in the case at $x = 0.25$ doping, a two-dimensional orbital polarons are formed at $x \sim 0.31$. In the two dimensional orbital polaron, a P^H site is surrounded by four P^{JT_2} polarons in the xy plane such that the lobes of the occupied of the P^{JT_2} polarons point towards the hole. The charge ordering in the xy plane as well as z direction is similar as in the $x = 0.4$ case except at few sites. This is in good agreement with the experimental evidences of presence of charge ordering at $x = 0.30$ of similar nature as of $x = 0.5$ doping [43, 52].

The ferromagnetic super-exchange dominates between Mn^{3+} sites due to participation of lower occupied e_g orbital on the first site and the higher unoccupied e_g orbital on the second sites. The xy planes are anti-ferromagnetically coupled in the z direction.

The presence of ferromagnetic (sites connected by blue bonds in Figure 4.14) and spin-canted (sites connected by yellow and green bonds in Figure 4.14) domains of $x = 0$ and $x = 0.5$ stoichiometry, respectively makes the metastable structure a prospective candidate to successfully demonstrate the experimentally observed metal-insulator transition in this region of phase diagram [133]. Yoshizawa et al. experimentally observed a metal-insulator transition at zero temperature in the presence of magnetic field of strength $\sim$4.0 T for x=0.3. Zhou et al. probed the system at x=0.3 by ultrafast photo-excitation and found the system in metastable state characterised by spin glassy and strain glassy behaviour [134]. These experimental findings further validate the importance of percolation mechanism within the present canted-spin metastable structure.

(a) 1st xy plane   (b) 2nd xy plane   (c) 3rd xy plane   (d) 4th xy plane
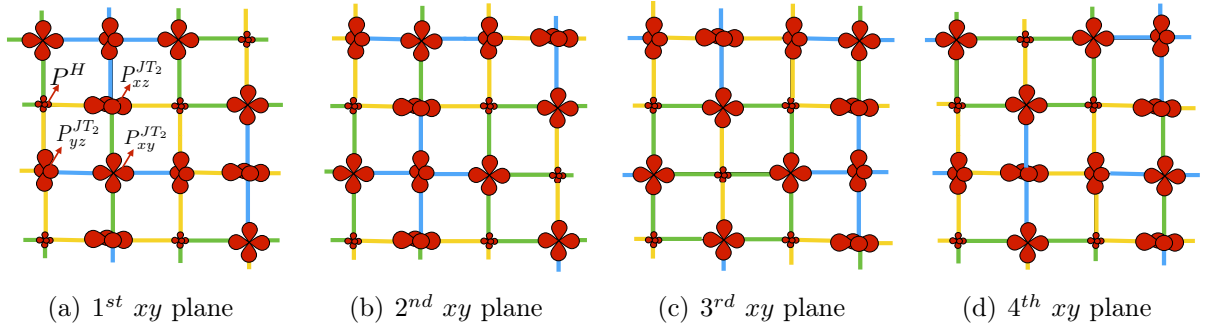
Figure 4.14: Orbital and spin structure of the four consecutive xy plane at $x\sim$0.31. The charge disproportion between sites is highlighted by the size of the orbital. Blue, yellow and green bond indicates the t_{2g} spin angle of $0^o - 25^o$ $40^o - 60^o$ and $70^o - 90^o$ between the Mn sites either side of the bond. A P^H hole site is surrounded by four P^{JT_2}-type polarons such that the lobes of the occupied orbitals of the polaron points towards the hole. The charge ordering is stacked in the z direction.

4.9 System above half doped ($1>x>0.5$)

Theoretically, one would expect qualitatively similar trends for x and $x-1$ doping. However, experiments suggest a strong asymmetry in the electron-poor and electron-rich region of the phase diagram of perovskite manganite (Section 2.4). Although its possible to find a ferromagnetic-metallic phase for x<0.5 for the high-bandwidth manganites, such as $La_{1-x}Ca_xMnO_3$, there is no sign of metallic behaviour in the x>0.5 part of the phase diagram. The behaviour of the $Pr_{1-x}Ca_xMnO_3$ manganites is remarkably different for x<0.5 and x>0.5. While the periodicity of the superstructure changes drastically w.r.t. doping for x>0.5 system [25, 45, 48, 49], the superstructures for x<0.5 predominantly inherit same periodicity as that of x=0.5 [43]. The experimental phase diagrams of the $Pr_xCa_{1-x}MnO_3$ series indicate insulating homogenous phases throughout the doping region above half doping, except 0.89>x>0.85 where the system shows phase-coexistence.

Our study reveal a stable CE-phase close to $x\sim0.55$, a insulating charge-striped phases, such as bi-stripe, Wigner-crystal, for $0.75>x>0.5625$ doping region and the C-type phase in $0.75>x>0.5625$ region. In the region $1.0>x>0.90$, certain kind of ferromagnetic clusters are formed due to the participation of the P^H, P^{Pl} and P^{Br} polarons, which are embedded in the G-type parent CMO system.

Table 4.7: Magnetic structure, average Mn-Mn distance in x/y and z direction (L_a and L_b), band gap and amplitude of octahedral distortion on individual sites below $x = 0.5$ doping. The $P^{U_{Mc}}$ and $P^{U_{Me}}$ sites indicate the central and corner sites of the P^U polaron, respectively. N_e indicates the total number of electrons and N_{tot} indicates the total number of Mn sites in the unit cell. Abbreviations: **DS**-double-stripe and **WC**- Wigner-crystal

doping	magnetic structure	site type	$\lvert Q_1 \rvert$	$\lvert Q_2 \rvert$	$\lvert Q_3 \rvert$	Lattice constant (A^o)	band gap (eV)
0	G_1	P^{JT_1}	0.0	0.0	0.0	L_a=3.854 L_c=3.854	*
0.75	C_2	$P^{U_{Mc}}$ $P^{U_{Me}}$ P^H	0.003 0.002 0.005	0.281 0.042 0.007	0.222 0.045 0.016	L_a=3.8630 L_c=3.9790	0.537
0.75	C_2	$P^{U_{Mc}}$ $P^{U_{Me}}$ P^H	0.003 0.002 0.005	0.281 0.043 0.007	0.222 0.046 0.016	L_a=3.8634 L_c=3.9783	0.537
0.66	WC	$P^{U_{Mc}}$ P^H	0.226 0.036	0.166 0.030	0.238 0.046	L_a=3.948 L_c=3.856	0.61
0.625	DS	$P^{U_{Mc}}$ $P^{U_{Me}}$	0.203 0.020	0.186 0.024	0.240 0.054	L_a=3.960 L_c=3.856	0.53
0.53	CE_2	$P^{U_{Mc}}$ P^{JT_2} $P^{U_{Me}}$	0.249 0.009 0.009	0.167 0.297 0.031	0.253 0.272 0.068	L_a=3.9838 L_c=3.8629	0.5385

4.9.1   Low-temperature spin-canted CE structure (x~0.55)

Similar to the electron-rich side, the addition of holes in the CE-type structure at x=0.5 drive the system towards the phase-competition region (denoted as VI in Figure 1.9) at low temperature. Figure 4.1 indicates a strong probability of the system towards the canted-spin metastable structure together with the phase-separated structure at low temperature.

Figure 4.15 and 4.16 illustrate the orbital ordering and spin arrangement of the two metastable states at x=0.53 and x=0.625 case obtained by the present model. Both the structures can be seen as a modified structure of CE-type structure of $x = 0.5$. The removal of an e$_g$ electron from the bonding state of the CE structure at x=0.5 creates a

hole (P^H). This additional hole is expected to reside mainly on the central Mn^c sites of the P^U polaron. The system would exhibit higher tendency of phase coexistence if the additional hole position together with the positions of the remaining P^U polarons and the spin structure in the locality of the additional P^H hole remain unchanged, but this is not the case at x=0.53.
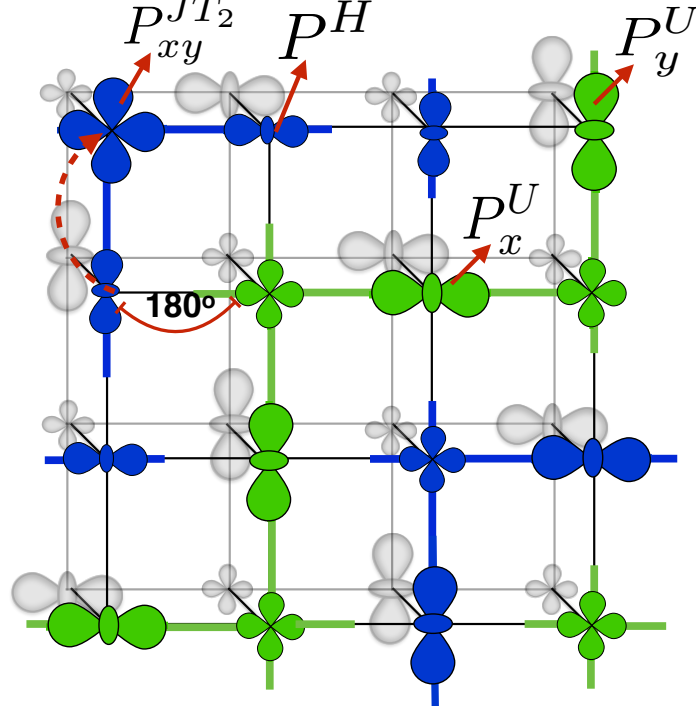
Figure 4.15: Orbital and spin structure of the two consecutive xy plane of the CE-type order at x=0.53. The charge disproportion between the sites is highlighted by the size of the orbital. The t_{2g} spins of the blue and green colored sites are anti-ferromagnetically coupled. The hole introduced to the CE-structure at half-doping on the M^c central site of the P_x^U (P_y^U) shift a nearby P_y^U (P_x^U) polaron one lattice point simultaneously to decreases the e-e interaction on one of its M^e sites. Moreover, the local strain developed at the site of the P^H hole is absorbed as the P^U polaron changes to the $P_{xy}^{JT_2}$ polaron. The spin configuration remain same as that of the CE-type of x=0.5.

The stability of the CE-type spin order is evident at x=0.53 where only the position of a single P^U polaron in the vicinity of the extra P^H site is altered, as shown in Figure 4.15. The additional hole above $x = 0.5$ form a local disorder. The spin structure remains completely collinear CE-type. There are two local interactions that are important to understand at x=0.53: the e-e repulsion on the M^e site of the P^U polaron and the local elastic field developed in the surrounding of the additional P^H site above $x = 0.5$ in the CE-structure.

A removal of an e_g electron leaves behind a localised P^H hole in the original CE-type structure of x=0.5 case. This additional P^H hole (indicated by blue P^H site in Figure 4.15) is located in-between the M^e sites connected to the adjacent P^U polarons on the either sides. To reduce the e-e repulsion on the shared M^e sites, one of the P^U polaron from the same ferromagnetic zig-zag chain (blue ferromagnetic chain) adjacent the P^H

hole is shifted towards the hole. This shifting of the P^U polaron is indicated by red dashed arrow, see Figure 4.15. The symmetry of the elastic strain induced at the newly shifted P^U site by the JT distortion of the nearby M^c sites is absorbed by converting the P^U into $P^{JT_2}_{xy}$ polaron. Thus, the e-e repulsion and the elastic field prompt the system towards a stronger charge-ordered structures above half doping.

The CE-type spin order is stable for certain doping span above x=0.5. At x=0.625, we observe a structure with simultaneous single and double charge-stripe running diagonally in the xy plane (Figure 4.16). The transition from the CE-type structure at x=0.5 to the Wigner-crystal phase at x=0.66 (discussed in Section 4.9.2) can be considered continuous. As discussed above, the removal of an e_g electron from the CE structure of x=0.5 creates an isolated P^U polaron. Introducing additional holes into the system would lead to several isolated P^U polarons. Instead of arranging themselves randomly, these remaining isolated P^U polarons form a single-stripe of charge that runs diagonally as shown in Figure 4.16.
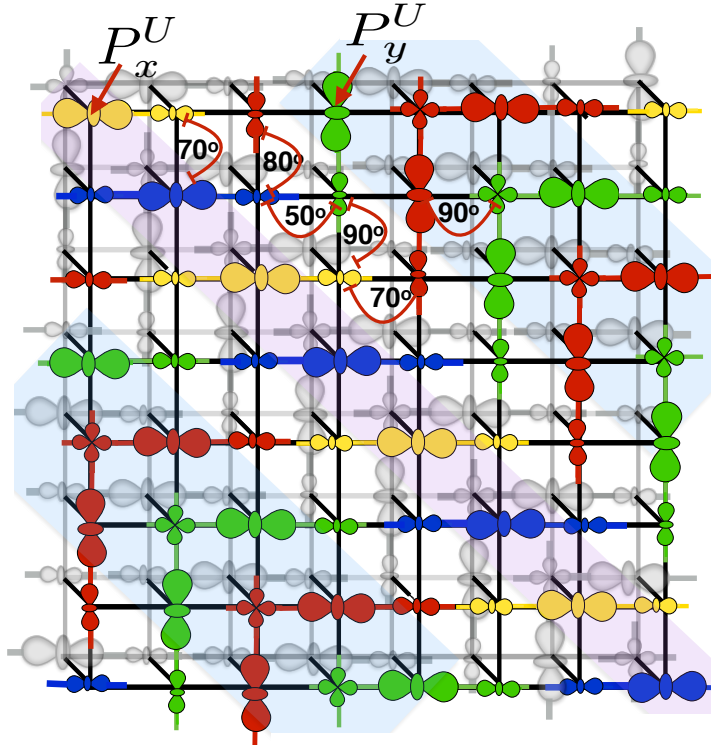
Figure 4.16: The orbital and spin structure of the two consecutive xy plane of the stripe-phase at x=0.625. The shape of the occupied orbital indicates the type of the orbital order and their color (blue, green, red and yellow) implies different spin orientation of the sites. The spin angles between different polaron sites are indicated. The charge disproportion between the sites is highlighted by the size of the orbital, i.e, larger the orbital size, larger will be the charge residing on the site and vice-versa. The region shaded in pink and blue are the single and bi-stripe charge ordering running diagonally in the xy plane. There is no charge stacking in the z direction. The sites of the 1st xy plane are anti-ferromagnetically coupled to the sites of the 2nd xy plane except at the M^c sites of the P^U_y polaron sites where the spin angle is 70°–90°.

To obtain the structure at x=0.625, we use a comparatively larger unit cell in the x and

y direction, i.e. a 8×8×2 sized with 3×3×3 k-point grid. The orbital ordering and the spin arrangement at x=0.625 is described in Figure 4.16. At this doping, its possible for one-third of the P^U polarons to not share any M^e sites, but rest of the two-third still share common M^e. To minimise the e-e repulsion and lattice strain, these two sets of P^U polarons form single and double charge-stripe shown by regions shaded in pink and blue respectively in the 1st xy plane; see Figure 4.16. We call this phase as mixed-stripe phase. The charge ordering pattern is modulated in the z direction. The mixed-stripe phase presented here has charge ordering in the z direction also besides the xy plane unlike other phases in the phase diagram which do not show charge ordering in the z direction. The similar stripes in the 1st and 2nd plane are separated from each others. It must be noted that the charge ordering temperature is highest in this region in the experimental phase diagram of $Pr_{1-x}Ca_xMnO_3$ manganites [25], which further make this mixed-stripe structure a good candidate to describe this particular doping region.

4.9.2 Charge stripe at x∼0.66

At x=2/3, every P^U polaron in the lattice is separated as it does not share M^e sites with other P^U polarons. The system displays a tendency towards the formation of regular patterns, such as bi-stripe and Wigner-crystal that has been also reported from several experiments (denoted as VIII in Figure 1.9) [45, 48, 49]. The formation of bi-stripe and Wigner-crystal cannot be seen in isolation from the CE-type structure of the x=0.5 case. Indeed, there is a point in the doping regime when the removal of the e_g electrons from the bonding states of the CE phase at x=0.5 leaves behind a structure where all of the P^U polarons can stay separated from each other without sharing any M^e site in the lattice. At this doping, the P^U polarons avoid going into random sites in the lattice as there distribution is highly selective due to strong correlation between them through the strain field induced by the local JT distortion of the P^U polarons. This long-range elastic interaction of the lattice due to the JT distorted octahedra at Mn^c sites of the P^U polaron opposes any kind of phase separation driving the system towards the formation of stripes (Figure 4.17). The importance of elastic interaction in formation of the stripe-phase has also been pointed out by Khomskii and Kugel et al. [95]. The charge separation is maximum in the Wigner-crystal phase. On the other hand, one-half of the M^e sites are shared by two P^U polaron in the bi-stripe phase.

We study the bi-stripe and Wigner-crystal phase with the **II-type** unit cell and compare their energies. The Wigner-crystal turns out to be the most stable structure as its energy per Mn is lower than the bi-stripe phase by 4 meV. In the Wigner-crystal structure with
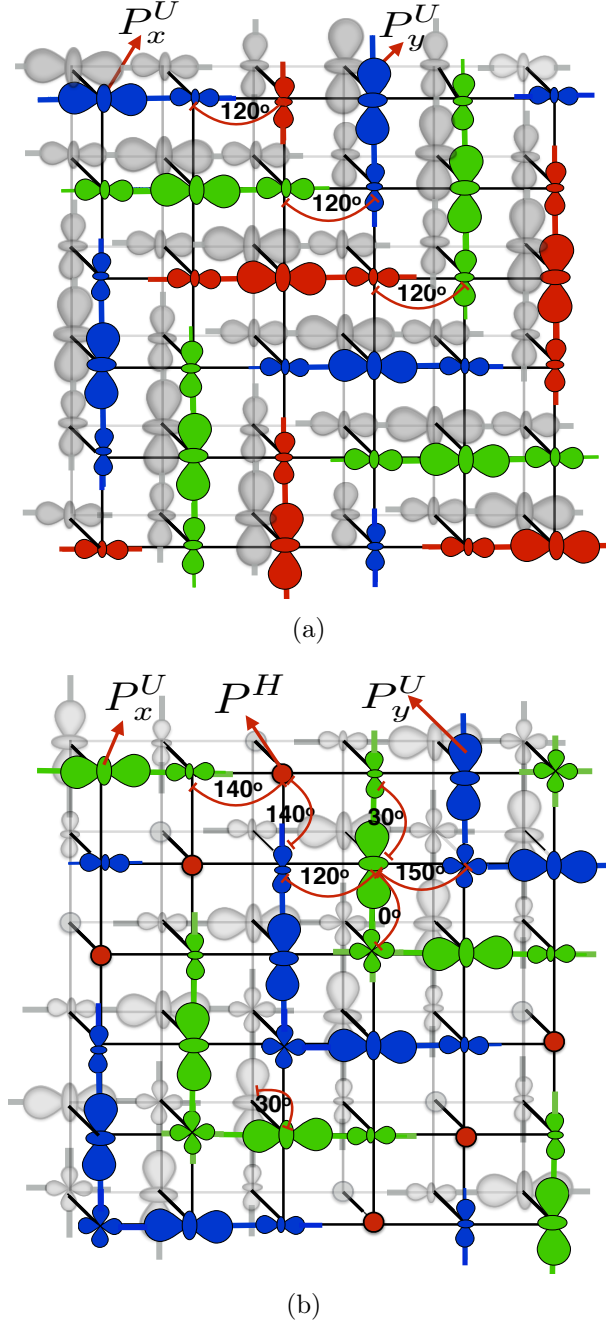
Figure 4.17: Orbital and spin structure of the Wigner-crystal (a) and the bi-stripe (b) phase at x=0.675 with 6×6×2 sized unit cell. The charge disproportion between the sites is highlighted by the size of the orbital. The blue, green and red colored orbitals imply different spin orientation of the sites. The holes are indicated by circles. While the P^U polarons do not share any M^e sites in the Wigner-crystal phase (a), one of the M^e site of each of the P^U polaron is shared in Bi-stripe phase (b). The spin ordering between the Mn^c sites along z direction in the case of bi-stripe phase (b) is ferromagnetic due to super-exchange interaction between empty state on first Mn^c and occupied state on second Mn^c and vice-versa.

anti-ferromagnetically coupled xy plane in the z direction has lower energy than the corresponding structure with ferromagnetically coupled xy planes.

The orbital ordering and the magnetic structure of the Wigner-crystal phase is depicted

in Figure 4.17. The charge-stripe in the Wigner-crystal is the domain of the electron-rich region of the M^c sites of the P^U polarons that are separated from each other by the domain wall of the electron poor M^e sites. The double exchange mechanism dominates between the ferromagnetic sites within the P^U polarons. In the z direction, the super-exchange interaction between the t_{2g} states endorses anti-ferromagnetic magnetic order and hence, the spins of the nearest P^U polarons in the z directions are antiparallel. The super-exchange interaction between lower occupied e_g orbital on the M^e site of the P^U polarons and the upper unoccupied e_g orbital on a M^e site of the adjacent P^U polarons in the xy plane favours weak ferromagnetism and hence, the spin angle between two adjacent P^U polarons in the xy plane changes from 180° to 120°, see Figure 4.17 (a).

The orbital and magnetic order of the bi-stripe phase is shown in Figure 4.17 (a). The charge-stripe in the bi-stripe phase can be assumed as a domain of the electron-rich region separated from each other by the domain wall of the holes. Although the charge ordering remain in-phase like that of the Wigner-crystal phase in the z direction, the orbital ordering in the z direction in the bi-stripe phase is not same, but rotated by 90°. The M^c site of the P_x^U (P_y^U) on the 1st xy plane is on the top of the M^c site of the P_y^U (P_x^U) polaron of the 2nd xy plane. While the double exchange mechanism within P^U polaron favours almost ferromagnetic spin order with spin angle of 30° within the P^U polarons, the super-exchange mechanism between the t_{2g} states of the sites of the adjacent P^U in the xy plane promotes anti-ferromagnetism and thus, the spin angle between M^c sites of the adjacent P^U polaron in the xy plane is 120°.

4.9.3   C-type phase at x=0.75)

Going from $x{\sim}0.66$ to $x{\sim}0.75$ doping, the present model suggests a transition from the Wigner-crystal phase to the C-type magnetic order is observed. This C-type region is indicated as IX in Figure 1.9. Our model produces two degenerate structure as ground states at x=0.75 doping. The orbital and magnetic order of these two structure are illustrated in Figure 4.18 and 4.19. In both the structures, the P^U polarons order themselves along the z direction. There is a strong charge disproportion between the M^e and M^c sites of the P^U polarons. The arrangement of these P^U polarons is not random and largely depends on the e-e interaction on the M^e sites of the P^U polarons. The onsite e-e interaction on the M^e sites favours separated P^U polarons where they do not share any common M^e site. Both the structures are close to the ideal C-type magnetic (see Figure 1.6).

In the first structure, the distance between the charge-rich sites, i.e., M^c sites, of the P^U polarons is maximum as illustrated in Figure 4.18. Jirak et al. [25] suggested a
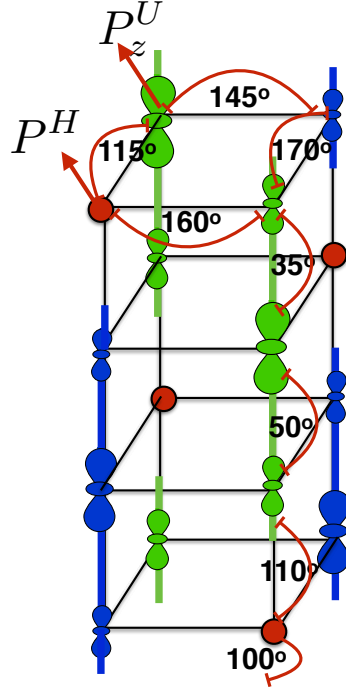
Figure 4.18: Orbital and spin ordering of the four consecutive 2×2 xy plane of the first C-type structure at x=0.75. The charge disproportion between the sites is highlighted by the size of the orbital. The blue, green and red colored sites imply different directions of the t_{2g} spins on the corresponding sites. The t_{2g} spin angle between sites within the P^U polaron is 35° and 45°. The x and y directions are not identical in the structure as there remain a asymmetry within spin angles. The distance between P^U polarons is maximum.

(a) 1st xz plane   (b) 2nd xz plane   (c) 3rd xz plane   (d) 4th xz plane
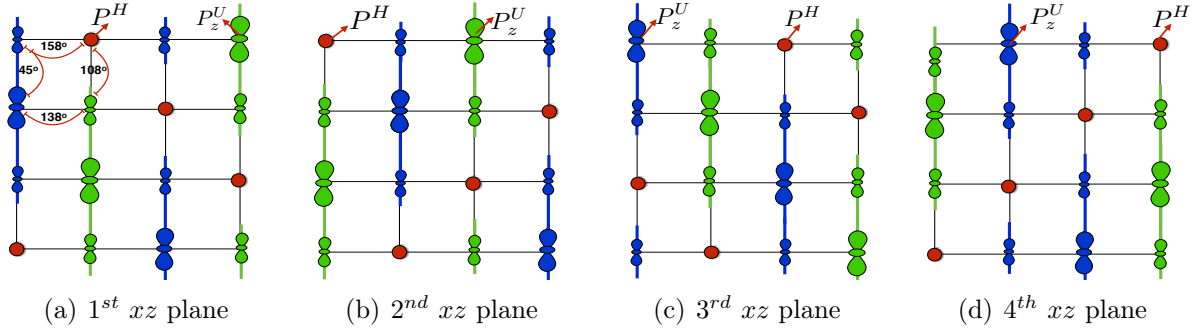
Figure 4.19: Orbital and spin structure of the four consecutive xz planes of the second C-type order at x=0.75. The charge disproportion between the sites is highlighted by the size of the orbital. The Blue, green and red colored sites imply different directions of the t_{2g} spins on the corresponding sites. Similar to the first structure (as described in Figure 4.18), the P^U polarons are oriented in the z direction.

similar orbital ordering at x=0.75 doping from the experimentally obtained diffraction pattern of the x=0.8 case with the C-type magnetic ordering. The strong double-exchange mechanism in the z direction within the sites of the P^U polarons (shown in blue and green) promotes ferromagnetism, which is confirmed by the small spin angles (35° and 50°). This ferromagnetic chain of the P^U polarons in the z direction is very similar to the ideal C-type structure except that the continuous ferromagnetic spin order in the z direction is interrupted by the weak anti-ferromagnetic coupling (spin angle of around 100°-110°)

between the M^e sites and P^H holes. On the other hand, a weak ferromagnetic interaction between the M^c site and hole P^H (shown in red) decreases the spin angle between these sites to 115° in the xy plane.

In the second structure, a continuous charge stripe runs diagonally in all the three planes, .i.e, xy, xz, and zx planes, as shown in Figure 4.19. It is worth mentioning that while the P^U polarons do not share common M^e sites to avoid the onsite Coulomb repulsion, they are still allowed to form continuous charge stripe diagonally in all the three planes due to the absence of any long range e-e interaction term. A weak super-exchange interaction between the occupied e_g orbital of the P_z^U polaron (shown in blue and green) and the e_g orbital pointing towards P_z^U polaron of the nearby P^H (shown in red) sites favours ferromagnetism decreasing cthe spin angle between these sites from 180° to 108° degree in the z-direction. The anti-ferromagnetic coupling between the t_{2g} spins favours larger spin angle (135°-160°) between sites within xy plane.

In our present model, both the structure are degenerate as we do not include any long-range e-e interaction term. The long-range Coulomb repulsion term in the Hamiltonian is expected to stabilise the first structure discussed above (Figure 4.18) over this second structure (Figure 4.19).

4.9.4 Ferromagnetic clusters within $1<x<0.89$ region

Before discussing the phase-separated $0.89>x>0.85$ region of the phase-diagram, we first discuss the $1<x<0.89$ doping region. There are several experimental studies which confirm presence of electron-rich ferromagnetic clusters of finite sizes embedded in the G-type parent CMO system [51, 58]. To figure out the nature of charge defects in the electron doped CMO system, we carried out calculations with CMO (N_e=0) system by adding electrons to it. The system shows the tendency of electron localisation by forming clusters of parallel spin sites. Recently, there are also theoretical studies which hint towards the presence of spin polarons (.i.e., electrons trapped in the local ferromagnetic clusters) forming magnetic clusters in this region of the phase diagram [135, 136]. Bondarenko et al. [135] studied stability of ferromagnetic clusters of different sizes as a function of doping in the $1>x>0.85$ region. In the present work, we also study the stability of the 7-, 12-, 17- and 21-site ferromagnetic clusters, mentioned by Bondarenko et al. [135], together with other additional clusters. Figure 4.20 shows the geometry of these ferromagnetic cluster involving different number of sites.

We perform calculations with the unit cell of **III-type** (see Table H.10) with frozen-spin configurations corresponding to each ferromagnetic cluster (described in Figure 4.20)
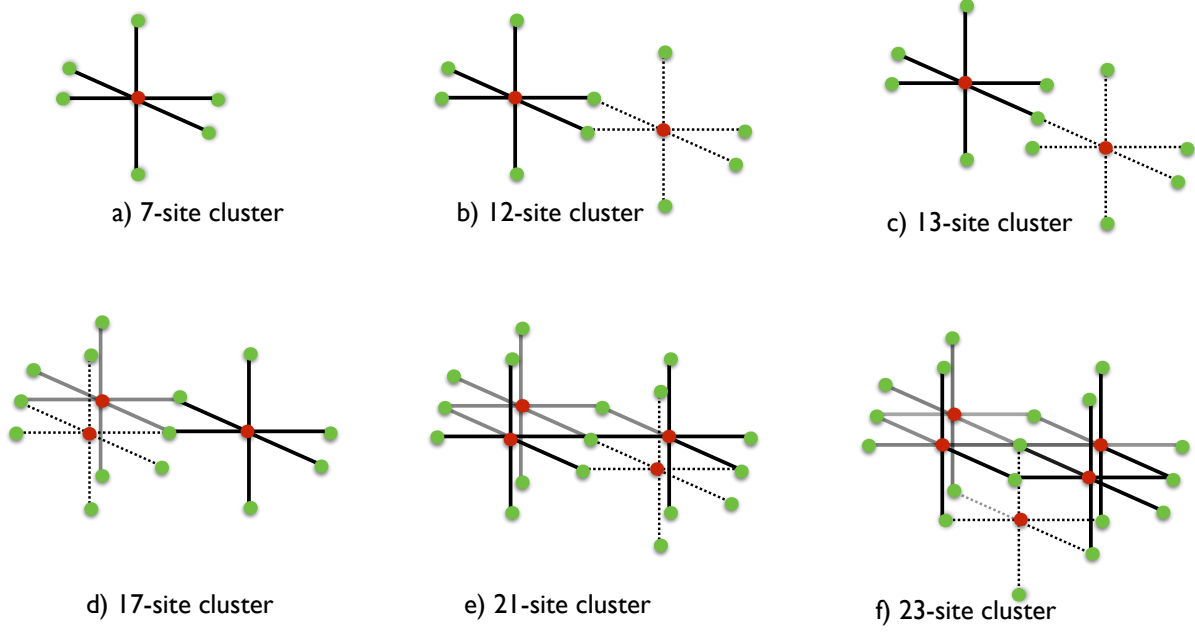
Figure 4.20: Different kinds of ferromagnetic cluster possible in the $1 > x > 0.89$ doping region. The Mn sites are shown in blue and red solid circle. The spin flipping at red Mn sites leads to ferromagnetic atmosphere around the site creating a 7-site ferromagnetic cluster. This ferromagnetic cluster grows in size on flipping spins on the additional red sites (c-f) forming clusters of sites 12, 17, 21, 23... etc. The 13-site ferromagnetic cluster (c) is the P^{Lr} polaron as described in Figure 4.1 and Section 4.2

isolated in the unit cell. The calculations are performed with variable number of electrons (N_e). The energy verses N_e graph in Figure 4.21 compares the energy per Mn site with single ferromagnetic cluster of lowest energy at each N_e. The number of sites of the ferromagnetic cluster corresponding to lowest energy at any N_e is also indicated. We find that the energy of larger ferromagnetic cluster is lower than the smaller ferromagnetic cluster as the number of electron N_e increases, but the system with these larger sized cluster has no band gap and metallic in nature (for cluster involving above 26-sites).

The stability of the structure with a single large-sized ferromagnetic cluster over a structure with many-smaller ferromagnetic cluster at particular doping is an important aspect to be studied. To find out this, we select ferromagnetic cluster at each N_e corresponding to lowest energy. These lowest energy structures are indicated by blue solid circle in Figure 4.21. In the lowest energy ferromagnetic cluster with fewer electrons (N_e=1 to 8), the electrons occupy the bonding states formed by hybridisation of the e_g states of a single Mn site (indicated by red site in Figure 4.20) with the nearby Mn sites (indicated by green sites in Figure 4.20). These resulting bonding states are mainly localised on single sites (red site in Figure 4.20). On the other hand, the electrons in the larger ferromagnetic clusters below N_e=8 are highly delocalised and the resulting structure is metallic with no band gap as mentioned above.

Interestingly, the P^{Lr} polaron is the most stable polaron in $1 > x > 0.85$ region of the phase
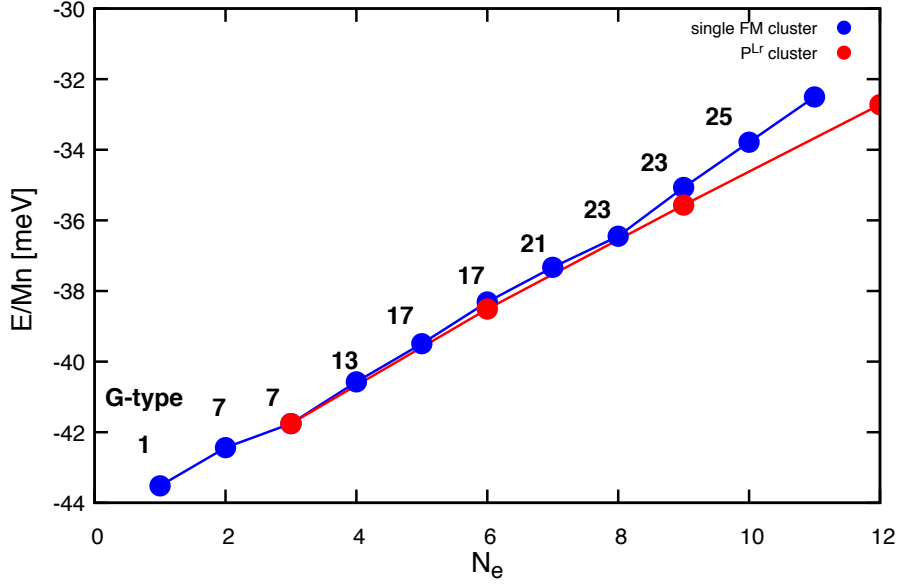
Figure 4.21: Energy versus number of electrons N_e graph comparing the energy per Mn of the system with single ferromagnetic cluster (blue) and only P^{Lr} polarons (red). Blue solid symbol represent the lowest energy corresponding to a single ferromagnetic cluster in the system. The size of the ferromagnetic cluster is indicated. The red solid symbol are the energies of the structure with only P^{Lr} polaron. As the number of electron increases system the stability of the size of the ferromagnetic cluster increase. The system with only P^{Lr} polaron is stable at each N_e indicating the stability of phase with several small P^{Lr} polarons over the phase with just a single ferromagnetic cluster of comparatively bigger size

diagram as the energy per Mn for at each N_e is lowest in the case if only P^{Lr} type polarons are present in the system (see Figure 4.21). The number of electron trapped within a single P^{Lr}. The nature of orbitial ordering on individual sites of the P^{Lr} polaron is three as shown in Figure 4.1 (see Section 4.2 for discussion).

As discussed above, the structure with a bigger ferromagnetic cluster is not as stable as the structure with several P^{Lr} polarons. This is contradicts the previous study by Bondarenko et al. [135] where it is shown that the size of the ferromagnetic polaron goes on increases while increasing the electron in the system. The size of the ferromagnetic clusters detected experimentally in this doping region is around ∼10 nm [51, 58], which is also in good agreement with the length of the P^{Lr} polaron in the direction connecting the two M^c sites through M^{c-c} site (see Figure 4.1). Bondarenko et al. [135] hinted towards a gradual development of a long range ferromagnetic order as the size of the ferromagnetic cluster increases on doping electron in the system. This is in contrast to the experimental observations that do not detect any ferromagnetic order within this doping range [51, 58], which further validate the presence of the smaller P^{Lr} polaron.

Figure 4.22 shows the orbital ordering and spin structure at x=0.89 for six consecutive 6× 6 xy planes. The x∼0.89 is the critical doping below which the system can accommodate these P^{Lr} clusters separated from each other, without sharing any M^e site. The onsite

inter-orbital e-e interaction tries to keep these clusters away from each others. As long as the lattice can accommodate these thirteen-site P^{Lr} polarons, the system remains insulating because the electrons are confined within their respective polarons. This region is $1>x>0.89$ and is denoted by X in Figure 1.9. There are total eight P^{Lr} polarons in the system: four in the 1st xy plane and four in the 2nd xy plane. The strain field induced by two M^c sites of the P^{Lr} polaron is absorbed by the orthogonal orbital ordering on the

(a) 1st xy plane

(b) 2nd xy plane

(c) 3rd xy plane

(d) 4th xy plane

(e) 5th xy plane

(f) 6th xy plane
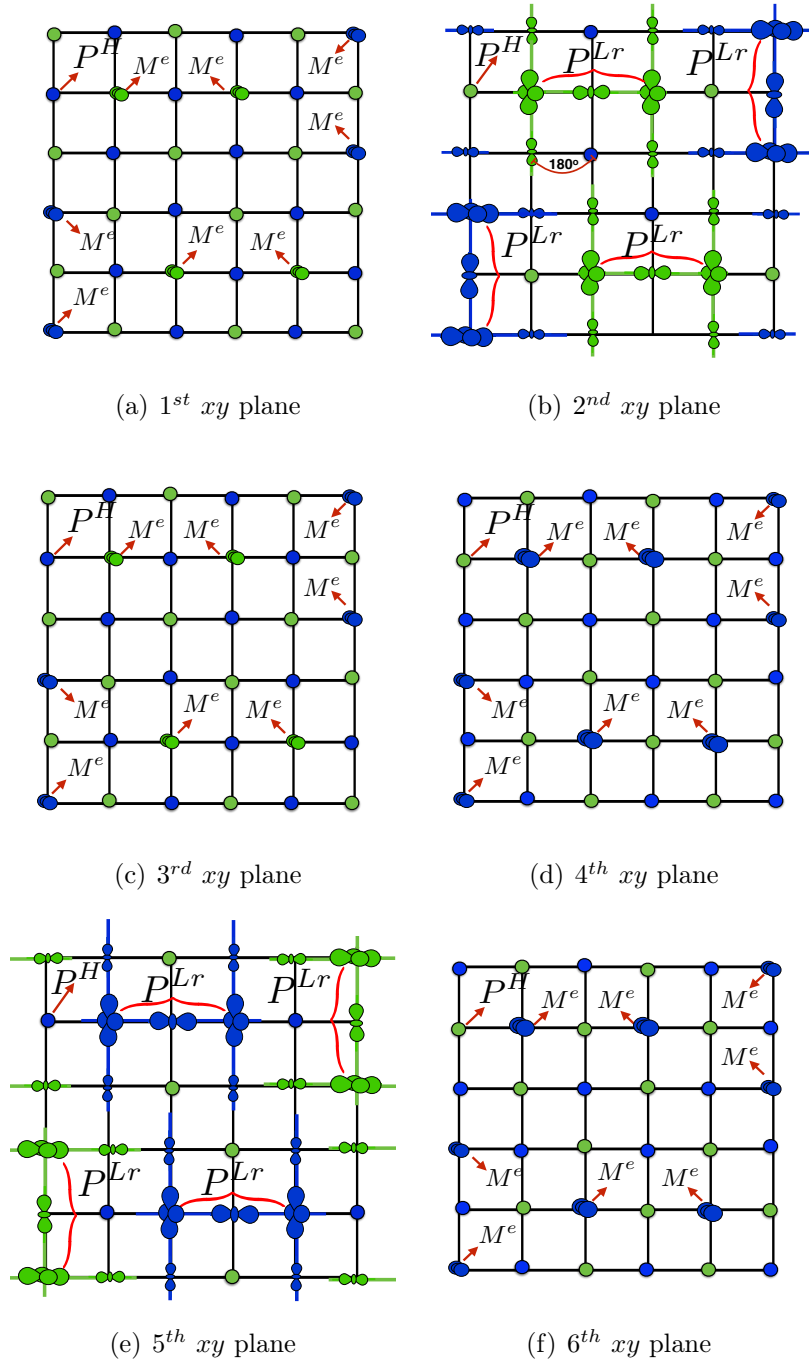
Figure 4.22: Orbital and spin structure of the six consecutive xy planes of the electron doped CMO system at $x = 0.89$. The charge disproportion between sites is highlighted by the size of the orbital. The blue and green colored sites imply sites with opposite t_{2g} spins directions. The M^e sites indicated in the 2nd and 6th xy planes correspond to the M^e sites of the P^{Lr} polarons of the 1st xy plane. The M^e sites of the 3nd and 5th xy planes correspond to the M^e sites of the P^{Lr} polarons of the 4th xy plane.

M^{c-c} site of the same polaron. Hence as a whole, the system expands symmetrically in all directions validating the experimental picture of almost cubic structure in this doping region. All eight P^{Lr} polarons are separated and do not share any M^e site. The system

cannot accommodate any additional P^{Lr} polaron. If additional electrons are added below $x = 0.89$ doping, the system undergoes phase-separation.

In between the C-type phase at $x=0.75$ and the phase with ferromagnetic clusters in the G-type matrix at $x\sim 0.89$, the competition between the kinetic energy and e-e interaction, locally, results in a non-collinear spin alignment and phase separation. Instead of large-sized ferromagnetic clusters, the experimental observations hint towards a phase-separation scenario in the doping region $0.89>x>0.85$, which will be discussed in Section 4.9.5.

4.9.5   Phase competition and spin-canting $(0.90>x>0.85)$

Before going into the physics of the system in the region $0.89>x>0.85$ (denoted as XI in Figure 1.9). It is important to look at the one-particle energy spectrum of the system and the nature of the states above the Fermi level at $x\sim 0.91$, which are to be filled when extra electrons are added below $x\sim 0.89$. All of the states, occupied and unoccupied, at $x\sim 0.89$ in a structure with P^{Lr} polarons can be classified into the following sets:

Bonding states $|\mathbf{V_i^b}\rangle$: These are set of the occupied bonding states below the Fermi level and are mainly concentrated on central sites Mn^c and Mn^{c-c} of the P^{Lr} polarons, as mentioned in Section 4.9.1.

Anti-bonding states $|\mathbf{V_i^{ab}}\rangle$: - These set of the anti-bonding states are orthogonal to $|V_i^b\rangle$ and are primarily concentrated on Mn^e corner sites of the polarons. They energetically lie very high above the fermi level.

Non-bonding states $|\mathbf{V_i^{nb}}\rangle$: - These are the non-bonding states orthogonal to $|V_i^b\rangle$. They are unoccupied below $x\sim 0.89$ and lie close to the Fermi level in the energy spectrum.

Localised states $|\mathbf{U_i^c}\rangle$: - These states shift higher in energy during the e_g level splitting on Mn^c and Mn^{c-c} due to octahedral distortion.

Localised states $|\mathbf{U_i^e}\rangle$: - These are the set of onsite states that are confined to the Mn_j^e's corner sites and are orthonormal to the onsite e_g orbitals on these sites that contribute to $|V_i^b\rangle$. They are unoccupied and lie above the fermi level.

As one go above doping $x\sim 0.89$, the unoccupied non-bonding $|V_i^{nb}\rangle$ states close to the Fermi level start filling. Due to the non-dispersive nature of these non-bonding bands and the anti-ferromagnetic alignment of spins between sites of different polarons, it is very likely that these additional electrons gain extra kinetic energy by going into weak bonding states formed by the $|V_i^{nb}\rangle$ states that belong to two nearby P^{Lr} polarons. This is facilitated by the spin-canting. Hence, the total energy density $\mathcal{E}$ is almost constant

for the electron doping within certain region, i.e., $0.90 > x > 0.85$. This region in the phase diagram is ascribed to the phase-separation region with the domains of P^{Lr} clusters and C-type phase coexisting in the background of the G-type matrix with spin-canting [51, 58].

4.10 Summary

In the present chapter, we studied the complete phase diagram of the $\text{Pr}_{1-x}\text{Ca}_x\text{MnO}_3$ manganites with our proposed model. The system is observed as insulating across the entire doping region.

We report distinct phases at $x=0.125$ and $x=0.25$ doping case besides the CE-structure and A-type structure at $x=0$ and $x=0.5$ doping below half doping.

A insulating phase with B-type magnetic order is predicted at $x=0.25$. The Mn^{3+} sites exhibit a $d_{x^2-y^2}/d_{y^2-z^2}/d_{z^2-x^2}$-type (cross-orbital ordering) orbital ordering instead of earlier proposed axial $d_{3x^2-r^2}/d_{3y^2-r^2}/d_{3z^2-r^2}$-type. The lobes of orbitals at Mn^{3+} sites are directed towards the nearby holes. In the insulating phase at $x=0.25$, the B-type magnetic order is stabilised not only by the double exchange mechanism between holes and Mn^{3+} sites, but also the ferromagnetic super-exchange interaction between the occupied $d_{x^2-y^2}/d_{y^2-z^2}/d_{z^2-x^2}$-type orbital and the empty $d_{3z^2-r^2}/d_{3x^2-r^2}/d_{3y^2-r^2}$-type orbitals on the Mn^{3+} sites.

The holes (P^H) at $x=0.125$ are confined within particular xy planes that are isolated from each others. Within the xy plane, the e-e interaction keeps restrict the size of the hole-rich domains.

The lattice constants obtained by the present tight-binding model contradicts the experimentally verified lattice constants in the low-doped system close to $x=0$. It would be interesting to investigate the role of tilting on the hopping elements which may lead to these deviations in this low-doped region of the phase diagram.

Several low-lying insulating metastable structures are detected in the region $0.25 < x < 0.5$. The introduction of the electron-induced disorders in the CE-type structure leads to formation of these metastable structures. Due to high configurational-entropy associated with these metastable structures, these are important candidates to understand the properties of the system in high-temperature region of the phase diagram.

The $\text{Pr}_{1-x}\text{Ca}_x\text{MnO}_3$ manganite reveals the propensity towards phase-separation around $x=0.185$ and $0.5 > x > 0.375$ below half doping. At low temperature, the system around $x=0.185$ tends to exhibit coexistence of the B-type and A-type phases. The additional

electrons below x=0.5 in the $0.5 > x > 0.375$ doping range are localised on single sites while rest of the system remains more or less CE-type with x=0.5 stoichiometry. Hence, it can be seen as a large scale phase-separation.

In the electron-poor side of the phase diagram, our model predicts only a single phase-coexistence region, i.e., $0.89 > x > 0.85$. In $0.5 < x < 0.625$ region, additional holes above x=0.5 doping are localised on certain sites destroying a local orbital ordering in the CE-type system.

These additional holes are not distributed randomly but correlated by long-range strain field induced at the site of these additional hole. At x=0.625, we observe a structure with simultaneous appearance single and bi-stripe running diagonally in the xy direction. This mixed-stripe structure can be seen as a variant of the CE-type or Wigner-crystal phase. At x=0.66, the Wigner-crystal phase is lower in energy than the bi-stripe phase. The Wigner-crystal phase has a similar kind of charge-ordering as the CE-type phase in the z direction.

The C-type structure covers a large part of the phase diagram, i.e., $0.75 < x < 0.85$. The Mn^{3+} sites exhibit $d_{3z^2 - r^2}$-type orbital ordering in the z direction which is also the ferromagnetic direction in the C-type phase.

Lastly, we observe certain seven- and thirteen-sites large ferromagnetic cluster embedded into the G-type structure within $1 > x > 0.89$ doping region. The finite size of these ferromagnetic clusters contradicts with the large sized ferromagnetic clusters previously predicted by other theoretical studies. The experimental observation of the nanoscale sized magnetic clusters in the G-type matrix validates our study in the high-doped region of the phase diagram.

Chapter 5

Relaxation dynamics in one-dimensional system

The processes that involve non-radiative transitions between electronic states are not only interesting from the experimental point of view but also a challenging theoretical task as such studies require to include non-adiabaticity, which contains far more complexities than the usual adiabatic approaches such as the Born-Oppenheimer approximation. To understand these processes it is important to go beyond such approximations. It is recognised by now that, particularly the conical intersections that are non-adiabatic interaction, have a very strong effect on the dynamics of a system and recombination rates [137, 138], which sometimes may lead to new relaxation mechanism pathways in solids. In the present chapter, we formulate the excitation process and the numerical integration approaches to study the relaxation processes of the charge carriers, with major focus on the physics in the proximity of the conical intersections. We determine the characteristic timescale of the electron, spin and lattice degrees of freedom in one-dimensional systems. Later, in this chapter, the relaxation process of isolated single electron (isolated trimer polaron) and dimerised phase (Zener polaron at half doping $x = 0.5$) in the one-dimensional chain are discussed in detail.

5.1   Electromagnetic field

A classical electromagnetic field can be described by a plane wave expansion. A plane wave of wave vector $\vec{k}$ travelling in the x direction can be described by the vector potential which is given as:

$$\vec{A}(\vec{r}, t) = \vec{e}_A A_o e^{i(\vec{k}x - \omega t)} + \vec{e}_A A_o^* e^{-i(\vec{k}x - \omega t)}. \tag{5.1}$$

The corresponding electric and magnetic field associated with the vector potential above defined is given by

$$\vec{E}(\vec{r}, t) = -\frac{\partial}{\partial t}\vec{A}(\vec{r}, t) \tag{5.2}$$

$$\vec{B}(\vec{r}, t) = \nabla \times \vec{A}(\vec{r}, t) \tag{5.3}$$

5.2   Poynting vector $\vec{S}$ and field intensity I

Let us suppose an electron bounded to an atom interacts with the plane wave described by the vector potential of form:

$$\vec{A}(\vec{r}, t) = \frac{1}{2}\left[\vec{e}_A A_o e^{i(\vec{k}.\vec{r}-\omega t)} + \vec{e}_A A_o^* e^{-i(\vec{k}.\vec{r}-\omega t)}\right] \tag{5.4}$$

The electric field corresponding to the vector potential, according to Equation 5.2, is given by

$$\vec{E}(\vec{r}, t) = -\frac{\partial}{\partial t}\vec{A}(\vec{r}, t) = \frac{1}{2}i\omega\left[\vec{e}_A A_o e^{i(\vec{k}.\vec{r}-\omega t)} - \vec{e}_A A_o^* e^{-i(\vec{k}.\vec{r}-\omega t)}\right]. \tag{5.5}$$

In a similar way, the magnetic field, according to Equation 5.3, is

$$\vec{B}(\vec{r}, t) = \nabla \times \vec{A}(\vec{r}, t) = \frac{1}{2}i\vec{k} \times \left[\vec{e}_A A_o e^{i(\vec{k}.\vec{r}-\omega t)} - \vec{e}_A A_o^* e^{-i(\vec{k}.\vec{r}-\omega t)}\right]. \tag{5.6}$$

From the Coulomb gauge condition $\nabla.\vec{A}(\vec{r}, t) = 0$, we have

$$\vec{k}.[\vec{e}_A A_o(\omega)e^{i(\vec{k}.\vec{r}-\omega t)} - \vec{e}_A A_o^*(\omega)e^{-(i\vec{k}.\vec{r}-\omega t)}] = 0. \tag{5.7}$$

The cross product of the electric (Equation 5.5) and magnetic field (Equation 5.6) is given by

$$\vec{E}(\vec{r}, t) \times \vec{B}(\vec{r}, t) = \frac{\omega\vec{k}}{4}\left[2|A_o(\omega)|^2 - A_o(\omega).A_o(\omega)e^{2i(\vec{k}.\vec{r}-\omega t)} - A_o^*(\omega).A_o^*(\omega)e^{-2i(\vec{k}.\vec{r}-\omega t)}\right] \tag{5.8}$$

Taking the time average $\langle\vec{E}(\vec{r}, t) \times \vec{B}(\vec{r}, t)\rangle$, we have

$$\langle\vec{E}(\vec{r}, t) \times \vec{B}(\vec{r}, t)\rangle = \frac{1}{2}\omega|A_o(\omega)|^2\vec{k}. \tag{5.9}$$

The pointing vector $\vec{S}$ associated with a field is described by

$$\vec{S} = \frac{1}{\mu_o} \vec{E} \times \vec{B}. \tag{5.10}$$

Here, μ_o is the vacuum permeability. $\vec{S}$ has the direction perpendicular to $\vec{E}$ and $\vec{B}$. It is the measure of the flow of energy travelling through the space per unit area and per unit time and has the SI unit joules/m^{2}s. The time average of $\vec{S}$ is

$$\langle \vec{S} \rangle = \frac{1}{\mu_o} \langle \vec{E}(\vec{r}, t) \times \vec{B}(\vec{r}, t) \rangle = \frac{1}{2} c \epsilon_o \omega^2 |A_o(\omega)|^2. \tag{5.11}$$

This is what called as intensity $I = \langle \vec{S} \rangle$. Here, ϵ_o is the permittivity of free space. The intensity I is a power per unit area and has a unit W/m^2. We use the above expression throughout our calculation and result sections to obtain the vector potential amplitude A_o from the intensity I that is provided to us by experimentalists. In Appendix B, the value of A_o is derived from the available experimental information from Raiser et al. [101]. We use the same A_o value in our calculations unless stated otherwise.

5.3 Interaction of a bound electron with a EM wave

If an electromagnetic field interacts with an electron that is bounded by a potential V(r), the complete Hamiltonian of the electron in the atom is written as

$$
\begin{aligned}
\mathcal{H} &= \frac{1}{2m}(-i\hbar\nabla + e\vec{A})^2 + e\phi + V(r) \\
\mathcal{H} &= \frac{\hbar^2}{2m}\nabla^2 - \frac{ie\hbar}{2m}\vec{A}.\nabla - \frac{ie\hbar}{2m}\nabla.\vec{A} + \frac{e^2}{2m}\vec{A}^2 + e\phi + V(r) \\
\mathcal{H} &= \frac{\hbar^2}{2m}\nabla^2 - \frac{ie\hbar}{2m}\vec{A}.\nabla + \frac{e^2}{2m}\vec{A}^2 + V(r)
\end{aligned} \tag{5.12}
$$

where the Coulomb gauge condition $\nabla.\vec{A}(\vec{r}, t) = 0$ is used which also leads $\phi = 0$ (scalar potential). The term $-\frac{ie\hbar}{2m}\vec{A}.\nabla$ in the above expression describes the interaction of a bounded electron with an external field defined by the vector potential $\vec{A}(\vec{r}, t)$ (Equation 5.1).

5.4   Dipole approximation and Fermi-Golden rule

Substituting $\vec{A}(\vec{r}, t)$ from Equation 5.1 in Hamiltonian 5.13, we obtain an expression with two terms in A_o, i.e., with $\vec{A}_o$ and $\vec{A}_o^*$. We define both these terms of Hamiltonian separately by $\mathcal{H}_{i,-}$ and $\mathcal{H}_{i,+}$ as follows:

$$\mathcal{H}_{i,-} = -\frac{ie\hbar}{m}\vec{A}_o e^{i\vec{k}.\vec{r}}.\nabla \tag{5.13}$$

and

$$\mathcal{H}_{i,+} = -\frac{ie\hbar}{m}\vec{A}_o^* e^{-i\vec{k}.\vec{r}}.\nabla. \tag{5.14}$$

In the presence of the electromagnetic field, the probability of the transition between the initial ϕ_i and final ϕ_f state of the system when the system absorb a photon of energy $\hbar\omega$ is given by the Fermi-Golden rule [139, 140]. According to the Fermi Golden rule, the probability $W_{i\to f}$ of the transition from the initial state ϕ_i to the final state ϕ_f is given by

$$
\begin{aligned}
W_{i\to f}(\omega) &= \frac{2\pi}{\hbar}\left|\langle f|\mathcal{H}_{i,\mp}|i\rangle\right|^2 \times \delta(E_f - E_i \mp \hbar\omega) \\
&= \frac{2\pi e^2\hbar}{m^2}\left|\vec{A}_o^*(\omega). \int d\vec{r} e^{\pm\vec{k}.\vec{r}}\phi_f^*\nabla\phi_i(\vec{r})\right|^2 \times \delta(E_f - E_i \mp \hbar\omega).
\end{aligned}
\tag{5.15}
$$

The delta function in the above equation expresses the energy conservation during the process. Under the approximation that the $\vec{k}.\vec{r}$ is very small in the region where the wave functions have appreciable values, we neglect the exponential part in the above integrand. Thus, the probability $W_{i\to f}$ is expressed as

$$W_{i\to f}(\omega) = \frac{2\pi e^2\hbar}{m^2}\left|\vec{A}_o^*(\omega). \int d\vec{r}\phi_f^*\nabla\phi_i(\vec{r})\right|^2 \times \delta(E_f - E_i \mp \hbar\omega) \tag{5.16}$$

5.5 Initial state for photo excitation: Peierls substitution

To study the transport properties, we present here a full quantum mechanical evolution of the electrons, driven far from the equilibrium in the presence of an external electromagnetic field. The effect of the external electromagnetic field is incorporated by the Peierls substitution method [141]. According to the method, we change the phase factor of the terms that have coupling elements between atomic orbitals in the original Hamiltonian. The tight binding Hamiltonian that we introduced in Chapter 3 includes only nearest-neighbour hopping. The hopping matrix element $T_{\alpha,\beta,R,R'}$ used in 2.11 and defined in 2.12, 2.13 and 2.14 between α orbital at site R and β orbital at site R' is modified as

$$T_{\alpha,\beta,R,R'}(t) = T_{\alpha,\beta,R,R'}e^{i\phi_{R,R'}(t)} \tag{5.17}$$

where

$$\phi(t) = \frac{e}{\hbar} \int_R^{R'} \vec{A}'(\vec{r},t)d\vec{r} \tag{5.18}$$

$\vec{A}'(\vec{r},t)$ is the vector potential given by

$$\vec{A}'(\vec{r},t) = \vec{A}(\vec{r},t)g(t) \tag{5.19}$$

We choose a spatially homogeneous and time varying field. Furthermore, we assume a Gaussian type function,

$$g(t) = e^{\frac{-t^2}{2cw}} \tag{5.20}$$

to introduce the time-dependence in the excitation pulse, which resembles a short laser pulse shape in the ultrafast spectroscopy experiments.

Substituting the $\vec{A}(\vec{r},t)$ from Equation 5.1 into 5.20, we have

$$\vec{A}'(\vec{r}, t) = \frac{1}{2}\Big(\vec{e}_A A_o e^{i(\vec{k}x - \omega t)} + \vec{e}_A A_o^* e^{-i(\vec{k}x - \omega t)}\Big)g(t) \tag{5.21}$$

In the long wavelength limit, the Peierls phase $e^{\phi}(t)$, where $\phi(t)$ is defined in Equation 5.18, reduces to $e^{\phi'(t)}$ (see Appendix D) where,

$$\phi'(t) = \frac{e}{\hbar}\vec{e}_A(\vec{R}_\alpha - \vec{R}'_\beta)Re[A_o e^{i\omega t}]g(t). \tag{5.22}$$

5.6 Radiative and non radiative relaxation

The ability of a system to prolong long-lived excitations, such as electronic or polaronic excitations, plays a critical role in the photovoltaic functionality of the systems. The recombination process is a fundamental physical process through which the charge carriers from high energy state relax back into lower energy states. These transitions between energy levels can be radiative or non-radiative. While the radiative recombination involves absorption and emission of the electromagnetic radiation, during the non-radiative recombination processes, the energy of an electron converts to some other form. For example, in the non-radiative recombination, the energy may be converted into the vibrational energy of the lattice, i.e., phonons, which may further dissipate into heat due to several reasons, such as friction at the interface of layers of two different material. The energy loss due to these non-radiative processes decreases the overall efficiency of the systems to channel these excitation energies into some other useful form. The non-radiative recombination is very common in semiconductors and occurs due to arbitrary defects present in the system, such as dislocation, impurity atom, vacancies, etc [142–146]. Such defects have additional energy levels that lie in the forbidden gap of the semiconductor, which act as recombination centres through which the recombination occurs.

There are also other non-radiative recombination processes, such as conical intersections and Auger recombination, which may not be important in the case of semiconductors but play an important role in the relaxation mechanism of other systems. In the Auger recombination, the extra energy available through the electron-hole recombination is transferred to another electron by its excitation to higher energy bands [144].

During a relaxation process, in exploring a region of lower energy, a system may run into the region where two potential energy surfaces come closer and can touch each other. A

conical intersection (explained in more details in Section 5.7.2) is a case where the two potential energy surfaces become degenerate or intersect. Sometimes more than two potential energy surfaces also intersect at the conical interactions [147]. The Born-Oppenheimer approximation breaks down in the vicinity of such intersections allowing the non-adiabatic processes to occur. The non-adiabatic processes involve non-radiative change in the electronic state of the system. Here, we first look into the Born-Oppenheimer approximation and its breakdown before going to further discussion on the conical intersection. Throughout this discussion, the matrices and vectors will be indicated by bold font. The operators will be denoted by hat $(\hat{})$ on the top.

5.7   Non-adiabatic dynamics

To study the dynamics of a system, the time-dependent Schrodinger equation of the system with electronic and nuclear degrees of freedom, which is given by

$$\hat{H}\Psi(\vec{x}, \vec{R}, t) = i\hbar \frac{\partial}{\partial t}\Psi(\vec{x}, \vec{R}, t) \tag{5.23}$$

is needed to be solved. In the above equation, $\hat{H}$ is the Hamiltonian of the system. While the $\vec{R}$ is the set which represents the nuclear coordinates, the vector $\vec{x}$ is the combined notation for electron position in space and its spin σ ($\sigma = \{\uparrow, \downarrow\}$), which actually follows the orthonormality

$$\langle \vec{r}, \sigma | \vec{r}', \sigma' \rangle = \delta_{\vec{r}' - \vec{r}}\delta_{\sigma, \sigma'}. \tag{5.24}$$

The complete non-relativistic Hamiltonian of the system, composed of electrons and atoms, is given by

$$\hat{H} = \hat{T}^n + \hat{T}^e + \hat{V}_e(\vec{r}) + \hat{V}_N(\vec{R}) + \hat{V}_{eN}(\vec{r}, \vec{R}) \tag{5.25}$$

where $\hat{T}^e$ and $\hat{T}^n$ are the kinetic energy operator of the electrons and the nuclei, respectively. The last three terms, $\hat{V}_e(\vec{r})$, $\hat{V}_N(\vec{R})$ and $\hat{V}_{eN}(\vec{r}, \vec{R})$ in the above equation correspond to the electron-electron, nuclear-nuclear and electron-nuclear interactions, respectively. By separating the Hamiltonian in terms of the electronic $\hat{H}^e$ and nuclei $\hat{H}^n$ part, we get

$$\hat{H} = \hat{H}^n + \hat{H}^e \tag{5.26}$$

where the electronic Hamiltonian $\hat{H}^e$ is

$$\hat{H}^e(\vec{R}) = \hat{T}^e + \hat{V}_e(\vec{r}) + \hat{V}_{eN}(\vec{r}, \vec{R}) \tag{5.27}$$

and depends parametrically on $\vec{R}$ through $\hat{V}_{eN}$.

The electronic wave functions are obtained by solving the equation

$$\hat{H}^e(\vec{R})\psi_i^e(\vec{x}, \vec{R}) = E_i^e(R)\psi_i^e(\vec{x}, \vec{R}). \tag{5.28}$$

Here, it must be noted that there is a different set of these equations for each nuclear configuration $\vec{R}$, and hence, the nuclear coordinates $\vec{R}$ in $\psi_i^e(\vec{x}, \vec{R})$ are not independent variables but just parameters.

The eigenfunctions $\psi_i^e(\vec{x}, \vec{R})$ can be used as a basis set to expand the total wave function $\Psi(\vec{x}, \vec{R})$,

$$\Psi(\vec{x}, \vec{R}, t) = \sum_i \psi_i^e(\vec{x}, \vec{R})\chi_i(\vec{R}, t) \tag{5.29}$$

to solve the Schrodinger equation (Equation 5.23) where $\chi_i(R, t)$ are the nuclei wave functions which are expansion coefficients in the above equation. Equation 5.29 is known as the Born-Huang expansion, and it is exact unless we truncate it. Substituting the form of $\Psi(\vec{x}, \vec{R}, t)$ from Equation 5.29 into the Schrodinger equation, multiplying the resulting equation by $\psi_j^e(\vec{x}, \vec{R})$ from right and integrating over the coordinates $\vec{r}$, we obtain

$$[\hat{T}^n + E_j^e(\vec{R})]\chi_j(\vec{R}) - \sum_i \hat{\Lambda}_{ji}(\vec{R})\chi_i(\vec{R}) = E\chi_j(\vec{R}) \tag{5.30}$$

where we have used $\hat{H}\Psi(\vec{x}, \vec{R}) = E\Psi(\vec{x}, \vec{R})$. The coupling operator $\hat{\Lambda}_{ji}$ in Equation 5.30 depends on the electronic states i and j,

$$\hat{\Lambda}_{ji}(\vec{R}) = \delta_{ji}\hat{T}^n - \langle\psi_j|\hat{T}^n|\psi_i\rangle \tag{5.31}$$

In rectangular coordinates, the kinetic energy operator of the nuclei is

$$\hat{T}^n = -\frac{\hbar^2}{2M}\nabla_{\vec{R}}^2. \tag{5.32}$$

Here, $\nabla^2 = \boldsymbol{\nabla}.\boldsymbol{\nabla}$ is a Laplacian operator, and M is the suitable mass-scale.

Using the form 5.32 for $\hat{T}^n$, Equation 5.31 becomes,

$$\hat{\Lambda}_{ji}(\vec{R}) = 2\boldsymbol{F}_{ij}(\vec{R}).\frac{\hbar}{i}\nabla_{\vec{R}} + K_{ij}(\vec{R}). \tag{5.33}$$

The $K_{ij}(\vec{R})$ and $F_{ij}(\vec{R})$ are obtained when $\frac{\hbar}{i2m}\boldsymbol{\nabla}_{\vec{R}}$ and $\frac{\hbar^2}{2M}\nabla_{\vec{R}}^2$ act on the wave functions $\psi_i^e(\vec{x}, \vec{R})$ of the electrons as follows:

$$F_{ij}(R) = \frac{1}{2M}\langle \psi_i^e(\vec{x}, \vec{R})|\frac{\hbar}{i}\nabla_{\vec{R}}\psi_j^e(\vec{x}, \vec{R})\rangle \tag{5.34}$$

and

$$K_{ij}(\vec{R}) = \frac{1}{2M}\sum_{\alpha}\langle \psi_i^e(\vec{x}, \vec{R})|\hbar^2\nabla_{\vec{R}}^2\psi_j^e(\vec{x}, \vec{R})\rangle \tag{5.35}$$

The angled bracket $\langle...\rangle$ terms in Equation 5.34 and 5.35 imply the complete integration over electronic coordinates $\vec{r}$, and $\nabla_{\vec{R}}$ is the gradient w.r.t. the atomic coordinates $\vec{R}$.

The terms $F_{ij}(\vec{R})$ is known as the derivative coupling vector and $K_{ij}(\vec{R})$ is the scalar coupling term. The diagonal term $K_{ii}(\vec{R})$ is the non-adiabatic correction for a single PES, which is called as diagonal Born-Oppenheimer corrections (DBOCs). There are methods which are widely used in high-accuracy quantum chemistry calculations where DBOC are computed [148–151]. For $i \neq j$, $F_{ij}(\vec{R})$ is the non-adiabatic coupling between states i and j, and it is a degree of variation of the wave function of electron with respect to the atomic coordinates and is dependent on the energy difference between state i and j [152].

$$\boldsymbol{F}_{ij}(\vec{R}) = \frac{\langle \psi_i^e(\vec{x}, \vec{R})|\boldsymbol{\nabla}_{\vec{R}}\hat{H}^e|\psi_j^e(\vec{x}, \vec{R})\rangle}{E_j^e - E_i^e} \tag{5.36}$$

Using Equation 5.33 and 5.35, and the relation

$$K = \left(\frac{\hbar}{i} \boldsymbol{\nabla}_{\vec{\boldsymbol{R}}} \cdot \boldsymbol{F}\right) + \boldsymbol{F}.\boldsymbol{F}, \tag{5.37}$$

the nuclear Schrodinger equation is written as

$$\left[-\frac{1}{2M}(\hbar^2 \boldsymbol{\nabla}_{\vec{\boldsymbol{R}}} + \boldsymbol{F})^2 + \boldsymbol{E^e}\right]\boldsymbol{\chi}(\vec{R}, t) = i\hbar \frac{\partial \boldsymbol{\chi}(\vec{R}, t)}{\partial t}. \tag{5.38}$$

Equation 5.38 has analogies with the gauge theories [153, 154]. Let us now discuss the possible approximations to solve Equation 5.38. By following the description by Worth et al. [155], we discuss these approximation and other aspects in greater details in next section.

5.7.1 Born-Oppenheimer approximation

Let us again rewrite Equation 5.30 into another form,

$$[\hat{T}^n \boldsymbol{I} + \boldsymbol{E^e}(\vec{R}) + \hat{\Lambda}]\boldsymbol{\chi}(\vec{R}, t) = i\hbar \frac{\partial \boldsymbol{\chi}(\vec{R}, t)}{\partial t}. \tag{5.39}$$

The above Schrodinger equation involves infinite but complete set of the adiabatic electronic states characterised by energies E_i^e (Equation 5.28). As we know from the nature of the nonadiabatic coupling (Equation 5.36) that only the couplings between the states that are close in energies are significant, the set of these electronic states can be truncated to include only these relevant states. This kind of approximation which includes only finite set $\{g\}$ of electronic states decoupling them from rest of the adiabatic states is know as group Born-Oppenheimer approximation of the full Schrodinger equation, which is

$$[\hat{T}^n \boldsymbol{I} + \boldsymbol{E^{e\{g\}}}(\vec{R}) + \hat{\Lambda}^{\{g\}}]\boldsymbol{\chi}(\vec{R}, t) = i\hbar \frac{\partial \boldsymbol{\chi^{\{g\}}}(\vec{R}, t)}{\partial t}. \tag{5.40}$$

Now, the size of $\hat{\Lambda}^{\{g\}}$ depends on the number of the electronic states included in the set $\{g\}$. The Born-Oppenheimer approximation is the limiting case of the group Born-Oppenheimer approximation where the number of these states reduces to one. Thus, under Born-Oppenheimer approximation, the complete wave function is represented by just a single product in the place of ansatz of Equation 5.29, i.e.,

$$\Psi(\vec{x}, \vec{R}) = \chi(\vec{R}, t)\boldsymbol{\psi^e}(\vec{x}, \vec{R}) \tag{5.41}$$

The resulting Schrodinger equation has only diagonal non-adiabatic coupling operator $\hat{\Lambda} = \hat{\Lambda}_{ii}$ where i is the state of the interest. According to Equation 5.41 and 5.33, the derivative coupling becomes $\hat{\Lambda}_{ii} = \frac{K_{ii}}{2M}$. Sometimes, Equation 5.39 with the wave function of the form 5.41 is referred as the adiabatic approximation. We do not refer this as the adiabatic approximation and reserve the name for another approximation.

If the non-adiabatic coupling matrix $\hat{\Lambda}$ is completely ignored, all of the E_i^e states become decoupled, and this is known as adiabatic approximation.

$$[\hat{T}^n \boldsymbol{I} + \boldsymbol{E^e}(\vec{R})]\boldsymbol{\chi}(\vec{R}, t) = i\hbar \frac{\partial \boldsymbol{\chi}(\vec{R}, t)}{\partial t} \tag{5.42}$$

Born and Oppenheimer used perturbation theory to justify the use the ansatz defined in Equation 5.41. The separability of the electronic and atomic motion is argued on the relation in Equation 5.33 where the large mass term in the denominator makes the non adiabatic coupling weaker. The lighter electron adapts instantaneously to the movement of the atoms. The slow nuclei remain almost frozen w.r.t. the electrons whereas the fast moving electrons create potential energy landscape for the nuclei. Hence, within the Born-Oppenheimer approximation, electrons and atoms can be treated independently and the total wave function of the system is a product of the electronic $\psi_i^e(\vec{x}, \vec{R})$ and the nuclear wave functions $\chi_i(R, t)$ for any state i.

The Born-Oppenheimer approximation is valid as long as the two energy surfaces are well separated from each other. Thus, the problem of finding the complete wave function is now separated into finding out the individual wave functions of the nuclei and electronic system. The solutions of the electronic part of the Schrodinger equation generate the potential energy surfaces (PES). These solutions give an energy for every fixed position of the nuclei. When the energy is plotted as a function of atomic configurations, it gives us potential energy surfaces as a $(3N)$ dimensional surface. Every electronic state has its own potential energy surface.

In the present thesis, we work under the Born-Oppenheimer approximation to study the relaxation dynamics of the excited manganite. The Born-Oppenheimer approximation holds in most of the situation but fails in the processes where the so called non-adiabatic effects dominate [156, 157]. The non-adiabatic processes are promoted by the close

proximity of the potential energy surfaces. An important example is the vicinity of the conical intersection where the approximation breaks down as a consequence of which the dynamics of the nuclear and electronic motion cannot be treated decoupled. Let us discuss the case of the conical intersection in more detail in the diabatic representation.

5.7.2   Conical intersection

The probability of a non-radiative transition between the states i and j depends on the derivative coupling F_{ij} (Equation 5.36) between them. It is clear from Equation 5.36 that this coupling is inversely proportional to the energy difference between the involved states. So, if the gap between the two states is smaller, the coupling is stronger. At there intersection, this difference is zero, and hence the coupling become infinite which leads to an efficient way of the non-radiative transition between two states. It is easier to understand the topology around such points if we move to the diabatic representation. In the diabatic representation, a unitary transformation of the adiabatic electronic wave functions of Equation 5.29 is performed at each point in the space. Conical intersections are interesting points that occur between adiabatic surfaces where often the avoided crossing is expected. In the subset of the two degrees of freedom in which the intersection of the potential energy surface occurs at a specific point, the two surfaces form a double cone [158–160]. Figure 5.1 shows a conical intersection described by a double cone geometry. At conical intersection, two direction Q_1 and Q_2 are distinguishable such that the potential energy function create a double cone in the vicinity of the degeneracy. The remaining $(n-2)$ subspace describe the surface of the crossing. The degeneracy is lifted away from the point of intersection in the (Q_1, Q_2) plane.

In the vicinity of the conical intersection, a small variation in atom positions results in a large change in the electronic wave function. The conical intersection plays a major role in the ultrafast radiationless processes as predicted by Teller in 1937 [161] and extremely important to understand the relaxation mechanism in the ultrafast pump-probe experiments that are indirect ways to detect these conical intersections [162–164].

In the present and the next chapter, we study the relaxation processes where the prime focus is on the transition through these conical intersections. In doing so, the non-adiabatic effects are ignored. There are several techniques developed to circumvent the failure of the Born-Oppenheimer approximation [165–170]. One of them is the widely recognised algorithm, Tully's fewest switches surface hopping (FSSH) where the nuclei evolve classically and their propagation along the adiabatic potential energy surface is subjected to the stochastic hops between potential energy surfaces [165]. To get a good insight into the role of non-adiabatic dynamics close to different conical intersections, techniques
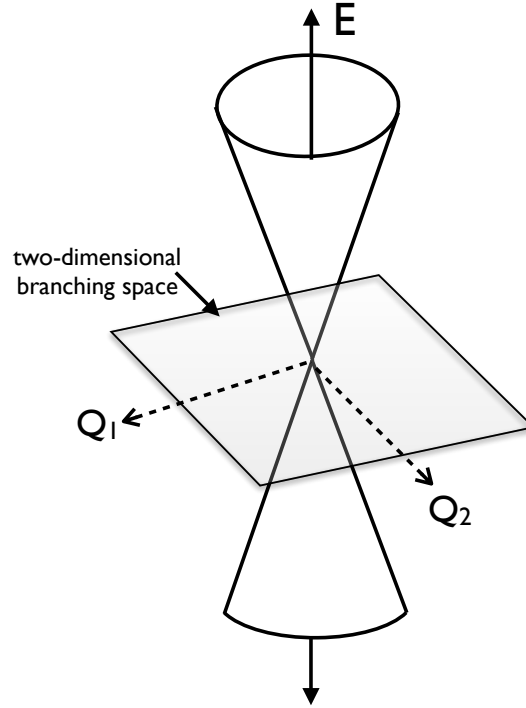
Figure 5.1: A double cone configuration describing a conical intersection

other than the Born-Oppenheimer approximation may be employed, the surface-hopping simulations being one among them [165]. In this thesis work, we do not employ any of these methods.

5.8   Energy carrier in one-dimensional system

We study the results of the optical pulse excitation, generation of charge carrier, such as spin-polaron (i.e., electron trapped in local ferromagnetic environment) and lattice-polaron (electron trapped in local atomic distortion, also referred as just 'polaron'), etc., and dynamics of these carriers in the context of the one-dimensional system. Furthermore, the role of spin and atomic degrees of freedom in relaxation of the excited system will be examined.

Firstly, we implement the Peierls substitution technique, described in Section 5.5, to study the optical excitation process. Secondly, the numerical solution of the time-dependent Schrodinger equation (described in Appendix C) is used to describe the evolution of one-particle wave functions for the e_g electrons, and the two-dimensional spinor for the t_{2g} spins while the atoms are treated classically and their corresponding Newton equations (Section 2.5) of motion is used. Table 5.1 summarises the parameters used in the study of the dynamics in the one-dimensional system.

Δ_t=0.040 a.u.	$M_R = 29164$ a.u.	M_{lc}=8.0 × 10^{10} a.u
k-points=1	$N_{sites} = 16$ (for x=0.5)	A'_o=0.01, 0.02
	$N_{sites} = 60$ (for single electron)	0.03 a.u.
c_w= 200 fs.	Polarisation direction ($\vec{A}$)= x	Breathing mode (Q_1) = No

Table 5.1: Parameters used to study the relaxation dynamics of one-dimensional chain. The symbols are defined Section 2.5.2 and all other necessary parameters are given in Table 2.2

5.9 Optical absorption

We consider two cases: a single electron and a dimerised phase at $x = 0.5$ in the one-dimensional chain (see Chapter 3). The calculations are performed on the 60-site one-dimensional unit cell that consists of corner-connected O-octahedra. The single electron in this unit cell settles down into a bonding state of a trimer. The density of the states projected on the three sites of the trimer is shown in Figure 5.2 (a) together with the nature of the states and the possible transitions. When the system is exposed to an external electromagnetic field, it shows optical absorption due to the excitation of an electron of the trimer from the low-lying bonding state of the trimer to the respective upper empty non-bonding as shown in side schematic of Figure 5.2.

Similarly, the dimerised system at $x = 0.5$ being in a Zener polaronic state, discussed in Chapter 3, shows optical absorption due to the excitation of the electrons from the bonding state of a dimer (Zener polaron) to the corresponding anti-bonding states. The density of states projected within the two sites of the dimer and the nature of the states are shown in Figure 5.2 (b). There is no transition from the bonding state to the π-states as theses π-states are orthogonal to the direction of the chain.

5.9.1 Single electron dynamics: Light cone behaviour

When an one-dimensional system with just a single electron in it is excited, a characteristic light-cone dynamics of the localised excitation is observed. Figure 5.3 shows the charge density dynamics for $t < 100$ fs. Once the electron is excited from the bonding of the trimer to the corresponding non-bonding states, the corner and central sites of the trimer become polarised triggering charge oscillations within the trimer. The charge oscillations has a characteristic frequency in the range $\sim 130 - 150$ THz (Figure 5.3) and last for $\sim 80\,fs$ for the intermediate intensity-field (i.e., for $A_o = 0.02$ case as shown in Figure 5.3). Its clear from Figure 5.3 that the frequency of this oscillations does not depend on the intensity of the external field. During this time ($t < 80\,fs$), the charge densities at the two corner sites of the trimer oscillate out of phase to each other. In the
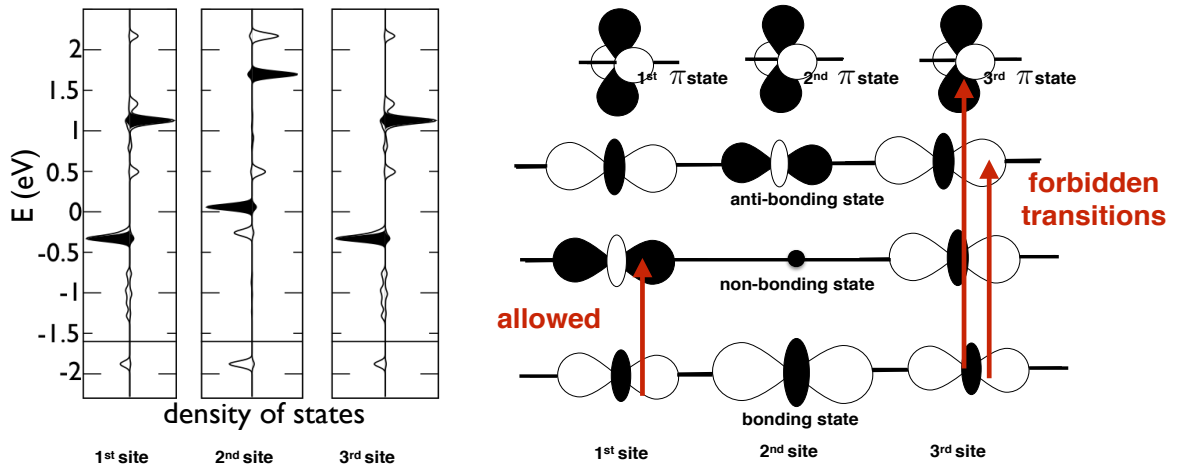
(a) Density of states of a single electron projected on the trimer sites (left) and nature of the bonding, non-bonding, anti-bonding and π states in case of single electron (right)
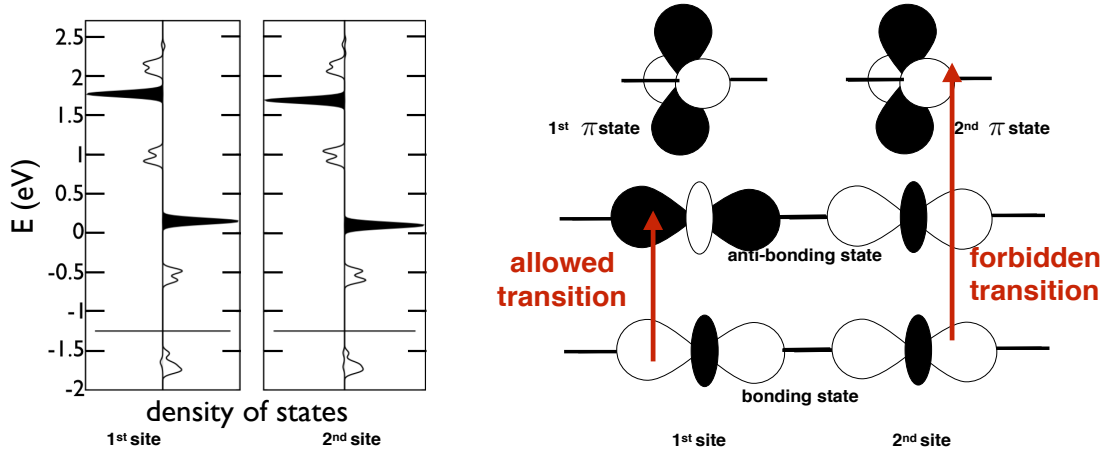
(b) Density of states of a electron in the zener polaron projected on two sites of the dimer (left) and nature of the bonding, non-bonding and π states in case of electron in zener polaron (right)

Figure 5.2: Density of states and possible transitions for a single electron system (a) and zener polaron system at $x = 0.5$ (b). The filled states shows the π states orthogonal to the direction of the chain. The black and white in the electron states shows opposite phases of the wave functions (c,d).

systems with nearest-neighbour interactions, these excitations in the form of quasiparticles are expected to spread out from their initial position, i.e., the initial trimer position in our case, within light like cones.

The light cone behaviour can be recognised by the charge densities spreading out to nearby sites from Figure 5.4. The nature of evolution of the light-cone can be ballistic or diffusive. While the scattering length or the mean-free path of the carrier in the ballistic evolution is of the same order of magnitude as that of the sample size, the carrier is repeatedly scattered in the diffusive evolution. Thus, the former is a feature of a freely propagating excitation in the non-interacting environment and the latter is for the scattering-induced propagation in the presence of interactions. We try to fit the
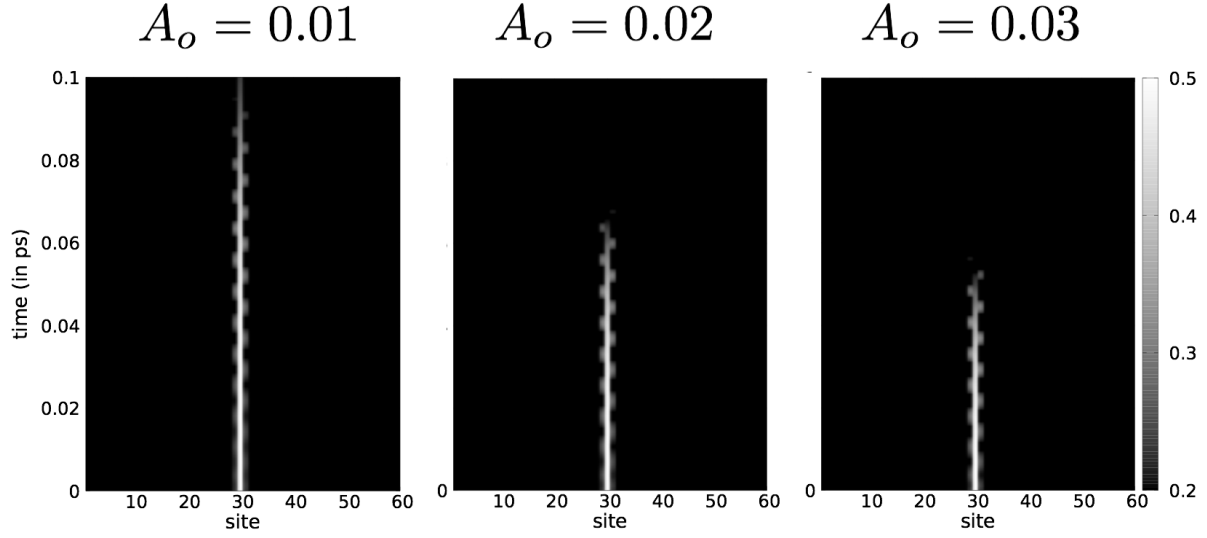
Figure 5.3: Dynamics of a single electron in one-dimensional chain for three different initial intensity of the excitations on shorter timescale (0-0.1 ps). As the electron excite from the bonding to the non-bonding state of the trimer, a charge transfer takes place from corner to corner sites of the trimer. The polarisation between the corner and central sites of the trimer result in dipole oscillations with the trimer. the charge density on two corners of the sites of trimer is oscillating out of phase from each other. While the frequency of the charge oscillation does not depend on the intensity of the external field, the amplitude of the charge oscillation strongly depend on field intensity. Higher the field intensity, the larger is the amplitude of oscillations.

present motion with the ballistic model. We get the characteristic velocity $\sim 75 \times 10^3$ m/s. This velocity in real material is related to the longitudinal velocity of sound which range between $5000 - 7000$ m/s in manganites [171, 172]. As our model is a one-dimensional model, the direct analogy of the obtained speed is difficult to make.

It is to be noted from Figure 5.5 that the light cone behaviour exists for $t < 0.50$ ps. As the excited electron goes into the non-bonding state of the trimer, the increased charge densities at the corner sites of this trimer initiate structural dynamics at these sites. The Q_3 modes at the corner sites of the trimer start increasing and the same at the central site of the trimer decreases. The oscillations of the O atoms around the corner sites also alter the nearby octahedra due to the cooperative effect spreading the structural disturbance around the trimer sites out to other sites along the chain. The coupling between the electron and phononic system is clearly visible in Figure 5.5 which shows the Q_3 mode following the charge density.

The initial excitation localised on the corner sites of the trimer spreads outward to other sites. Due to the periodic boundary conditions, the light cones travelling in the opposite directions interfere with each other near the corner sites of the chain forming standing waves at these sites, as shown in Figure 5.4 between 0.15-0.22 ps on the corner of the chain.
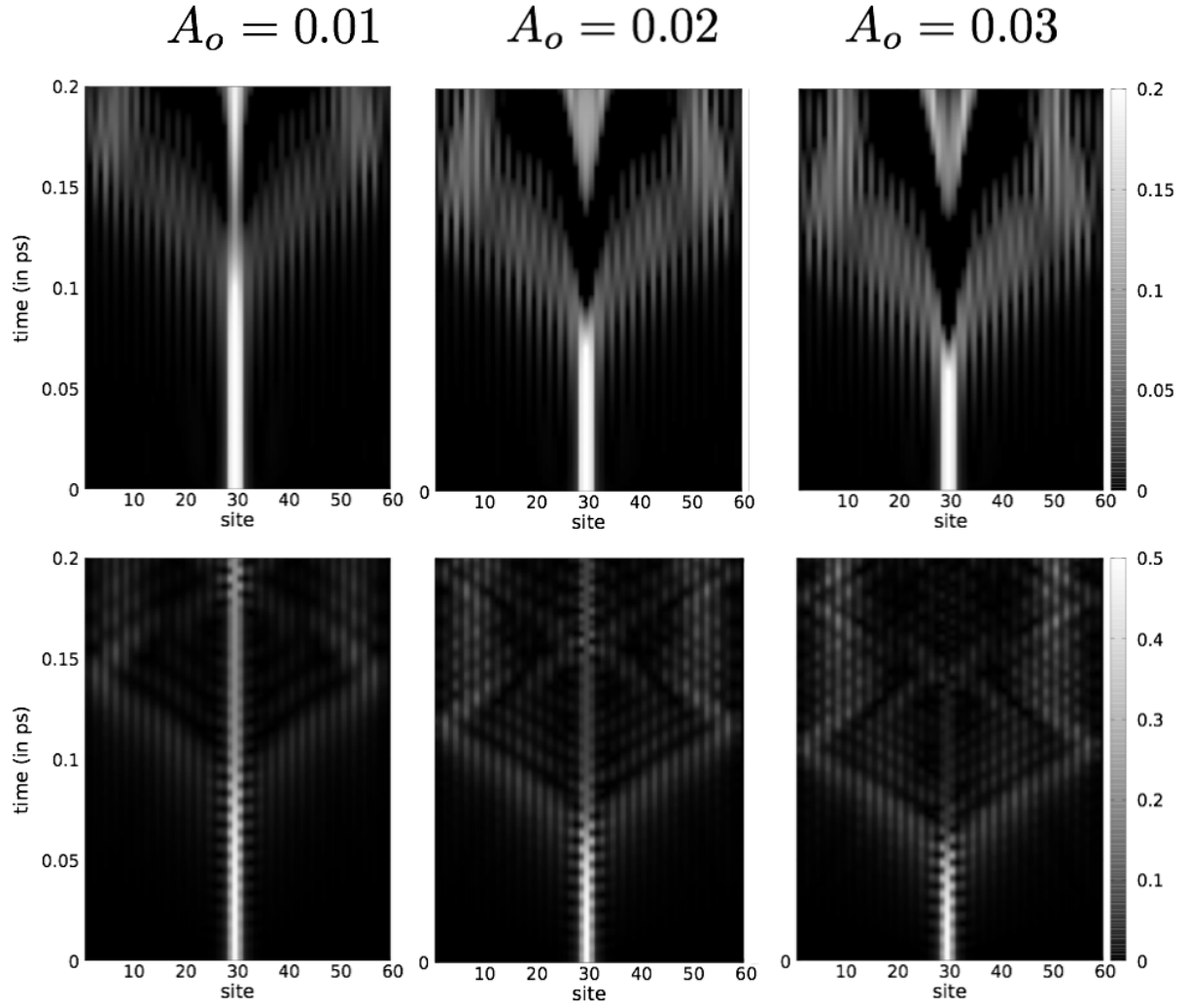
Figure 5.4: Dynamics of single electron in one-dimensional system on shorter timescale (0-0.2 ps). Bottom- dynamics of charge density on individual sites. In all of three cases, the excitation spread to other sites of the chain by forming a light cone in all the three cases. In low-intensity excitations, the electron mainly remain in the ground state which is evident from the charge density present on the initial sites of the trimer. In the high-intensity excitations, this charge density of the electron in the ground state completely vanishes and the dynamics can be purely regarded as the evolution of the of the excitations in the form of light cones. Top- dynamics of the Q_3 mode on individual sites. The atomic structure acts slowly (at 60 fs) and follows the charge and facilitate the spreading of the excitation to other sites.

The nature of the excitation is preserved while spreading out from the initial trimer sites. During the light-cone spreading, the charge separation process leads to the localisation of charge on a few sites. It can be seen in Figure 5.6 that the charge localises around the initial trimer sites at $t \sim 0.6$ ps. At the same time, there is also a weak localisation of charges over few sites (visible in Figure 5.6) that is around five lattice sites away from the initial trimer sites. The charge localisation instigates the spins at these sites forming of the polaron of same nature, i.e., the trimer polaron, which we start with. Now onwards, the relaxation dynamics is dominated by thermally-activated polaron hopping
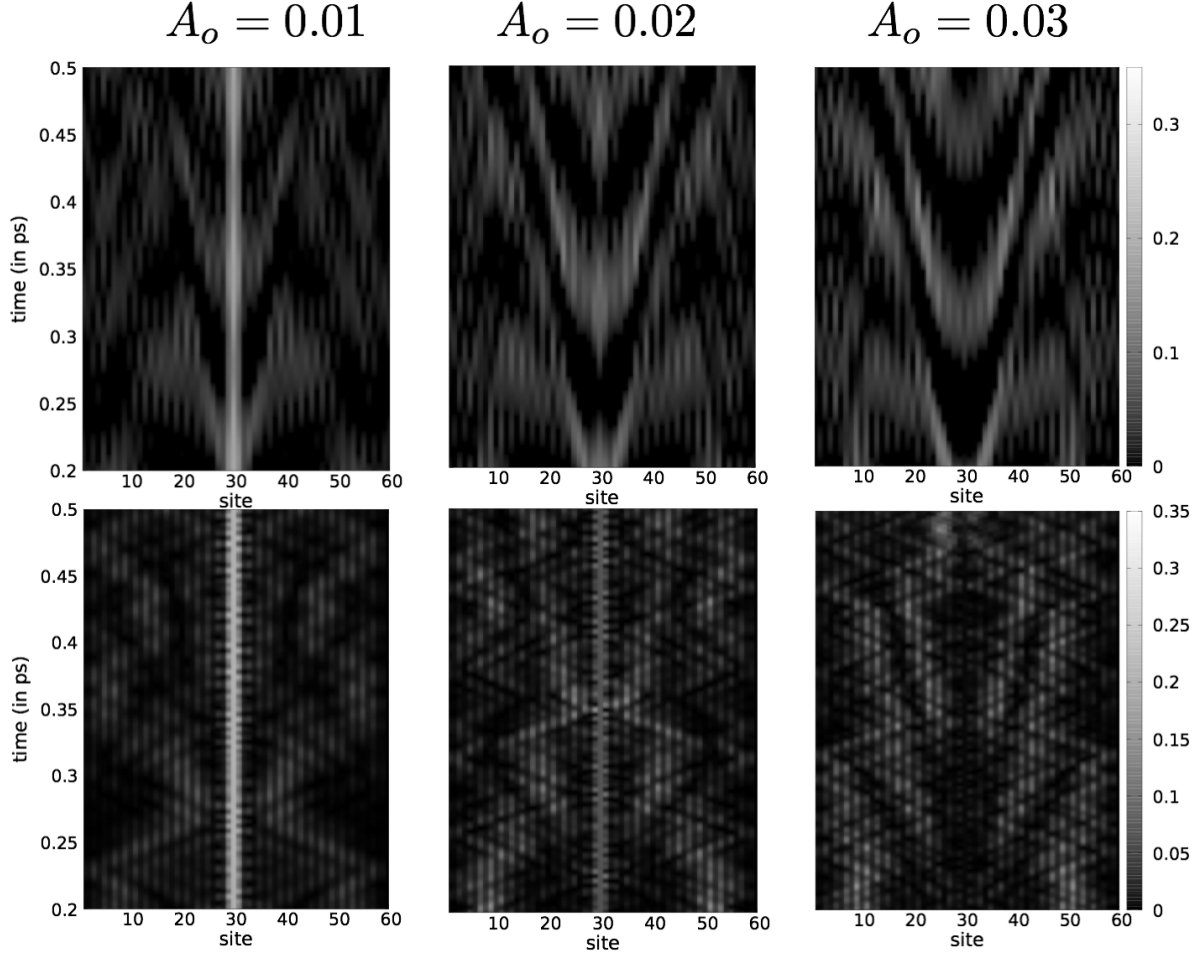
Figure 5.5: Relaxation of single electron system for three different initial intensity of the excitations on shorter timescale (0-0.5 ps). Bottom- dynamics of charge density on individual sites. Due to periodic boundary conditions, the light cone travelling in different directions meet at the corner sites and hence, we see standing wave of charge density on these sites (for example, on the edges between $0.05 - 0.2$ ps). For the low and intermediate intensities ($A_o = 0.01$ and $A_o = 0.02$), the charge density on the initial sites of the trimer is due to the ground state electrons. In high-intensity case, the ground state become completely empty and no charge density is observed on the initial sites of the trimer. Top- dynamics of the Q_3 mode on individual sites. The Q_3 mode follows the charge density.

which initiates at $t \sim 0.60$ ps (Figure 5.6)

5.9.2   Small polaron hopping: Brownian motion

From $t > 0.60$ ps onwards, the spin-lattice assisted thermally-activated polaron hopping is the dominating process. The t_{2g} spins of the polaron and nearby sites continuously rotate aligning themselves almost ferromagnetically to facilitate the electron to delocalise over these nearby pair of sites. Similarly, the atomic distortion associated with the polaron sites also penetrates to these nearby sites lowering the energy barrier of the polaron hopping. Figure 5.6 shows the response of the charge density, spin angles and Q_3 modes
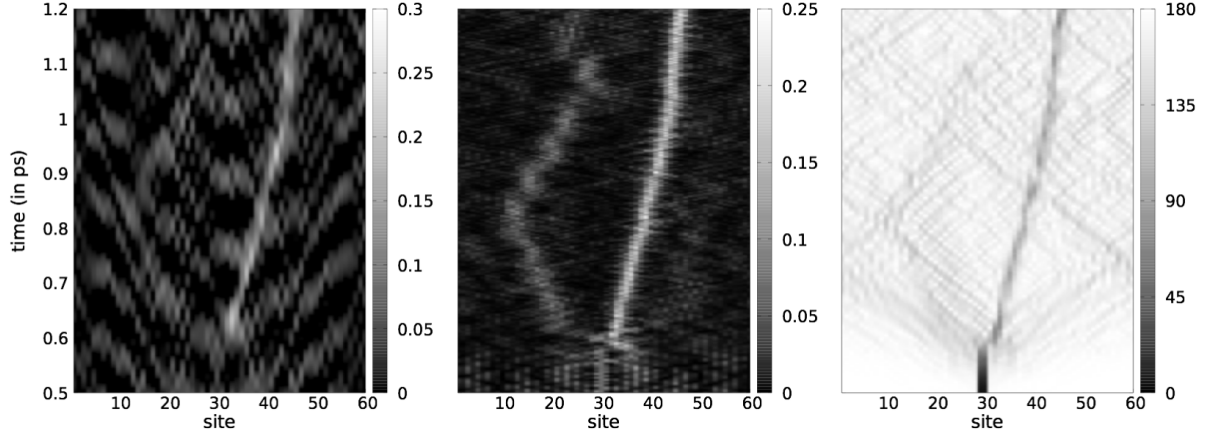
Figure 5.6: Single electron relaxation on longer timescale (0-1.25 ps). Dynamics of charge density (Middle), Q_3 mode (Left), and inter-site spin angle (Right). Once the charge get localised within few sites at $t \sim 0.6$ ps, it forms a small polaron at these sites. Now onwards, a random motion of polaron is observed. The Q_3 mode follows the charge-density. The spins are anti-ferromagnetically arranged across the entire chain except the initial position of trimer. The localisation of the charge alters the t_{2g} spins of the sites forming ferromagnetic atmosphere at the charge-rich sites. Now the t_{2g} spins remain strongly coupled to the electron and create a continuous ferromagnetic environment for the polaron to propagate through the Brownian motion.

at individual sites for the one-dimensional system with a single electron in it on the larger timescale.

We can understand the above polaron motion in the context of random motion, i.e., the Brownian motion of charge transport. The probability of polaron hopping in the thermally-activated process is proportional to $e^{-\beta \Delta E}$ where ΔE is the energy difference between the initial and final states of the involved polaron while β is a constant that depends on the temperature [173]. In the present case, ΔE depends on various factors, such as spin and atomic configurations of the nearby sites w.r.t. the polaron sites. This lattice and the spin facilitated charge carrier propagates throughout the chain. We track the dynamics over a few pico seconds during which this random hopping remains the most important process. The process of polaron hopping persists at least up to $t \sim 12$ ps which is the total time of the dynamics that we tracked in our study. The decay of this polaron hopping process is suppressed as we do not employ any dissipative channel in our present model.

5.10 Zener polaron

The one-dimensional chain at $x = 0.5$ shows dimerisation where the electrons are confined over the bonding state of the ferromagnetically coupled sites of the dimer. The system shows strong absorption at ~ 1.5 eV due to the excitation of the electrons from the

bonding states to the anti-bonding states of the dimer as shown in Figure 5.2. In the next sections, we consider two cases: the low-intensity excitation and the high-intensity excitation at this $x = 0.5$ doping.
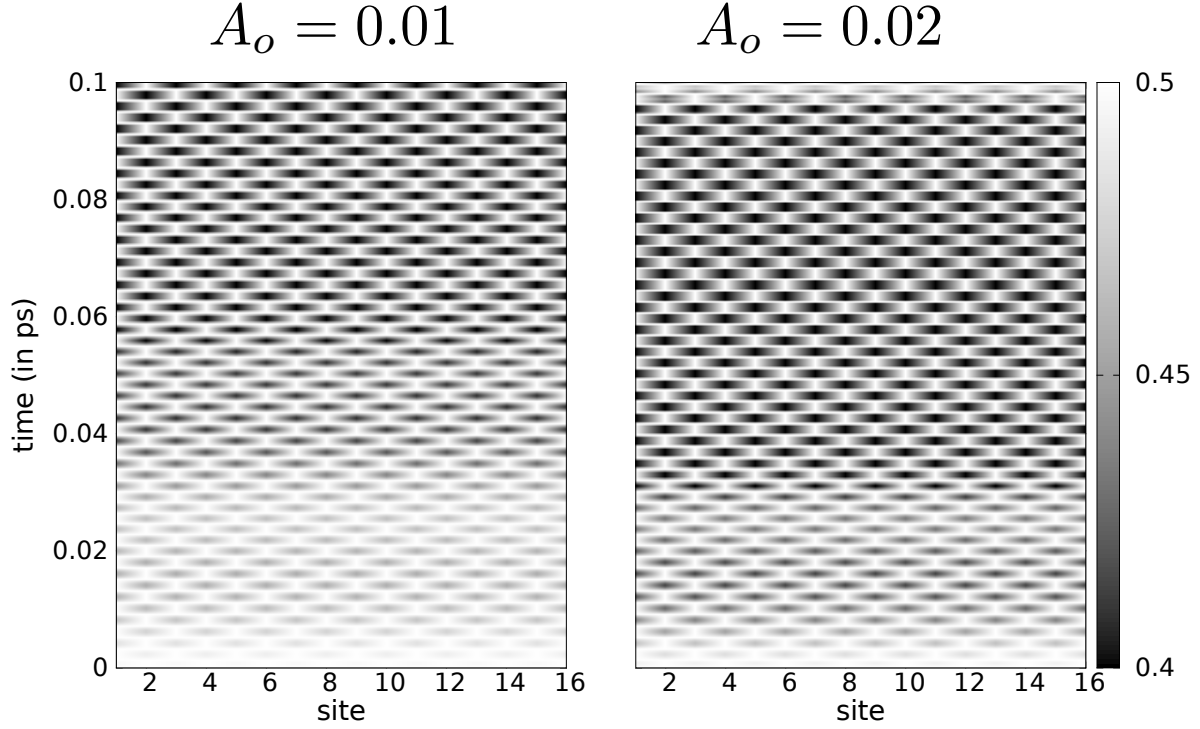
Figure 5.7: Dynamics of charge density on shorter timescale $t = 0 - 0.1$ ps at $x = 0.5$ for low (Left) and high-intensity (Right) excitations. The excited anti-bonding states that are equally spread on two sites within the dimer is highly unstable charge oscillations within each dimer are observed. The amplitude of the charge oscillation depends on the intensity of the external field. Higher the intensity, the larger is the the amplitude of the charge oscillations.

5.10.1   Low intensity excitation

In the dimerised phase at $x = 0.5$, the polarons are confined to their initial sites even after the excitation as the atomic structure is weakly perturbed in the low-intensity excitations. Figure 5.7 shows the initial charge dynamics during the excitation process ($t \sim 0 - 0.1$ ps). As the symmetry of the bonding and anti-bonding states of the dimer (i.e., Zener polaron) is different, charge oscillations within each dimer are observed (Figure 5.7) that instigate the atomic oscillations on the dimer sites also. These charge oscillations on the individual sites of dimer are out of phase. The amplitude of the charge oscillations depends on the field strength. Higher the intensity of the excitation, the larger is the amplitude of the corresponding charge densities within dimer sites. Figure 5.8 shows the response of the charge density, spin angles and Q_3 phonon mode at individual sites of the 16-site one-dimensional chain in the dimerised phase on longer timescale $t \sim 0.5 - 1.2$ ps.
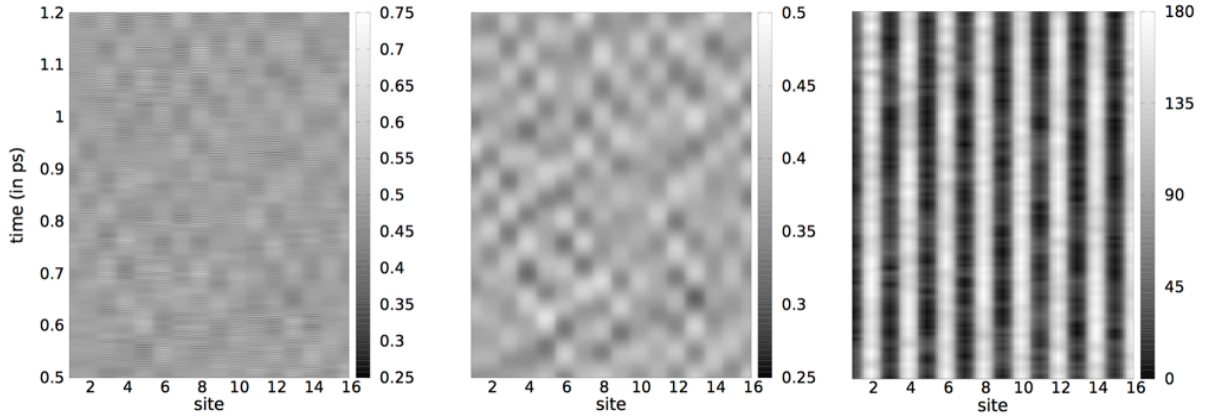
Figure 5.8: Low intensity excitation. Dynamics of charge density (Left), Q_3 mode (Middle) and spin angle (Right) at individual sites at $x = 0.5$ on longer timescale (0.5-1.2 ps). The electron in the anti-bonding state shows the tendency to localise on one of the site in the trimer. As the population of the anti-bonding state is not high enough to strongly perturb the atomic and spin structure of the system, the excitation remain confined to the respective dimers. The occupied majority states of a dimer interacts with the empty minority states of the nearby dimer. This interaction is very weak as the nearby dimers are anti-ferromagnetically coupled to each others.

As two nearby dimers are anti-ferromagnetically coupled, they interact very slowly and weakly. This interaction of nearby dimers is due to the coupling of the occupied majority states of a Zener polaron with the empty minority state of the nearby Zener polaron anti-ferromagnetically coupled to the former. This interaction is assisted through a slow rotation of the respective t_{2g} spins as shown in Figure 5.8. The interaction between Zener polarons depends on the J_{AF} coupling. Smaller the J_{AF}, the larger is the the interaction. In the Figure 5.8, it is clearly seen that the perturbation of the spin and atomic structure is not large enough to facilitate the electron to relax to ground state by localising on one of the site of the dimer

5.10.2 High intensity excitation: Population inversion and formation of JT polarons

To study the effect of the intensity of the electromagnetic field on the relaxation process, we study the Zener polaronic phase at $x = 0.5$ again under high-intensity external field. Higher the intensity of the light field, the larger is the occupancy of the anti-bonding states of the dimer. In the high excitation field, the system may undergo population inversion where the occupancy of the anti-bonding states of a dimer is higher than that of the corresponding bonding state. Here, we consider this case of the population inversion. The response of the charge, Q_3 mode and spin degrees of freedom is shown in Figure 5.9. For such a strong initial perturbation in the electronic system, the Q_3 phonon modes and t_{2g} spins react very quickly at $t \sim 0.35$ ps, see Figure 5.9, making the sites within the

dimer highly polarised with respect to each other. The frequency of the charge density and phonon mode oscillations is higher in comparison to the low-intensity excitation case, discussed in previous section.
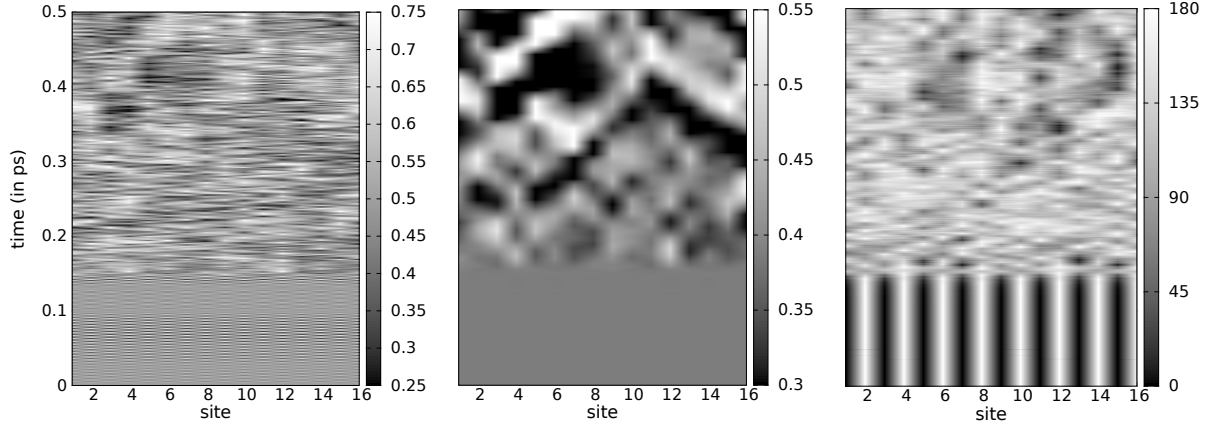
Figure 5.9: High-intensity excitation: dynamics of electron density (Left), Q_3 mode (Middle) and spin angle (Right) at individual sites at $x = 0.5$. Left- Intially, the charge density is equal at each site in the dimerised phase. The population of the anti-bonding states of individual Zener polaron go on increasing until a population inversion situation is encountered. Middle- once the population of anti-bonding states become larger than the bonding-states, the electronic structure become highly-unstable. The electrons start localising on individual site by forming JT polaron. Right- the charge localisation on individual sites of dimer is facilitated by the anti-ferromagnetic alignment of the t_{2g} spins. Thereafter, the relaxation process is dominated by the dynamics of the JT polarons.

Strong dipole oscillations for sites within dimer are observed; see Figure 5.7 (left).

The electrons in the anti-bondings states of the dimers have the tendency to localise over individual sites of the corresponding dimers. The t_{2g} spins being faster degree of freedom react quickly to these dipole oscillations allowing the relaxation of the system through conical intersection as the configuration of the t_{2g} spins within the dimers turns anti-ferromagnetic instantaneously. After the conical intersection, the electrons get trapped into individual sites of the respective dimers lowering overall energy of the system. These newly trapped electrons in the octahedral distortion of the individual sites that are anti-ferromagnetically coupled to each others is nothing but 'JT polarons'. Now these JT polarons randomly hop from one site to other when the configuration of the t_{2g} spins between these sites turns weakly parallel.

5.11   Summary

In this chapter, we observed clear features of spreading of the excitations within light-like cones in the case of a single electron in the one-dimensional system on shorter timescale just after excitation. Furthermore, the small polaron hopping is the dominating process

on larger timescale. In the case of the Zener polaron system, a different kind of relaxation dynamics is observed that depends on the kind of excitations. While the Zener polaron remains the quasiparticle in weak excitation limit that happens to have long lifetime, the formation of JT polarons through spin assisted conical intersection and the subsequent polaron hopping constitute a major part of the relaxation mechanism in the high-intensity excitations. In next chapter, we focus on the excitation and relaxation mechanism in real three dimensional systems.

Chapter 6

Optical excitation and relaxation in three-dimensional system

In this chapter, we study the detailed optical excitation and subsequent relaxation dynamics in the real three-dimensional manganite by mean of the ab-initio molecular dynamics. We use the time-dependent Schrodinger equation for spins and electronic system, as discussed in previous chapter. The dynamical information of the electronic, lattice and spin part of the system is monitored to show the overall microstructure evolution. Moreover, the nature of the charge carrier and the long lived transient states (metastable states) formed during dynamics is analysed in detail. Firstly, we study the excitation and subsequent relaxation process that involve the transition from the CE-type phase of half doping, where the charge ordered state with the CE-type magnetic order convert to a state without any charge ordering at low temperature. Secondly, we study the effect of the intensity of external light pulse on the relaxation processes.

6.1   Inclusion of strain wave propagation

It is necessary that our present model adopted for studying the relaxation dynamics, discussed in Chapter 2, must have the flexibility that allows compression and expansion of the system in certain directions. This kind flexibility in turn permits the propagation of a large-wavelength acoustic phonon modes that are responsible for strain effects in manganite [174, 175]. This effect is included in our present tight-binding model by considering the lattice constants, i.e., a, b and c of Equation 2.1 as dynamical variable instead of mere constants. These lattice constant variables have their own equation of motion like the other degrees of freedom. The mass of the lattice variable, M_{lc}, is determined by fixing the resulting frequency of acoustic wave approximately equal to the frequency of the strain wave ~ 25 GHz observed experimentally in manganites. We assume the direction of propagation of the strain wave be c and use the $CaMnO_3$ system to fix the mass M_{lc}. Table 6.1 summarises the parameters that are used for study in the present chapter.

Δ_t=0.040 a.u.	$M_R = 29164$ a.u.	M_{lc}=8.0 × 10^{10} a.u
k-grid=1 × 1 × 1	c_w= 200 fs.	unit cell = 8 × 8 × 4
A'_o=0.05, 0.04, 0.03 and 0.015 a.u.	Polarisation direction ($\vec{A}$ vector) $\frac{x+y}{\sqrt{2}}$	doping $(x) = 0.5$

Table 6.1: The symbols are defined Section 2.5.2 and all other necessary parameters are given in Table 2.2

Before going into the result sections, we first discuss the CE-type structure at $x = 0.5$ in greater details (already discussed in Section 5.7). Here, we mainly focus on the construction of the set of the Wannier states which can be used to describe this CE-type structure and, then this set of Wannier states is used to study the subsequent dynamics after excitation.

6.2   Initial structure: CE-type phase

We choose the half-doped CE structure with the unit cell size of 8 × 8 × 4 size as the initial system to study the dynamics. As described in Section 5.7 of Chapter 5, the zig-zag fashioned ferromagnetic chains arranged in the xy planes that are anti-ferromagnetically coupled to each other in the z direction in the CE-type phase. The three-site x or y segment of the zig-zag chain forms a trimer of parallel spin sites. The resulting electronic structure of the trimer oriented in the x direction can be described by the Wannier states [15] such that the filled state $|w_1\rangle$ is expressed as:

$$|w_1\rangle = |c, ax\rangle \cos(\alpha) + (|l\rangle + |r\rangle)\frac{\sin(\alpha)}{\sqrt{2}} \tag{6.1}$$

Here, $|c, ax\rangle$ is the axial $d_{3x^2-r^2}$-type orbital, which is localised over the M^c central site. $|l\rangle$ and $|r\rangle$ are the orbital on M^e corner sites on left and right side of the M^c central site, respectively, as shown in Figure 6.1. The $|l\rangle$ and $|r\rangle$ orbitals on M^e sites are pointing towards M^c site, i.e., in the x direction. The $|l\rangle$ and $|r\rangle$ can be written as a linear combination of two e$_g$ orbitals on left and right side as follows:

$$|l\rangle = (|l, d_{3z^2-r^2}\rangle + |l, d_{3x^2-y^2}\rangle)\frac{1}{\sqrt{2}} \tag{6.2}$$

$$|r\rangle = (|r, d_{3z^2-r^2}\rangle + |r, d_{3x^2-y^2}\rangle)\frac{1}{\sqrt{2}} \tag{6.3}$$

(a) **Total Density of state projected on the four Wannier states**

(b) **Four Wannier states corresponding to a single trimer**
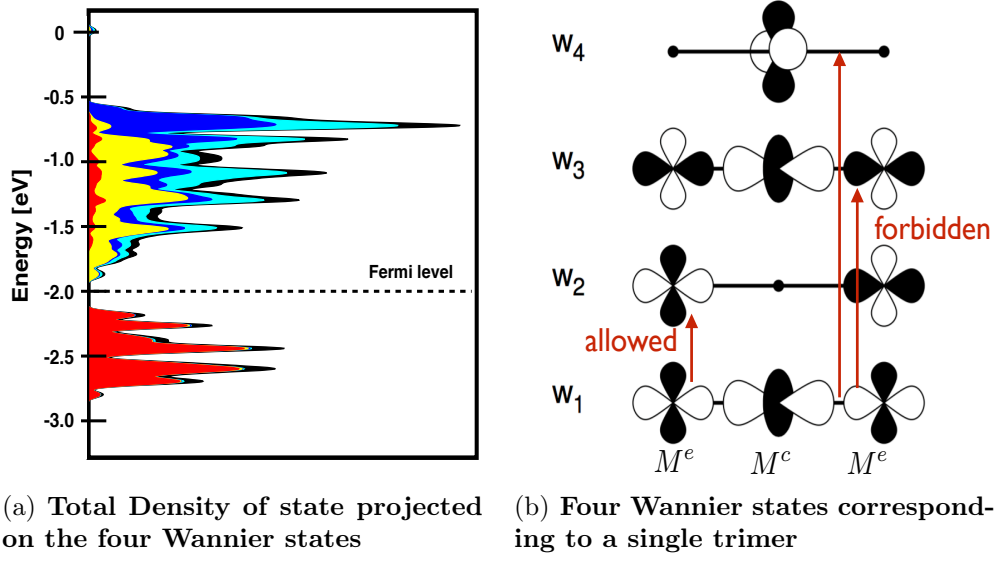
Figure 6.1: Density of states of the CE-type structure at $x = 0.5$ (a) projected on to the four Wannier states (b). (a) contribution from $|w_1\rangle$ shown in red, $|w_2\rangle$ in yellow, $|w_3\rangle$ in blue and $|w_4\rangle$ in cyan. (b) The four Wannier states involving three sites of a trimer: a central M^c site and two corner M^e. The density of states (x axis) versus energy (y axis) shows the low lying occupied state correspond to $|w_1\rangle$ state. The states just above The Fermi level are non-bonding in nature $|w_2\rangle$. Above these two state are the orthogonal $|w_4\rangle$ states localised on the central sites of the trimer. The $|w_3\rangle$ states lie above all of the states are of anti-bonding nature. Th electron from the ground state can excite to only the non-bonding state as other transitions are forbidden.

Now the corresponding upper lying $|w_2\rangle$ non-bonding state and the $|w_3\rangle$ anti-bonding state orthogonal to the $|w_1\rangle$ bonding state are as follows:

$$|w_2\rangle \;=\; (|l\rangle - |r\rangle)\frac{1}{\sqrt{2}} \tag{6.4}$$

$$|w_3\rangle \;=\; |c, ax\rangle \sin(\alpha) - (|l\rangle + |r\rangle)\frac{\cos(\alpha)}{\sqrt{2}} \tag{6.5}$$

$$\tag{6.6}$$

The $|eq\rangle$ equatorial orbital localised on the M^c site of the trimer oriented in the x direction (see Figure 6.2),

$$|w_4\rangle \;=\; |eq\rangle, \tag{6.7}$$

is $d_{z^2-y^2}$-type, orthogonal to the low-lying states $|w_1\rangle$, $|w_2\rangle$ and $|w_3\rangle$.

Similarly, the Wannier states for the trimer oriented along the y direction can be expressed by replacing the sign of the $d_{x^2-y^2}$-type state in equations (6.3) and (6.3).

The Wannier states defined in Equation 6.1-6.7 (i.e., $|w_1\rangle$, $|w_2\rangle$, $|w_3\rangle$ and $|w_4\rangle$) form a complete set of basis states to understand the electronic structure of the CE-type phase.

An one-particle electron state in the CE zig-zag chain can be expressed by a linear combination of the this basis states. The density of states of the the CE-type structure at $x = 0.5$ obtained by our model projected on the above Wannier functions is shown in Figure 6.1 with the corresponding Wannier states. Clearly, the occupied states are mainly $|w_1\rangle$-type (red) and the lowest unoccupied states above the Fermi level are mostly $|w_2\rangle$ states (red). $|w_3\rangle$ (blue) and $|w_4\rangle$ (cyan) states energetically remain above them where the former state lies higher in energy than the latter. The charge on the corner M^e and central M^c site is $0.5 \pm \Delta$, where $\Delta = 0.25$ is the charge disproportion. Experimentally, it has been verified for a long time [34] that the charge ordering in the xy CE plane stacks along the z-axis rather than being shifted by one lattice point from one plane to the next. This kind of charge stacking can also be verified by our CE-type results [15].

6.3   Excitation process: optical absorption

The photo-excitation in manganites can occur through both d-d and p-d kind transitions in the spectral energy range ~ 0.5-2.3 eV [15, 176–179]. While the d-d kind transitions are transitions between the 3d states of Mn atom, the p-d transitions are between O-2p states and the Mn-d states [180, 181]. The strength of these transitions depend on various factor. Primarily, it depends on the densities of the initial and final states, and the transition probabilities between them. The transitions observed experimentally in the optical energy spectrum centred around ~ 0.5-0.75 eV mainly consist of the dipole allowed transition from the occupied e_g state, below the Fermi level, to higher e_g states, see Figure 6.1. The charge transfer p-d kind transitions are dominating in the higher energy range [15, 176–179]. The study of the p-d kind transitions requires an explicit inclusion of O-2p states that we down-fold in our present model.

Any occupied e_g state $|w_o\rangle$ of the CE-structure at any given time during dynamics can be expanded in the complete basis set of the orthogonal Wannier states, i.e., $|w_1\rangle$, $|w_2\rangle$, $|w_3\rangle$ and $|w_4\rangle$ (Section 6.2) as follows:

$$|w_o\rangle = \sum_m c_{w_m} |w_m\rangle \tag{6.8}$$

Here $m = 1, 2...4$

Figure 6.1 shows the allowed and forbidden transitions in the CE-type system at $x = 0.5$ on the symmetry basis with the help of the Wannier states. The wide absorption band (Figure 6.2) in our calculations is due to strong dipole allowed transition from filled the bonding $|w_1\rangle$ state to the non-bonding $|w_2\rangle$ state of the trimer segment of the CE chain as shown in 6.1. Other transitions, such as $|w_1\rangle \rightarrow |w_3\rangle$ and $|w_1\rangle \rightarrow |w_4\rangle$, are dipole forbidden. The $|w_1\rangle \rightarrow |w_2\rangle$ transition occurs as a result of charge transfer from the M^c central to M^c corner site of the trimer of the zig-zag CE chain. The band gap across which the $|w_1\rangle \rightarrow |w_2\rangle$ transition occurs develops due to JT distortion as well as hybridisation of the e_g orbitals of three sites of the trimer which shifts the resulting bonding state lower.
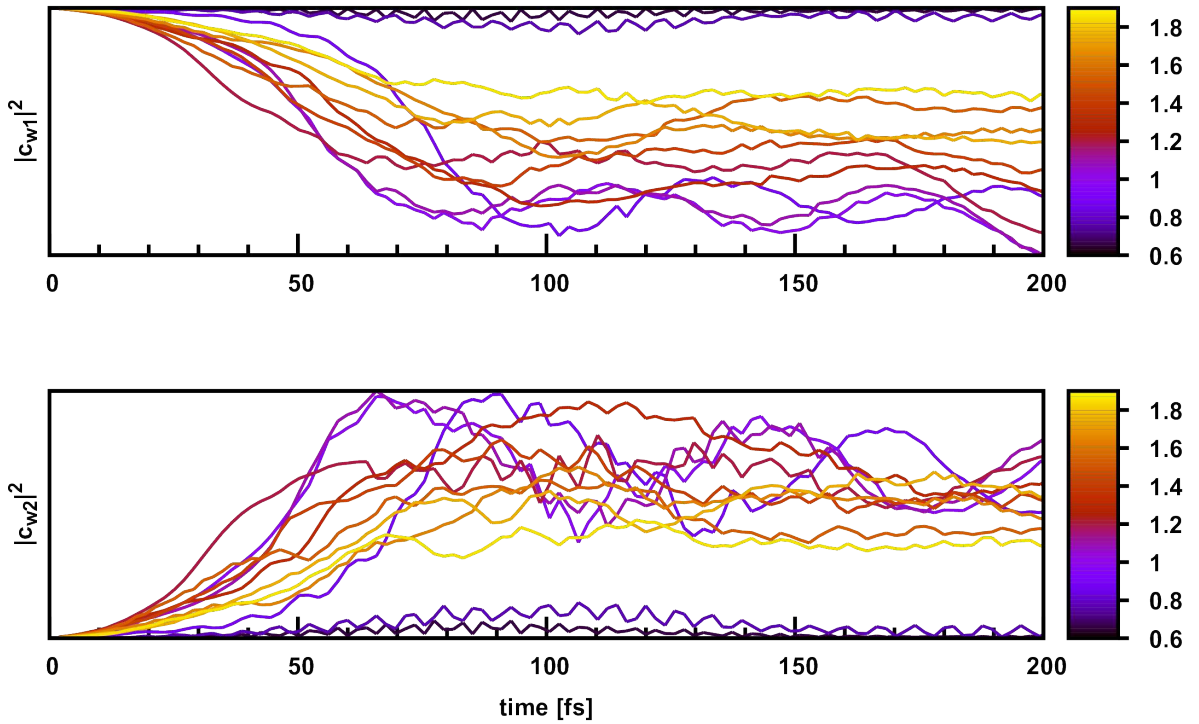
Figure 6.2: Propagation of $|c_{w_2}|^2$ and $|c_{w_1}|^2$ values summed over all the trimers of the unit cell indicating the contribution towards $|w_o\rangle$ occupied state from the $|w_2\rangle$ (solid lines) and $|w_1\rangle$ (dashed lines), respectively. Wannier states as a function of energy of the light pulse. The energy values of the colorbox on the right are in eV. The system shows absorption for wide range of photon energies which are in the range $0.80 - 1.80$ eV. The maximum absorption by the system in external light pulse take place around around 0.96 eV.

We study the excitation process in the CE-type system as a function of the energy ($h\nu$) of the light pulse. $t = 0 - 200$ fs is the duration of the pulse after which the light pulse is switched off. This is the duration of the ultrafast laser pulse used in the referred experiment [101].

Figure 6.2 shows the energy ($h\nu$) dependence of the propagation of the projections of the occupied states on the four Wannier states (Section 6.2) during the entire excitation

process period. Clearly, the CE-type structure shows optical absorption in a large energy spectrum.

It is clear from the energy $h\nu$ dependence that the absorption can occur in wide energy spectrum ranging from 0.80-1.80 eV. A maximum of absorption peak corresponds to 0.96 eV energy. The experiments attribute this broad absorption peak in the absorption spectra to a transition between Jahn-Teller split Mn-d e_g states, either occurring as an intra-site or as an inter-site transition between Mn^{3+} and Mn^{4+} sites [15, 176–179].
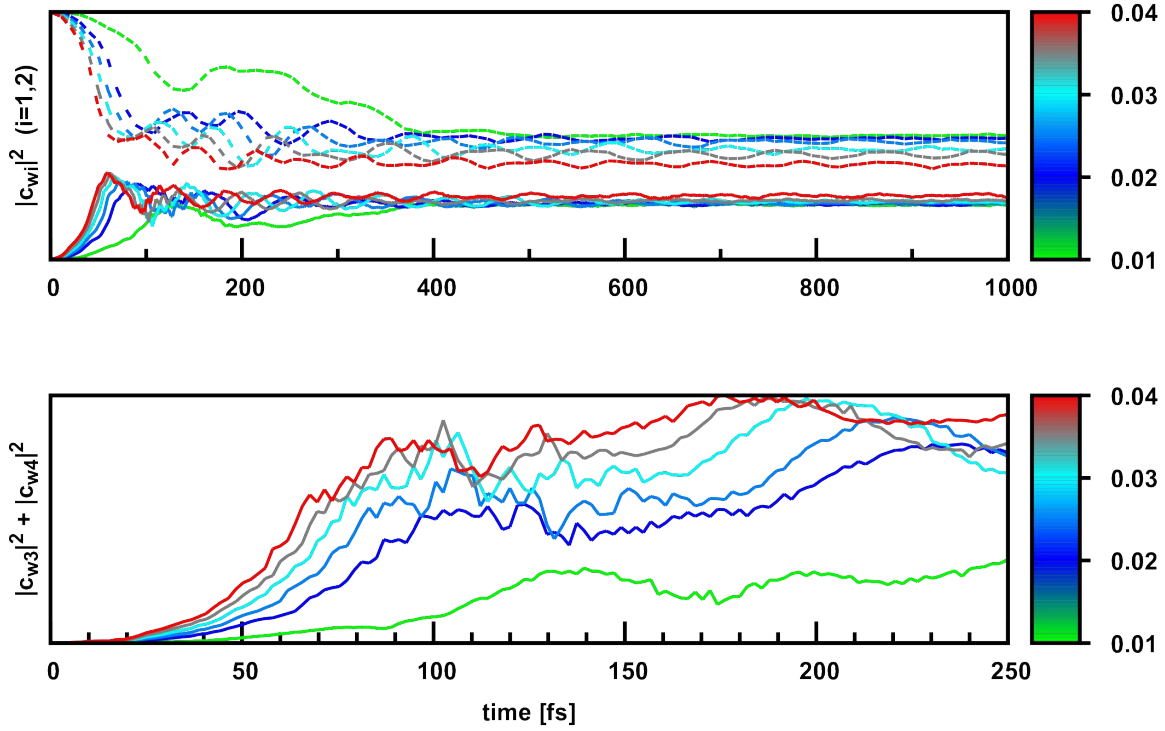
Figure 6.3: Evolution of the $|c_{w_i}|^2$ coefficients defined in Equation 6.8 as a function of the intensity of pulse. Top- Propagation of $|c_{w_2}|^2$ (solid lines) and $|c_{w_1}|^2$ (dashed lines) values summed over all the trimers of the unit cell. Bottom- Propagation of the ($|c_{w_3}|^2 + c_{w_4}|^2$) values summed over all the trimers of the unit cell. The values of the colorbox on the right are the A_o values in a.u. units.

We use a light pulse of energy 0.96 eV, which is the energy corresponding to the maximum absorption in Figure 6.2 to study the Intensity I dependence. We can tune the intensity I of the light pulse by A_o (Equation 5.11) as I $\propto |A_o|^2$. The smaller value of A_o corresponds to the low-intensity light pulse while the larger value of A_o means the high-intensity pulse as described in Appendix B. We discuss the present system dynamics at four different intensities i) A_{o1}=0.01 (case I^{st}), ii) A_{o1}=0.02 (case 2nd), iii) A_{o3}=0.03 (case 3rd) and A_{o4}=0.04 (case 4th). These four intensities cases will now be referred by case I^{st}, 2nd, 3rd and 4th.

Figure 6.3 shows the propagation of the absolute value $|c_{w_m}|^2$ of the coefficients of the four Wannier states (c_{w_1}, c_{w_2}, c_{w_3} and c_{w_4}) (Equation 6.8) corresponding to the occupied

$|w_o\rangle$ state for different intensities of the external light pulse. Clearly, higher the intensity I, the lesser is the contribution from the $|w_1\rangle$ state.

The excitation process not only involves the primary excitation of $|w_1\rangle \rightarrow |w_2\rangle$-type but also involves other secondary excitation processes $|w_2\rangle \rightarrow |w_3\rangle$, $|w_2\rangle \rightarrow |w_4\rangle$ or $|w_3\rangle \rightarrow |w_4\rangle$ types. These secondary processes are confirmed by Figure 6.3 (bottom) which shows the total contribution of the $|w_3\rangle$ and $|w_4\rangle$ states in the occupied state $|w_o\rangle$. It must be also noticed from Figure 6.3 that as the intensity $I \propto |A_o|^2$ increases, the population of the excited states $|w_2\rangle$, $|w_3\rangle$ and $|w_4\rangle$ increases. It is clear that while the $|w_2\rangle$ states contribute significantly at all intensities (Equation 6.5) besides the initial $|w_1\rangle$ state, the contribution from the $|w_3\rangle$ and $|w_4\rangle$ states is not negligible at higher intensities.

As the intensity of the external pulse significantly affects the population of excited electrons, this in turn influence the overall relaxation process of the system. Interestingly, the relaxation processfor the system subjected to the low-intensity light pulse goes through a magnetic transition from the CE-type anti-ferromagnetic of localised polarons in a charge ordered state to the A-type anti-ferromagnetic phase with no charge ordering. This results in a metal-insulator transition (discussed in Section 6.4.1). In the high-intensity laser pulse, the interference of the, relatively, fast spin dynamics close to the conical intersection drives the system into the G-type anti-ferromagnetic phase. The comparative high frequency of the lattice oscillations (discussed in Section 6.4.2) ultimately leads to the formation of single-site JT polarons. Thereafter, the relaxation process involves thermally activated hopping of these JT polaron in the disordered system which has a longer lifetime with a strong temperature dependence.

6.4   Initial high-frequency phonon modes

During the excitation, as the non-bonding states $|w_2\rangle$ start populating, shown in Figure 6.4, the atomic structure of the M^e corner sites alter because the non-bonding states mainly belong to the M^e sites of the trimer of the zig-zag CE chain. Here, we discuss two cases - low-intensity relaxation physics ($\mathbf{1^{st}}$ case) and high-intensity relaxation physics ($\mathbf{4^{th}}$ case).

Figure 6.5 and 6.6 illustrate dynamics of electron density, spin and Q_i modes of individual sites between time 0-1000 fs for **case $\mathbf{1^{st}}$** and $\mathbf{2^{nd}}$, respectively. Due to the charge transfer from the M^c central site to the M^e corner site of the trimer as a result of the excitation of electrons from the $|w_1\rangle$ to $|w_2\rangle$ (Figure 6.4), the phonons start to respond at 30 fs, as shown in Figure 6.5 (a) and 6.6 (a). The Q_2 (pink) and Q_3 (green) amplitudes of the M^c sites start decreasing, and the Q_3 amplitude of the M^e sites start increasing with
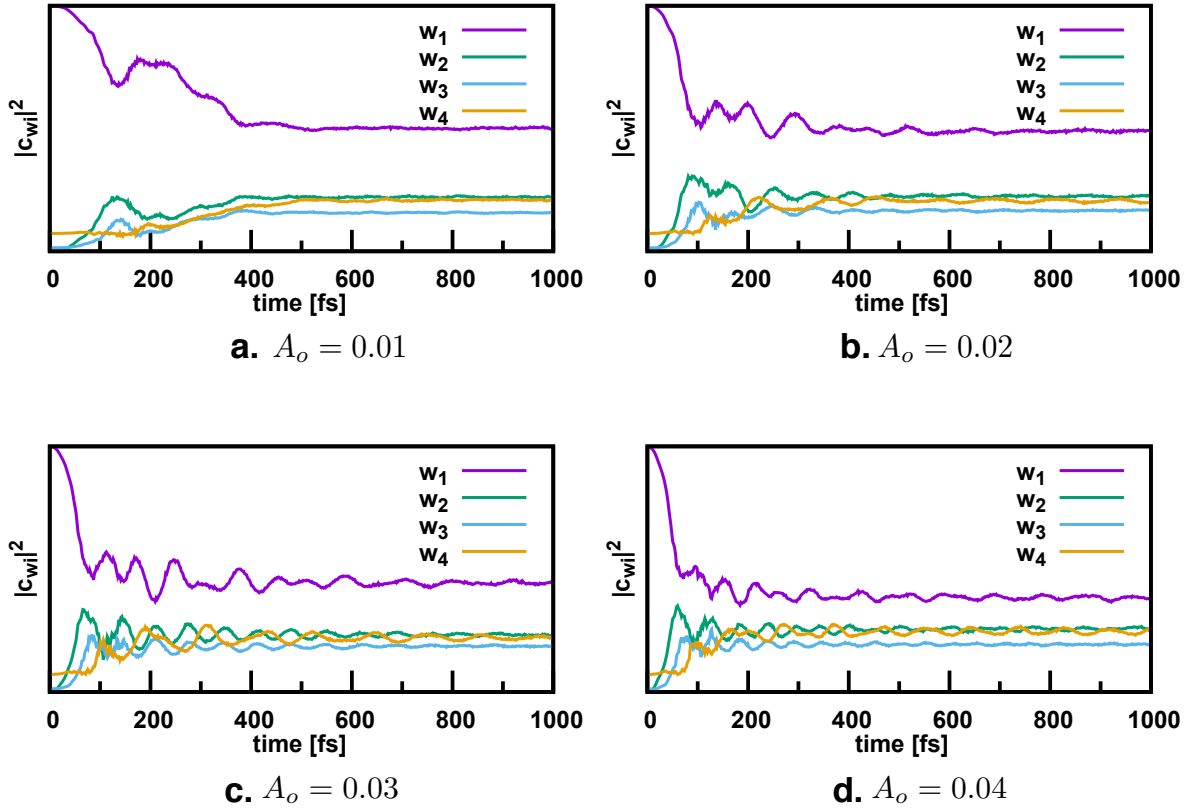
Figure 6.4: Evolution of the absolute values of $|c_{w_m}|$ coefficient (summed over all trimers of the unit cell) corresponding to $|w_o\rangle$ occupied state for four different intensities. The intensity of excitation increases from (a) to (d). The $|c_{w_m}|$ oscillations corresponds to Q_i modes phonon oscillations. The $|w_2\rangle$ states (green) constitute significantly to the excited electrons in case (a) of the low-intensity excitation. As the intensity of excitation increases, the $|w_3\rangle$ and $|w_4\rangle$ states contribute significantly towards the $|w_o\rangle$ occupied state. In case (d), the density of excited electron is almost equal in all the excited states at $t \sim 100$ fs.

negative value. The octahedra around the M^c sites start shrinking along the CE chain due to decreased electron density in the $|w_1\rangle$ state. On the other hand, the octahedra around the M^e sites start expanding in the ab plane (-ve Q_3), i.e., the CE plane, due to the newly occupied $|w_2\rangle$ non-bonding states. The t_{2g} spins at this timescale remain frozen as the interaction of the partially occupied majority-spin $|w_1\rangle$ or $|w_2\rangle$ states with the minority-spin state of the nearby antiparallel CE chains is still weak.

Figure 6.4 shows the evolution of the coefficients $|c_m|^2$ of the four Wannier states corresponding to the occupied state $|w_o\rangle$ (Equation 6.8) for different intensities. This set of Wannier states serves a good basis set only up to certain time (0-300 fs). During the low intensity excitation process, the secondary excitation processes $|w_2\rangle \to |w_3\rangle$ and $|w_2\rangle \to |w_4\rangle$ is negligible as shown in Figure 6.4.
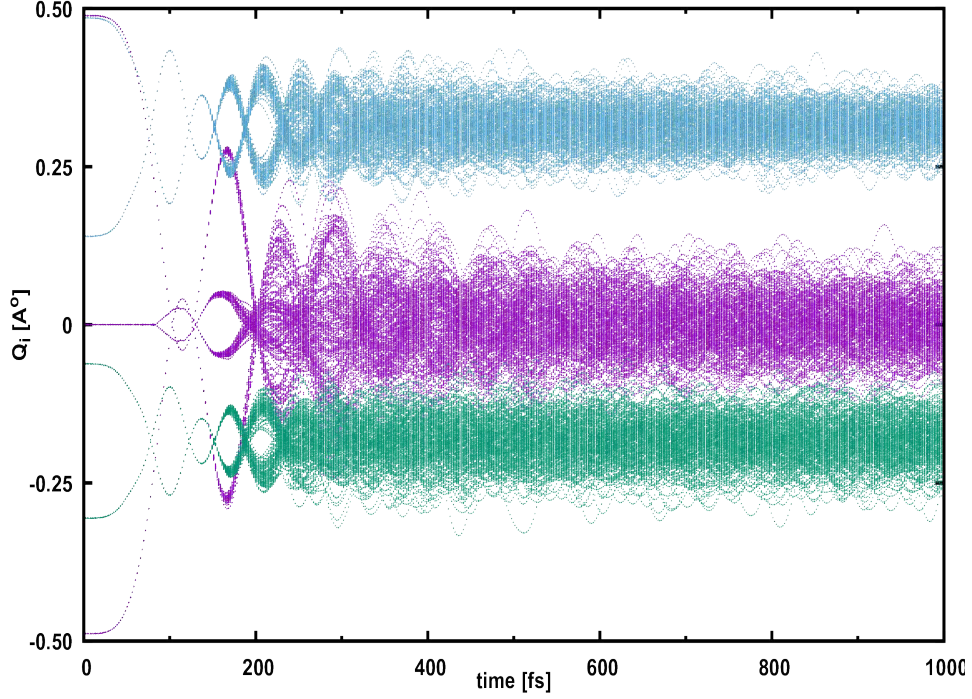
(a) **dynamics of Q_1 (blue), Q_2 (pink) and Q_3 (green) modes**: The positive and negative value of the Q_2 mode correspond to expansion of the octahedron in the x and y directions, respectively. The negative value of Q_3 mode corresponds to expansion of octahedron in the xy plane with simultaneous compression in z direction while its positive value indicates compression in the xy plane and expansion in the z direction.

(b) **dynamics of the t_{2g} spin angles between pair of the Mn sites along x (pink), y (green) and z (blue) directions**

(c) **dynamics of charge densities on individual Mn sites**

Figure 6.5: Low-intensity excitation: dynamics of Q_i modes (a), t_{2g} spin angles (b) and charge density (c) on individual sites of the CE-type structure. Initially, the charge densities on the M^c sites is larger than the M^e sites. During excitation of the e_g electron from $|w_1\rangle$ state to the $|w_1\rangle$ state leads to charge-transfer from M^c to M^e sites resulting in increased electron density on M^c sites. Initial, the strong oscillations in the electron density is due to the oscillations of the strong Q_2 mode on the M^c site. The amplitude of the Q_2 mode and the charge density oscillations decrease over time. The anti-ferromagnetic bonds between M^c and the nearby M^e sites of the adjacent zig-zag chain break as the planar orbital ordering on the M^c site. This result in decrease of t_{2g} spin angles between sites belonging to adjacent zig-zag chain from 180° to $0^o - 70^o$ within xy plane
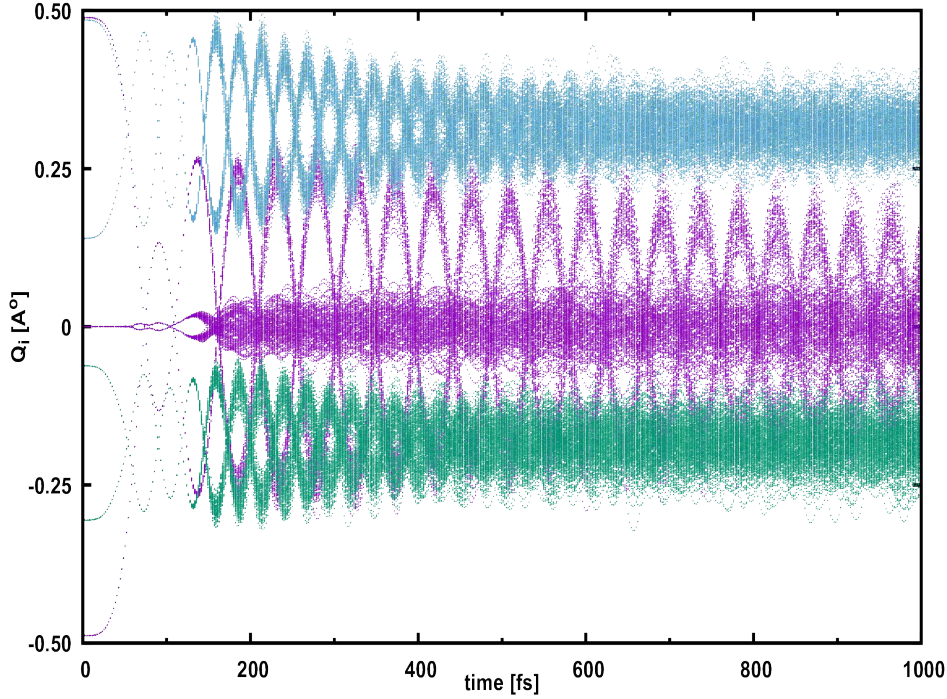
(a) **dynamics of Q_1 (blue), Q_2 (pink) and Q_3 (green) modes**: The positive and negative value of the Q_2 mode correspond to expansion of the octahedron in the x and y directions, respectively. The negative value of Q_3 mode corresponds to expansion of octahedron in the xy plane with simultaneous compression in z direction while its positive value indicates compression in the xy plane and expansion in the z direction.

(b) **dynamics of the t_{2g} spin angles between pair of the Mn sites along x (pink), y (green) and z (blue) directions**

(c) **dynamics of charge densities on individual Mn sites**

Figure 6.6: High-intensity excitation: dynamics of Q_i modes (a), t_{2g} spin angles (b) and charge density (c) on individual sites of the CE-type structure. Initially, the charge densities on the M^c sites is larger than the M^e sites. During excitation of the e_g electron from the $|w_1\rangle$ state to the $|w_1\rangle$ state leads to charge-transfer from M^c to M^e sites resulting in increased electron density on M^e sites. The strong initial oscillations in the electron density is due to the oscillations of the strong Q_2 mode oscillations on the M^c site. The amplitude of the Q_2 mode oscillations are stronger than the low-intensity case (Figure 6.5 (a)). The ferromagnetic bonds between M^c and the nearby M^e sites within same zig-zag chain break due to rotation of the orbital ordering by 90° on the M^c site turning the 0° t_{2g} spin angles to $150^o - 180^o$ within xy plane at around $t \sim 175$ fs.

The amplitude and frequency of the oscillating Q_1, Q_2 and Q_3 modes depend on the intensity of the light pulse. The phonons of the system subjected to the high-intensity pulse have higher amplitude and frequency of oscillations in comparison to the system initially subjected to the low intensity pulse. The frequency of the phonon modes for **case 1st** and **case 2nd** (Figure 6.5 (a) and Figure 6.6 (a)) are on terahertz timescale. The observed charge modulation on the terahertz timescale is also detected in these class of manganites experimentally [174, 182, 183]. The charge follows the phonon modes and as a consequence, the electron density on individual sites fluctuate with high-frequency oscillating behaviour simultaneously with Q_1, Q_2 and Q_3 modes at the early stage of the thermalisation. The frequency of the electron density fluctuations is similar to that of the Q_1 breathing mode (Figure 6.5 (c) and 6.6 (c)), which directly couples the isotropic expansion of octahedron to the electron density on that site.

6.4.1 Low-intensity excitations: case 1st

For the low-intensity light pulse (**case 1st**), the density of the excited electrons is not large enough to strongly perturb the atomic structure such that the Q_2 modes of the M^c central sites of the trimer change their sign. During a complete cycle of the oscillation of the onsite Q_2 modes on the M^c sites, as shown in Figure 6.5 (a), the Q_2 mode does not change its sign. The octahedron expanded initially in the x/y direction on the M^c site of the trimer relaxes into the symmetrically distorted structure in the xy plane with equally stretched bonds in the x and y direction. During the second half cycle of the Q_2 mode, it again expands in the same x/y direction and comes back to its original structure but now with a weaker amplitude of the Q_2 mode.

We try to describe the electronic structure of the segment of the CE chain at important instances during this complete cycle of the Q_2 mode on the M^c central site of the trimer with the help of Figure 6.7. As the Q_2 mode on the M^c site of the trimer decreases, the lowest axial $|w_1\rangle$ state turns into planar $d_{x^2-y^2}$-type corresponding to the atomic structure with negative Q_3 values in Figure 6.5 (a). This change of the orbital polarisation on the M^c sites from axial to planar type endorses interaction between adjacent zig-zag chains that are anti-ferromagnetically coupled to each other. The interaction between adjacent chains occurs through t_{2g} spins. The spin angles between the $M_\uparrow^c$ central site of spin $\uparrow$ trimer and nearby $M_\downarrow^e$ corner sites of the spin $\downarrow$ chain decrease slowly. It takes several cycles of the Q_3 mode (around 1000 fs from Figure 6.5 (b)) to turn these spin angle from 180° to $0^o - 70^o$, as clear from spin angles values of the pairs of the Mn sites in the x and y directions.
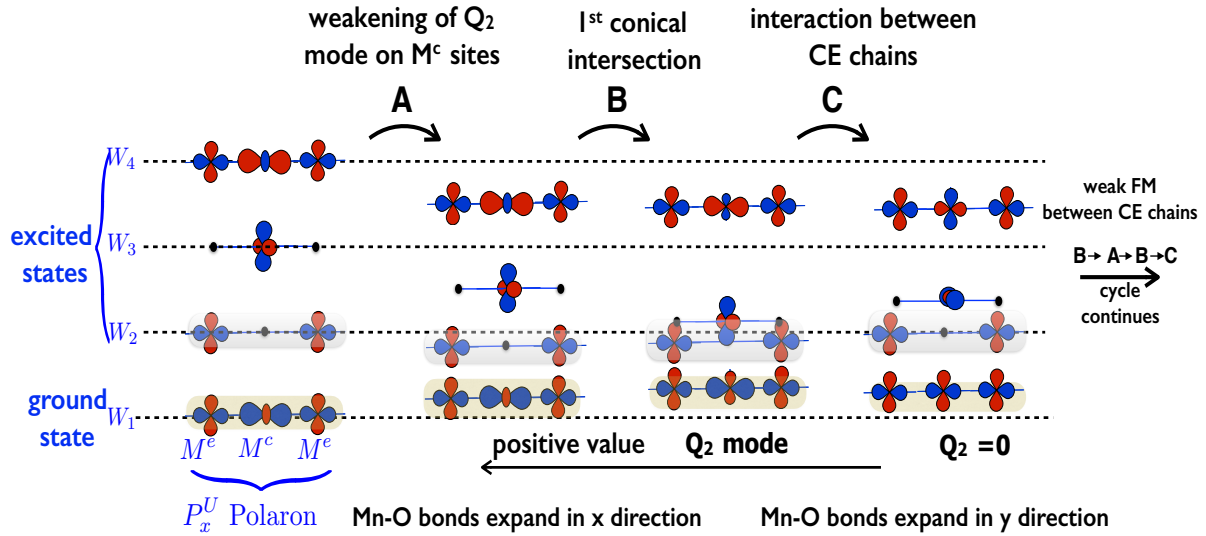
(a) **The first half cycle of the Q_2 mode on the central M^c site of the trimer along x direction** : The yellow shaded state is the W_1 ground state and the grey shaded state W_2 is the excited state. The W_3 states shift lower due to decreasing Q_2 mode on the M^c site. The orbital ordering on the M^c site changes from $d_{3x^2-r^2}$-type to $d_{x^2-y^2}$-type leading to a conical intersection between W_3 and W_2 states. As the orbital on the M^c site points now towards the M^e sites of the adjacent anti-ferromagnetic chain, a weak ferromagnetic interaction develops between the M^c and the M^e sites of the adjacent CE chain.
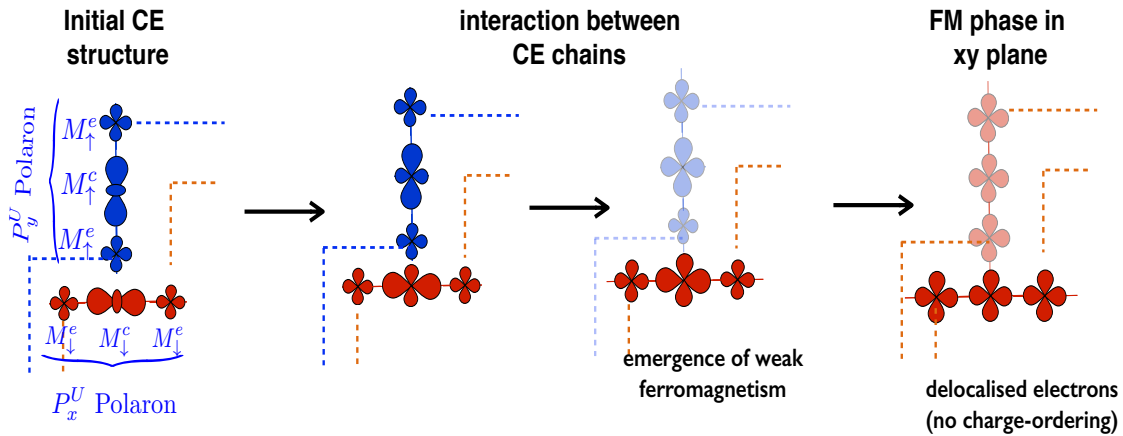
(b) **Evolution of the orbital ordering and spin structure**: blue and red indicate sites with opposite spin. As the orbital ordering on the M^c site changes to $d_{x^2-y^2}$-type, the anti-ferromagnetic coupling between the M^c and nearby M^e sites of the adjacent antiparallel zig-zag chain become weak leading to emergence of ferromagnetism which is shown by faded color in the third and fourth configuration.

Figure 6.7: Low-intensity excitations. (a) Evolution of Wannier states. (b) orbital ordering with corresponding spin structure of a trimer segment in the CE-type chain at $x = 0.5$

In Figure 6.5 (a), the initial high-frequency Q_2 Jahn-teller mode appears to decay slowly and lasts up to several picosecond (not shown in the graph but we follow the dynamics for several 6-7 picoseconds). The electron density oscillations decays much faster (see Figure 6.5). Hence, the electron subsystem thermalises on ultrafast timescale leaving behind the non-thermalised lattice subsystem. The subsequent thermalisation of the

atomic system is spin assisted. The experimental studies also suggest the presence of two-component relaxation where the fast relaxation process on ultrafast timescale corresponds to electronic and lattice system and the lattice-spin assisted relaxation dominates on the picosecond timescale [184, 185].

The slow decay of the Q_2 modes leads to the partial destruction of the orbital polarisation pattern on the M^c site while all the Mn sites still remain spin polarised due to the large Hund's coupling. The orbital ordering on the M^c sites of a trimer of the CE chain is now no more axial but planar. The destruction of the orbital polarisation is furthermore enhanced by the t_{2g} spins which respond at sub-picosecond scale ($t > 175$ fs (Figure 6.5 (b)). The xy CE plane turns almost ferromagnetic around $t \sim 1000$ fs (Figure 6.5). Now, the e_g electrons delocalise within the xy plane due to the emergence of ferromagnetism in the xy plane, which is evident from Figure 6.5 (c) that indicates comparably weaker charge disproportion on the M^e and M^c sites. This state with no charge ordering is a long-lived state. We track the dynamics upto 6-7 ps, during which the no charge ordering is established again.

6.4.2   Relaxation through conical intersection: case 4th

During the high-intensity light pulse (**case 4$^{\text{th}}$**), the density of the excited electrons becomes comparable to that of the electrons in the ground state $|w_1\rangle$, which is shown in Figure 6.4 (d). The large population of the excited electrons in the non-bonding states strongly disturbs the atomic structure of the M^c central sites of the trimers such that the Q_2 modes change their sign. This means during a first half cycle of the onsite Q_2 mode, the octahedron expanded initially in the x/y direction on the M^c site first almost relaxes and become symmetric in the xy plane and then, it expands again but now in the y/x direction (i.e., rotate 90° in the xy plane from its original configuration). During the second half cycle, the octahedron again comes back to its original distorted geometry, as shown in the one complete cycle of the Q_2 modes on the M^c sites in Figure 6.6.

The electronic structure of the system during the complete Q_2 cycle is illustrated in Figure 6.8 (a). The $d_{x^2-3r^2}/d_{3y^2-r^2}$-type $|w_1\rangle$ states not only shift higher in energy but also slowly convert first to $d_{x^2-y^2}$-type planar states and then, to $d_{y^2-z^2}/d_{x^2-z^2}$-type axial states in the the first-half cycle of the high amplitude Q_2 oscillations. In the second-half cycle, the $|w_1\rangle$ states again convert back to the original axial type. Hence, the lowest state $|w_1\rangle$ rotates 90° in the xy plane due to the rotation of the atomic structure by 90° in the xy plane in the first half cycle and returns back to original form in the second half.
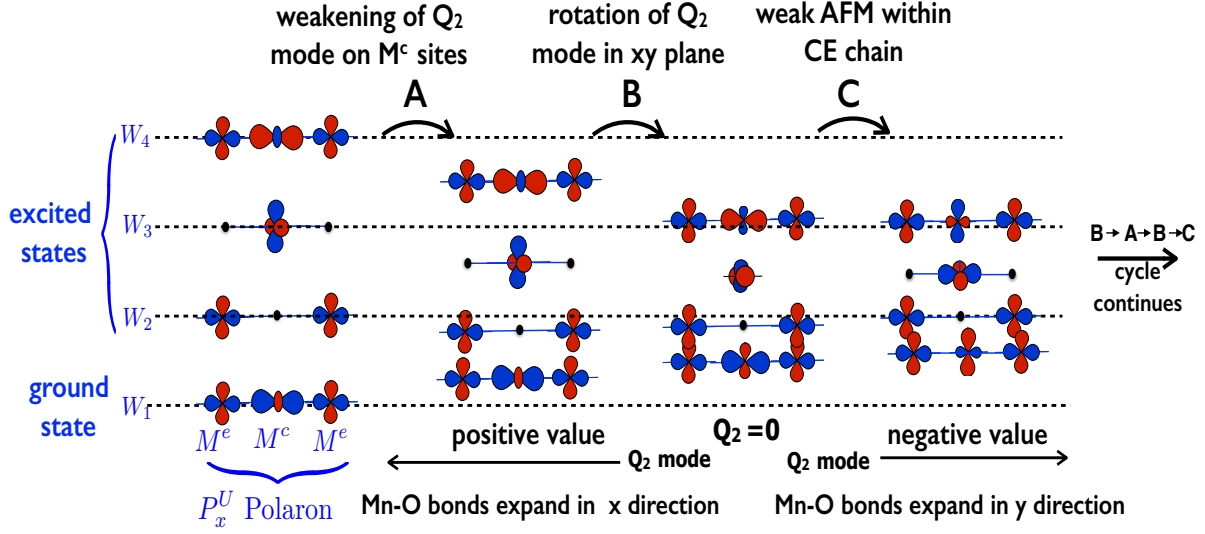
(a) **The first half cycle of the Q_2 mode on the M^c site of the trimer along x direction** : As the Q_2 mode on the M^c site decreases, the Jahn-Teller induced gap between W_1 and W_3 states decreases. Similar to the low-intensity excitation, the orbital ordering on the M^c site changes from $d_{3x^2-r^2}$-type to $d_{x^2-y^2}$-type. In addition to it, the orbital ordering on the M^c site further changes from $d_{x^2-y^2}$-type to $d_{3y^2-r^2}$-type. Hence, the orbital ordering is rotated by 90° in the xy plane on the M^c site. The Q_2 mode on the M^c site changes sign from original positive to negative.
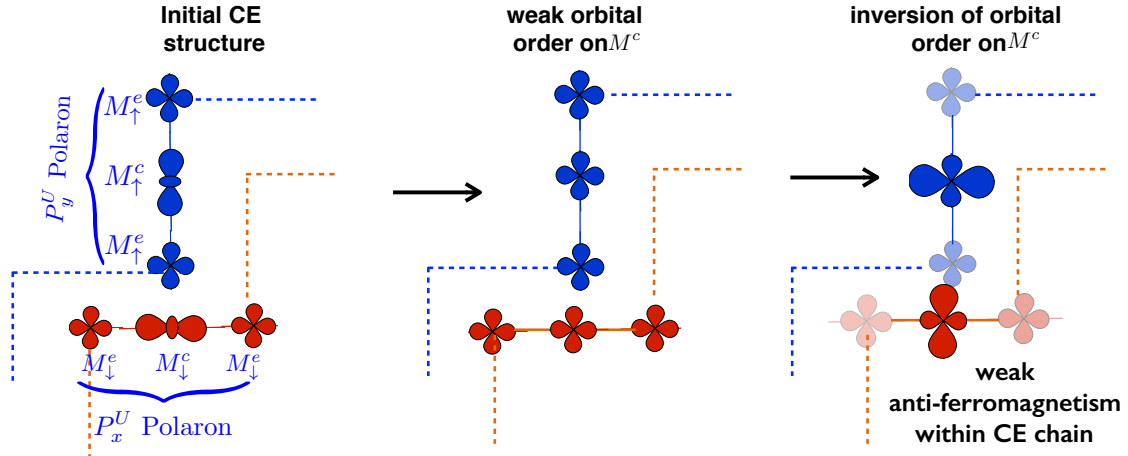
(b) **Evolution of the orbital ordering and spin structure**: blue and red indicate sites with opposite spin. As the orbital ordering on the M^c site is rotated by 90°, the ferromagnetic coupling between the M^c and M^e sites become weak, which is shown by fading color in the third configuration. A weak anti-ferromagnetic coupling between the M^c and M^e site within the CE chain develops.

Figure 6.8: High-intensity excitations. (a) Evolution of Wannier states. (b) orbital ordering with corresponding spin structure of a trimer segment in the CE-type chain at $x = 0.5$

In Figure 6.5, the complete cycle of the Q_2 modes corresponds to the conversion of the negative Q_2 mode into the positive Q_2 mode and vice-versa on the M^c central sites. It is in contrast to the low-intensity pulse(**case 1$^{\text{st}}$**) where the $|w_1\rangle$ states converts only to $d_{x^2-y^2}$-type states during small amplitude phonon oscillations (Figure 6.7 (a)).

The rotation of the orbital ordering on the M^c site (Figure 6.8 (b)) instigates the t$_{2g}$

spin degrees. The t_{2g} spins rotate breaking the ferromagnetic bonds between the M^e and M^c site within the CE chain, which is evident from Figure 6.6, where the original 0° (ferromagnetic bond) t_{2g} spin angles of all of the spin pairs in the x and y direction turn slowly almost to 180° (anti-ferromagnetic bond) around ~ 200 fs. The system undergoes a magnetic transition from the CE-type to the G-type. Single-site JT polarons are formed due to trapping of the e_g electrons within individual sites of the trimers that are now anti-ferromagnetically coupled to each other. This is a spin mediate conical intersection where the bonding ($|w_1\rangle$), non-bonding ($|w_2\rangle$) and anti-bonding ($|w_3\rangle$) states collapse ($t \sim 175$ fs in Figure 6.5) into localised states on the three sites of the trimer segment. From now onwards ($t > 200$ fs in Figure 6.6), the relaxation mechanism is dominated by thermally activated hopping of the newly formed JT polarons.

6.5 Summary

The t_{2g} spins play an important role in the relaxation of the excited three-site polarons, i.e., trimer P^U polarons (see Section 5.2 and 5.7), into single-site JT polarons, i.e., P^{JT_1} polarons (see Section 5.2) in the high-intensity excitation. The dynamics of the atomic structure plays a crucial role in the former case where the rotation of the atomic structure of the M^c site of the P^U polarons in the xy plane incites the t_{2g} spins of the M^e sites of the polaron to break the ferromagnetic bond with the M^c site aligning them anti-ferromagnetically to it. Hence, the strongly disturbed lattice degrees of freedom assist the t_{2g} spins to relax the e_g electrons through conical intersection on the ultrafast timescale. On the other hand, the initial charge ordered state in the low-intensity excitation losses charge ordering over time as the magnetic order changes from the initial CE-type into the A-type with the ferromagnetic xy layers that anti-ferromagnetically coupled in the z direction. Hence, a long-lived state with characterised by no charge ordering can be achieved by controlling the excitation process itself as we discussed in the case $\mathbf{1^{st}}$ of the low-intensity excitations.

Chapter 7

Summary and future outlook

The perovskite manganites have been intensively studied since the experimental observation of colossal magneto resistance and multiferroicity. The materials manifest a rich phase diagram with several electronic, atomic and magnetic orders. Many of the peculiar properties across the phase diagram are still poorly understood. The observation of long-lived states in these materials again renewed the interest in these materials towards their photovoltaic properties. It is challenging from the theoretical perspective to predict the nature of these long-lived states. This thesis work covers the following aspects of the $Pr_{1-x}Ca_xMnO_3$ manganite series from a proposed tight-binding model.

- We study the phase-diagram of a hypothetical one-dimensional manganite chain.

- The excitation and subsequent relaxation of electrons under external light pulse is analysed in the one-dimensional case.

- We explore a complete low-temperature phase diagram of the three-dimensional $Pr_{1-x}Ca_xMnO_3$ manganite series.

- The role of spins and lattice degrees of freedom in the relaxation of externally excited three-dimensional $Pr_{1-x}Ca_xMnO_3$ manganites is investigated.

With the experimental observation of the CMR effect in the region of phase inhomogeneity The manganites , the theoretical challenges lie in describing the nature of these inhomogeneous phases

Before understanding the complex physics, involving various degrees of freedom, of the three-dimensional manganites, we choose to study a comparably simpler one-dimensional system. We propose a coarse-grained polaron model for a one-dimensional manganite system (Figure 3.1). This polaron model is capable of describing the low-temperature phase-diagram of the hypothetical one-dimensional manganites.

When the manganite chain is subjected to a light pulse, a spreading of excitations throughout the chain in the form of light-like cones is observed on the femtosecond timescale (Figure 5.4). A sudden charge localisation triggers the t_{2g} spin degrees resulting in the formation of polaron (Figure 5.6). On the longer timescale, the relaxation

dynamics is dominated by the thermally activated polaron hopping once the atomic degree of freedom kicks in. This thermally activated polaron hopping is characterised by the Brownian like polaron motion.

The relevant length and time scales from the phase-diagram and relaxation dynamics study of the one-dimensional system facilitated us to approach the three-dimensional systems systematically.

Our model reproduces essential features of the low-temperature experimental phase diagram of the three-dimensional $Pr_{1-x}Ca_xMnO_3$ manganite series. Earlier, either different theoretical models were employed or different set of parameters were used to study individual regions of the phase digram. We put forward a comprehensive study of the phase-diagram with a unique set of model parameters. The non-collinear spin phases, such as spiral and canted spin, have not been yet investigated thoroughly in the context of manganites. The flexibility to study these non-collinear spin structures is also one of the important aspects of our model. With large system size, our model is also capable of capturing the phase-coexistence scenerio.

Our study confirms seven distinct phases at $x=$ 0, 0.125, 0.25, 0.5, 0.66, 0.75 and 0 doping. At $x=0.95$, our model hints towards the presence of charge-rich ferromagnetic clusters embedded in the parent G-type electron poor system (Figure 4.2). Furthermore, several new low-energy metastable states are obtained with characteristic magnetic and atomic structures at $x=$ 0.31, 0.375, 0.43, 0.53 and 0.625 (Figure 4.2). These metastable structures are promising candidate to understand some of the key experimental findings.

We verify the earlier theoretical results showing the A-, CE- and G-type magnetic structure at $x=0$, 0.5 and 0, respectively. At $x=0.125$, the holes are localised on Mn^{4+} sites and form a canted A-type magnetic structure (Figure 4.13). At $x=0.25$, our model predicts an insulating phase with the B-type magnetic order. In this B-type order, a Mn^{4+} hole site is surrounded by Mn^{3+} sites with $d_{x^2-y^2}/d_{y^2-z^2}/d_{z^2-x^2}$-type orbital ordering (Figure 4.12). The lobes of the orbitals on the Mn^{3+} sites are pointing towards the hole.

Below $x=0.5$, the model predicts two distinct homogenous phases: the Wigner crystal phase at $x=0.66$ and the C-type phase at $x=0.75$. While the Wigner-crystal phase is studied earlier, our model shows a new spiral spin structure associated to it. The Wigner crystal phase with charge-stripe has Mn^{3+} sites in the local environment of the Mn^{4+} sites (Figure 4.17). The Mn^{3+} sites with $d_{3x^2-r^2}/d_{3y^2-r^2}$-type orbital ordering form charge-stripes running diagonally in the xy plane. Introducing additional holes to the Wigner-crystal phase drives the system into the C-type magnetic phase at $x=0.75$. The charge ordering structure obtained by our model at $x=0.75$ agrees with the charge ordering within the experimentally proposed C-type magnetic order. In the C-type structure,

the axial $d_{3z^2-r^2}$-type orbital ordering on the Mn^{3+} sites are directing along the ferromagnetic direction (Figure 4.18 and 4.19). The electrons in the hole-rich system above x=0.89 form ferromagnetic clusters in the parent G-type system (Figure 4.22). The size of the ferromagnetic cluster is thirteen−sites which is in good agreement with the experimentally verified finite size ferromagnetic clusters [51, 58].

In between the regions of the distinct phases mentioned above, several new metastable states are obtained from our model. The metastable states in the vicinity of the CE-type homogenous phase at x=0.5 are characterised by the localised disorders associated with the newly added holes and electrons. The energetically low-lying metastable states at x=0.375 shows the coexistence of two phases. These two phases have the stoichiometry of x=0.5 and x=1 (Figure 4.10). The metastable state at x=0.31 shows the charge ordering of x=0.5 case agreeing with the recent experimental evidences [43, 186]. Interestingly, the non-collinear spin structure in the xy plane makes this metastable a promising state to describe the observed CMR effect which is at maximum around $x\sim$0.3 (Figure 4.14). At $x = 0.625$, the model hints towards a mixed-stripe phase in which the Wigner-crystal like single stripes and the CE-type double stripes coexist (Figure 4.16).

The study of the three-dimensional manganites under an external light pulse shows two different relaxation pathways that depends on the intensity of the light pulse. When the CE-type structure at $x = 0.5$ is subjected to the low-intensity light pulse, a long-lived e_g electron state with no charge ordering is observed (Section 6.4.1). The initial charge-ordering is destroyed due to the appearance of ferromagnetism in the xy plane. In the high-intensity light pulse, the excited electrons relax through the conical intersections and form single-site JT polarons on sub-picosecond timescale (Section 6.4.2). The conical intersection process is assisted by the high-amplitude oscillation of the atoms such that the atomic distortion pattern rotate by 90° in the xy CE plane. The subsequent dynamics that involves t_{2g} spin degrees leads to a magnetic transition from the CE-type to the G-type antiferromagnetic phase. The electronic system is in the ground state, but the spin-assisted thermally activated JT polaron hopping prevails on the longer timescale.

7.0.1   Future outlook

Our three-dimensional phase diagram presented in the thesis uses the model with uniform hopping. The effects of the steric disturbances, such as the tilting of Mn-O-Mn bond and Mn-O bond stretching, on the overall hopping matrix elements are not incorporated in the model. Ignoring these effects results in discrepancy in the theoretical and experimental phase diagram in the region close to x=0 in the phase diagram where the JT splitting and tilting of Mn-O-Mn bond is strong [25]. A careful study with a site-dependent hopping

model can describe this region better. Furthermore, studying the effect of tilting in the other regions of the phase diagram may answer several unanswered questions. For example, the $Pr_{1-x}Ca_xMnO_3$ system at $x = 0.4$ shows the Zener polaronic phase without any charge-ordering [54]. The non-uniform Mn-O-Mn tilting pattern between the sites within a x or y segment of the zig-zag chain in the CE-type structure may lead to the dimerisation within the segment.

With the Monte-Carlo like simulations, our proposed one- and three-dimensional coarse-grained polaron model can be used to describe the phase diagram of the manganites at high temperatures, which theoretically still remains largely unexplored. In spite of extensive theoretical work on manganites in recent years, a number of questions still remain open. For example, the presence and role played by these polarons near insulator-to-metal transition temperature or if the percolation of metallic regions within the background of a non-conducting matrix is responsible for the spontaneous decrease in resistivity in the CMR region of phase diagram. These interesting aspects can be looked into and analysed in greater details by the time-dependent study of the excitation and relaxation processes. In the present thesis work, we implemented techniques, such as Peierls substitution method and time-dependent Schrodinger equation to study the relaxation in the simple one-dimensional and three-dimensional systems. It would be interesting to study the relaxation dynamics in the high temperature region by incorporating the Nose-Hover thermostat (briefly discussed in the thesis). The study will help us to understand the physics of the metal-insulator transitions, CMR effect as well as the presence and nature of the long-lived excitations found experimentally in these series of compounds.

Appendix A

Coulomb interaction

Here, we extract the onsite Coulomb energy in the subset of the e_g orbitals. We use the cubic harmonics $d_{3z^2-r^2}$ and $d_{x^2-y^2}$ for the e_g orbital. Starting with the general Hartree-Fock like expression, the interaction energy is

$$
\begin{aligned}
E &= \frac{1}{2}\sum_{n,m} f_m f_n \int d^4x \int d^4x' \frac{e^2 \psi_n^*(\vec{x})\psi_m^*(\vec{x}')\psi_n(\vec{x})\psi_m(\vec{x'})}{4\pi\epsilon_0|\vec{r}-\vec{r'}|} \\
&- \frac{1}{2}\sum_{m,n} f_m f_n \int d^4x \int d^4x' \frac{e^2 \psi_n^*(\vec{x})\psi_m^*(\vec{x}')\psi_m(\vec{x})\psi_n(\vec{x'})}{4\pi\epsilon_0|\vec{r}-\vec{r'}|} \\
&= \frac{1}{2}\sum_{\alpha,\beta,\gamma,\delta} \int d^4x \int d^4x' \frac{e^2 \chi_\alpha^*(\vec{x})\chi_\beta^*(\vec{x}')\chi_\gamma(\vec{x})\chi_\delta(\vec{x'})}{4\pi\epsilon_0|\vec{r}-\vec{r'}|} \\
&\times \sum_{m,n} f_m f_n \Big\{ \langle\psi_n|\pi_\alpha\rangle\langle\psi_m|\pi_\beta\rangle\langle\pi_\gamma|\psi_n\rangle\langle\pi_\delta|\psi_m\rangle - \langle\psi_n|\pi_\alpha\rangle\langle\psi_m|\pi_\beta\rangle\langle\pi_\gamma|\psi_m\rangle\langle\pi_\delta|\psi_n\rangle \Big\} \\
&= \frac{1}{2}\sum_{\alpha,\beta,\gamma,\delta} W_{\alpha,\beta,\gamma,\delta}\Big(\rho_{\gamma,\alpha}\rho_{\delta,\beta} - \rho_{\delta,\alpha}\rho_{\gamma,\beta} \Big).
\end{aligned}
\tag{A.1}
$$

Here, the Coulomb matrix elements $W_{\alpha,\beta,\gamma,\delta}$ are defined as,

$$
W_{\alpha,\beta,\gamma,\delta} = \int d^4x \int d^4x' \frac{e^2 \chi_\alpha^*(\vec{x})\chi_\beta^*(\vec{x}')\chi_\gamma(\vec{x})\chi_\delta(\vec{x'})}{4\pi\epsilon_0|\vec{r}-\vec{r'}|}
\tag{A.2}
$$

where $\alpha,\beta,\gamma,\delta \in \{a,b\}$ (a=$d_{3z^2-r^2}$ and b=$d_{x^2-y^2}$).

The number of possible matrix elements $W_{\alpha,\beta,\gamma,\delta}$ are $2^4 = 16$. From A.2, it can also be shown that in the e_g subset, the matrix elements which have odd number of orbitals of particular symmetry vanish [187]. Furthermore, using the identities $W_{\alpha,\beta,\gamma,\delta}=W_{\gamma,\beta,\alpha,\delta}=W_{\alpha,\delta,\gamma,\beta}=W_{\gamma,\delta,\alpha,\beta}$ for real orbitals, many of these matrix elements turn out to be same. The following table lists these 16 possible matrix elements in terms of four parameters U, J, J' and U':

α	a	a	a	a	a	a	a	a	b	b	b	b	b	b	b	b
β	a	a	a	a	b	b	b	b	a	a	a	a	b	b	b	b
γ	a	a	b	b	a	a	b	b	a	a	b	b	a	a	b	b
δ	a	b	a	b	a	b	a	b	a	b	a	b	a	b	a	b
$W_{\alpha,\beta,\gamma,\delta}$	U	0	0	$J'(=J)$	0	U'	J	0	0	J	U'	0	$J'(=J)$	0	0	U

Out of these four different parameters, the parameter J', termed as pair hopping amplitude [187], is not independent as the way $W_{\alpha,\beta,\gamma,\delta}$ are defined (see Equation A.2), J' is equal to J [187]. At last, the Coulomb Energy can be expressed by just three independent parameters U, U' and J which are also known as Kanamori parameters [188]. These are

$$
\begin{aligned}
U &= W_{a\sigma,a\sigma',a\sigma,a\sigma'} \\
&= W_{b\sigma,b\sigma',b\sigma,b\sigma'} \\
U' &= W_{a\sigma,b\sigma',a\sigma,b\sigma'} \\
J &= W_{a\sigma,b\sigma',b\sigma,a\sigma'} \\
&= W_{a\sigma,a\sigma',b\sigma,b\sigma'}.
\end{aligned}
\tag{A.3}
$$

The Coulomb energy A.1 within the e_g subset has the form:

$$
\begin{aligned}
E &= \frac{1}{2} \sum_{\alpha,\beta,\gamma,\delta} W_{\alpha,\beta,\gamma,\delta} \Big(\rho_{\gamma,\alpha}\rho_{\delta,\beta} - \rho_{\delta,\alpha}\rho_{\gamma,\beta} \Big) \\
&= \frac{1}{2} \sum_{\sigma,\sigma'} W_{a\sigma,a\sigma',a\sigma,a\sigma'} \Big(\rho_{a\sigma,a\sigma}\rho_{a\sigma',a\sigma'} - \rho_{a\sigma',a\sigma}\rho_{a\sigma,a\sigma'} \Big) \\
&+ \frac{1}{2} \sum_{\sigma,\sigma'} W_{a\sigma,b\sigma',a\sigma,b\sigma'} \Big(\rho_{a\sigma,a\sigma}\rho_{b\sigma',b\sigma'} - \rho_{b\sigma',a\sigma}\rho_{a\sigma,b\sigma'} \Big) \\
&+ \frac{1}{2} \sum_{\sigma,\sigma'} W_{a\sigma,b\sigma',b\sigma,a\sigma'} \Big(\rho_{b\sigma,a\sigma}\rho_{a\sigma',b\sigma'} - \rho_{a\sigma',a\sigma}\rho_{b\sigma,b\sigma'} \Big) \\
&+ \frac{1}{2} \sum_{\sigma,\sigma'} W_{a\sigma,a\sigma',b\sigma,b\sigma'} \Big(\rho_{b\sigma,a\sigma}\rho_{b\sigma',a\sigma'} - \rho_{b\sigma',a\sigma}\rho_{b\sigma,a\sigma'} \Big).
\end{aligned}
\tag{A.4}
$$

We define the diagonal matrix element of density matrix as

$$
n_{\sigma,\alpha} = \rho_{\sigma\alpha,\sigma\alpha}.
\tag{A.5}
$$

Now using the Kanamori parameters (Equation A.3) and A.5, we have

$$
\begin{aligned}
E \;=\;& \frac{U}{2}\sum_{\sigma_1,\sigma_2,\alpha_1} n_{\alpha_1,\sigma_1}n_{\alpha_1,\sigma_2} + \frac{U'}{2}\sum_{\sigma_1,\sigma_2,\alpha_1\neq\alpha_2} n_{\alpha_1,\sigma_1}n_{\alpha_2,\sigma_2} \\
&- \frac{U}{2}\sum_{\sigma_1,\sigma_2,\alpha_1}\rho_{\alpha_1\sigma_1,\alpha_1\sigma_2}\rho_{\alpha_1\sigma_2,\alpha_1\sigma_1} - \frac{U'}{2}\sum_{\sigma_1,\sigma_2,\alpha_1\neq\alpha_2}\rho_{\alpha_1\sigma_1,\alpha_2\sigma_2}\rho_{\alpha_2\sigma_2,\alpha_1\sigma_1} \\
&+ \frac{J}{2}\sum_{\sigma_1,\sigma_2,\alpha_1\neq\alpha_2}\rho_{\alpha_1\sigma_1,\alpha_2\sigma_1}\rho_{\alpha_2\sigma_2,\alpha_1\sigma_2} - \frac{J}{2}\sum_{\sigma_1,\sigma_2,\alpha_1\neq\alpha_2}\rho_{\alpha_1\sigma_2,\alpha_1\sigma_1}\rho_{\alpha_2\sigma_1,\alpha_2\sigma_2} \\
&+ \frac{J}{2}\sum_{\sigma_1,\sigma_2,\alpha_1\neq\alpha_2}\rho_{\alpha_1\sigma_1,\alpha_2\sigma_1}\rho_{\alpha_1\sigma_2,\alpha_2\sigma_2} - \frac{J}{2}\sum_{\sigma_1,\sigma_2,\alpha_1\neq\alpha_2}\rho_{\alpha_1\sigma_2,\alpha_2\sigma_1}\rho_{\alpha_1\sigma_1,\alpha_2\sigma_2} \qquad\text{(A.6)}
\end{aligned}
$$

$$
\begin{aligned}
E \;=\;& \frac{U}{2}\left(\sum_{\sigma_1,\alpha_1} n_{\alpha_1,\sigma_1}n_{\alpha_1,\sigma_1} + \sum_{\sigma_1\neq\sigma_2,\alpha_1} n_{\alpha_1,\sigma_1}n_{\alpha_1,\sigma_2}\right) \\
&+ \frac{U'}{2}\left(\sum_{\sigma_1,\alpha_1\neq\alpha_2} n_{\alpha_1,\sigma_1}n_{\alpha_2,\sigma_1} + \sum_{\sigma_1\neq\sigma_2,\alpha_1\neq\alpha_2} n_{\alpha_1,\sigma_1}n_{\alpha_2,\sigma_2}\right) \\
&- \frac{U}{2}\left(\sum_{\sigma_1,\alpha_1}\rho_{\alpha_1\sigma_1,\alpha_1\sigma_1}\rho_{\alpha_1\sigma_1,\alpha_1\sigma_1} + \sum_{\sigma_1\neq\sigma_2,\alpha_1}\rho_{\alpha_1\sigma_1,\alpha_1\sigma_2}\rho_{\alpha_1\sigma_2,\alpha_1\sigma_1}\right) \\
&- \frac{U'}{2}\left(\sum_{\sigma_1,\alpha_1\neq\alpha_2}\rho_{\alpha_1\sigma_1,\alpha_2\sigma_1}\rho_{\alpha_2\sigma_1,\alpha_1\sigma_1} + \sum_{\sigma_1\neq\sigma_2,\alpha_1\neq\alpha_2}\rho_{\alpha_1\sigma_1,\alpha_2\sigma_2}\rho_{\alpha_2\sigma_2,\alpha_1\sigma_1}\right) \\
&+ \frac{J}{2}\left(\sum_{\sigma_1,\alpha_1\neq\alpha_2}\rho_{\alpha_1\sigma_1,\alpha_2\sigma_1}\rho_{\alpha_2\sigma_1,\alpha_1\sigma_1} + \sum_{\sigma_1\neq\sigma_2,\alpha_1\neq\alpha_2}\rho_{\alpha_1\sigma_1,\alpha_2\sigma_1}\rho_{\alpha_2\sigma_2,\alpha_1\sigma_2}\right) \\
&- \frac{J}{2}\left(\sum_{\sigma_1,\alpha_1\neq\alpha_2}\rho_{\alpha_1\sigma_1,\alpha_1\sigma_1}\rho_{\alpha_2\sigma_1,\alpha_2\sigma_1} + \sum_{\sigma_1\neq\sigma_2,\alpha_1\neq\alpha_2}\rho_{\alpha_1\sigma_1,\alpha_1\sigma_2}\rho_{\alpha_2\sigma_2,\alpha_2\sigma_1}\right) \\
&+ \frac{J}{2}\left(\sum_{\sigma_1,\alpha_1\neq\alpha_2}\rho_{\alpha_1\sigma_1,\alpha_2\sigma_1}\rho_{\alpha_1\sigma_1,\alpha_2\sigma_1} + \sum_{\sigma_1\neq\sigma_2,\alpha_1\neq\alpha_2}\rho_{\alpha_1\sigma_1,\alpha_2\sigma_1}\rho_{\alpha_1\sigma_2,\alpha_2\sigma_2}\right) \\
&- \frac{J}{2}\left(\sum_{\sigma_1,\alpha_1\neq\alpha_2}\rho_{\alpha_1\sigma_1,\alpha_2\sigma_1}\rho_{\alpha_1\sigma_1,\alpha_2\sigma_1} + \sum_{\sigma_1\neq\sigma_2,\alpha_1\neq\alpha_2}\rho_{\alpha_1\sigma_1,\alpha_2\sigma_2}\rho_{\alpha_1\sigma_2,\alpha_2\sigma_1}\right) \\
&\hspace{12cm}\text{(A.7)}
\end{aligned}
$$

Specifically, within the cubic harmonics of e_g subset, $U' = U - 2J$ [187]. At the end, we have

$$
\begin{aligned}
E \;=\;& \underbrace{\frac{U}{2}\left(\sum_{\sigma_1 \neq \sigma_2, \alpha_1} n_{\alpha_1,\sigma_1} n_{\alpha_1,\sigma_2}\right)}_{\text{intra-orbital}} - \frac{U}{2}\left(\sum_{\sigma_1 \neq \sigma_2, \alpha_1} \rho_{\alpha_1\sigma_1,\alpha_1\sigma_2}\rho_{\alpha_1\sigma_2,\alpha_1\sigma_1}\right) \\
&+ \underbrace{\frac{U-3J}{2}\left(\sum_{\sigma_1, \alpha_1 \neq \alpha_2} n_{\alpha_1,\sigma_1} n_{\alpha_2,\sigma_1}\right)}_{\text{inter-orbital same spin}} - \frac{U-3J}{2}\left(\sum_{\sigma_1, \alpha_1 \neq \alpha_2} \rho_{\alpha_1\sigma_1,\alpha_2\sigma_1}\rho_{\alpha_2\sigma_1,\alpha_1\sigma_1}\right) \\
&+ \underbrace{\frac{U-2J}{2}\sum_{\sigma_1 \neq \sigma_2, \alpha_1 \neq \alpha_2} n_{\alpha_1,\sigma_1} n_{\alpha_2,\sigma_2}}_{\text{inter-orbital diff. spin}} - \frac{U-2J}{2}\sum_{\sigma_1 \neq \sigma_2, \alpha_1 \neq \alpha_2} \rho_{\alpha_1\sigma_1,\alpha_2\sigma_2}\rho_{\alpha_2\sigma_2,\alpha_1\sigma_1} \\
&- \frac{J}{2}\sum_{\sigma_1 \neq \sigma_2, \alpha_1 \neq \alpha_2} \rho_{\alpha_1\sigma_1,\alpha_1\sigma_2}\rho_{\alpha_2\sigma_2,\alpha_2\sigma_1} + \frac{J}{2}\sum_{\sigma_1 \neq \sigma_2, \alpha_1 \neq \alpha_2} \rho_{\alpha_1\sigma_1,\alpha_2\sigma_1}\rho_{\alpha_2\sigma_2,\alpha_1\sigma_2} \\
&- \frac{J}{2}\sum_{\sigma_1 \neq \sigma_2, \alpha_1 \neq \alpha_2} \rho_{\alpha_1\sigma_1,\alpha_2\sigma_2}\rho_{\alpha_1\sigma_2,\alpha_2\sigma_1} + \frac{J}{2}\sum_{\sigma_1 \neq \sigma_2, \alpha_1 \neq \alpha_2} \rho_{\alpha_1\sigma_1,\alpha_2\sigma_1}\rho_{\alpha_1\sigma_2,\alpha_2\sigma_2} \quad \text{(A.8)}
\end{aligned}
$$

Appendix B

Determination of amplitude of the vector potential (A'_o)

The quantities usually measured during experiments are the laser energy and its distribution in space and the pulse duration Γ_o. They are used to evaluate the laser intensity. The laser intensity is

$$I = \langle \vec{S} \rangle = \frac{1}{2} c \epsilon \omega^2 \langle A_o^2 \rangle = \frac{1}{2} c \epsilon \omega^2 \langle A_o^2 \rangle, \tag{B.1}$$

which is defined in Equation 5.11 and its SI unit is W/m^2.

We use the information given in the reference [101] to obtain the value A_o.

No. of pulse per second $N_p = 440 s^{-1} = 1.064 \times 10^{-14}$ a.u.

Pump power $P_p = 350 \times 10^{-6} W = 0.00194187896$ a.u.

Energy per pulse $E_p = \frac{P_p}{N_p} = 800 \times 10^{-9}$ J= 5360.42 a.u.

Single pulse duration $\Gamma_o = 100 fs = 100 \times 10^{-15}$ s=4134.13 a.u.

There is additional information given: averaged surface power density 2.5×10^{10} W/cm^2 at the focal spot of a diameter of 200 μm. This is the pump intensity which is same that we defined above by I.

The spot size area $b_a = 3.14 \times 10^{-8}$ m^2

The energy transferred per unit area per unit time associated with a single pulse of the laser is

$$S = \frac{E_p}{\Gamma_o b_a} \tag{B.2}$$

$$S = \frac{800 \times 10^{-9}}{(100 \times 10^{-15})(3.14 \times 10^{-8})} = 2.547 \times 10^{14} \text{ W/m}^2 \tag{B.3}$$

This value is similar to what is given as power density I in the experimental detail. The total energy transferred by the laser beam per pulse per unit area which last for 100 fs is given by

$$E_p = I \Gamma_o = 2.5 \times 10^{14} \times (100 \times 10^{-15}) = 20.5 \text{ J/m}^2 \tag{B.4}$$

Now for our model, we consider the pulse as Gaussian function in time. Writing $A'_o(t)$ as a Gaussian function instead of a constant A'_o, The equation

$$A'_o(t) = A_o e^{\frac{-t^2}{2c_w^2}} \qquad (B.5)$$

The width (FWHM) of the function is given by the variable c_w and the maximum value of the function is given by the pre factor A_o. We define the width of the Gaussian pulse such that the full width at tenth of the maximum is equal to the pulse duration Γ_o used in the experiments. The $\Gamma_o = 100 fs$ value gives us the width c_{10} of the Gaussian function at tenth of its maximum value.

The factor A_o can be calculated by the following equation

$$\frac{1}{2} A_o^2 c\epsilon\omega^2 \int e^{\frac{-t^2}{c_w^2}} dt = 20.5 \qquad (B.6)$$

$$\frac{1}{2} A_o^2 c\epsilon\omega^2 (\sqrt{\pi}c_w) = 20.5 \qquad (B.7)$$

Now we have the following information about the pump experiments

$$FWHM = 2\sqrt{2\ln 2}\ c = 2.35482c \qquad (B.8)$$

$$c_w = \frac{W_{fwhm}}{2.35482} \text{ or } c = \frac{W_{fwtm}}{4.29193} \qquad (B.9)$$

The factor A_o can be calculated by using the above information of experiments. We integrate over the time domain to get the total energy E_o radiated per unit surface area of the sample.

$$\frac{\sqrt{\pi}}{2} A_o^2 c\epsilon\omega^2 c_w = E_p \qquad (B.10)$$

$$A_o^2 \omega^2 = \frac{4\sqrt{\pi} \times E_p}{c_w \times c} \qquad (B.11)$$

Below we find out the A_o value by adopting the atomic units:

$E_p = \frac{20.5 \times (5.2918 \times 10^{-11})^2}{4.3597 \times 10^{-18}} = 11.3736$ a.u.

$W_{fwhm} = \frac{100 \times 10^{-15}}{2.4188 \times 10^{-17}} = 1755.66$ a.u.

$c_w = \frac{100 \times 10^{-15}}{2.3548 \times 2.4188 \times 10^{-17}}$ a.u.

$c = 137$ a.u ,

$\omega = \frac{E_{ex}}{\hbar} = E_{ex}$ as $\hbar = 1$ a.u.

$$A_o^2\omega^2 = \frac{4\sqrt{\pi} \times 20.5 \times (5.2918 \times 10^{-11})^2 \times 2.3548 \times 2.4188 \times 10^{-17}}{4.3597 \times 10^{-18} \times 100 \times 10^{-15} \times 137} \tag{B.12}$$

$$A_o^2\omega^2 = 38.8125 \times 10^{-8} \tag{B.13}$$

$$A_o = \frac{6.2299 \times 10^{-4}}{0.057} = 0.0109 \text{ a.u.} \tag{B.14}$$

This above A_o value is extracted from the experimental details provided in reference [101]. We study the relaxation dynamics in the presence of light field with A_o in the range **0.0050-0.0400 a.u**.

Appendix C

Numerical integration of TDSE equation

work credit: Prof. P. E. Blöchl

We use the integration method inspired by the second-order differential method proposed by A. Askar et al. [189] to solve the time dependent Schrodinger equation of wave function which describes e_g electrons and spinors which describes the spin degrees of freedom of t_{2g} states.

$$
\begin{aligned}
|\psi(t+\Delta)\rangle &= e^{-\frac{i}{\hbar}\hat{H}\Delta}\psi(t)\rangle \\
&= e^{-\frac{i}{\hbar}\hat{E}\Delta}e^{-\frac{i}{\hbar}(\hat{H}-E\hat{I})\Delta}|\psi(t)\rangle \\
e^{\frac{i}{\hbar}E\Delta}|\psi(t+\Delta)\rangle &= e^{-\frac{i}{\hbar}(\hat{H}-E\hat{I})\Delta}|\psi(t)\rangle \\
&= \cos\Big(-\frac{1}{\hbar}(\hat{H}-E\hat{I})\Delta\Big)|\psi(t)\rangle + i\,\sin\Big(-\frac{1}{\hbar}(\hat{H}-E\hat{I})\Delta\Big)|\psi(t)\rangle \\
&= \frac{1}{2}\Big(e^{-\frac{i}{\hbar}(\hat{H}-E\hat{I})\Delta} + e^{+\frac{i}{\hbar}(\hat{H}-E\hat{I})\Delta}\Big)|\psi(t)\rangle \\
&\quad - \frac{i}{\hbar}\Big(\hat{H}-E\hat{I}\Big)\Delta|\psi(t)\rangle + i\Big[\,\sin\Big(-\frac{1}{\hbar}(\hat{H}-E\hat{I})\Delta\Big) - \frac{1}{\hbar}(\hat{H}-E\hat{I})\Delta\Big]|\psi(t)\rangle \\
&= \frac{1}{2}\Big(e^{\frac{1}{\hbar}E\Delta}|\psi(t+\Delta)\rangle + e^{-\frac{1}{\hbar}E\Delta}|\psi(t-\Delta)\rangle\Big) - \frac{i}{\hbar}\Big(\hat{H}-E\hat{I}\Delta\Big)|\psi(t)\rangle \\
&\quad + i\underbrace{\Big[\,\sin\Big(-\frac{1}{\hbar}(\hat{H}-E\hat{I})\Delta\Big) - \frac{1}{\hbar}(\hat{H}-E\hat{I})\Delta\Big]|\psi\rangle}_{O(\Delta^2)} \quad\quad (C.1)
\end{aligned}
$$

Ignoring the last term of the order of $O(\Delta^2)$, we finally have

$$
e^{\frac{i}{\hbar}E\Delta}|\psi(t+\Delta)\rangle = e^{-\frac{i}{\hbar}E\Delta}|\psi(t-\Delta)\rangle - \frac{2i\Delta}{\hbar}\Big(\hat{H}-E\hat{I}\Big)|\psi(t)\rangle \quad\quad (C.2)
$$

$$
|\psi(t+\Delta)\rangle = e^{\frac{i}{\hbar}E\Delta}\Big[e^{-\frac{i}{\hbar}E\Delta}|\psi(t-\Delta)\rangle - \frac{2i\Delta}{\hbar}\Big(\hat{H}-E\hat{I}\Big)|\psi(t)\rangle\Big] \quad\quad (C.3)
$$

We use C.3 for the propagation of the electron e_g and t_{2g} spinors.

The propagation of wave functions of the state n is

$$|\psi_n(+)\rangle \;=\; e^{\frac{i}{\hbar}E_n\Delta}\Big[e^{-\frac{i}{\hbar}E_n\Delta}|\psi_n(-)\rangle - \frac{2i\Delta}{\hbar}(\hat{H} - E_n\hat{I})|\psi_n(0)\rangle\Big] \qquad \text{(C.4)}$$

where the energy E_n is given by the expectation value of energy

$$E_n = \frac{\langle\psi(0)|\hat{H}|\psi(0)\rangle}{\langle\psi(0)|\psi(0)\rangle} \qquad \text{(C.5)}$$

Following are two considerations that need to be fulfilled to study the time evolution with C.4

- initial conditions are specified by choosing

$$|\psi_n(-)\rangle \;=\; (1 + \frac{1}{\hbar}\hat{H}\frac{\Delta}{n})^n|\psi(0)\rangle \qquad \text{(C.6)}$$

- regular correction steps during dynamics project out backward solution

$$|\psi_n(0)\rangle \;=\; |\psi_n(0)\rangle + \frac{1}{4}\Big(|\psi_n(+)\rangle e^{\frac{i}{\hbar}E_n\Delta} - 2|\psi_n(0)\rangle + |\psi_n(-)\rangle e^{\frac{i}{\hbar}E_n\Delta}\Big) \qquad \text{(C.7)}$$

Appendix D

Peierls substitution: initial state for optical excitation

work credit: Prof. P. E. Blöchl

Lets assume a Hamiltonian

$$\hat{H} = \frac{1}{2m_e}(\vec{p} - q\vec{A})^2 + V(\vec{r}) \tag{D.1}$$

in a basis of local orbitals $|\chi_\alpha\rangle$

We use the ansatz,

$$\langle\vec{r}|\tilde{\chi}_\alpha\rangle = \exp\left[\frac{i}{\hbar}q\int_{R_\alpha}^{\vec{r}} d\vec{r'}\vec{A}(\vec{r},t)\right]\langle\vec{r}|\chi_\alpha\rangle \tag{D.2}$$

where the integral of the vector potential is path dependent. Furthermore, we assume that the path is a straight line from the central atom $\vec{R_\alpha}$ to the position $\vec{r}$. substituting the above ansatz D.1, we get

$$
\begin{aligned}
\langle\vec{r}|(\vec{p} - q\vec{A})|\tilde{\chi}_\alpha\rangle &= \left(\frac{\hbar}{i}\vec{\nabla} - q\vec{A}\right)\langle\vec{r}|\tilde{\chi}_\alpha\rangle \\
&= \exp\left[\frac{i}{\hbar}q\int_{R_\alpha}^{\vec{r}} d\vec{r'}\vec{A}(\vec{r},t)\right]\left(\frac{\hbar}{i}\vec{\nabla} - q\vec{A}(\vec{r},t) + q\vec{A}(\vec{r},t)\right)\langle\vec{r}|\chi_\alpha\rangle \\
&= \exp\left[\frac{i}{\hbar}q\int_{R_\alpha}^{\vec{r}} d\vec{r'}\vec{A}(\vec{r},t)\right]\langle\vec{r}|\vec{p}|\chi_\alpha\rangle \tag{D.3}
\end{aligned}
$$

$$
\begin{aligned}
\langle \tilde{\chi}_\alpha | \hat{H}_o | \tilde{\chi}_\beta \rangle &= \langle r | \Big(\frac{1}{2m_e}(\vec{p} - q\vec{A})^2 + V(\vec{r}) \Big) \\
&\times \Big(\int dr'' |\vec{r''}\rangle \exp\Big[\frac{i}{\hbar}q \int_{R_\alpha}^{\vec{r''}} d\vec{r'}\vec{A}(\vec{r},t)\Big] \langle \vec{r''}| \Big) |\chi_\alpha\rangle \\
&= \exp\Big[\frac{i}{\hbar}q \int_{R_\alpha}^{\vec{r}} d\vec{r'}\vec{A}(\vec{r},t)\Big] \Big(\frac{\hbar}{i}\vec{\nabla} - q\vec{A}(\vec{r},t) + q\vec{A}(\vec{r},t) \Big) \langle \vec{r}|\chi_\alpha\rangle \\
&= \exp\Big[\frac{i}{\hbar}q \int_{R_\alpha}^{\vec{r}} d\vec{r'}\vec{A}(\vec{r},t)\Big] \langle \vec{r}| \frac{\vec{p}^2}{2m_e} + V(\vec{r})|\chi_\alpha\rangle \\
&= \exp\Big[\frac{i}{\hbar}q \int_{R_\alpha}^{\vec{r}} d\vec{r'}\vec{A}(\vec{r},t)\Big] \langle \vec{r}|\hat{H}_o|\chi_\alpha\rangle
\end{aligned}
\tag{D.4}
$$

The above equation gives the matrix element

$$
\begin{aligned}
\langle \vec{r}|\hat{H}|\tilde{\chi}_\alpha \rangle &= \langle \chi_\alpha | \exp\Big[-\frac{i}{\hbar}q\Big(\int_{R_\alpha}^{\vec{r}} d\vec{r'}\vec{A}(\vec{r},t) - \int_{R_\beta}^{\vec{r}} d\vec{r'}\vec{A}(\vec{r},t) \Big) \Big] \hat{H}_o|\chi_\beta\rangle \\
&= \exp\Big[\frac{i}{\hbar}q \int_{R_\alpha}^{\vec{r}} d\vec{r'}\vec{A}(\vec{r},t)\Big] \\
&\times \langle \chi_\alpha | \exp\Big[-\frac{i}{\hbar}q\Big(\int_{R_\alpha}^{R_\beta} d\vec{r'}\vec{A}(\vec{r},t) + \int_{\vec{r}}^{R_\beta} d\vec{r'}\vec{A}(\vec{r},t) + \int_{R_\beta}^{\vec{r}} d\vec{r'}\vec{A}(\vec{r},t) \Big) \Big] \hat{H}_o|\chi_\beta\rangle \\
&= \exp\Big[-\frac{i}{\hbar}q \int_{R_\alpha}^{\vec{r}} d\vec{r'}\vec{A}(\vec{r},t)\Big] \langle \chi_\alpha | e^{\frac{i}{\hbar}q\Phi_{\alpha,\beta(\vec{r})}} \hat{H}_o|\chi_\beta\rangle
\end{aligned}
\tag{D.5}
$$

We define a phase $\Phi_{\alpha,\beta(\vec{r})}$, which appear in the above equation D.5, as

$$
\Phi_{\alpha,\beta(\vec{r})} = \int_{R_\alpha}^{R_\beta} d\vec{r'}\vec{A}(\vec{r},t) + \int_{\vec{r}}^{R_\beta} d\vec{r'}\vec{A}(\vec{r},t) + \int_{R_\beta}^{\vec{r}} d\vec{r'}\vec{A}(\vec{r},t).
\tag{D.6}
$$

This is nothing but a magnetic flux through triangle $(\vec{R}_\alpha, \vec{R}_\beta, \vec{r})$

The factor

$$
\exp\Big[-\frac{i}{\hbar}q \int_{R_\alpha}^{\vec{r}} d\vec{r'}\vec{A}(\vec{r},t)\Big]
$$

is the Peierls phase which vanishes in large wave-vector limit.

The wave functions are obtained from eigenvalue problem

$$
\sum_\beta \Big[-\frac{i}{\hbar}q \int_{R_\alpha}^{R_\beta} d\vec{r'}\vec{A}(\vec{r},t)\Big][\tilde{H}_{\alpha,\beta} - \epsilon_n \tilde{O}_{\alpha,\beta}]c_{\alpha,n} = 0
\tag{D.7}
$$

with

$$
\begin{aligned}
\tilde{H}_{\alpha,\beta} &= \langle\chi_\alpha|e^{\frac{i}{\hbar}\Phi_{\alpha,\beta}(\vec{r}}\hat{H}_o|\chi_\beta\rangle \\
\tilde{O}_{\alpha,\beta} &= \langle\chi_\alpha|e^{\frac{i}{\hbar}\Phi_{\alpha,\beta}(\vec{r})}|\chi_\beta\rangle
\end{aligned}
\tag{D.8}
$$

as

$$
\begin{aligned}
\langle\vec{r}|\psi_n\rangle &= \sum_\alpha \langle\vec{r}|\tilde{\chi}_\alpha\rangle c_{\alpha,n} \\
&= \sum_\alpha \exp\Big[-\frac{i}{\hbar}q\int_{R_\alpha}^{\vec{r}} d\vec{r'}\vec{A}(\vec{r},t)\Big]\langle\vec{r}|\tilde{\chi}_\alpha\rangle c_{\alpha,n}
\end{aligned}
\tag{D.9}
$$

The Peierls substitution is without approximation if $\Phi_{\alpha,\beta}(\vec{r})$ is kept finite. The basis set needs to be local and can be non-orthogonal.

D.1 Electromagnetic field

Describe the excitation using electromagnetic field

$$
\vec{A}(\vec{r},t) = \frac{1}{2}\Big(\vec{e}_A A_o e^{i(\vec{k}x-\omega t)} + \vec{e}_A A_o^* e^{-i(\vec{k}x-\omega t)}\Big)\Phi(\vec{r},t) = 0
$$

$g(t)$ is a smooth envelope function which is normalized to one. We take it as a real number A_o is a complex amplitude. Now we take the long-wave length limit

$$
\begin{aligned}
\vec{A}(\vec{r},t) &= \vec{e}_A\frac{1}{2}\Big(A_o e^{i(\vec{k}x-\omega t)} + A_o^* e^{-i(\vec{k}x-\omega t)}\Big)g(t) \\
&+ \vec{e}_A\frac{1}{2}\Big(A_o i\vec{k}\vec{r}e^{i(\vec{k}x-\omega t)} + A_o^* i\vec{k}\vec{r}e^{-i(\vec{k}x-\omega t)}\Big)g(t) + O(|\vec{k}|^2)
\end{aligned}
\tag{D.10}
$$

The Peierls phase is in the long-wave length limit,

$$
\exp\Big[\frac{i}{\hbar}q\int_{R_\alpha}^{R_\beta} d\tilde{r'}\tilde{A}(\tilde{r},t)\Big] \sim \exp\Big[\frac{i}{\hbar}q\tilde{e}_A(\tilde{R}_\alpha-\tilde{R}_\beta)\mathrm{Re}[A_o e^{i\omega t}]g(t)\Big]
\tag{D.11}
$$

Appendix E

Verlet algorithm

The equation of motion, which is second order differential equation in the presence of friction is expressed by

$$m\ddot{x} = F(x) - \gamma\dot{x} \tag{E.1}$$

where m is the mass of the classical particle, x(t) is the displacement vector at time t, $F(x) =$ is the force on the particle and γ is the term responsible for friction which is proportional to the velocity of the particle.

Equation E.1 is discretised by choosing a time step $\Delta > 0$ and replacing the first and second order derivative by,

$$
\begin{aligned}
\dot{x} &\to \frac{x(t+\Delta) - x(t-\Delta)}{2\Delta} \\
\ddot{x} &\to \frac{x(t+\Delta) - 2x(t) + x(t-\Delta)}{\Delta^2}
\end{aligned} \tag{E.2}
$$

Finally we have

$$x(t+\Delta) = x(t)\frac{2}{1+a} - x(t-\Delta)\frac{1-a}{1+a} + F\frac{\Delta^2}{m(1+a)} \tag{E.3}$$

with $a = \frac{\gamma\Delta}{2m}$.

Appendix F

k-space grid

By exploiting the Bloch theorem for a periodic system, it is possible to replace any integrals in real space over the entire system (infinite system) by integrals over the (finite) first Brillouin zone in reciprocal space. In practice, we choose a finite k-space grid as we assume the solutions to the Schroedinger equation changes smoothly with k, and we take summation over all the points in k-space grid instead of integral over entire k space.

We find out the choice of dimensions of k-space grid by repeating a sequence of calculations for size of k-space grid and choosing the one that gives us converged results.

Let us assume our unit cell has N_1, N_2 and N_3 Mn sites in the x, y and z directions, respectively. The corresponding reciprocal lattice vectors are following:

$$G_a = \frac{2\pi \times N_2 \times N_3}{N_1 \times N_2 \times N3} \tag{F.1}$$

$$G_b = \frac{2\pi \times N_1 \times N_3}{N_1 \times N_2 \times N3} \tag{F.2}$$

$$G_c = \frac{2\pi \times N_1 \times N_2}{N_1 \times N_2 \times N3} \tag{F.3}$$

Now we set our k-space grid. Let us take a k-points grid of N_{k_1}, N_{k_2} and N_{k_3} dimensions. The k-space vectors $K_{\vec{j},i_1,i_2,i_3}$ that we include in our calculations and falls in first Brillouin zone of reciprocal space, are as follows:

$$K_{1,i_1,i_2,i_3} = -\frac{G_a}{2} + (i_1 - 1)\frac{G_a}{(N_{k_1} \times N_{k_2} \times N_{k_3})} \tag{F.4}$$

$$K_{2,i_1,i_2,i_3} = -\frac{G_b}{2} + (i_2 - 1)\frac{G_b}{(N_{k_1} \times N_{k_2} \times N_{k_3})} \tag{F.5}$$

$$K_{3,i_1,i_2,i_3} = -\frac{G_c}{2} + (i_3 - 1)\frac{G_c}{(N_{k_1} \times N_{k_2} \times N_{k_3})} \tag{F.6}$$

where $i_1 = 1,2,...N_{k_1}$, $i_2 = 1,2,...N_{k_2}$, and $i_3 = 1,2,...N_{k_3}$.

Appendix G

Hamiltonian matrix elements from the generalized Dos

The present content is from appendix section of Sotoudeh et al. [15].
work credit: Prof. P. E. Blöchl

Here we show how the Hamilton matrix elements can be obtained from the generalised Density of states of a first-principles calculation.

G.1 Hamiltonian of a non-orthonormal basis set

Let $|\psi_n\rangle$ be the Kohn-Sham states of a density- functional calculation and let f_n be their occupation. The Kohn Sham states are eigenstates of the Kohn-Sham Hamiltonian $\hat{H}$ with energies ϵ_n. We construct a basis-set of local orbitals $|\chi_\alpha\rangle$ by projecting the projector functions $|p_\alpha\rangle$ onto the Kohn-Sham states in a given energy window [a, b]. We denote the set of states with energies in the window by M.

$$|\chi_\alpha\rangle = \sum_{n\epsilon M} |\psi_n\rangle\langle\psi_n|p_\alpha\rangle \tag{G.1}$$

Hamilton and overlap matrix for this basis-set can be expressed by the generalised Density of states, which has matrix elements

$$|\chi_\alpha\rangle = \sum_{n\epsilon M} |\psi_n\rangle\langle\psi_n|p_\alpha\rangle \tag{G.2}$$

The matrix elements $H_{\alpha,\beta}$ of the Hamiltonian and those, $O_{\alpha,\beta}$ of the overlap matrix elements are

$$H_{\alpha,\beta} = \langle\chi_\alpha|\hat{H}|\chi_\beta\rangle = \int_a^b d\epsilon D_{\alpha,\beta}(\epsilon)\epsilon \tag{G.3}$$

$$O_{\alpha,\beta} = \langle \chi_\alpha | \chi_\beta \rangle = \int_a^b d\epsilon D_{\alpha,\beta}(\epsilon) \tag{G.4}$$

G.2   Hamiltonian of an orthonormal basis set

We assume an orthonormal basis set for the proposed tight-binding model. Here, we perform an approximate orthonormalisation.

$$|\chi'_\alpha\rangle = \sum_\beta |\chi'_\beta\rangle (\boldsymbol{O}^{-\frac{1}{2}})_{\beta,\alpha} \tag{G.5}$$

The new Hamiltonian h in the $\{|\chi'_\alpha\rangle\}$ basis set is evaluated to first order in the off-diagonal elements of the Hamiltonian and overlap matrix. This gives,

$$
\begin{aligned}
h_{\alpha,\beta} &= \frac{H_{\alpha,\beta}}{\sqrt{O_{\alpha,\alpha}O_{\beta,\beta}}} - \frac{1}{2}\Big(\frac{H_{\alpha,\alpha}}{O_{\alpha,\alpha}} + \frac{H_{\beta,\beta}}{O_{\beta,\beta}}\Big) \times \Big(\frac{O_{\alpha,\beta}}{\sqrt{O_{\alpha,\alpha}O_{\beta,\beta}}} - \delta_{\alpha,\beta}\Big) & \text{(G.6)} \\
&= \epsilon_{\alpha,\beta} + t_{\alpha,\beta} & \text{(G.7)}
\end{aligned}
$$

where

$$
\begin{aligned}
\epsilon_\alpha &= \frac{H_{\alpha,\alpha}}{O_{\alpha,\alpha}} & \text{(G.8)} \\
\Delta_{\alpha,\beta} &= \frac{O_{\alpha,\beta}}{\sqrt{O_{\alpha,\alpha}O_{\beta,\beta}}} - \delta_{\alpha,\beta} & \text{(G.9)} \\
t_{\alpha,\beta} &= \frac{H_{\alpha,\beta}}{\sqrt{O_{\alpha,\alpha}O_{\beta,\beta}}} - \epsilon_\alpha\delta_{\alpha,\beta} - \frac{\epsilon_\alpha + \epsilon_\beta}{2}\Delta_{\alpha,\beta} & \text{(G.10)}
\end{aligned}
$$

The diagonal elements of the matrix t of the hopping parameters vanishes. The Hamilton-matrix elements used to extract the hopping parameter t_{hop} are obtained from Equation G.7 by inserting Equations G.3 and G.4.

G.3   Splitting of onsite orbitals

To obtain the hopping parameters, the orbitals are expressed in a local coordinate system suitable for a individual Mn-O-Mn bridge. The $d_{3z^2-r^2}$ orbitals are assumed to be along the local z-axis and directed towards the bridging oxygen atom of the Mn-O-Mn bridge. The three onsite energies ϵ_α obtained from the onsite energies of the three octahedral axes contain the full information for the onsite Hamiltonian of a given Mn-site. The quantity of interest for the parameterisation is the energy separation of the two onsite levels,

which enters the parameter determination as $\Delta^\uparrow$ and $\Delta^\downarrow$, respectively. For each site, we obtain the onsite hamiltonian expectation values $\bar{h}_{i,i}$ for three non-orthonormal orbitals $d_{3x^2-r^2}$, $d_{3y^2-r^2}$, $d_{3z^2-r^2}$ aligned with the three octahedral axes from the corresponding level energies ϵ_α. The bar on top of the symbol $\bar{h}_{i,i}$ shall avoid confusion with the matrix elements in the basis $\{|a\rangle, |b\rangle\}$

The splitting Δ between the two levels can be evaluated from the matrix elements $\bar{h}_{i,i}$ as

$$\Delta = 2\sqrt{2}\sqrt{\frac{1}{3}\left[\bar{h}_{i,i} - \left(\frac{1}{3}\sum_{j=1}^{3}\bar{h}_{i,i}\right)\right]^2} \tag{G.11}$$

The matrix elements $\bar{h}_{ii}$ correspond to the level energy in Equation G.7 and G.10

Appendix H

Additional data: measurable quantities

Here, we include the measurable physical quantities for different set of magnetic orders for the entire range of doping in the $P_{1-x}Ca_xMnO_3$ series manganites. The calculations are performed in two ways:

Collinear spins: The calculations with collinear spins are performed by optimising the structure by keeping the spin degrees of freedom fixed.

Non-collinear spins: The non-collinear calculations are performed by following the above scheme of the **collinear spins** calculation unless the system is close to convergence. Thereafter, the spins are allowed to optimise themselves with other degrees of freedom.

During the calculations, two precautions are needed:

- Before we continue with the non-collinear spin calculations, there must be sufficient kinetic energy available to the variable degrees of freedom to come out of the local minima of the atomic and collinear spin arrangement. This way we allow the system to explore the new minima in the nearby phase-space which has lower energy than the one we start with.

- On the other hand, we also make sure to not continue with the non-collinear spin calculations far away from the convergence where the variable degrees of freedom have large kinetic energies. If we do not follow this, we may end up with high energy metastable states with point defects characterised by several local spins and atomic disorders. Sometimes, we need to repeat these calculations several times to obtain the low-lying metastable states.

Table H.1: Energy per Mn, average Mn-Mn length L_a and L_c in the x/y and z direction, respectively, and the band gap as a function of number of electron N_e. The symbol A_1 and A_2 refers to collinear and non-collinear calculations, respectively for the A-type magnetic phase. N_e indicates the total number of electrons and N_{tot} indicates the total number of Mn sites in the unit cell.

N_e	N_{tot}	magnetic structure	E/Mn [eV]	L_a (A°)	L_b (A°)	band gap [eV]
16	64	A_1	1.2315	3.9341	3.8370	0.2267
18	64	A_1	1.3879	3.9426	3.8377	0.0343
20	64	A_1	1.5434	3.9518	3.8374	0.1273
22	64	A_1	1.7001	3.9598	3.8393	0.1244
24	64	A_1	1.8564	3.9683	3.8401	0.2727
26	64	A_1	2.0155	3.9743	3.8460	0.0005
28	64	A_1	2.1728	3.9801	3.8523	0.2291
30	64	A_1	2.3310	3.9895	3.8513	0.1709
32	64	A_1	2.4883	4.0026	3.8430	0.2762
34	64	A_1	2.6531	4.0191	3.8280	0.0035
36	64	A_1	2.8165	4.0285	3.8271	0.0030
38	64	A_1	2.9821	4.0299	3.8421	0.0120
40	64	A_1	3.1391	4.0119	3.8960	0.1480
42	64	A_1	3.3002	4.0139	3.9099	0.2144
44	64	A_1	3.4627	4.0111	3.9333	0.2411
46	64	A_1	3.6246	4.0189	3.9358	0.2280
48	64	A_1	3.7895	4.0154	3.9606	0.3355
50	64	A_1	3.9538	4.0174	3.9745	0.2525
52	64	A_1	4.1149	4.0132	4.0007	0.3377
54	64	A_1	4.2834	4.0153	4.0144	0.3165
56	64	A_1	4.4378	4.0077	4.0476	0.6653
56*	64	A_1	4.7166	3.9094	3.8175	0.7170
58	64	A_1	4.6087	4.0120	4.0569	0.3826
60	64	A_1	4.7673	4.0067	4.0853	0.5597
62	64	A_1	4.9312	4.0041	4.1085	0.5532
64	64	A_1	5.0931	4.0009	4.1326	0.9698
72	72	A_1	5.0932	4.0007	4.1326	0.9708
216	216	A_1	5.0932	4.0008	4.1327	0.9700
64*	64	A_1 with experimental lattice vector	5.3619	3.9796	3.7928	0.9192
42	64	A_2	3.2919	3.9967	3.9443	0.4977
44	64	A_2	3.4555	3.9977	3.9601	0.5200
46	64	A_2	3.6183	4.0094	3.9548	0.4346
54	64	A_2	4.2778	4.0153	4.0145	0.4343
56	64	A_2	4.4345	4.0068	4.0494	0.6493
58	64	A_2	4.6054	4.0099	4.0611	0.4414
60	64	A_2	4.7656	4.0068	4.0851	0.5744
62	64	A_2	4.9305	4.0044	4.1079	0.7181

Table H.2: Energy per Mn, average Mn-Mn length L_a and L_c in the x/y and z direction, respectively, and band gap as a function of number of electron N_e. The symbol B_1 and B_2 refers to collinear and non-collinear calculations for the B-type magnetic phase, respectively. N_e indicates the total number of electrons and N_{tot} indicates the total number of Mn sites in the unit cell.

N_e	N_{tot}	magnetic structure	E/Mn [eV]	L_a (A°)	L_b (A°)	band gap [eV]
16	64	B_1	1.2345	3.9031	3.8990	0.0079
18	64	B_1	1.3868	3.9077	3.9076	0.0152
20	64	B_1	1.5409	3.9136	3.9136	0.0022
22	64	B_1	1.6962	3.9200	3.9186	0.0000
24	64	B_1	1.8528	3.9234	3.9299	0.0000
26	64	B_1	2.0093	3.9286	3.9374	0.0008
28	64	B_1	2.1664	3.9358	3.9409	0.0005
30	64	B_1	2.3248	3.9400	3.9503	0.0000
32	64	B_1	2.4833	3.9470	3.9543	0.0019
34	64	B_1	2.6424	3.9533	3.9595	0.0016
36	64	B_1	2.8026	3.9611	3.9617	0.0016
38	64	B_1	2.9642	3.9670	3.9679	0.0000
40	64	B_1	3.1261	3.9726	3.9747	0.0008
42	64	B_1	3.2894	3.9780	3.9817	0.0008
44	64	B_1	3.4529	4.0111	3.9333	0.2411
46	64	B_1	3.6170	3.9870	3.9994	0.0000
48	64	B_1	3.7704	3.9970	3.9974	0.2060
50	64	B_1	3.9389	4.0040	4.0012	0.0095
52	64	B_1	4.1062	4.0098	4.0076	0.0014
54	64	B_1	4.2750	4.0147	4.0157	0.0016
56	64	B_1	4.4443	4.0210	4.0210	0.0109
58	64	B_1	4.6148	4.0275	4.0257	0.0014
60	64	B_1	4.7856	4.0320	4.0347	0.0005
62	64	B_1	4.9552	4.0412	4.0343	0.0506
64	64	B_1	5.1238	4.0448	4.0448	0.6659

Table H.3: Energy per Mn,average Mn-Mn length L_a and L_c in the x/y and z direction, respectively, and band gap as a function of number of electron N_e. The symbol C_1 and C_2 refers to collinear and non-collinear calculations, respectively for the C-type magnetic phase. N_e indicates the total number of electrons and N_{tot} indicates the total number of Mn sites in the unit cell.

N_e	N_{tot}	magnetic structure	E/Mn [eV]	L_a (A°)	L_b (A°)	band gap [eV]
16	64	C_1	1.2172	3.8625	3.9800	0.4931
18	64	C_1	1.3809	3.8663	3.9904	0.1132
20	64	C_1	1.5432	3.8675	4.0060	0.0778
22	64	C_1	1.7034	3.8661	4.0266	0.0014
24	64	C_1	1.8629	3.8673	4.0420	0.0027
26	64	C_1	2.0206	3.8692	4.0562	0.0024
28	64	C_1	2.1781	3.8700	4.0725	0.0000
30	64	C_1	2.3331	3.8695	4.0913	0.0008
32	64	C_1	2.4869	3.8700	4.1083	0.4963
34	64	C_1	2.6522	3.8817	4.1028	0.4446
36	64	C_1	2.8148	3.8956	4.0928	0.4615
38	64	C_1	2.9824	3.9088	4.0843	0.3840
40	64	C_1	3.1429	3.9197	4.0803	0.5584
42	64	C_1	3.3051	3.9294	4.0789	0.5437
44	64	C_1	3.4689	3.9406	4.0744	0.5948
46	64	C_1	3.6318	3.9513	4.0708	0.5448
48	64	C_1	3.7943	3.9597	4.0719	0.6351
50	64	C_1	3.9584	3.9702	4.0688	0.6082
52	64	C_1	4.1232	3.9828	4.0615	0.6218
54	64	C_1	4.2885	3.9939	4.0572	0.6204
56	64	C_1	4.4611	4.0073	4.0484	0.6207
58	64	C_1	4.6192	4.0144	4.0519	0.8294
60	64	C_1	4.7856	4.0252	4.0483	0.5992
62	64	C_1	4.9614	4.0384	4.0397	0.5546
64	64	C_1	5.1221	4.0473	4.0400	0.7304
16	64	C_2	1.2160	3.8634	3.9783	0.5372
16	64	C_2	1.2159	3.8630	3.9790	0.5372
18	64	C_2	1.3752	3.8751	3.9727	0.2362
20	64	C_2	1.5319	3.8892	3.9625	0.1867
22	64	C_2	1.6904	3.9005	3.9578	0.0014
24	64	C_2	1.8497	3.9106	3.9555	0.4580
26	64	C_2	2.0200	3.8735	4.0475	0.0493
28	64	C_2	2.1691	3.9328	3.9470	0.2846
30	64	C_2	2.3330	3.8708	4.0888	0.0166
32	64	C_2	2.4869	3.8700	4.1083	0.4963
34	64	C_2	2.6506	3.8817	4.1028	0.4327
36	64	C_2	2.8081	3.9552	3.9737	0.3889
38	64	C_2	2.9679	3.9508	4.0004	0.4689
40	64	C_2	3.1331	3.9472	4.0254	0.3646
42	64	C_2	3.2949	3.9656	4.0065	0.3540
44	64	C_2	3.4583	3.9621	4.0314	0.4585
46	64	C_2	3.6211	3.9702	4.0330	0.4667

Table H.4: Energy per Mn, average Mn-Mn length L_a and L_c in the x/y and z direction, respectively, and band gap as a function of number of electron N_e. The symbol G_1 and G_2 refers to collinear and non-collinear calculations, respectively for the G-type magnetic phase. N_e indicates the total number of electrons and N_{tot} indicates the total number of Mn sites in the unit cell.

N_e	N_{tot}	magnetic structure	E/Mn [eV]	L_a (A°)	L_b (A°)	band gap [eV]
16	64	G_1	1.2424	3.8970	3.9111	0.8780
18	64	G_1	1.3994	3.8991	3.9248	0.0465
20	64	G_1	1.5600	3.9127	3.9156	0.0188
22	64	G_1	1.7158	3.9028	3.9532	0.0389
24	64	G_1	1.8767	3.9123	3.9520	0.5483
26	64	G_1	2.0365	3.9281	3.9383	0.5978
28	64	G_1	2.1963	3.9729	3.8666	0.7225
30	64	G_1	2.3573	3.9417	3.9470	0.7078
32	64	G_1	2.5189	3.9470	3.9542	0.7761
34	64	G_1	2.6816	3.9564	3.9533	0.7625
36	64	G_1	2.8440	3.9578	3.9684	0.7763
38	64	G_1	3.0066	3.9636	3.9748	0.8036
40	64	G_1	3.1701	3.9756	3.9687	0.7861
42	64	G_1	3.3331	3.9791	3.9795	0.8517
44	64	G_1	3.4965	3.9845	3.9867	0.8702
46	64	G_1	3.6607	3.9831	4.0074	0.8406
48	64	G_1	3.8237	3.9715	4.0483	0.9334
50	64	G_1	3.9878	4.0297	3.9498	0.9597
52	64	G_1	4.1514	3.9858	4.0556	0.9769
54	64	G_1	4.3154	3.9936	4.0578	1.0044
56	64	G_1	4.4795	4.0024	4.0581	1.0354
58	64	G_1	4.6437	4.0177	4.0454	1.1132
60	64	G_1	4.8082	4.0482	4.0023	1.1467
62	64	G_1	4.9726	4.0417	4.0332	1.1715
64	64	G_1	5.1374	4.0447	4.0450	1.1578

Table H.5: Energy per Mn, average Mn-Mn length L_a and L_c in the x/y and z direction, respectively, and band gap as a function of number of electron N_e. The symbol CE_1 and CE_2 refers to collinear and non-collinear calculations, respectively for the CE-type magnetic phase. N_e indicates the total number of electrons and N_{tot} indicates the total number of Mn sites in the unit cell.

N_e	N_{tot}	magnetic structure	E/Mn [eV]	L_a (A°)	L_b (A°)	band gap [eV]
22	64	CE_1	1.6983	3.9588	3.8411	0.4155
24	64	CE_1	1.8532	3.9653	3.8461	0.4977
26	64	CE_1	2.0096	3.9717	3.8512	0.4901
28	64	CE_1	2.1656	3.9758	3.8608	0.5374
30	64	CE_1	2.3215	3.9838	3.8629	0.5385
32	64	CE_1	2.4771	3.9895	3.8693	0.7216
34	64	CE_1	2.6440	3.9830	3.9001	0.4678
36	64	CE_1	2.8069	3.9717	3.9407	0.7377
38	64	CE_1	2.9753	3.9724	3.9571	0.4601
40	64	CE_1 **(I-type)**	3.1280	3.9781	3.9635	0.6460
40	64	CE_1 **(II-type)**	3.1393	3.9807	3.9582	0.5701
42	64	CE_1	3.3030	3.9859	3.9659	0.4446
44	64	CE_1	3.3030	3.9961	3.9634	0.2958
46	64	CE_1	3.6335	4.0007	3.9720	0.5725
48	64	CE_1	3.7994	3.9948	4.0019	0.5774
22	64	CE_2	1.6926	3.9323	3.8942	0.4084
24	64	CE_2	1.8532	3.9650	3.8466	0.4868
26	64	CE_2	2.0096	3.9715	3.8515	0.4838
28	64	CE_2	2.1656	3.9758	3.8608	0.5374
30	64	CE_2	2.3215	3.9838	3.8629	0.5385
31	64	CE_2	2.3993	3.9758	3.8608	0.5374
33	64	CE_2	2.5608	3.9891	3.8789	0.4863
34	64	CE_2	2.6432	3.9837	3.8987	0.3611
36	64	CE_2	2.8053	3.9718	3.9405	0.5668
38	64	CE_2	2.9679	3.9794	3.9430	0.4792
40	64	CE_2	3.1288	3.9857	3.9484	0.4601
42	64	CE_2	3.2934	4.0041	3.9295	0.4136
44	64	CE_2	3.4570	4.0047	3.9461	0.2713
46	64	CE_2	3.6154	3.9961	3.9814	0.2471
48	64	CE_2	3.7797	4.0079	3.9755	0.4463
24	72	WC_1	1.6352	3.9472	3.8583	0.5488
24	72	BS_1	1.6372	3.9512	3.8504	0.3760
24	72	WC_2	1.6341	3.9483	3.8560	0.6087
24	72	BS_2	1.6372	3.9425	3.8678	0.5132
48	128	DS_2	1.8489	3.9602	3.8561	0.5300

Table H.6: Energy per Mn, average Mn-Mn length L_a and L_c in the x/y and z direction, respectively, and band gap as a function of number of electron N_e. The symbol E_1 and E_2 refers to collinear and non-collinear calculations, respectively for the E-type magnetic phase. N_e indicates the total number of electrons and N_{tot} indicates the total number of Mn sites in the unit cell.

N_e	N_{tot}	magnetic structure	E/Mn [eV]	L_a (A°)	L_b (A°)	band gap [eV]
26	64	E_1	2.0236	3.9848	3.8250	0.5573
28	64	E_1	2.1820	3.9925	3.8276	0.5415
30	64	E_1	2.3388	4.0085	3.8133	0.5690
32	64	E_1	2.4942	4.0222	3.8038	0.6449
34	64	E_1	2.6589	4.0254	3.8153	0.5554
36	64	E_1	2.8219	4.0257	3.8326	0.5976
38	64	E_1	2.9839	4.0245	3.8530	0.5750
40	64	E_1	3.1453	4.0218	3.8762	0.6697
42	64	E_1	3.3071	4.0231	3.8915	0.7755
44	64	E_1	3.4713	4.0229	3.9097	0.7336
26	64	E_2	2.0095	3.9585	3.8777	0.4903
28	64	E_2	2.1658	3.9613	3.8898	0.4650
30	64	E_2	2.3227	3.9711	3.8882	0.4708
32	64	E_2	2.4784	3.9801	3.8881	0.7086
34	64	E_2	2.6433	3.9616	3.9428	0.4612
36	64	E_2	2.8087	3.9732	3.9376	0.4343
38	64	E_2	2.9698	3.9891	3.9238	0.3883
40	64	E_2	3.1348	4.0020	3.9158	0.4754
42	64	E_2	3.2987	4.0020	3.9338	0.5478
44	64	E_2	3.4601	4.0044	3.9468	0.4672

Table H.7: Ferromagnetic clusters in the $0.89 < x < 1$ doping region: Energy per Mn, average Mn-Mn length L_a and L_c in the x/y and z direction, respectively, and band gap as a function of number of electron N_e. The symbol P_i^{Br} and P_j^{Lr} refers to the presence of i number of five-site breathing polaron and j number of thirteen-site large polarons in the system. G_1 refers to pure G-type magnetic order. N_e indicates the total number of electrons and N_{tot} indicates the total number of Mn sites in the unit cell.

N_e	N_{tot}	polaron type or magnetic order	E/Mn [eV]	L_a (A°)	L_b (A°)	band gap [eV]
1	216	G_1	-0.0210	3.8554	3.8543	0.2667
2	216	P_1^{Br}	0.0022	3.8561	3.8557	0.3083
3	216	P_1^{Lr}	0.0258	3.8567	3.8573	0.2667
6	216	P_2^{Lr}	0.0966	3.8588	3.8612	0.3083
9	216	P_3^{Lr}	0.1671	3.8605	3.8652	0.2419
12	216	P_4^{Lr}	0.2375	3.8620	3.8701	0.3048
15	216	P_5^{Lr}	0.3085	3.8649	3.8720	0.3047
18	216	P_6^{Lr}	0.3794	3.8675	3.8745	0.2133
21	216	P_7^{Lr}	0.4503	3.8699	3.8772	0.2370
24	216	P_8^{Lr}	0.5212	3.8803	3.8722	0.2601

Table H.8: Amplitude of octahedral distortion on various sites for individual doping case below $x = 0.5$ doping. The $P^{U_{Mc}}$ and $P^{U_{Me}}$ sites indicate the central and corner sites of the P^U polaron, respectively. N_e indicates the total number of electrons and N_{tot} indicates the total number of Mn sites in the unit cell. Abbreviation used: A_1- collinear A-type, A_2- collinear A-type, B_1- collinear B-type, CE_2- non-collinear CE-type, CE_1- collinear CE-type

N_e	N_{tot}	magnetic structure	site type	$\|Q_1\|$ (A°)	$\|Q_2\|$ (A°)	$\|Q_3\|$ (A°)	$\sqrt{Q_1^2 + Q_2^2}$ (A°)	$\sqrt{Q_1^2 + Q_2^2 + Q_3^2}$ (A°)
64	64	A_1	P^{JT_1}	0.289	0.153	0.110	0.327	0.345
60	64	A_2	P^{JT_1}	0.285	0.098	0.090	0.303	0.317
			P^{JT_2}	0.000	0.374	0.100	0.374	0.388
			P^H	0.000	0.082	0.137	0.082	0.160
56	64	A_2	P^{JT_1}	0.283	0.036	0.070	0.287	0.295
			P^{JT_2}	0.003	0.344	0.081	0.344	0.353
			P^H	0.000	0.049	0.155	0.049	0.162
48	64	B_1	P^{JT_2}	0.153	0.159	0.294	0.239	0.379
			P^H	0.005	0.010	0.110	0.011	0.110
44	64	A_2	P^{JT_2}	0.140	0.206	0.284	0.278	0.398
			P^H	0.015	0.017	0.092	0.024	0.096
40	64	CE_2	$P^{U_{Mc}}$	0.242	0.137	0.274	0.292	0.400
			P^{JT_2}	0.156	0.224	0.287	0.273	0.397
			$P^{U_{Me}}$	0.021	0.018	0.088	0.033	0.094
40	64	CE_2 **I-type** (1st xy plane)	$P^{U_{Mc}}$	0.242	0.137	0.274	0.292	0.400
			P^{JT_2}	0.156	0.224	0.287	0.273	0.397
40	64	CE_2 **I-type** (2nd, 3rd & 4th xy plane)	$P^{U_{Mc}}$	0.242	0.137	0.274	0.292	0.400
			$P^{U_{Me}}$	0.030	0.009	0.097	0.032	0.102
40	64	CE_2 **I-type** (3rd xy plane)	$P^{U_{Mc}}$	0.242	0.137	0.274	0.292	0.400
			P^{JT_2}	0.001	0.035	0.070	0.035	0.078
36	64	CE_2	$P^{U_{Mc}}$	0.290	0.085	0.273	0.305	0.409
			P^{JT_2}	0.182	0.166	0.273	0.247	0.368
			$P^{U_{Me}}$	0.010	0.028	0.074	0.032	0.082
34	64	CE_2	$P^{U_{Mc}}$	0.272	0.132	0.264	0.305	0.404
			P^{JT_2}	0.196	0.095	0.250	0.218	0.332
			$P^{U_{Me}}$	0.006	0.030	0.077	0.031	0.088
32	64	CE_1	$P^{U_{Mc}}$	0.259	0.163	0.257	0.306	0.400
			$P^{U_{Mc}}$	0.000	0.033	0.074	0.033	0.081

Table H.9: Amplitude of octahedral distortion on various sites for $x = 0.375$ doping. The $P^{U_{Mc}}$ and $P^{U_{Me}}$ sites indicate the central and corner sites of the P^U polaron, respectively. N_e indicates the total number of electrons and N_{tot} indicates the total number of Mn sites in the unit cell. Abbreviation used: CE_2- non-collinear CE-type

N_e	N_{tot}	magnetic structure	site type	$\|Q_1\|$ (A°)	$\|Q_2\|$ (A°)	$\|Q_3\|$ (A°)	$\sqrt{Q_1^2 + Q_2^2}$ (A°)	$\sqrt{Q_1^2 + Q_2^2 + Q_3^2}$ (A°)
40	64	CE$_2$ **II-type**	$P^{U_{Mc}}$	0.258	0.096	0.270	0.289	0.396
			P^{JT_2}	0.150	0.214	0.289	0.261	0.390
			$P^{U_{Me}}$	0.029	0.023	0.085	0.042	0.095
40	64	CE$_2$ **II-type** (1st xy plane)	$P^{U_{Mc}}$	0.258	0.096	0.270	0.289	0.396
			P^{JT_2}	0.150	0.214	0.289	0.261	0.390
40	64	CE$_2$ **II-type** (2nd, 3rd & 4th xy plane)	$P^{U_{Mc}}$	0.258	0.096	0.270	0.289	0.396
			$P^{U_{Me}}$	0.029	0.023	0.085	0.042	0.095

Table H.10: Amplitude of octahedral distortion on various sites for individual doping case above $x = 0.5$ doping. The $P^{U_{Mc}}$ and $P^{U_{Me}}$ sites indicate the central and corner sites of the P^U polaron, respectively. N_e indicates the total number of electrons and N_{tot} indicates the total number of Mn sites in the unit cell. Abbreviation used: G_1- collinear G-type , C_2- non-collinear C-type, WC_2- Wigner crystal phase, CE_2- non-collinear CE-type, CE_1- collinear CE-type, DS_2- double-stripe phase (non-collinear).

| N_e	N_{tot}	magnetic structure	site type	$\|Q_1\|$ (in A°)	$\|Q_2\|$ (in A°)	$\|Q_3\|$ (A°)	$\sqrt{Q_1^2 + Q_2^2}$ (A°)	$\sqrt{Q_1^2 + Q_2^2 + Q_3^2}$ (A°)
0	64	G$_1$	P^{JT_1}	0.0	0.0	0.0	0.0	0.0
16	64	C$_2$	$P^{U_{Mc}}$	0.003	0.281	0.222	0.281	0.359
			$P^{U_{Me}}$	0.002	0.042	0.045	0.042	0.062
			P^H	0.005	0.007	0.016	0.009	0.018
16	64	C$_2$	$P^{U_{Mc}}$	0.003	0.281	0.222	0.281	0.359
			$P^{U_{Me}}$	0.002	0.043	0.046	0.043	0.063
			P^H	0.005	0.007	0.016	0.009	0.018
24	72	WC	$P^{U_{Mc}}$	0.226	0.166	0.238	0.280	0.368
			P^H	0.036	0.030	0.046	0.047	0.066
62	128	DS	$P^{U_{Mc}}$	0.203	0.186	0.240	0.283	0.371
			$P^{U_{Me}}$	0.020	0.024	0.054	0.035	0.067
28	64	CE$_2$	$P^{U_{Mc}}$	0.249	0.159	0.243	0.299	0.385
			P^{JT_2}	0.000	0.307	0.275	0.307	0.412
			$P^{U_{Me}}$	0.009	0.027	0.065	0.031	0.076
30	64	CE$_1$	$P^{U_{Mc}}$	0.249	0.167	0.253	0.303	0.395
			P^{JT_2}	0.009	0.297	0.272	0.297	0.403
			$P^{U_{Me}}$	0.009	0.031	0.068	0.034	0.077

Appendix I

Atomic and spin structure

Here, we include the plots of the atomic structure and spin order directly obtained through our calculations for each of the doping case, which is discussed in Chapter 4. Below is the scheme to read the graphs.

The top part of each figure show the atomic structure plot and the bottom part shows the corresponding spin structure in the consecutive xy planes (Z=1,2,3...) of the unit cell. The dashed black grid is the grid of Mn sites. The integer values on the y and x axis indicate the indexing (x,y) of the Mn sites in the xy plane.

Top: The horizontal and vertical line (i.e., green or red) at each Mn site indicate the deviation of the O-O bond length of the MnO_6 octahedra surrounding that Mn site, from the CMO system in the x and y directions, respectively. The radius of the circle indicate the deviation of the O-O bond length in the z direction. The green and red imply the positive (increase in the bond length) and negative (decrease in the bond length) deviations of these O-O bond lengths, respectively.

Bottom: The horizontal and vertical lines (i.e., green or red lines) at each Mn site indicate the components of the t_{2g} spin in the x and y directions, respectively. The radius of the circle around each Mn site shows the z component of the t_{2g} spin of that Mn atom. The green and red imply the positive and negative spin components, respectively.
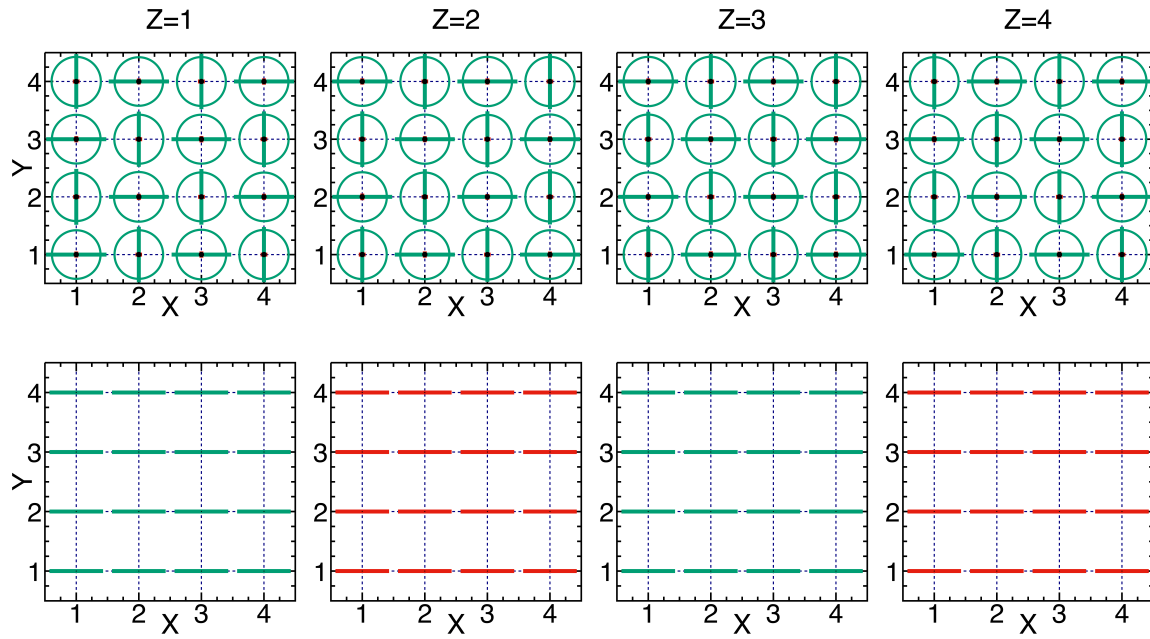
Figure I.1: $x = 0$: with variable lattice constants
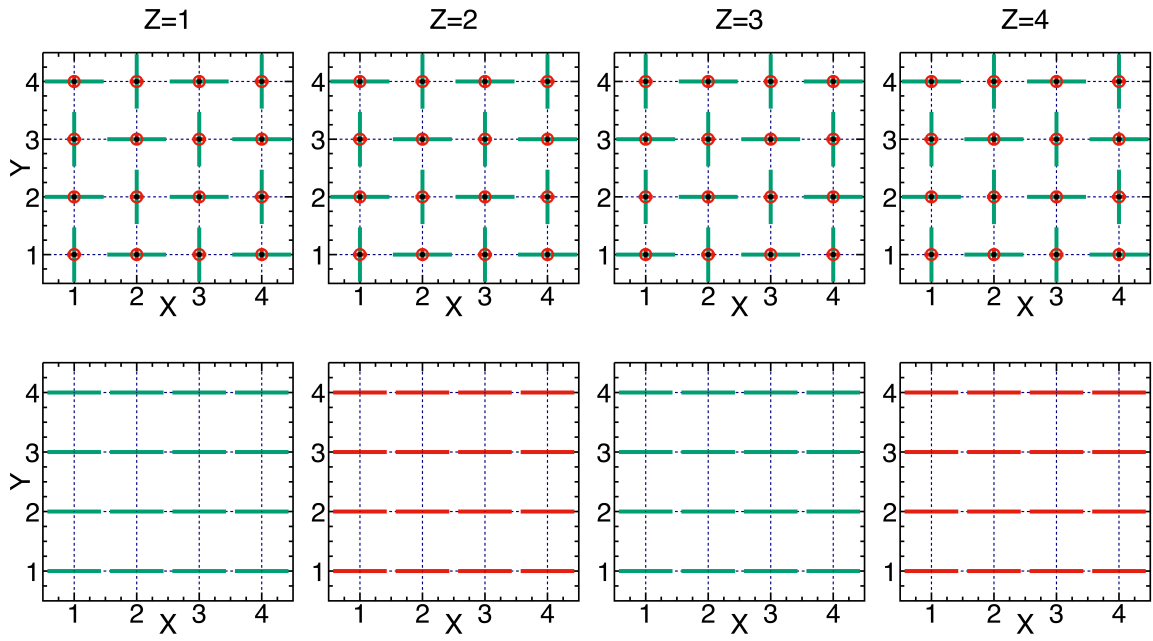
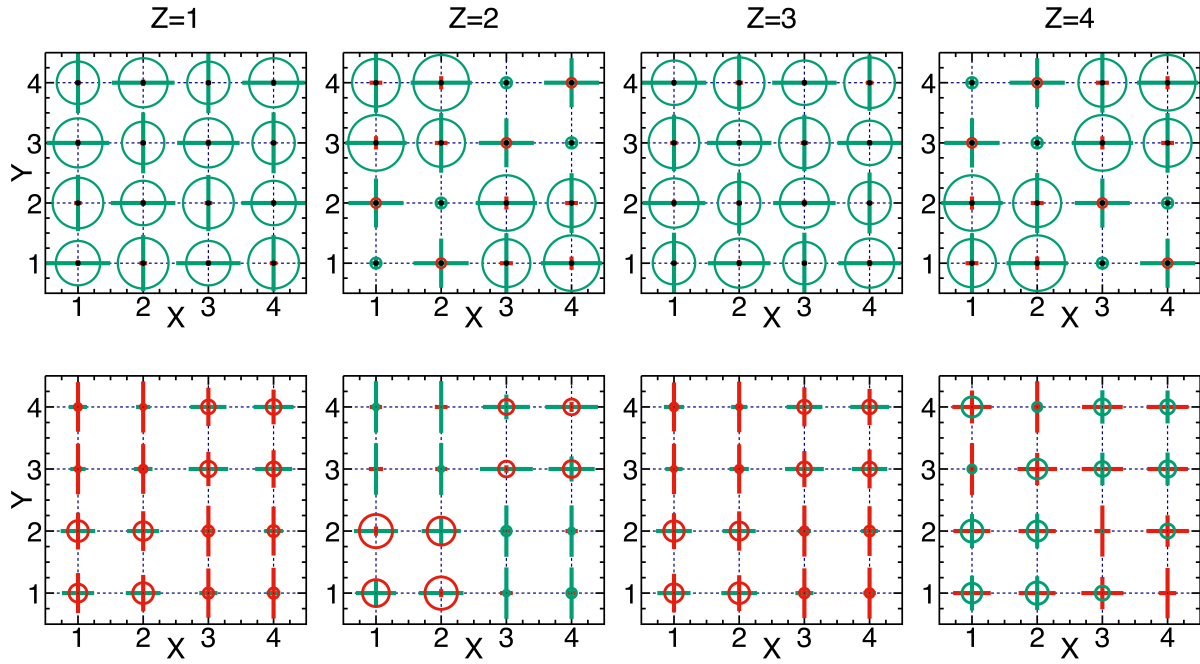**Figure I.2:** $x = 0$: with experimental lattice constant

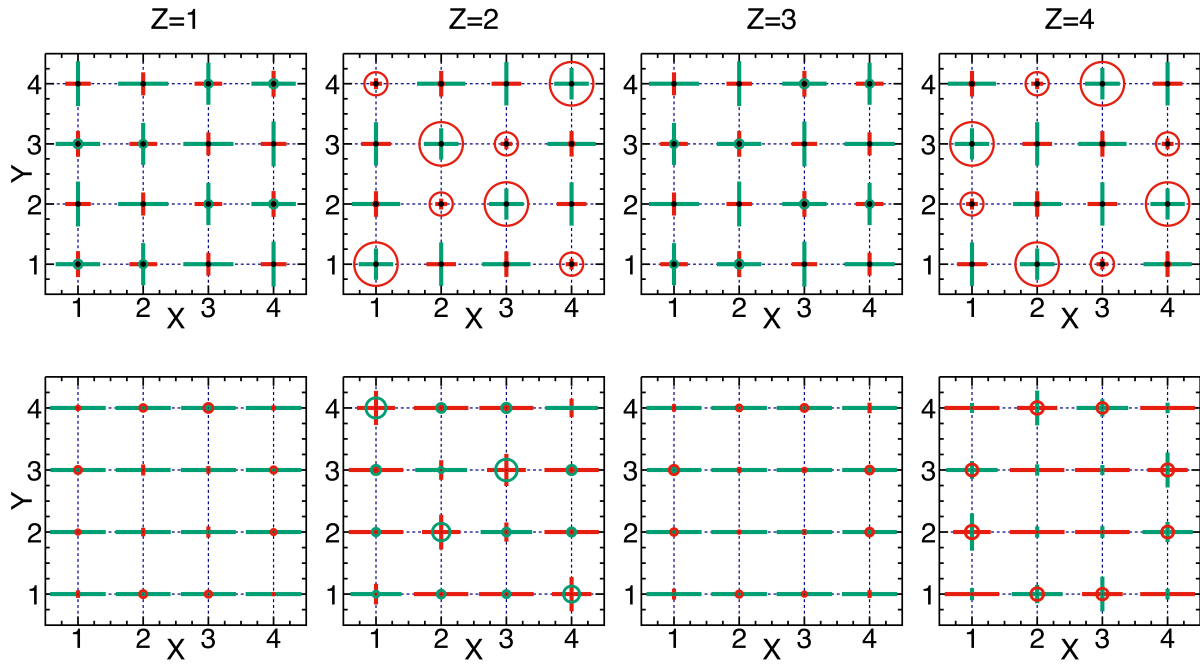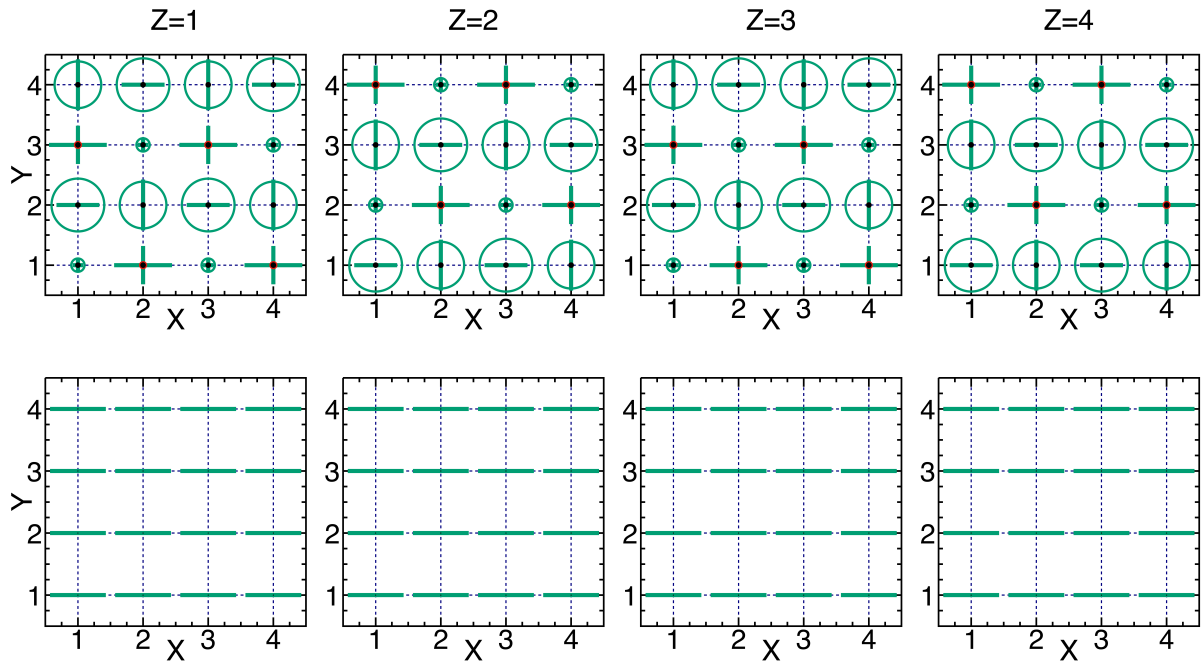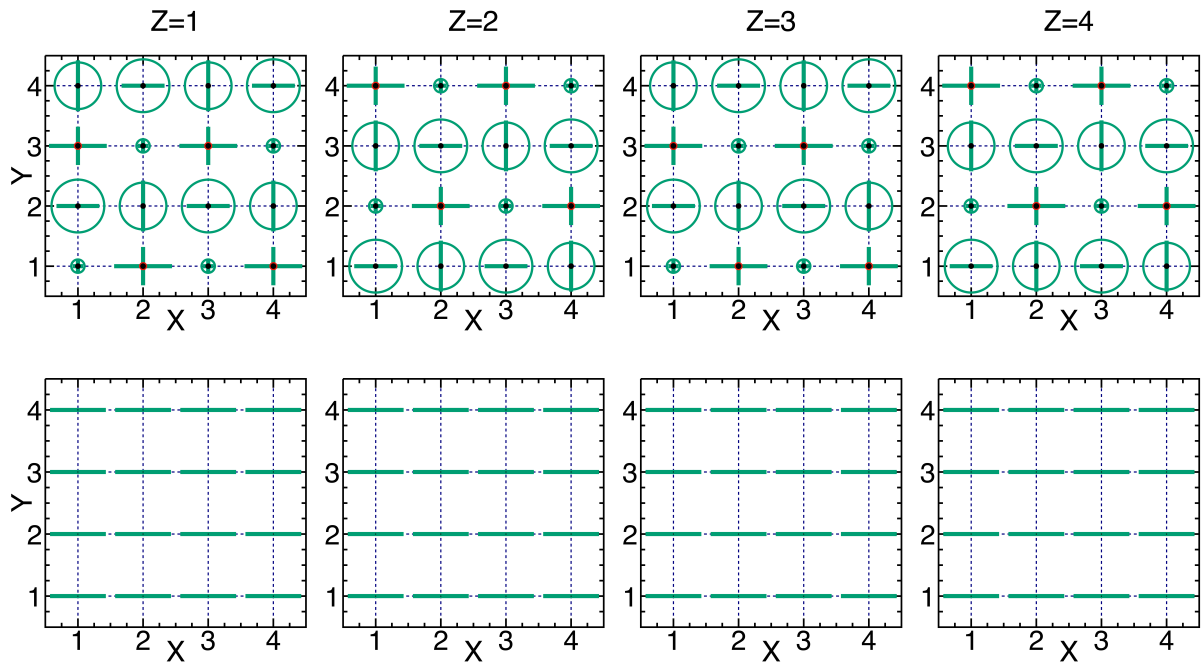**Figure I.3:** $x = 0.125$: with variable lattice constants

Figure I.4: $x = 0.125$: with experimental lattice constant

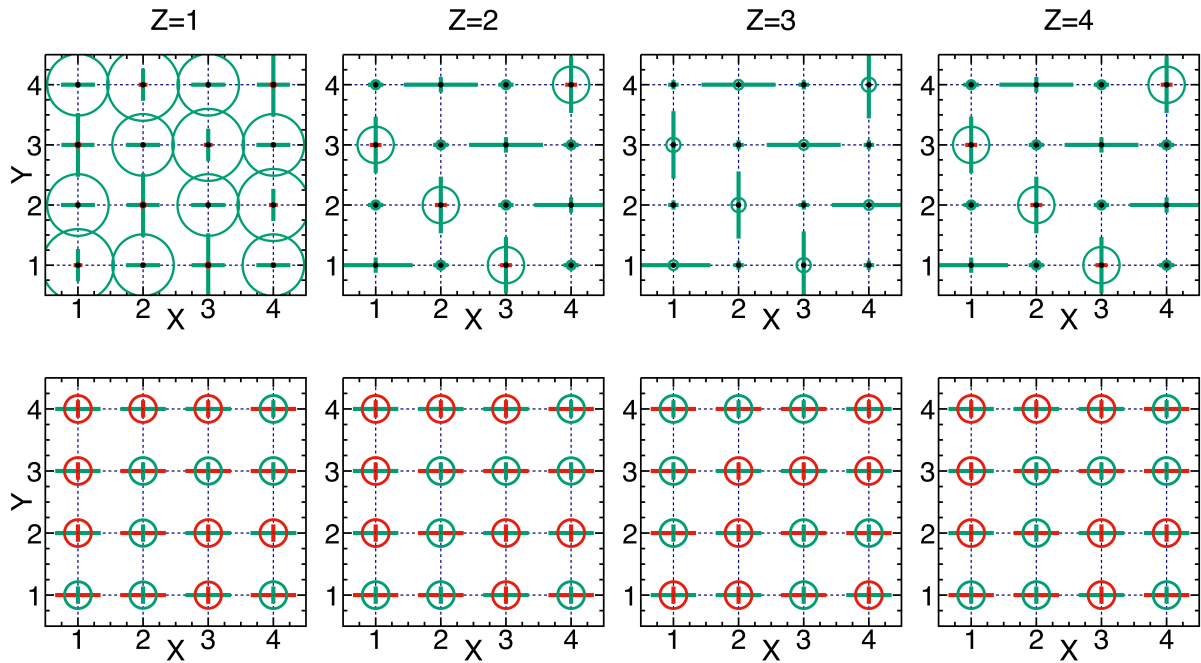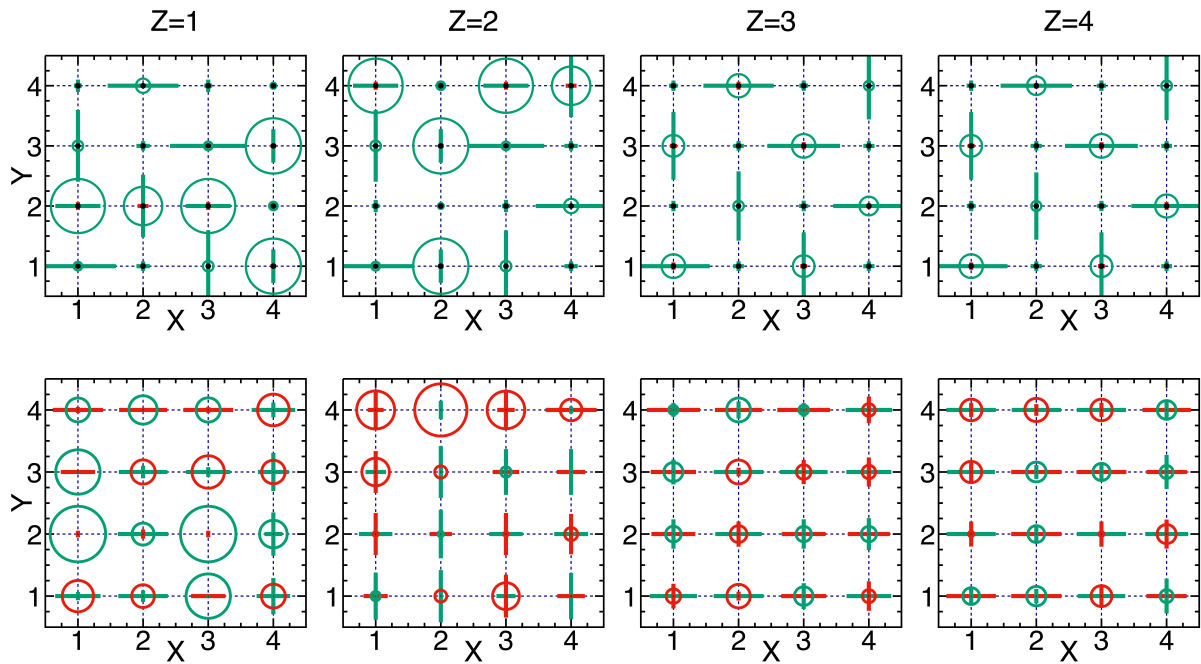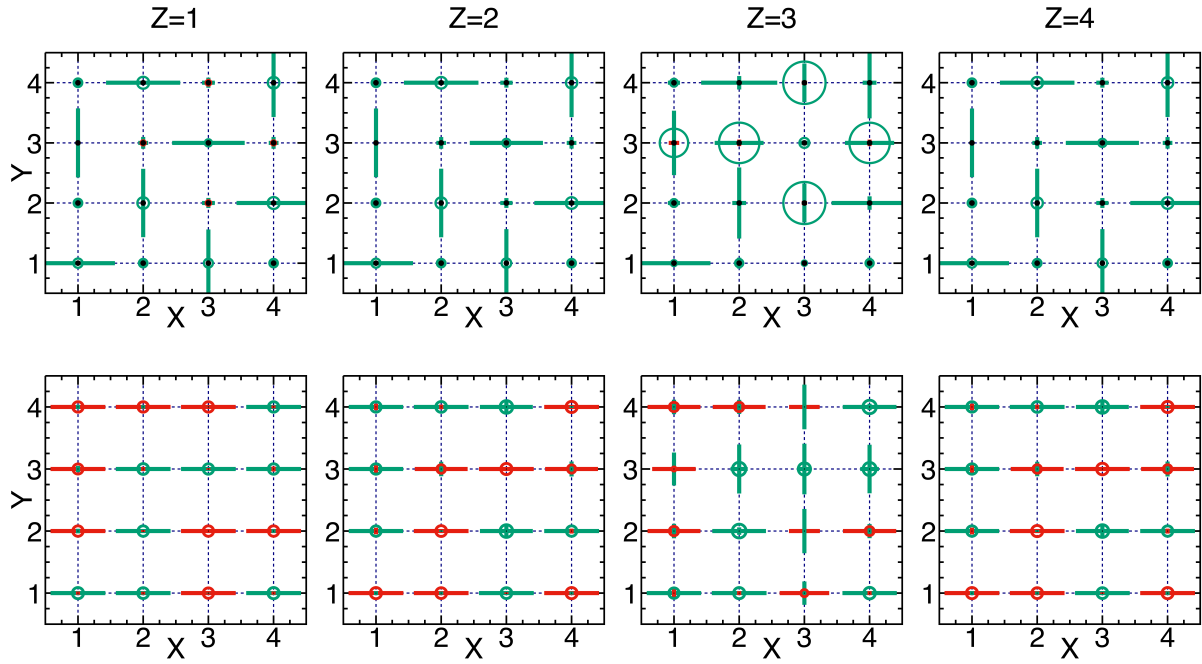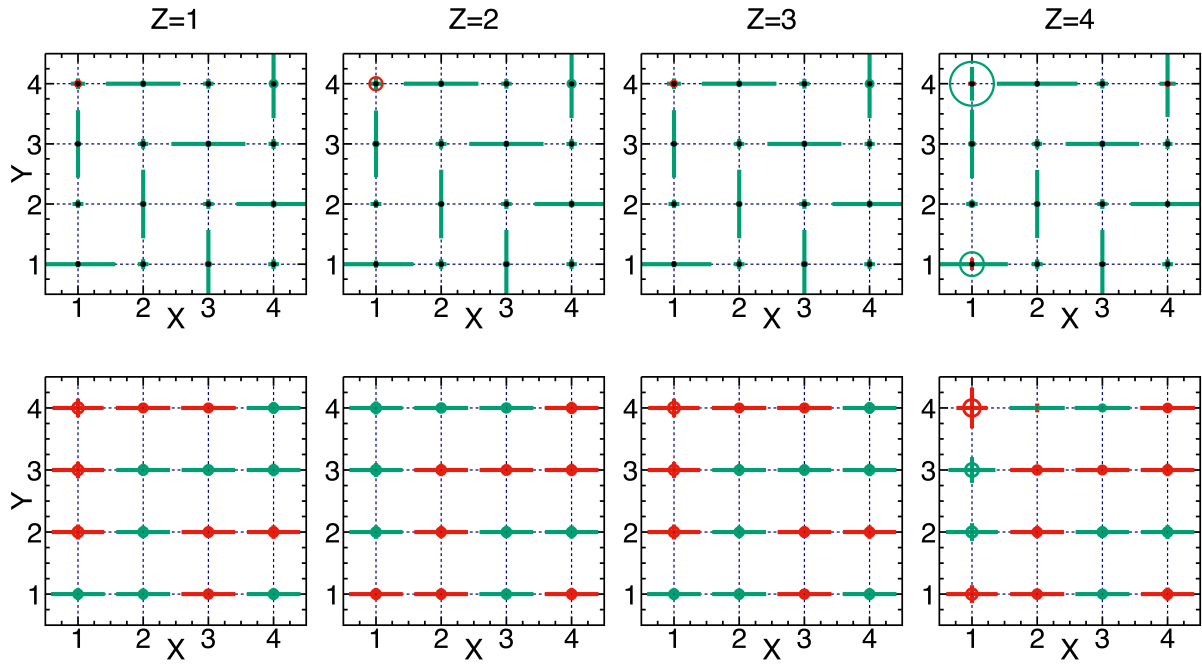**Figure I.5:** $x = 0.25$: with variable lattice constants

Figure I.6: $x = 0.25$: with experimental lattice constant
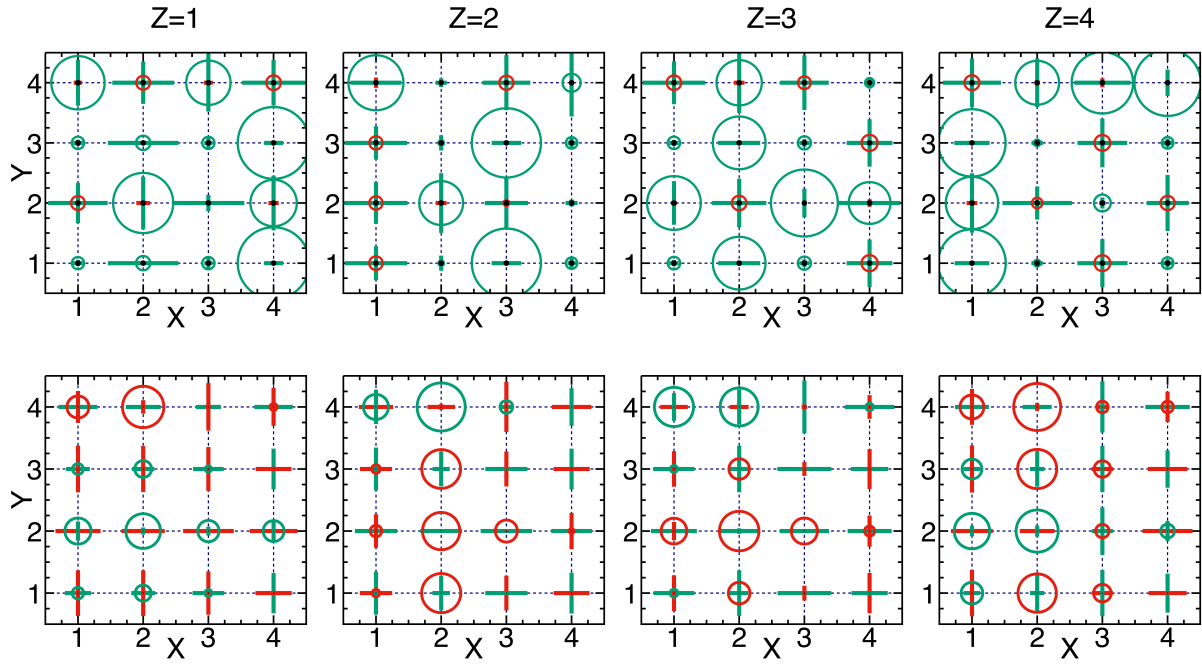
Figure I.7: $x = 0.31$
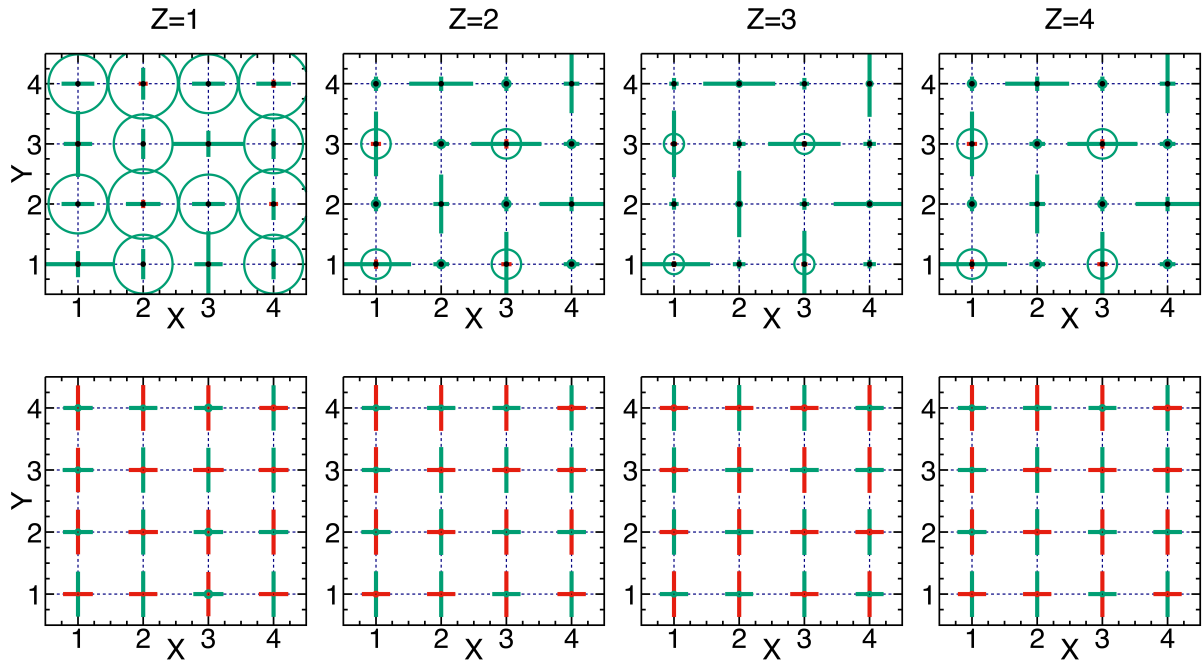
Figure I.8: $x = 0.375$ **I-type**

Figure I.9: $x = 0.375$ **II-type**

Figure I.10: $x = 0.436$

Figure I.11: $x = 0.469$

Figure I.12: single electron doped in the CE-type structure at $x = 0.5$
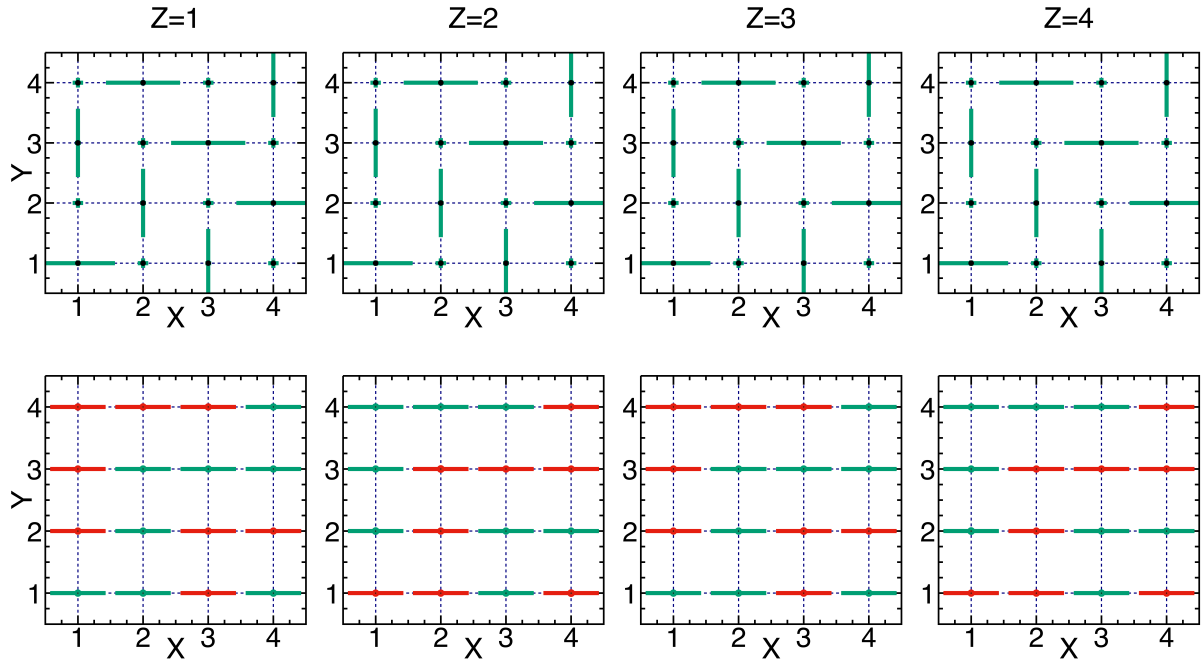
Figure I.13: $x = 0.5$
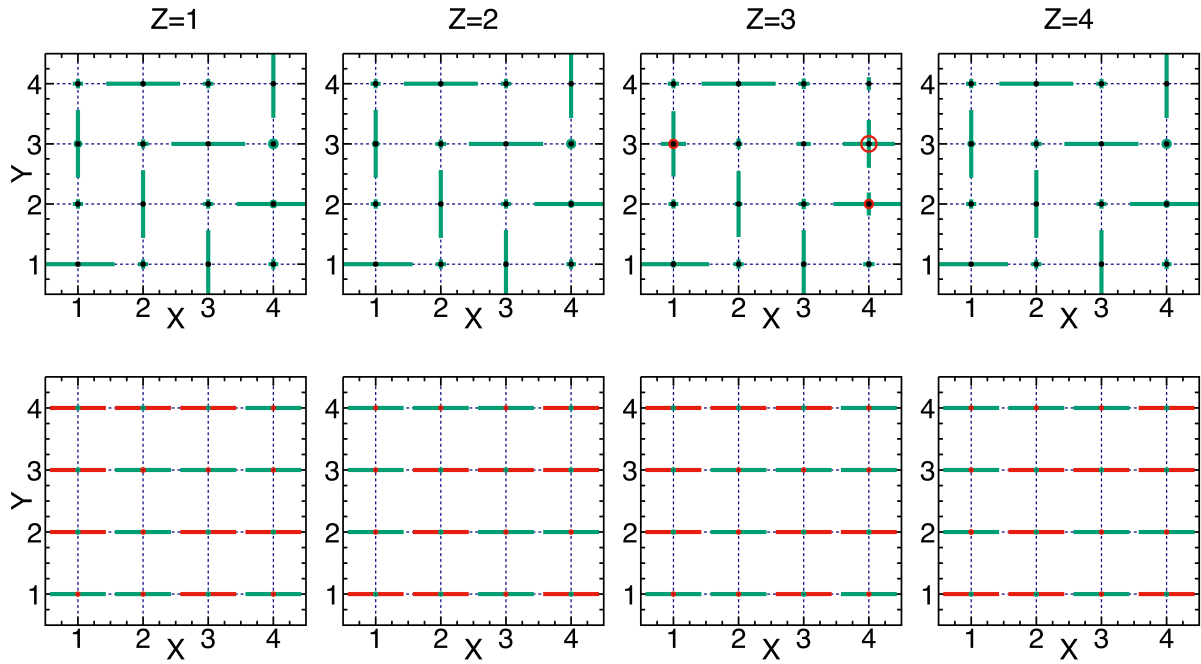
Figure I.14: single hole doped in the CE-type structure at $x = 0.5$
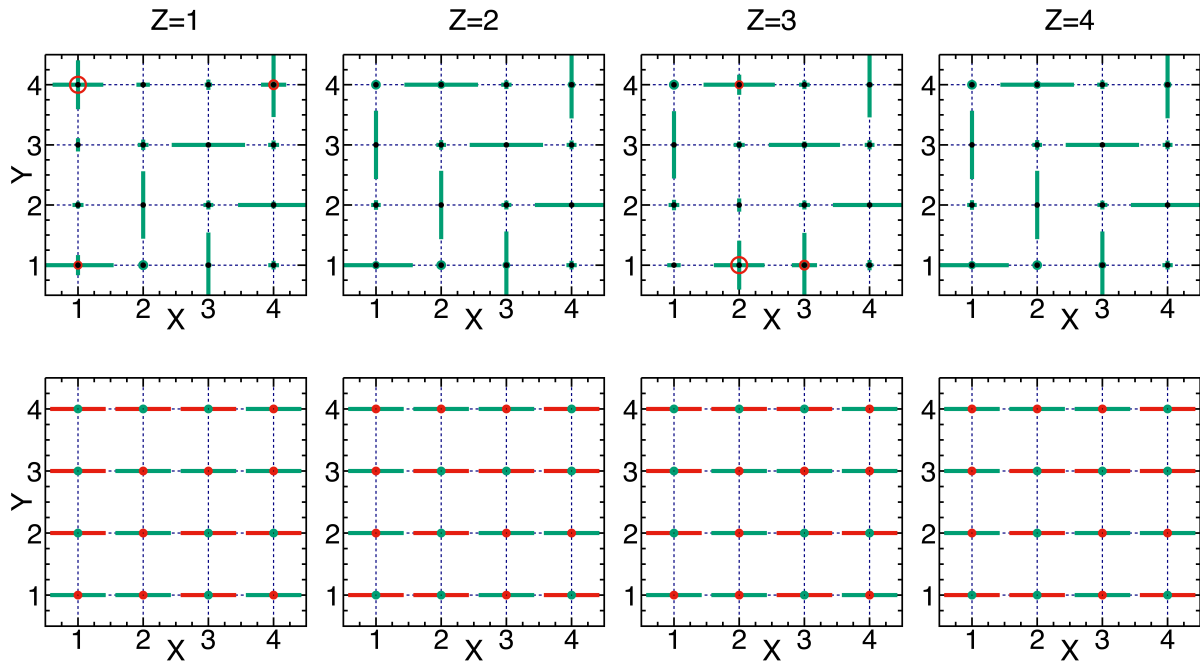
Figure I.15: $x = 0.53$
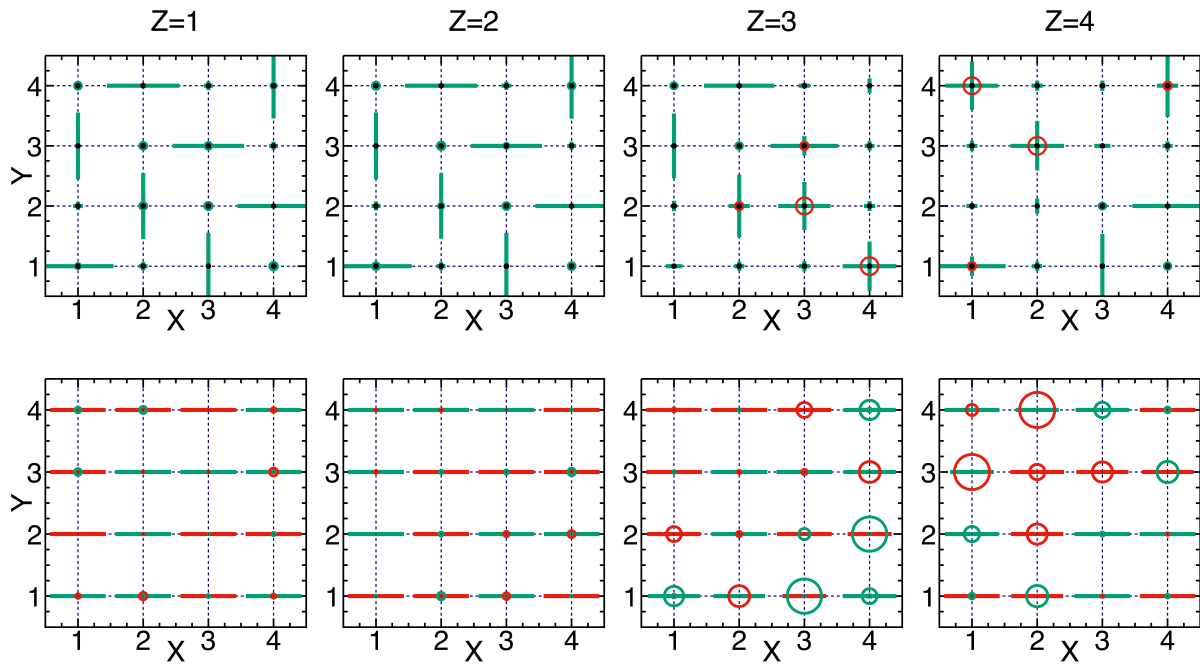
Figure I.16: $x = 0.563$
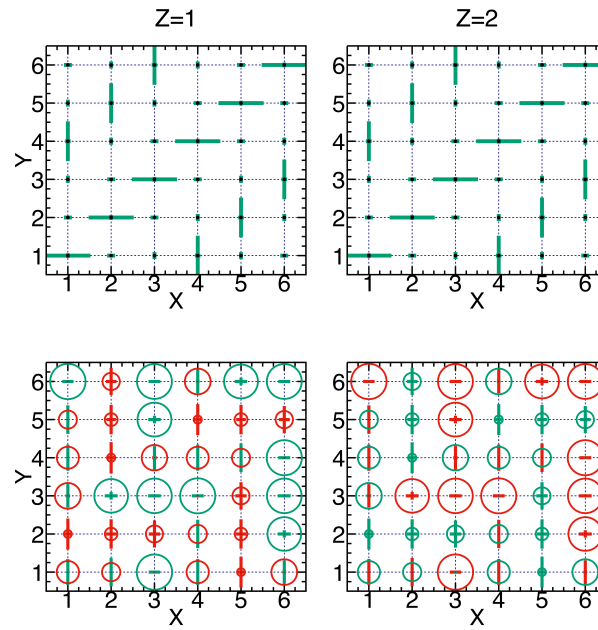
Figure I.17: Wigner crystal phase at $x = 0.66$
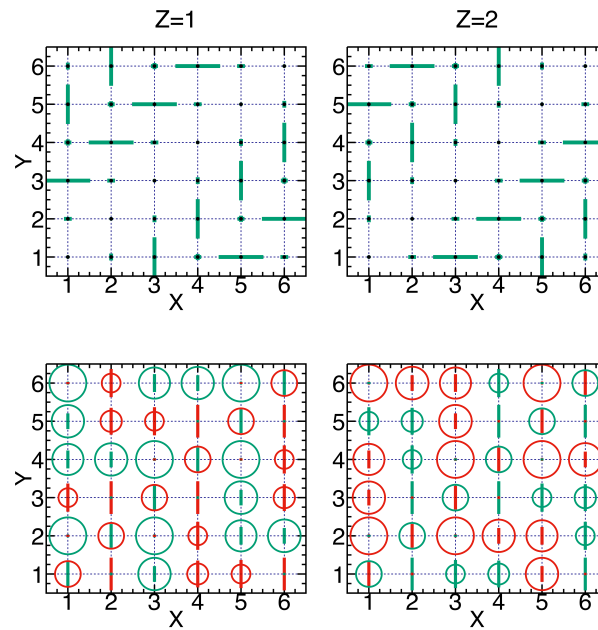
Figure I.18: Bistripe phase at $x = 0.66$

Figure I.19: first of the two degenerate state at $x = 0.75$

Figure I.20: second of the two degenerate state at $x = 0.75$

Bibliography

[1]   K. H. Kim, J. H. Jung, T. W. Noh, *Physical Review Letters* **1998**, *81*, 1517–1520.

[2]   P. A. Lee, N. Nagaosa, X.-G. Wen, *Rev. Mod. Phys.* **2006**, *78*, 17–85.

[3]   J. B. Torrance, P. Lacorre, A. I. Nazzal, E. J. Ansaldo, C. Niedermayer, *Phys. Rev. B* **1992**, *45*, 8209–8212.

[4]   R. von Helmolt, J. Wecker, B. Holzapfel, L. Schultz, K. Samwer, *Phys. Rev. Lett.* **1993**, *71*, 2331–2333.
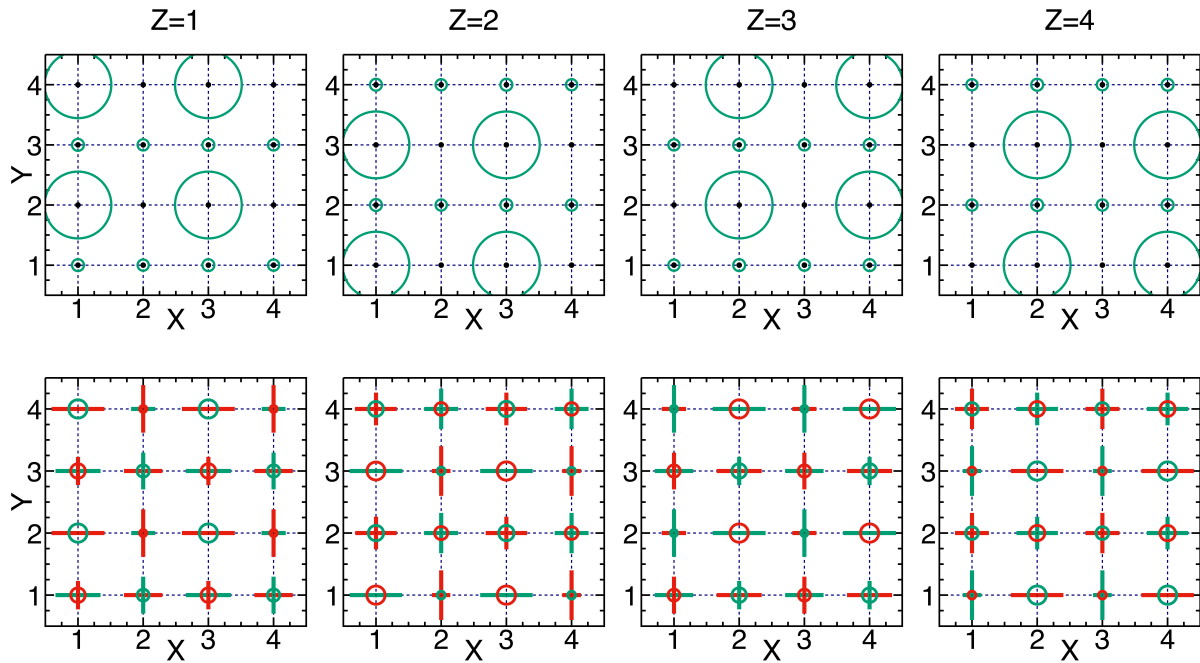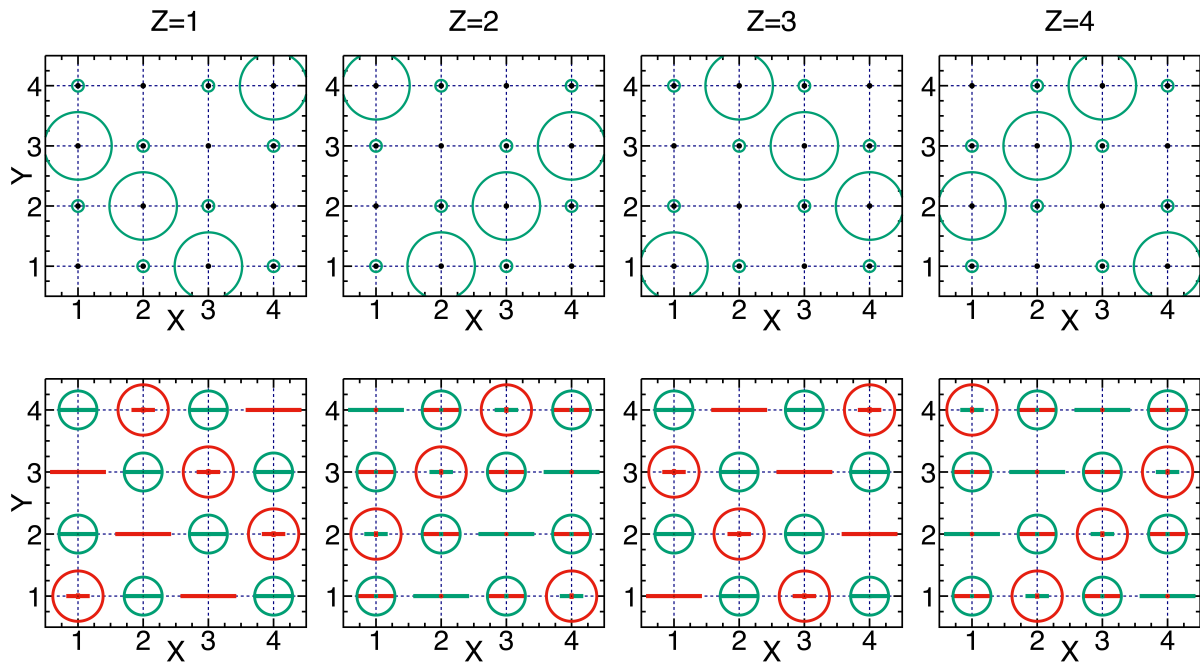
[5]   K. Chahara, T. Ohno, M. Kasai, Y. Kozono, *Applied Physics Letters* **1993**, *63*, 1990–1992.

[6]   C. Zener, *Phys. Rev.* **1951**, *82*, 403–405.

[7]   P. W. Anderson, H. Hasegawa, *Phys. Rev.* **1955**, *100*, 675–681.

[8]   A. J. Millis, B. I. Shraiman, R. Mueller, *Phys. Rev. Lett.* **1996**, *77*, 175–178.

[9]   A. J. Millis, P. B. Littlewood, B. I. Shraiman, *Phys. Rev. Lett.* **1995**, *74*, 5144–5147.

[10]   A. J. Millis, *Nature* **1998**, *392*, 147–150.

[11]   A. Sawa, T. Fujii, M. Kawasaki, Y. Tokura, *Applied Physics Letters* **2005**, *86*, 112508.

[12]   G. Saucke, J. Norpoth, C. Jooss, D. Su, Y. Zhu, *Phys. Rev. B* **2012**, *85*, 165315.

[13]   Y. Tokura, *Journal of the Physical Society of Japan* **2006**, *75*, 011001.

[14]   H. Ichikawa, S. Nozawa, T. Sato, A. Tomita, K. Ichiyanagi, M. Chollet, L. Guerin, N. Dean, A. Cavalleri, S.-i. Adachi, T.-h. Arima, H. Sawa, Y. Ogimoto, M. Nakamura, R. Tamaki, K. Miyano, S.-y. Koshihara, *Nat Mater* **2011**, *10*, 101–105.

[15]   M. Sotoudeh, S. Rajpurohit, P. Blöchl, D. Mierwaldt, J. Norpoth, V. Roddatis, S. Mildner, B. Kressdorf, B. Ifland, C. Jooss, *Phys. Rev. B* **2017**, *95*, 235150.

[16]   A. S. Alexandrov, A. M. Bratkovsky, *Phys. Rev. Lett.* **1999**, *82*, 141–144.

[17]   G.-m. Zhao, V. Smolyaninova, W. Prellier, H. Keller, *Phys. Rev. Lett.* **2000**, *84*, 6086–6089.

[18]   L. Vasiliu-Doloc, S. Rosenkranz, R. Osborn, S. K. Sinha, J. W. Lynn, J. Mesot, O. H. Seeck, G. Preosti, A. J. Fedro, J. F. Mitchell, *Phys. Rev. Lett.* **1999**, *83*, 4393–4396.

[19]   P. Dai, J. A. Fernandez-Baca, N. Wakabayashi, E. W. Plummer, Y. Tomioka, Y. Tokura, *Phys. Rev. Lett.* **2000**, *85*, 2553–2556.

[20]   V. M. Goldschmidt, *Naturwissenschaften* **1926**, *14*, 477–485.

[21] H. Y. Hwang, S.-W. Cheong, P. G. Radaelli, M. Marezio, B. Batlogg, *Phys. Rev. Lett.* **1995**, *75*, 914–917.

[22] P. G. Radaelli, G. Iannone, M. Marezio, H. Y. Hwang, S.-W. Cheong, J. D. Jorgensen, D. N. Argyriou, *Phys. Rev. B* **1997**, *56*, 8265–8276.

[23] M. N. Iliev, M. V. Abrashev, H.-G. Lee, V. N. Popov, Y. Y. Sun, C. Thomsen, R. L. Meng, C. W. Chu, *Phys. Rev. B* **1998**, *57*, 2872–2877.

[24] Martın-Carrón, L., de Andrés, A., *Eur. Phys. J. B* **2001**, *22*, 11–16.

[25] Z. Jirák, S. Krupička, Z. Šimša, M. Dlouhá, S. Vratislav, *Journal of Magnetism and Magnetic Materials* **1985**, *53*, 153–166.

[26] P. W. Anderson, *Phys. Rev.* **1950**, *79*, 350–356.

[27] H. Kramers, *Physica* **1934**, *1*, 182–192.

[28] J. B. Goodenough, *Physical Review* **1955**, *100*, 564–573.

[29] J. Kanamori, *Journal of Physics and Chemistry of Solids* **1959**, *10*, 87–98.

[30] C. Zener, *Phys. Rev.* **1951**, *82*, 403–405.

[31] M. A. Ruderman, C. Kittel, *Phys. Rev.* **1954**, *96*, 99–102.

[32] K. Yosida, *Phys. Rev.* **1957**, *106*, 893–898.

[33] T. Kasuya, *Progress of Theoretical Physics* **1956**, *16*, 45–57.

[34] E. O. Wollan, W. C. Koehler, *Phys. Rev.* **1955**, *100*, 545–563.

[35] W. Koehler, E. Wollan, *Journal of Physics and Chemistry of Solids* **1957**, *2*, 100–106.

[36] J. B. Goodenough, A. Wold, R. J. Arnott, N. Menyuk, *Phys. Rev.* **1961**, *124*, 373–384.

[37] K. Tobe, T. Kimura, Y. Tokura, *Phys. Rev. B* **2004**, *69*, 014407.

[38] Y. Tokura, Y. Tomioka, *Journal of Magnetism and Magnetic Materials* **1999**, *200*, 1–23.

[39] P. .-.-G. de Gennes, *Phys. Rev.* **1960**, *118*, 141–154.

[40] R. Kajimoto, H. Mochizuki, H. Yoshizawa, S. Okamoto, S. Ishihara, *Phys. Rev. B* **2004**, *69*, 054433.

[41] F. Moussa, M. Hennion, F. Wang, P. Kober, J. Rodrıguez-Carvajal, P. Reutler, L. Pinsard, A. Revcolevschi, *Phys. Rev. B* **2003**, *67*, 214430.

[42] A. Pimenov, M. Biberacher, D. Ivannikov, A. Loidl, V. Y. Ivanov, A. A. Mukhin, A. M. Balbashov, *Phys. Rev. B* **2000**, *62*, 5685–5689.

[43] M. v. Zimmermann, C. S. Nelson, J. P. Hill, D. Gibbs, M. Blume, D. Casa, B. Keimer, Y. Murakami, C.-C. Kao, C. Venkataraman, T. Gog, Y. Tomioka, Y. Tokura, *Phys. Rev. B* **2001**, *64*, 195133.

[44] C. Martin, A. Maignan, M. Hervieu, B. Raveau, *Phys. Rev. B* **1999**, *60*, 12191–12199.

[45] P. G. Radaelli, D. E. Cox, L. Capogna, S.-W. Cheong, M. Marezio, *Phys. Rev. B* **1999**, *59*, 14440–14450.

[46] M. S. Reis, V. S. Amaral, J. P. Araújo, P. B. Tavares, A. M. Gomes, I. S. Oliveira, *Phys. Rev. B* **2005**, *71*, 144413.

[47] S. Y. Zhou, Y. Zhu, M. C. Langner, Y.-D. Chuang, P. Yu, W. L. Yang, A. G. Cruz Gonzalez, N. Tahir, M. Rini, Y.-H. Chu, R. Ramesh, D.-H. Lee, Y. Tomioka, Y. Tokura, Z. Hussain, R. W. Schoenlein, *Phys. Rev. Lett.* **2011**, *106*, 186404.

[48] M. T. Fernández-Dıaz, J. L. Martınez, J. M. Alonso, E. Herrero, *Phys. Rev. B* **1999**, *59*, 1277–1284.

[49] S. Mori, C. H. Chen, S. .-.-W. Cheong, *Nature* **1998**, *392*, 473.

[50] S. Cox, J. C. Lashley, E. Rosten, J. Singleton, A. J. Williams, P. B. Littlewood, *Journal of Physics: Condensed Matter* **2007**, *19*, 192201.

[51] M. M. Savosta, P. Novák, M. Maryško, Z. Jirák, J. Hejtmánek, J. Englich, J. Kohout, C. Martin, B. Raveau, *Phys. Rev. B* **2000**, *62*, 9532–9537.

[52] S. Grenier, J. P. Hill, D. Gibbs, K. J. Thomas, M. v. Zimmermann, C. S. Nelson, V. Kiryukhin, Y. Tokura, Y. Tomioka, D. Casa, T. Gog, C. Venkataraman, *Phys. Rev. B* **2004**, *69*, 134419.

[53] M. R. Lees, J. Barratt, G. Balakrishnan, D. M. Paul, C. Ritter, *Phys. Rev. B* **1998**, *58*, 8694–8703.

[54] A. Daoud-Aladine, J. Rodrıguez-Carvajal, L. Pinsard-Gaudart, M. T. Fernández-Dıaz, A. Revcolevschi, *Phys. Rev. Lett.* **2002**, *89*, 097205.

[55] L. Wu, R. F. Klie, Y. Zhu, C. Jooss, *Phys. Rev. B* **2007**, *76*, 174210.

[56] C. Jooss, L. Wu, T. Beetz, R. F. Klie, M. Beleggia, M. A. Schofield, S. Schramm, J. Hoffmann, Y. Zhu, *Proceedings of the National Academy of Sciences* **2007**, *104*, 13597–13602.

[57] J. Stankiewicz, J. Sesé, J. Garcıa, J. Blasco, C. Rillo, *Phys. Rev. B* **2000**, *61*, 11236–11239.

[58] E. Granado, C. D. Ling, J. J. Neumeier, J. W. Lynn, D. N. Argyriou, *Phys. Rev. B* **2003**, *68*, 134440.

[59] P. Littlewood, *Nature* **1999**, *399*, 529.

[60] M. Uehara, S. Mori, C. H. Chen, S.-W. Cheong, *Nature* **1999**, *399*, 560–563.

[61] N. A. Babushkina, L. M. Belova, D. I. Khomskii, K. I. Kugel, O. Y. Gorbenko, A. R. Kaul, *Phys. Rev. B* **1999**, *59*, 6994–7000.

[62] E. Dagotto, T. Hotta, A. Moreo, *Physics Reports* **2001**, *344*, 1–153.

[63] J. van den Brink, G. Khaliullin, D. Khomskii, *Phys. Rev. Lett.* **1999**, *83*, 5118–5121.

[64] T. Hotta, A. L. Malvezzi, E. Dagotto, *Phys. Rev. B* **2000**, *62*, 9432–9452.

[65] E. Dagotto, S. Yunoki, A. L. Malvezzi, A. Moreo, J. Hu, S. Capponi, D. Poilblanc, N. Furukawa, *Phys. Rev. B* **1998**, *58*, 6414–6427.

[66] P. W. Anderson, *Phys. Rev.* **1959**, *115*, 2–13.

[67] K. I. Kugel', D. I. Khomskiĭ, *Soviet Journal of Experimental and Theoretical Physics* **1973**, *37*, 725.

[68] S. Ishihara, M. Yamanaka, N. Nagaosa, *Phys. Rev. B* **1997**, *56*, 686–692.

[69] T. Egami, D. Louca, *Journal of Superconductivity* **1999**, *12*, 23–26.

[70] D. Louca, T. Egami, E. L. Brosha, H. Röder, A. R. Bishop, *Phys. Rev. B* **1997**, *56*, R8475–R8478.

[71] S. J. L. Billinge, R. G. DiFrancesco, G. H. Kwei, J. J. Neumeier, J. D. Thompson, *Phys. Rev. Lett.* **1996**, *77*, 715–718.

[72] H. Röder, J. Zang, A. R. Bishop, *Phys. Rev. Lett.* **1996**, *76*, 1356–1359.

[73] J. A. Vergés, V. Martın-Mayor, L. Brey, *Phys. Rev. Lett.* **2002**, *88*, 136401.

[74] S. Yunoki, A. Moreo, E. Dagotto, *Phys. Rev. Lett.* **1998**, *81*, 5612–5615.

[75] C. Şen, G. Alvarez, E. Dagotto, *Phys. Rev. Lett.* **2010**, *105*, 097203.

[76] S. Yunoki, T. Hotta, E. Dagotto, *Phys. Rev. Lett.* **2000**, *84*, 3714–3717.

[77] S. Mori, C. H. Chen, S.-W. Cheong, *Phys. Rev. Lett.* **1998**, *81*, 3972–3975.

[78] A. Moreo, S. Yunoki, E. Dagotto, *Science* **1999**, *283*, 2034–2040.

[79] Y. Moritomo, *Phys. Rev. B* **1999**, *60*, 10374–10377.

[80] D. D. Sarma, D. Topwal, U. Manju, S. R. Krishnakumar, M. Bertolo, S. La Rosa, G. Cautero, T. Y. Koo, P. A. Sharma, S.-W. Cheong, A. Fujimori, *Phys. Rev. Lett.* **2004**, *93*, 097202.

[81] R. P. Prasankumar, S. Zvyagin, K. V. Kamenev, G. Balakrishnan, D. M. Paul, A. J. Taylor, R. D. Averitt, *Phys. Rev. B* **2007**, *76*, 020402.

[82] V. J. Emery, S. A. Kivelson, *Physica C Superconductivity* **1993**, *209*, 597–621.

[83] U. Löw, V. J. Emery, K. Fabricius, S. A. Kivelson, *Phys. Rev. Lett.* **1994**, *72*, 1918–1921.

[84] C. Castellani, C. Di Castro, M. Grilli, *Phys. Rev. Lett.* **1995**, *75*, 4650–4653.

[85] S. Haas, E. Dagotto, A. Nazarenko, J. Riera, *Phys. Rev. B* **1995**, *51*, 5989–5993.

[86] S. Yunoki, J. Hu, A. L. Malvezzi, A. Moreo, N. Furukawa, E. Dagotto, *Phys. Rev. Lett.* **1998**, *80*, 845–848.

[87] T. Mizokawa, D. I. Khomskii, G. A. Sawatzky, *Phys. Rev. B* **2000**, *63*, 024403.

[88] R. Kilian, G. Khaliullin, *Phys. Rev. B* **1999**, *60*, 13458–13469.

[89] C. Ederer, C. Lin, A. J. Millis, *Phys. Rev. B* **2007**, *76*, 155105.

[90] R. Ková čik, C. Ederer, *Phys. Rev. B* **2011**, *84*, 075118.

[91] R. Ková čik, S. S. Murthy, C. E. Quiroga, C. Ederer, C. Franchini, *Phys. Rev. B* **2016**, *93*, 075139.

[92] A. Mukherjee, W. S. Cole, P. Woodward, M. Randeria, N. Trivedi, *Physical Review Letters* **2013**, *110*, 157201.

[93] Z. Popovic, S. Satpathy, *Phys. Rev. Lett.* **2000**, *84*, 1603–1606.

[94] R. Y. Gu, C. S. Ting, *Phys. Rev. B* **2002**, *65*, 214426.

[95] D. I. Khomskii, K. I. Kugel, *Phys. Rev. B* **2003**, *67*, 134401.

[96] M. J. Calderón, A. J. Millis, K. H. Ahn, *Phys. Rev. B* **2003**, *68*, 100401.

[97] J. Burgy, A. Moreo, E. Dagotto, *Phys. Rev. Lett.* **2004**, *92*, 097202.

[98] C. Şen, G. Alvarez, E. Dagotto, *Phys. Rev. B* **2004**, *70*, 064428.

[99] R. Pankaj, S. Yarlagadda, *ArXiv e-prints* **2015**.

[100] M. Rini, R. Tobey, N. Dean, J. Itatani, Y. Tomioka, Y. Tokura, R. W. Schoenlein, A. Cavalleri, *Nature* **2007**, *449*, 72.

[101] D. Raiser, S. Mildner, B. Ifland, M. Sotoudeh, P. Blöchl, S. Techert, C. Jooss, *Advanced Energy Materials* **2017**, *7*, 1602174, 1602174–n/a.

[102] Y. Tomioka, T. Ito, A. Sawa, *Phys. Rev. B* **2018**, *97*, 014409.

[103] P. Barone, S. Picozzi, J. van den Brink, *Phys. Rev. B* **2011**, *83*, 233103.

[104] J. van den Brink, D. I. Khomskii, *Journal of Physics: Condensed Matter* **2008**, *20*, 434217.

[105] M. B. Salamon, M. Jaime, *Rev. Mod. Phys.* **2001**, *73*, 583–628.

[106] J. F. Janak, *Phys. Rev. B* **1978**, *18*, 7165–7168.

[107] R. Car, M. Parrinello, *Phys. Rev. Lett.* **1985**, *55*, 2471–2474.

[108] W. G. Hoover, *Phys. Rev. A* **1985**, *31*, 1695–1697.

[109] S. Nosé, *Molecular Physics* **1984**, *52*, 255–268.

[110] S. Nosé, *The Journal of Chemical Physics* **1984**, *81*, 511–519.

[111] L. Verlet, *Phys. Rev.* **1967**, *159*, 98–103.

[112] T. Köhler, S. Rajpurohit, O. Schumann, F. R. A. Biebl, M. Sotoudeh, S. C. Kramer, P. E. Blöchl, S. Kehrein, S. R. Manmana, *ArXiv e-prints* **2016**.

[113] T. Köhler, S. Rajpurohit, O. Schumann, S. Paeckel, F. R. A. Biebl, M. Sotoudeh, S. C. Kramer, P. E. Blöchl, S. Kehrein, S. R. Manmana, *Phys. Rev. B* **2018**, *97*, 235120.

[114] A. M. Glazer, *Acta Crystallographica Section B* **1972**, *28*, 3384–3392.

[115] J. Tikkanen, H. Huhtinen, P. Paturi, *IEEE Transactions on Magnetics* **2014**, *50*, 1–4.

[116] T. Hotta, S. Yunoki, M. Mayr, E. Dagotto, *Phys. Rev. B* **1999**, *60*, R15009–R15012.

[117] H. L. Ju, H.-C. Sohn, K. M. Krishnan, *Phys. Rev. Lett.* **1997**, *79*, 3230–3233.

[118] A. Y. Ignatov, N. Ali, S. Khalid, *Phys. Rev. B* **2001**, *64*, 014413.

[119] F. Bridges, C. H. Booth, M. Anderson, G. H. Kwei, J. J. Neumeier, J. Snyder, J. Mitchell, J. S. Gardner, E. Brosha, *Phys. Rev. B* **2001**, *63*, 214405.

[120]   G. Subıas, J. Garcıa, M. G. Proietti, J. Blasco, *Phys. Rev. B* **1997**, *56*, 8183–8191.

[121]   M. Abbate, F. M. F. de Groot, J. C. Fuggle, A. Fujimori, O. Strebel, F. Lopez, M. Domke, G. Kaindl, G. A. Sawatzky, M. Takano, Y. Takeda, H. Eisaki, S. Uchida, *Phys. Rev. B* **1992**, *46*, 4511–4519.

[122]   C. de Graaf, C. Sousa, R. Broer, *Phys. Rev. B* **2004**, *70*, 235104.

[123]   R. Bastardis, N. Guihéry, C. de Graaf, *Phys. Rev. B* **2006**, *74*, 014432.

[124]   C. H. Patterson, *Phys. Rev. B* **2005**, *72*, 085125.

[125]   G. Zheng, C. H. Patterson, *Phys. Rev. B* **2003**, *67*, 220404.

[126]   V. Ferrari, M. Towler, P. B. Littlewood, *Phys. Rev. Lett.* **2003**, *91*, 227202.

[127]   K. Ebata, H. Wadati, M. Takizawa, A. Fujimori, A. Chikamatsu, H. Kumigashira, M. Oshima, Y. Tomioka, Y. Tokura, *Phys. Rev. B* **2006**, *74*, 064419.

[128]   K. D. Chandrasekhar, A. K. Das, A. Venimadhav, *The Journal of Physical Chemistry C* **2014**, *118*, 27728–27734.

[129]   Y. Endoh, K. Hirota, S. Ishihara, S. Okamoto, Y. Murakami, A. Nishizawa, T. Fukuda, H. Kimura, H. Nojiri, K. Kaneko, S. Maekawa, *Phys. Rev. Lett.* **1999**, *82*, 4328–4331.

[130]   T. Inami, N. Ikeda, Y. Murakami, I. Koyama, Y. Wakabayashi, Y. Yamada, *Japanese Journal of Applied Physics* **1999**, *38*, 212.

[131]   D. E. Cox, T. Iglesias, E. Moshopoulou, K. Hirota, K. Takahashi, Y. Endoh, *Phys. Rev. B* **2001**, *64*, 024431.

[132]   Y. Yamada, J. Suzuki, K. Oikawa, S. Katano, J. A. Fernandez-Baca, *Phys. Rev. B* **2000**, *62*, 11600–11608.

[133]   H. Yoshizawa, H. Kawano, Y. Tomioka, Y. Tokura, *Phys. Rev. B* **1995**, *52*, R13145–R13148.

[134]   S. Y. Zhou, M. C. Langner, Y. Zhu, Y.-D. Chuang, M. Rini, T. E. Glover, M. P. Hertlein, A. G. C. Gonzalez, N. Tahir, Y. Tomioka, Y. Tokura, Z. Hussain, R. W. Schoenlein, *Scientific Reports* **2014**, *4*, 4050.

[135]   N. Bondarenko, Y. Kvashnin, J. Chico, A. Bergman, O. Eriksson, N. V. Skorodumova, *Phys. Rev. B* **2017**, *95*, 220401.

[136]   Y.-R. Chen, P. B. Allen, *Phys. Rev. B* **2001**, *64*, 064401.

[137]   W.-T. Peng, B. S. Fales, Y. Shu, B. G. Levine, *Chemical Science* **2018**, *9*, 681–687.

[138]   Y. Shu, B. G. Levine, *The Journal of Physical Chemistry C* **2015**, *119*, 1737–1747.

[139]   E. Fermi, *Zeitschrift für Physik* **1934**, *88*, 161–177.

[140]   P. A. M. Dirac, *Proceedings of the Royal Society of London A: Mathematical Physical and Engineering Sciences* **1927**, *114*, 243–265.

[141]   D. R. Hofstadter, *Phys. Rev. B* **1976**, *14*, 2239–2249.

[142]   R. N. Hall, *Phys. Rev.* **1952**, *87*, 387–387.

[143]   W. Shockley, W. T. Read, *Phys. Rev.* **1952**, *87*, 835–842.

[144] P. T. Landsberg, *physica status solidi (b)* **1962**, *41*, 457–489.

[145] A. M. Stoneham, *Reports on Progress in Physics* **1981**, *44*, 1251.

[146] J.-H. Yang, L. Shi, L.-W. Wang, S.-H. Wei, *Scientific Reports* **2016**, *6*, 21712.

[147] K. A. Kistler, S. Matsika, *The Journal of Chemical Physics* **2008**, *128*, 215102.

[148] A. Tajti, P. G. Szalay, A. G. Császár, M. Kállay, J. Gauss, E. F. Valeev, B. A. Flowers, J. Vázquez, J. F. Stanton, *The Journal of Chemical Physics* **2004**, *121*, 11599–11613.

[149] J. Gauss, A. Tajti, M. Kállay, J. F. Stanton, P. G. Szalay, *The Journal of Chemical Physics* **2006**, *125*, 144111.

[150] C. Hu, O. Sugino, K. Watanabe, *The Journal of Chemical Physics* **2011**, *135*, 074101.

[151] G. A. Meek, B. G. Levine, *The Journal of Physical Chemistry Letters* **2014**, *5*, PMID: 26279558, 2351–2356.

[152] S. Matsika, P. Krause, *Annual Review of Physical Chemistry* **2011**, *62*, PMID: 21219147, 621–643.

[153] B. Zygelman, *Phys. Rev. Lett.* **1990**, *64*, 256–259.

[154] C. Itzykson, J. B. Zuber, *Quantum Field Theory*, McGraw-Hill, New York, **1980**.

[155] G. A. Worth, L. S. Cederbaum, *Annual Review of Physical Chemistry* **2004**, *55*, PMID: 15117250, 127–158.

[156] T. Yonehara, K. Hanasaki, K. Takatsuka, *Chemical Reviews* **2012**, *112*, PMID: 22077497, 499–542.

[157] D. R. Yarkony, *Chemical Reviews* **2012**, *112*, PMID: 22050109, 481–498.

[158] G. J. Atchity, S. S. Xantheas, K. Ruedenberg, *The Journal of Chemical Physics* **1991**, *95*, 1862–1876.

[159] D. R. Yarkony, *Rev. Mod. Phys.* **1996**, *68*, 985–1013.

[160] G. A. Worth, L. S. Cederbaum, *Annual Review of Physical Chemistry* **2004**, *55*, PMID: 15117250, 127–158.

[161] E. Teller, *The Journal of Physical Chemistry* **1937**, *41*, 109–116.

[162] J.-M. L. Pecourt, J. Peon, B. Kohler, *Journal of the American Chemical Society* **2001**, *123*, PMID: 11603988, 10370–10378.

[163] C. E. Crespo-Hernández, B. Cohen, P. M. Hare, B. Kohler, *Chemical Reviews* **2004**, *104*, PMID: 15080719, 1977–2020.

[164] P. Hamm, G. Stock, *Phys. Rev. Lett.* **2012**, *109*, 173201.

[165] J. C. Tully, *The Journal of Chemical Physics* **1990**, *93*, 1061–1071.

[166] T. J. Martinez, M. Ben-Nun, R. D. Levine, *The Journal of Physical Chemistry* **1996**, *100*, 7884–7895.

[167] R. Kapral, G. Ciccotti, *The Journal of Chemical Physics* **1999**, *110*, 8919–8929.

[168] M. Ben-Nun, T. J. Martınez, J. Chem. Phys. **2000**, *112*, 6113–6121.

[169] Y. Kobori, R. Noji, S. Tsuganezawa, *The Journal of Physical Chemistry C* **2013**, *117*, 1589–1599.

[170] X. Li, J. C. Tully, H. B. Schlegel, M. J. Frisch, *The Journal of Chemical Physics* **2005**, *123*, 084106.

[171] Li, X. G., Zheng, R. K., Li, G., Zhou, H. D., Huang, R. X., Xie, J. Q., Wang, Z. D., *Europhys. Lett.* **2002**, *60*, 670–676.

[172] R. V., M. K. S., S. V., J. T., R. Baldev, *physica status solidi (a)* **2003**, *195*, 350–358.

[173] Y. Sun, X. Xu, Y. Zhang, *Journal of Physics: Condensed Matter* **2000**, *12*, 10475.

[174] V. Esposito, L. Rettig, E. Abreu, E. M. Bothschafter, G. Ingold, M. Kawasaki, M. Kubli, G. Lantz, M. Nakamura, J. Rittman, M. Savoini, Y. Tokura, U. Staub, S. L. Johnson, P. Beaud, *Phys. Rev. B* **2018**, *97*, 014312.

[175] D. Lim, V. K. Thorsmølle, R. D. Averitt, Q. X. Jia, K. H. Ahn, M. J. Graf, S. A. Trugman, A. J. Taylor, *Phys. Rev. B* **2005**, *71*, 134403.

[176] S. Mildner, J. Hoffmann, P. E. Blöchl, S. Techert, C. Jooss, *Phys. Rev. B* **2015**, *92*, 035145.

[177] N. N. Loshkareva, L. V. Nomerovannaya, E. V. Mostovshchikova, A. A. Makhnev, Y. P. Sukhorukov, N. I. Solin, T. I. Arbuzova, S. V. Naumov, N. V. Kostromitina, A. M. Balbashov, L. N. Rybina, *Phys. Rev. B* **2004**, *70*, 224406.

[178] C. Hartinger, F. Mayr, A. Loidl, T. Kopp, *Phys. Rev. B* **2006**, *73*, 024408.

[179] M. Quijada, J. Černe, J. R. Simpson, H. D. Drew, K. H. Ahn, A. J. Millis, R. Shreekala, R. Ramesh, M. Rajeswari, T. Venkatesan, *Phys. Rev. B* **1998**, *58*, 16093–16102.

[180] A. S. Moskvin, A. A. Makhnev, L. V. Nomerovannaya, N. N. Loshkareva, A. M. Balbashov, *Phys. Rev. B* **2010**, *82*, 035106.

[181] B. Ifland, J. Hoffmann, B. Kressdorf, V. Roddatis, M. Seibt, C. Jooss, *New Journal of Physics* **2017**, *19*, 063046.

[182] P. Beaud, A. Caviezel, S. O. Mariager, L. Rettig, G. Ingold, C. Dornes, S.-W. Huang, J. A. Johnson, M. Radovic, T. Huber, T. Kubacka, A. Ferrer, H. T. Lemke, M. Chollet, D. Zhu, J. M. Glownia, M. Sikorski, A. Robert, H. Wadati, M. Nakamura, M. Kawasaki, Y. Tokura, S. L. Johnson, U. Staub, *Nature Materials* **2014**, *13*, 923.

[183] N. Kida, M. Tonouchi, *Applied Physics Letters* **2001**, *78*, 4115–4117.

[184] J. Bielecki, R. Rauer, E. Zanghellini, R. Gunnarsson, K. Dörr, L. Börjesson, *Phys. Rev. B* **2010**, *81*, 064434.

[185] A. I. Lobad, R. D. Averitt, A. J. Taylor, *Phys. Rev. B* **2001**, *63*, 060410.

[186] C. S. Nelson, M. v. Zimmermann, Y. J. Kim, J. P. Hill, D. Gibbs, V. Kiryukhin, T. Y. Koo, S.-W. Cheong, D. Casa, B. Keimer, Y. Tomioka, Y. Tokura, T. Gog, C. T. Venkataraman, *Phys. Rev. B* **2001**, *64*, 174405.

[187] E. Dagotto, *Nanoscale phase separation and colossal magnetoresistance : the physics of manganites and related compounds*, Springer, Berlin, **2003**.

[188] J. Kanamori, *Progress of Theoretical Physics* **1963**, *30*, 275–289.

[189] A. Askar, A. S. Cakmak, *The Journal of Chemical Physics* **1978**, *68*, 2794–2798.